State Convergence-based Control of a Multi-Master-Single-Slave Non-linear Teleoperation System

Umar Farooq[1,3], Jason Gu[1], Mohamed El-Hawary[1], Valentina E. Balas[2], Marius M. Balas [2], Ghulam Abbas[4], Muhammad Usman Asad[1], Jun Luo[5]

[1]Department of Electrical and Computer Engineering Dalhousie University, Halifax, N.S. B3H 4R2, Canada

[2]Department of Automatics and Applied Software, "Aurel Vlaicu" University of Arad, Romania

[3]Department of Electrical Engineering, University of The Punjab, Quaid-e-Azam Campus, Lahore, 54590 Pakistan

[4]Department of Electrical Engineering, The University of Lahore, Pakistan

[5]School of Mechatronic Engineering and Automation, Shanghai University, China

umar.farooq@dal.ca, jason.gu@dal.ca, elhawary@dal.ca, valentina.balas@uav.ro, marius.balas@uav.ro, ghulam.abbas@ee.uol.edu.pk, usman.asad@dal.ca, luojun@shu.edu.cn

Abstract: This paper presents the design of a state convergence based control scheme, for a multi-master-single-slave nonlinear teleoperation system. The control objective is that the slave follows the weighted motion of the master systems, in free motion, and the master systems receive the scaled force feedback, while the slave system is in contact with the environment. To achieve the desired objectives, extended state convergence architecture is modified and appropriate control gains are chosen following a Lyapunov based stability analysis. MATLAB simulations considering a two-degree-of-freedom tri-master-single-slave nonlinear teleoperation system are provided to show the validity of the proposed scheme.

Keywords: state convergence method; multilateral teleo-peration system; nonlinear dynamics; MATLAB/Simulink

1 Introduction

Teleoperation refers to the control of a remote process and forms an important class of robotics due to its wide range of applications [1]. Typical units of a teleoperation system are a human operator, master manipulator, communication channel, slave manipulator and the environment. The working of the system is such that the human operator initiates the task through the use of a master manipulator which is installed at the local site. This task-related information is then transmitted over the communication channel to the remote environment where the slave manipulator performs the desired task. At the same time, slave manipulator provides a feedback, which is representative of the remote environment conditions, to the human operator through the master manipulator who then can guide the slave manipulator by adapting to the environment conditions. This form of teleoperation system is known as bilateral, as the information flows both ways as opposed to the unilateral version where the flow of information is from master to slave side only. Clearly, the bilateral scheme is more reliable because of the presence of the feedback connection which provides the operator with a feel of environment. On the other hand, the presence of the feedback connection in a bilateral system poses a great challenge mainly because of the time delay in the communication channel and the uncertainties of different units complicate the problem further. A variety of control laws have been proposed in literature to stabilize the bilateral systems against the time delays of the communication channel while providing the satisfactory task performance [2]-[4]. The groundbreaking works on the use of transmission line theory and the wave variables in bilateral teleoperation systems form the basis of many other algorithms [5], [6]. Such a class of algorithms is collectively referred to as passivity paradigm for the bilateral control of teleoperation systems and by far, is the most popular choice for designing bilateral systems due to their strong robustness to time delays [7]. The other types of bilateral algorithms include sliding mode control [8], H∞ control [9], Lyapunov-Krasovskii functional based control [10], disturbance observer based control [11], adaptive control [12], intelligent control [13]-[15] and the state convergence based control [16], [17].

In recent years, another class of teleoperation system, known as multilateral teleoperation systems, has emerged due to the need of performing the remote tasks in a cooperative fashion. In order to maintain the stability and to ensure the satisfactory task performance in such systems, various control algorithms have also been proposed. Small gain theorem based approach is presented in [21] for a multi-master-single-slave teleoperation system where the slave system is influenced by the master systems according to a weighting criterion and a force feedback is provided equally to all the master systems. Based on the theory of adaptive control and wave variables, the control of an uncertain single-master-multi-slave teleoperation system is discussed in [22] where each slave is made to follow the master commands in the presence of time varying delays. A disturbance

observer-based scheme is presented in [23] to control a multi-master-single-slave teleoperation system with different degrees-of-freedom. In this method, reaction force is estimated and a modal transformation is introduced to accomplish the position and force tracking tasks. A Lyapunov-based approach is presented in [24], [25] to design a multilateral controller for dual-master-single-slave nonlinear teleoperation system. The approximation ability of fuzzy logic control has been used in [26] to design an adaptive controller for uncertain dual-master-dual-slave teleoperation system.

This paper presents the design of a time-delayed multi-master-single-slave nonlinear teleoperation system based on the method of state convergence. In our earlier work [27], we have presented an extended state convergence control architecture where *k*-master systems can cooperatively control *l*-slave systems. However, this extended state convergence method is only applicable to linear teleoperation systems when the communication channel offers no time delays. These two limitations have been addressed in this paper by considering the nonlinear dynamics of master/slave systems and constant asymmetric communication time delays. A Lyapunov-based stability analysis is presented and control gains of the extended state convergence method are selected to ensure the stability of the multilateral system against the communication time delays and to achieve the zero tracking error of the slave system. In order to validate the proposed scheme, MATLAB simulations are performed on a tri-master-single-slave nonlinear teleoperation system.

2 Modeling of Multilateral Nonlinear Teleoperation System

We consider a nonlinear multilateral teleoperation system which is comprised of n-degrees-of-freedom p-master and single-slave manipulators as:

$$M_m^j\left(q_m^j\right)\ddot{q}_m^j + C_m^j\left(q_m^j, \dot{q}_m^j\right)\dot{q}_m^j + g_m^j\left(q_m^j\right) = \tau_m^j + F_h^j, \forall j = 1,2,...,p \tag{1}$$

$$M_s\left(q_s\right)\ddot{q}_s + C_s\left(q_s, \dot{q}_s\right)\dot{q}_s + g_s\left(q_s\right) = \tau_s - F_e \tag{2}$$

Where $\left(M_m^j, M_s\right) \in ¡^{n\times n}$, $\left(C_m^j, C_s\right) \in ¡^{n\times n}$ and $\left(g_m^j, g_s\right) \in ¡^{n\times 1}$ represent inertia matrices, coriolis/centrifugal matrices and gravity vectors for master/slave systems respectively. Also, $\left(q_m^j, q_s\right) \in ¡^{n\times 1}$, $\left(\dot{q}_m^j, \dot{q}_s\right) \in ¡^{n\times 1}$, $\left(\ddot{q}_m^j, \ddot{q}_s\right) \in ¡^{n\times 1}$, $\left(\tau_m^j, \tau_s\right) \in ¡^{n\times 1}$ and $\left(F_h^j, F_e\right) \in ¡^{n\times 1}$ represent the joint variables of master/slave

manipulators namely position, velocity, acceleration, torque and external force signals, respectively. In the sequel, the following properties of the master/slave manipulators (1)-(2) will be utilized in proving the stability of the closed loop teleoperation system:

Property 1: The inertia matrices are symmetric, positive definite and bounded i.e., there exists positive constants β_l and β_u such that $0 < \beta_l I < M(q) < \beta_u I \leq \infty$.

Property 2: A skew-symmetric relation exists between the inertia and coriolis/centrifugal matrices such that $x^T\left(\dot{M}(q) - 2C\left(q, \dot{q}\right)\right)x = 0, \forall x \in \mathbb{R}^n$.

Property 3: The coriolis/centrifugal force vectors are bounded i.e., there exists positive constant β_f such that $\left\| C\left(q, \dot{q}\right)\dot{q} \right\| \leq \beta_f \left\| \dot{q} \right\|$.

Property 4: If the joint variables $\dot{q}$ and $\ddot{q}$ are bounded, then the time derivative of coriolis/centrifugal matrices is also bounded.

In addition to the above properties, we make the following assumptions:

Assumption 1: The gravity force vectors for the master/slave manipulators are assumed to be known.

Assumption 2: The operators are assumed to be passive i.e., there exist positive constants $\rho_m^j, j = 1, 2, ..., p$ such that $-\rho_m^j < \int_0^{t_f} -F_h^j \dot{q}_m^j \, dt$. Also, the environment is assumed to be passive and is modeled by a spring-damper system i.e., $F_e = K_e q_s + B_e \dot{q}_s$ where $K_e \in \mathbb{R}^{n \times n}$ and $B_e \in \mathbb{R}^{n \times n}$ are positive definite diagonal matrices.

In addition to the above properties and assumptions, we will use the following lemmas in proving the stability of the multilateral teleoperation formed by (1), (2):

Lemma 1: For any vector signals $x, y \in \mathbb{R}^n$ and scalar $\gamma > 0$, time delay T and positive definite matrix $K \in \mathbb{R}^{n \times n}$, the following inequality holds over the time interval [0, t_f]: $-2\int_0^{t_f} \dot{x}^T K \int_0^T \dot{y}(t-\sigma) d\sigma dt \leq \gamma \int_0^{t_f} \dot{x}^T K x dt + \frac{T^2}{\gamma} \int_0^{t_f} \dot{y}^T K y dt$

Lemma 2: For the vector signal $x \in \mathbb{R}^n$ and the time delay T, the following inequality holds: $x(t-T) - x(t) = \int_0^T \dot{x}(t-\sigma) d\sigma \leq T^{1/2} \left\| \dot{x} \right\|_2$

3 Modified Extended State Convergence Architecture

The authors recently proposed an extended-state convergence architecture [27] for *k*-master-*l*-slave delay-free linear teleoperation system, which can be modeled on state space. The aim of the present study is to explore the applicability of the extended state convergence architecture for nonlinear multilateral teleoperation system in the presence of asymmetric constant communication delays. For simplicity, a multi-master-single-slave nonlinear teleoperation system is considered in this paper which can be observed in literature. Further, the extended state convergence architecture is slightly modified by eliminating the gain terms G_{ij} which are responsible for direct transmission of operators' forces to slave systems. However, all other control gain terms are kept the same. Since the gravity force vectors are assumed to be known, they are included in torque inputs and will therefore become part of the extended state convergence architecture. The modified state convergence architecture is shown in Figure 1 and various parameters defining the architecture are described below:

F_h^j: It represents the force exerted by the j^{th} operator onto the j^{th} master manipulator.

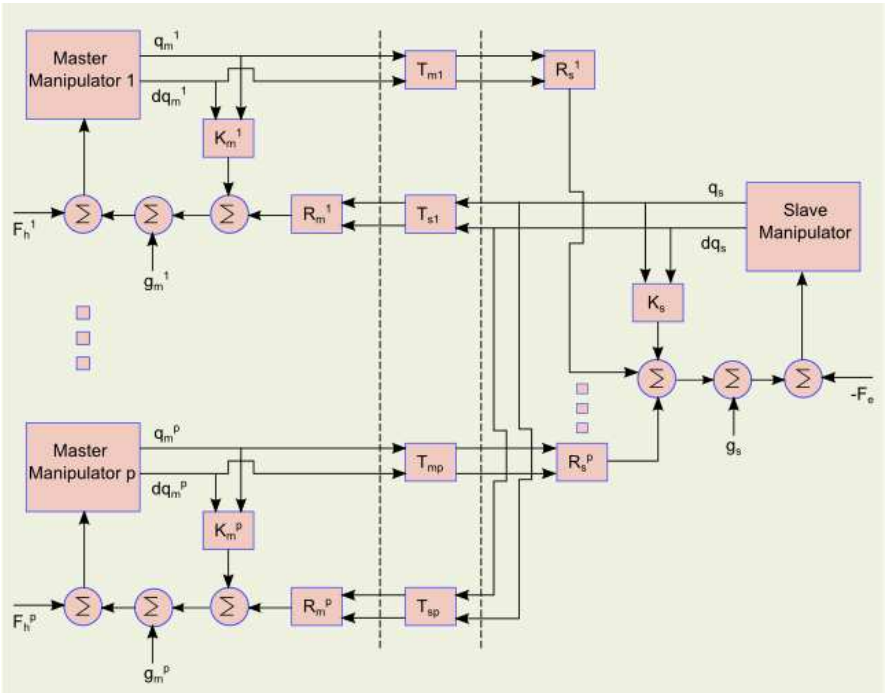

Figure 1
Modified extended state convergence architecture for multi-master-single-slave teleoperation

$K_m^j = \begin{bmatrix} K_{m1}^j & K_{m2}^j \end{bmatrix}$: It represents the stabilizing feedback gain for the j^{th} master manipulator. $K_{m1}^j \in \mathbb{R}^{n \times n}$ and $K_{m2}^j \in \mathbb{R}^{n \times n}$ are the state feedback gains for the j^{th} master's position and velocity signals respectively.

$K_s = \begin{bmatrix} K_{s1} & K_{s2} \end{bmatrix}$: It represents the stabilizing feedback gain for the slave manipulator. $K_{s1} \in \mathbb{R}^{n \times n}$ and $K_{s2} \in \mathbb{R}^{n \times n}$ are the state feedback gains for the slave's position and velocity signals respectively.

T_{mj}: It represents the constant time delay in the communication link connecting the j^{th} master system to the slave system.

T_{sj}: It represents the constant time delay in the communication link connecting the slave system to the j^{th} master system.

$R_s^j = \begin{bmatrix} R_{s1}^j & R_{s2}^j \end{bmatrix}$: It represents the influence of the motion signals generated by the j^{th} master manipulator (when operated by the jth human operator) into the slave manipulator. The matrices $R_{s1}^j \in \mathbb{R}^{n \times n}$ and $R_{s2}^j \in \mathbb{R}^{n \times n}$ weights the j^{th} master manipulator's position and velocity signals respectively.

$R_m^j = \begin{bmatrix} R_{m1}^j & R_{m2}^j \end{bmatrix}$: It represents the effect of slave's motion into the j^{th} master manipulator. The slave's position and velocity signals are weighted by the matrices $R_{m1}^j \in \mathbb{R}^{n \times n}$ and $R_{m2}^j \in \mathbb{R}^{n \times n}$ to influence the j^{th} master manipulator's motion.

4 Lyapunov-based Stability Analysis and Control Design

Using the modified extended state convergence architecture of figure 1, we intend to achieve the following control objectives:

Control Objective 1: The slave manipulator's motion is the weighted effect of the masters' manipulators' motion i.e.,

$$\lim_{t \to \infty} \left(q_s(t) - \sum_{j=1}^{p} \alpha_j q_m^j(t) \right) = 0 \tag{3}$$

Where α_j is a weighting factor which is used to scale the j^{th} master manipulator's motion and obeys the property: $\sum_{j=1}^{p} \alpha_j = 1$.

Control Objective 2: The static force reflected onto the j^{th} operator is a function of the environmental force and the other operator's applied torques i.e.,

$$F_h^j = f_j\left(F_e, F_h^{i,i\neq j,i=1,2,...,p}\right) \tag{4}$$

To achieve the above objectives and to show the system stability, state convergence-based closed loop multi-master-single-slave nonlinear teleoperation system will be analyzed using a Lyapunov-Krasovskii functional technique. Towards this end, we first write the control inputs for the master/slave systems using Figure 1 as:

$$\tau_m^j = g_m^j\left(q_m^j\right) + K_{m1}^j q_m^j + K_{m2}^j \dot{q}_m^j + R_{m1}^j q_s\left(t - T_{sj}\right) + R_{m2}^j \dot{q}_s\left(t - T_{sj}\right), \forall j = 1,2,...,p \tag{5}$$

$$\tau_s = g_s\left(q_s\right) + K_{s1} q_s + K_{s2} \dot{q}_s + \sum_{j=1}^{p} R_{s1}^j q_m^j\left(t - T_{mj}\right) + \sum_{j=1}^{p} R_{s2}^j \dot{q}_m^j\left(t - T_{mj}\right) \tag{6}$$

By plugging (5) in (1) and (6) in (2) and using the assumptions 2 and 3, the closed loop master/slave systems can be given as:

$$M_m^j \ddot{q}_m^j + C_m^j \dot{q}_m^j = K_{m1}^j q_m^j + K_{m2}^j \dot{q}_m^j + R_{m1}^j q_s\left(t - T_{sj}\right) + R_{m2}^j \dot{q}_s\left(t - T_{sj}\right) + F_h^j, \forall j = 1,2,...,p \tag{7}$$

$$M_s \ddot{q}_s + C_s \dot{q}_s = K_{s1} q_s + K_{s2} \dot{q}_s + \sum_{j=1}^{p} R_{s1}^j q_m^j\left(t - T_{mj}\right) + \sum_{j=1}^{p} R_{s2}^j \dot{q}_m^j\left(t - T_{mj}\right) - F_e \tag{8}$$

4.1 Position Coordination Behavior

We now show the stability analysis of the closed loop teleoperation system formed by (7) and (8) by introducing the following theorem:

Theorem 4.1: By selecting the control gains of the multi-master-single-slave teleoperation system (7), (8) as in (9) and on the satisfaction of the $p+1$ inequalities as in (10), the stability of the closed loop teleoperation system of (7), (8) can be demonstrated as in (11).

$$\begin{aligned} &K_{m1}^j = K_{s1} = -K, K_{m2}^j = K_{s2} = -3K_1, \forall j = 1,2,...,p \\ &R_{m1}^j = R_{s1}^j = \alpha_j K, R_{m2}^j = R_{s2}^j = 2\alpha_j K_1, \forall j = 1,2,...,p \end{aligned} \tag{9}$$

Where $K \in ¡^{n\times n}$ and $K_1 \in ¡^{n\times n}$ are positive definite diagonal matrices.

$$\begin{aligned}&\left(3-2\alpha_j\right)K_1-\frac{\alpha_j\gamma_{sj}}{2}K-\frac{\alpha_j T_{mj}^2}{2\gamma_{mj}}K>0,\forall j=1,2,...,p\\&K_1-\sum_{j=1}^{p}\frac{\alpha_j\gamma_{mj}}{2}K-\sum_{j=1}^{p}\frac{\alpha_j T_{sj}^2}{2\gamma_{sj}}K>0\end{aligned}\tag{10}$$

Where γ_{mj} , γ_{sj} are positive scalar constants.

$$\lim_{t\to\infty}=\dot{q}_m^j=\lim_{t\to\infty}=\dot{q}_s=\lim_{t\to\infty}=\ddot{q}_m^j=\lim_{t\to\infty}=\ddot{q}_s=0,\forall j=1,2,...,p\tag{11}$$

Proof: Consider the following Lyapunov-Krasovskii functional:

$$\begin{aligned}&V\left(\dot{q}_m^j,\dot{q}_s,q_m^j-q_s,q_s,q_m^j\right)=\frac{1}{2}\sum_{j=1}^{p}\dot{q}_m^{jT}M_m^j\dot{q}_m^j+\frac{1}{2}\dot{q}_s^{\,T}M_s\dot{q}_s+\frac{1}{2}q_s^{\,T}K_e q_s\\&\frac{1}{2}\sum_{j=1}^{p}\left(1-\alpha_j\right)q_m^{jT}Kq_m^j+\sum_{j=1}^{p}\int_0^t-\dot{q}_m^{jT}\left(\xi\right)F_h^j\left(\xi\right)d\xi+\int_0^t-\dot{q}_m^{jT}\left(\xi\right)F_e\left(\xi\right)d\xi+\\&\sum_{j=1}^{p}\rho_m^j+\frac{1}{2}\sum_{j=1}^{p}\alpha_j\left(q_m^j-q_s\right)^T K\left(q_m^j-q_s\right)+\sum_{j=1}^{p}\alpha_j\int_{t-T_{mj}}^{t}\dot{q}_m^{jT}\left(\xi\right)K_1\dot{q}_m^j\left(\xi\right)d\xi\\&+\sum_{j=1}^{p}\alpha_j\int_{t-T_{sj}}^{t}\dot{q}_s^{\,T}\left(\xi\right)K_1\dot{q}_s\left(\xi\right)d\xi\end{aligned}\tag{12}$$

By taking the time-derivative of (12) along the system trajectories defined by (7) and (8), and using the passivity assumption 2 along with the property 2 of the robot dynamics, we have:

$$\begin{aligned}&\dot{V}=\sum_{j=1}^{p}\dot{q}_m^{jT}\left(K_{m1}^j q_m^j+K_{m2}^j\dot{q}_m^j+R_{m1}^j q_s\left(t-T_{sj}\right)+R_{m2}^j\dot{q}_s\left(t-T_{sj}\right)\right)+\\&\dot{q}_s^{\,T}\left(K_{s1}q_s+K_{s2}\dot{q}_s+\sum_{j=1}^{p}R_{s1}^j q_m^j\left(t-T_{mj}\right)+\sum_{j=1}^{p}R_{s2}^j\dot{q}_m^j\left(t-T_{mj}\right)-K_e q_s-B_e\dot{q}_s\right)\\&+\dot{q}_s^{\,T}K_e q_s+\sum_{j=1}^{p}\left(1-\alpha_j\right)\dot{q}_m^{jT}Kq_m^j+\sum_{j=1}^{p}\alpha_j\dot{q}_m^{jT}K\left(q_m^j-q_s\right)+\\&\sum_{j=1}^{p}\alpha_j\dot{q}_s^{\,T}K\left(q_s-q_m^j\right)+\sum_{j=1}^{p}\alpha_j\dot{q}_m^{jT}K_1\dot{q}_m^j-\sum_{j=1}^{p}\alpha_j\dot{q}_m^{jT}\left(t-T_{mj}\right)K_1\dot{q}_m^j\left(t-T_{mj}\right)\\&+\sum_{j=1}^{p}\alpha_j\dot{q}_s^{\,T}K_1\dot{q}_s-\sum_{j=1}^{p}\alpha_j\dot{q}_s^{\,T}\left(t-T_{sj}\right)K_1\dot{q}_s\left(t-T_{sj}\right)\end{aligned}\tag{13}$$

After simplifying and grouping the terms in (13), we get:

$$\begin{aligned}
&\dot{V} = \sum_{j=1}^{p} \dot{q}_m^{jT} \left(K_{m1}^j + K \right) q_m^j + \sum_{j=1}^{p} \dot{q}_m^{jT} \left(R_{m1}^j q_s \left(t - T_{sj} \right) - \alpha_j K q_s \right) + \\
&\dot{q}_s^T \left(K_{s1} + \sum_{j=1}^{p} \alpha_j K \right) q_s + \sum_{j=1}^{p} \dot{q}_s^T \left(R_{s1}^j q_m^j \left(t - T_{mj} \right) - \alpha_j K q_m^j \right) + \\
&\sum_{j=1}^{p} \dot{q}_m^{jT} \left(K_{m2}^j + \alpha_j K_1 \right) \dot{q}_m^j + \sum_{j=1}^{p} \dot{q}_s^T \left(K_{s2} + \sum_{j=1}^{p} \alpha_j K_1 \right) \dot{q}_s - \dot{q}_s^T B_e \dot{q}_s \\
&+ \sum_{j=1}^{p} \dot{q}_m^{jT} R_{m2}^j \dot{q}_s \left(t - T_{sj} \right) + \sum_{j=1}^{p} \dot{q}_s^T R_{s2}^j \dot{q}_m^j \left(t - T_{mj} \right) - \\
&\sum_{j=1}^{p} \alpha_j \dot{q}_m^{jT} \left(t - T_{mj} \right) K_1 \dot{q}_m^j \left(t - T_{mj} \right) - \sum_{j=1}^{p} \alpha_j \dot{q}_s^T \left(t - T_{sj} \right) K_1 \dot{q}_s \left(t - T_{sj} \right)
\end{aligned} \tag{14}$$

By plugging the control gains of (9) in (14), and by adding and subtracting the terms $\sum_{j=1}^{p} \alpha_j \dot{q}_m^{jT} K_1 \dot{q}_m^j$, $\sum_{j=1}^{p} \alpha_j \dot{q}_s^T K_1 \dot{q}_s$ from (14), we have:

$$\begin{aligned}
&\dot{V} = \sum_{j=1}^{p} \alpha_j \dot{q}_m^{jT} K \left(q_s \left(t - T_{sj} \right) - q_s \right) + \sum_{j=1}^{p} \alpha_j \dot{q}_s^T K \left(q_m^j \left(t - T_{mj} \right) - q_m^j \right) \\
&- \sum_{j=1}^{p} \dot{q}_m^{jT} \left(3 - 2\alpha_j \right) K_1 \dot{q}_m^j - \dot{q}_s^T K_1 \dot{q}_s - \dot{q}_s^T B_e \dot{q}_s \\
&- \sum_{j=1}^{p} \alpha_j \left(\dot{q}_m^{jT} K_1 \dot{q}_m^j + \dot{q}_m^{jT} \left(t - T_{mj} \right) K_1 \dot{q}_m^j \left(t - T_{mj} \right) - 2 \dot{q}_s^T K_1 \dot{q}_m^j \left(t - T_{mj} \right) \right) \\
&- \sum_{j=1}^{p} \alpha_j \left(\dot{q}_s^T K_1 \dot{q}_s + \dot{q}_s^T \left(t - T_{sj} \right) K_1 \dot{q}_s \left(t - T_{sj} \right) - 2 \dot{q}_m^{jT} K_1 \dot{q}_s \left(t - T_{sj} \right) \right)
\end{aligned} \tag{15}$$

Now, we define the following error signals:

$$\begin{aligned}
e_{q_s^j} &= q_s - q_m^j \left(t - T_{mj} \right) \\
e_{q_m^j} &= q_m^j - q_s \left(t - T_{sj} \right)
\end{aligned} \tag{16}$$

By re-writing (15) in terms of the time-derivatives of the error signals of (16) and using the relation $q(t-T) - q(t) = -\int_0^T \dot{q}(t-\sigma) d\sigma$, we have:

$$\dot{V} = -\sum_{j=1}^{p} \alpha_j \dot{q}_m^{jT} K \int_0^{T_{sj}} \dot{q}_s(t-\sigma)d\sigma - \sum_{j=1}^{p} \alpha_j \dot{q}_s^T K \int_0^{T_{mj}} \dot{q}_m^j(t-\sigma)d\sigma -$$
$$\sum_{j=1}^{p} \dot{q}_m^{jT}(3-2\alpha_j) K_1 \dot{q}_m^j - \dot{q}_s^T K_1 \dot{q}_s - \dot{q}_s^T B_e \dot{q}_s - \sum_{j=1}^{p} \alpha_j \dot{e}_{q_s^j}^T K_1 \dot{e}_{q_s^j} \quad (17)$$
$$-\sum_{j=1}^{p} \alpha_j \dot{e}_{q_m^j}^T K_1 \dot{e}_{q_m^j}$$

By integrating (17) over the time interval [0, t_f] and using lemma 1, we get:

$$\int_0^{t_f} \dot{V}\, ds \le \sum_{j=1}^{p} \alpha_j \left(\frac{\gamma_{sj}}{2} \int_0^{t_f} \dot{q}_m^{jT} K \dot{q}_m^j\, ds + \frac{T_{sj}^2}{2\gamma_{sj}} \int_0^{t_f} \dot{q}_s^T K \dot{q}_s ds \right) +$$
$$\sum_{j=1}^{p} \alpha_j \left(\frac{\gamma_{mj}}{2} \int_0^{t_f} \dot{q}_s^T K \dot{q}_s\, ds + \frac{T_{mj}^2}{2\gamma_{mj}} \int_0^{t_f} \dot{q}_m^{jT} K \dot{q}_m^j\, ds \right) -$$
$$\sum_{j=1}^{p} \int_0^{t_f} \dot{q}_m^{jT}(3-2\alpha_j) K_1 \dot{q}_m^j\, ds - \int_0^{t_f} \dot{q}_s^T K_1 \dot{q}_s\, ds - \int_0^{t_f} \dot{q}_s^T B_e \dot{q}_s\, ds \quad (18)$$
$$-\sum_{j=1}^{p} \alpha_j \int_0^{t_f} \dot{e}_{q_s^j}^T K_1 \dot{e}_{q_s^j}\, ds - \sum_{j=1}^{p} \alpha_j \int_0^{t_f} \dot{e}_{q_m^j}^T K_1 \dot{e}_{q_m^j}\, ds$$

By grouping the terms in (18), we can simplify the bound on the time-derivative of the Lyapunov- Krasovskii functional as:

$$V(t_f) - V(0) \le -\sum_{j=1}^{p} \lambda_{\min} \left((3-2\alpha_j) K_1 - \frac{\alpha_j \gamma_{sj}}{2} K - \frac{T_{mj}^2}{2\gamma_{mj}} K \right) \left\| \dot{q}_m^j \right\|_2^2$$
$$-\sum_{j=1}^{p} \lambda_{\min} \left(K_1 - \frac{\alpha_j \gamma_{mj}}{2} K - \frac{T_{sj}^2}{2\gamma_{sj}} K \right) \left\| \dot{q}_s \right\|_2^2 - \sum_{j=1}^{p} \lambda_{\min}(\alpha_j K_1) \left\| \dot{e}_{q_s^j} \right\|_2^2 \quad (19)$$
$$-\sum_{j=1}^{p} \lambda_{\min}(\alpha_j K_1) \left\| \dot{e}_{q_m^j} \right\|_2^2 - \lambda_{\min}(B_e) \left\| \dot{q}_s \right\|_2^2$$

Now, if the inequalities in (10) are satisfied, the right hand side of (19) will remain negative. Since $V(0)$ and $V(t_f)$ are positive and right hand side of (19) is negative, it can be concluded that $V(t_f)$-$V(0)$ remains bounded ensuring that $V(t_f)$ will remain bounded. Taking the limit as $t_f \to \infty$ and using the robot properties, it can be said that the signals $\left\{ \dot{q}_m^j, \dot{q}_s, q_m^j - q_s, q_s, q_m^j \right\} \in L_\infty$ and $\left\{ \dot{q}_m^j, \dot{q}_s, \dot{e}_{q_s^j}, \dot{e}_{q_m^j} \right\} \in L_2$. To prove the system stability in the sense of (11), we have to show that the acceleration signals of master/slave systems and their time derivatives remain bounded. To this end, we rewrite (7) and (8) without external forces (since they are assumed to be passive and bounded) as:

$$\ddot{q}_m^j = \left(M_m^j\right)^{-1}\left[-C_m^j \dot{q}_m^j + K_{m1}^j q_m^j + K_{m2}^j \dot{q}_m^j + R_{m1}^j q_s\left(t-T_{sj}\right) + R_{m2}^j \dot{q}_s\left(t-T_{sj}\right)\right] \tag{20}$$

$$\ddot{q}_s = M_s^{-1}\left[-C_s \dot{q}_s + K_{s1} q_s + K_{s2} \dot{q}_s + \sum_{j=1}^{p} R_{s1}^j q_m^j\left(t-T_{mj}\right) + \sum_{j=1}^{p} R_{s2}^j \dot{q}_m^j\left(t-T_{mj}\right)\right] \tag{21}$$

By considering the control gains of (9) along with (20) and (21), it is now required to show that the signals $\left\{q_m^j - \alpha_j q_s\left(t-T_{sj}\right), q_s - \sum_{j=1}^{p}\alpha_j q_m^j\left(t-T_{mj}\right)\right\} \in L_\infty$. These signals can be written as:

$$\begin{aligned} q_m^j - \alpha_j q_s\left(t-T_{sj}\right) &= \left(q_m^j - \alpha_j q_s\right) + \alpha_j\left(q_s - q_s\left(t-T_{sj}\right)\right) \\ q_s - \sum_{j=1}^{p}\alpha_j q_m^j\left(t-T_{mj}\right) &= \left(q_s - \sum_{j=1}^{p}\alpha_j q_m^j\right) + \sum_{j=1}^{p}\alpha_j\left(q_m^j - \alpha_j q_m^j\left(t-T_{mj}\right)\right) \end{aligned} \tag{22}$$

The first set of parentheses on the right hand sides of (22) are bounded by virtue of $\left\{\dot{q}_m^j, \dot{q}_s, q_m^j - q_s\right\} \in L_\infty$ while the second set of parentheses are bounded by virtue of lemma 2 and $\left\{\dot{q}_m^j, \dot{q}_s\right\} \in L_\infty$. This implies that the left hand sides of (22) are also bounded. By using the properties 1 and 3 of the robot dynamics and the result $\left\{\dot{q}_m^j, \dot{q}_s, q_m^j - q_s, q_s, q_m^j, q_m^j - \alpha_j q_s\left(t-T_{sj}\right), q_s - \sum_{j=1}^{p}\alpha_j q_m^j\left(t-T_{mj}\right)\right\} \in L_\infty$, it can be concluded that the signals $\left\{\ddot{q}_m^j, \ddot{q}_s\right\}$ are bounded. Since the signals $\left\{\dot{q}_m^j, \dot{q}_s\right\}$ also belong to L_2, then by Barbalat's lemma: $\lim_{t\to\infty}\dot{q}_m^j = \lim_{t\to\infty}\dot{q}_s = \lim_{t\to\infty}\dot{e}_{q_m^j} = \lim_{t\to\infty}\dot{e}_{q_s^j} = 0$. Now, it is left to show the boundedness of the time derivatives of (20) and (21) to complete the proof. By taking their time derivatives, we have:

$$\begin{aligned} \frac{d\,\ddot{q}_m^j}{dt} = {} & \frac{d}{dt}\left(M_m^j\right)^{-1}\left[-C_m^j \dot{q}_m^j + K_{m1}^j q_m^j + K_{m2}^j \dot{q}_m^j + R_{m1}^j q_s\left(t-T_{sj}\right) + R_{m2}^j \dot{q}_s\left(t-T_{sj}\right)\right] \\ & + \left(M_m^j\right)^{-1}\frac{d}{dt}\left[-C_m^j \dot{q}_m^j + K_{m1}^j q_m^j + K_{m2}^j \dot{q}_m^j + R_{m1}^j q_s\left(t-T_{sj}\right) + R_{m2}^j \dot{q}_s\left(t-T_{sj}\right)\right] \end{aligned} \tag{23}$$

$$\frac{d\,\ddot{q}_s}{dt} = \frac{d}{dt}\left(M_s^{-1}\right)\left[-C_s\,\dot{q}_s + K_{s1}q_s + K_{s2}\,\dot{q}_s + \sum_{j=1}^{p} R_{s1}^{j} q_m^{j}\left(t-T_{mj}\right) + \sum_{j=1}^{p} R_{s2}^{j}\,\dot{q}_m^{j}\left(t-T_{mj}\right)\right] + M_s^{-1}\frac{d}{dt}\left[-C_s\,\dot{q}_s + K_{s1}q_s + K_{s2}\,\dot{q}_s + \sum_{j=1}^{p} R_{s1}^{j} q_m^{j}\left(t-T_{mj}\right) + \sum_{j=1}^{p} R_{s2}^{j}\,\dot{q}_m^{j}\left(t-T_{mj}\right)\right] \tag{24}$$

By using the properties 3 and 4 of the robot dynamics and the earlier result $\left\{\dot{q}_m^{j}, \dot{q}_s, q_m^{j}-q_s, q_s, q_m^{j}, q_m^{j}-\alpha_j q_s\left(t-T_{sj}\right), q_s-\sum_{j=1}^{p}\alpha_j q_m^{j}\left(t-T_{mj}\right), \ddot{q}_m^{j}, \ddot{q}_s\right\} \in L_\infty$, it can be concluded that the second derivative terms in (23) and (24) are bounded. The boundedness of the first derivative terms in (23) and (24) follows from the properties 1 and 2 of the robot dynamics, the boundedness of the signals $\left\{\dot{q}_m^{j}, \ddot{q}_m^{j}, \dot{q}_s, \ddot{q}_s\right\}$ and considering $\dot{M}^{-1} = -M^{-1}\dot{M}\,M^{-1} = -M^{-1}\left(C+C^{T}\right)M^{-1}$. Thus the right hand sides of (23) and (24) remain bounded implying that the signals $\left\{\ddot{q}_m^{j}, \ddot{q}_s\right\} \in L_\infty$ are uniformly continuous. Therefore, we have: $\lim_{t\to\infty}\ddot{q}_m^{j} = \lim_{t\to\infty}\ddot{q}_s = 0$. This completes the proof.

Theorem 4.2: The desired position of the slave system, as mentioned in (3), is achieved under the control gains of (9) and the condition that the signals $\left\{\dot{q}_s, \dot{q}_m^{j}, \ddot{q}_s, \ddot{q}_m^{j}, \dot{e}_{q_s^{j}}, \dot{e}_{q_m^{j}}\right\}$ converge to zero as $t \to \infty$.

Proof: The convergence of the signals $\left\{\dot{q}_s, \dot{q}_m^{j}, \ddot{q}_s, \ddot{q}_m^{j}, \dot{e}_{q_s^{j}}, \dot{e}_{q_m^{j}}\right\}$ has been shown in Theorem 4.1. Thus, by using the results from Theorem 4.1 and by substituting the control gains of (9) in (8), we have:

$$\lim_{t\to\infty}\left\| q_s - \sum_{j=1}^{p}\alpha_j q_m^{j}\left(t-T_{mj}\right)\right\| = 0 \tag{25}$$

By using the relation $q_m^{j}\left(t-T_{mj}\right) = q_m^{j} - \int_{t-T_{mj}}^{t}\dot{q}_m^{j}\left(\xi\right)d\xi$, and the result $\lim_{t\to\infty}\dot{q}_m^{j} = 0$, we can write (25) as: $\lim_{t\to\infty}\left\| q_s - \sum_{j=1}^{p}\alpha_j q_m^{j}\right\| = 0$. Thus, slave position coordination is achieved in the absence of environmental force as time goes to infinity and control objective 1 is achieved. This completes the proof.

4.2 Force Reflection Behavior

Let us now investigate the force experienced by the operators in steady state when the slave is in contact with the environment. Towards this end, the steady state behavior of the closed loop master systems' (when the velocity and acceleration signals converges to zero) is first found from (7) as:

$$K_{m1}^{j} q_{m}^{j} + R_{m1}^{j} q_{s}\left(t - T_{sj}\right) + F_{h}^{j} = 0, \forall j = 1, 2, ..., p \tag{26}$$

By using the relation $q_s\left(t - T_{sj}\right) = q_s - \int_{t-T_{sj}}^{t} \dot{q}_s\left(\xi\right) d\xi$ and the earlier result from stability analysis $\lim_{t\to\infty} \dot{q}_s = 0$, and the control gains of (9), operators' forces in (26) can be given as:

$$F_{h}^{j} = K\left(q_{m}^{j} - \alpha_{j} q_{s}\right), \forall j = 1, 2, ..., p \tag{27}$$

Similarly, the behavior of the slave system in steady state including the environmental force can be obtained from (8), (9) and two earlier theorems as:

$$F_{e} = -K q_{s} + \sum_{j=1}^{p} \alpha_{j} K q_{m}^{j} \tag{28}$$

By adding and subtracting $\sum_{j=1}^{p} \alpha_{j}^{2} K q_{s}$ from (28), we can write the environmental force in terms of operators' forces as:

$$F_{e} = \sum_{j=1}^{p} \alpha_{j} F_{h}^{j} - \left(1 - \sum_{j=1}^{p} \alpha_{j}^{2}\right) K q_{s} \tag{29}$$

From (29), it is evident that the environmental force is indeed proportional to the weighted effect of the operators' forces. Thus, the second control objective of (4) is also achieved.

5 Simulation Results

The proposed state convergence based scheme for multi-master-single-slave teleoperation system is verified in MATLAB/Simulink environment using a two degrees-of-freedom three masters and one slave manipulators with the dynamics of (1), (2). The corresponding inertia matrices, coriolis/centrifugal matrices and gravity vectors are given in (30)-(33):

$$M(q)=\begin{bmatrix} m_{11} & m_{12} \\ m_{21} & m_{22} \end{bmatrix}, C\left(q,\dot{q}\right)=\begin{bmatrix} c_{11} & c_{12} \\ c_{21} & c_{22} \end{bmatrix}, g(q)=\begin{bmatrix} g_1 \\ g_2 \end{bmatrix} \tag{30}$$

$$\begin{aligned} m_{11} &= m_2 l^2 + (m_1+m_2) l^2 + 2m_2 l^2 \cos(q_2) \\ m_{12} &= m_{21} = m_2 l^2 + m_2 l^2 \cos(q_2) \\ m_{22} &= m_2 l^2 \end{aligned} \tag{31}$$

$$\begin{aligned} c_{11} &= -\dot{q}_2 m_2 l^2 \sin(q_2), c_{12} = -\left(\dot{q}_1+\dot{q}_2\right) m_2 l^2 \sin(q_2) \\ c_{21} &= \dot{q}_1 m_2 l^2 \sin(q_2), c_{22} = 0 \end{aligned} \tag{32}$$

$$g_1 = a_g m_2 l \sin(q_1+q_2) + a_g (m_1+m_2) l \sin(q_1), g_2 = a_g m_2 l \sin(q_1+q_2) \tag{33}$$

Where m_1, m_2 are the masses of links 1 and 2 respectively; $l_1 = l_2 = l$ are the lengths of links and a_g is the acceleration due to gravity. By setting the parameters for the master systems as: $m_{1m} = m_{2m} = 2kg, l_m = 1m$ and the slave system as: $m_{1s} = m_{2s} = 10kg, l_s = 1m$ and by defining the alpha influencing factors for the master systems as: $\alpha_1 = 0.5, \alpha_2 = 0.3, \alpha_3 = 0.2$ and by setting the gamma values as unity and by assuming the time delays in the communication channel as: $T_{m1} = T_{s1} = 1s, T_{m2} = T_{s2} = 0.5s, T_{m3} = T_{s3} = 2s$, we solve the inequalities of (10) and subsequently select the decisive positive definite matrices as: $K = diag(20,10), K_1 = diag(40,20)$. The control gains for the multi-master-single-slave nonlinear teleoperation system can now be found using (9).

We first simulate the tri-master-single-slave nonlinear teleoperation system under the control of constant operators' forces and in the absence of environment forces. The human forces are $F_h^j(t) = F_{op}^j, t \le 150s, \left(F_{op}^1 = 5N, F_{op}^2 = 2N, F_{op}^3 = 3N\right)$ which vanish after 150 *sec*. The results for this simulation are shown in Figure 2. It can be seen that the multilateral system remains stable, owing to the boundedness of the signals and both the joint positions of the slave system converge to the desired references. We also consider the realistic case where the operators' forces vary linearly with time. The simulation results for this case are shown in Figure 3. It can again be seen that the slave position signals indeed follow the desired reference positions. Finally, we simulate the nonlinear teleoperation system in the presence of environment forces considering the constant operators' forces. The simulation results for this case are depicted in Figure 4 where the slave comes in contact with the environment at *t*=150 *sec*. After the contact is made, masters' positions are reduced and the slave is unable to follow the set references. This is in line with the theoretical results. The reduction in masters' positions is due to the force reflected onto the masters' systems by the slave system when it is in contact

with the environment while the error in slave's desired trajectory is the result of its direct interaction with the environment as can be seen from (28).

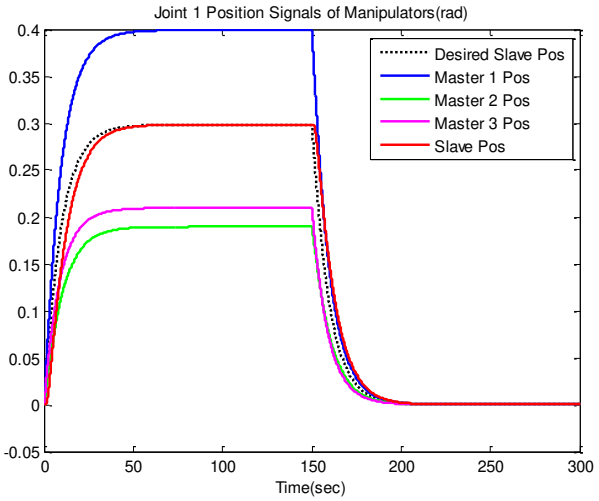

(a)

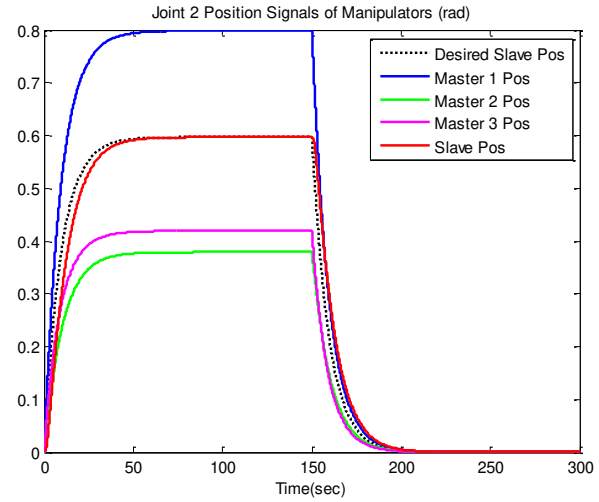

(b)

Figure 2

Tri-master-single-slave nonlinear teleoperation system with constant operator forces in free motion (a) Joint 1 position signals (b) Joint 2 position signals

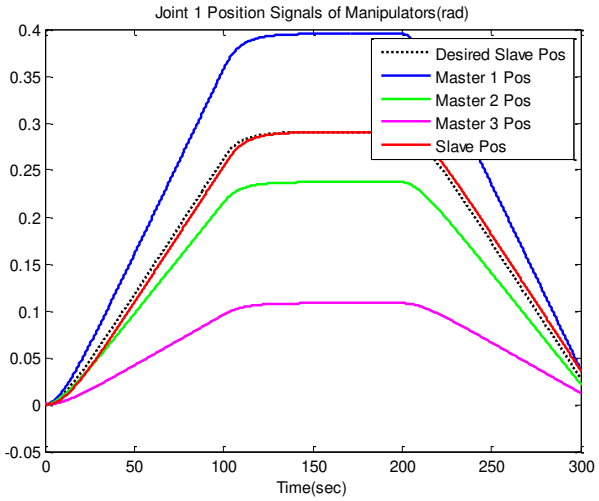

(a)

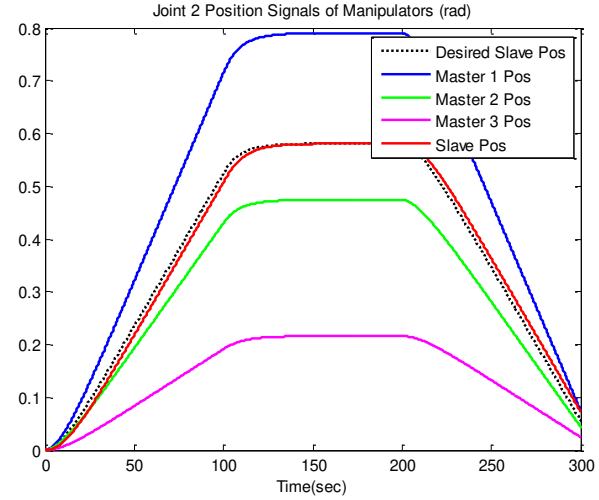

(b)

Figure 3
Tri-master-single-slave nonlinear teleoperation system with time varying operator forces in free motion
(a) Joint 1 position signals (b) Joint 2 position signals

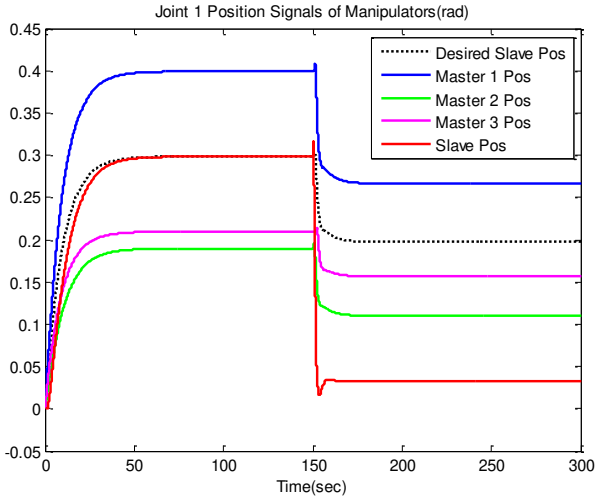

(a)

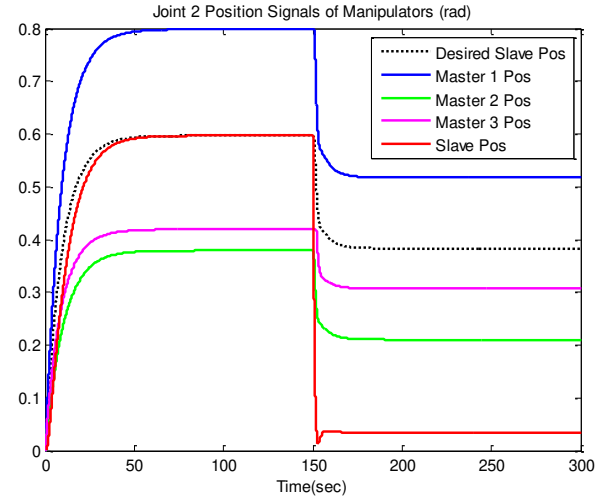

(b)

Figure 4

Tri-master-single-slave nonlinear teleoperation system in free plus contact motion (a) Joint 1 position signals (b) Joint 2 position signals

Conclusions

In this work, the design of a multi-master-single-slave nonlinear teleoperation system in the presence of asymmetric constant communication time delays is presented, based on the extended state convergence theory. A Lyapunov-based stability analysis is carried out to find the control gains for the modified extended

state convergence architecture. The efficacy of the proposed scheme is finally verified through simulations in the MATLAB/Simulink environment by considering a two degrees-of-freedom, tri-master-single-slave robotic system. Future work involves the design of state convergence based multilateral nonlinear teleoperation system in the presence of time varying delays with experimental validation.

Acknowledgement

This work was supported by Natural Sciences and Engineering Research Council of Canada and by Nova Scotia Graduate Scholar Program.

References

[1] M. Ferre, M. Buss, R. Aracil, C. Melchiorri, C. Balaguer: Advances in Telerobotics, Springer, 2007

[2] P. F. Hokayem, M. W. Spong: Bilateral teleoperation: an Historical Survey, Automatica, Vol. 42, 2006, pp. 2035-2057

[3] R. Muradore, P. Fiorini: A Review of Bilateral Teleoperation Algorithms, Acta Polytechnica Hungarica, Vol. 13, No. 1, 2016, pp. 191-208

[4] J. Artigas, G. Hirzinger: A Brief History of DLR's Space Telerobotics and Force Feedback Teleoperation, Acta Polytechnica Hungarica, Vol. 13, No. 1, 2016, pp. 239-249

[5] R. Anderson, M. W. Spong: Bilateral Control of Teleoperators with Time Delay: IEEE Transactions on Automatic Control, Vol. 34, No. 5, 1989, pp. 494-501

[6] G. Niemeyer, J. J. E. Slotine: Stable Adaptive Teleoperation, IEEE Journal of Oceanic Engineering, Vol. 16, No. 1, 1991, pp. 152-162

[7] J. Ryu, D. Kwon, B. Hannaford: Stable Teleoperation with Time-Domain Passivity Control, IEEE Transactions on Robotics and Automation, Vol. 20, No. 2, 2004, pp. 365-373

[8] A. Hace, M. Franc: FPGA Implementation of Sliding Mode Control Algorithm for Scaled Bilateral teleoperation, IEEE Transactions on Industrial Electronics, Vol. 9, No. 3, 2013, pp. 1291-1300

[9] M. Boukhnifer, A. Ferreira: H∞ Loop Shaping Bilateral Controller for a Two-fingered Tele-Micromanipulation System, IEEE Transations on Control Systems Technology, Vol. 15, No. 5, 2007, pp. 891-905

[10] S. Islam, P. X. Liu, A. El-Saddik: Bilateral Control of Teleoperation Systems, Vol. 20, No. 1, 2015, pp. 1-12

[11] A. Suzuki, K. Ohnishi: Frequency Domain Damping Design for Time Delayed Bilateral teleoperation System Based on Modal Space Analysis,

IEEE Transactions on Industrial Electronics, Vol. 60, No. 1, 2013, pp. 177-190

[12] L. Chan, F. Naghdy, D. Stirling: Application of Aadaptive Controllers in teleoperation Systems, IEEE Transactions on Human-Machine Systems, Vol. 44, No. 3, 2014, pp. 337-352

[13] V. T. Minh, F. M. Hashim: Adaptive Teleoperation System with Neural Network Based Multiple Model Control, Mathematical Problems in Engineering, Vol. 2010, pp. 1-16

[14] U. Farooq, J. Gu, M. El-Hawary, M. U. Asad, G. Abbas: Fuzzy Model Based Bilateral Control Design of Nonlinear teleoperation System Using Method of State Convergence, IEEE Access, Vol. 4, 2016, pp. 4119-4135

[15] U. Farooq, J. Gu, M. El-Hawary, V. E. Balas, M. U. Asad, G. Abbas: Fuzzy Model Based Design of a Transparent Controller for a Time Delayed Bilateral teleoperation System Through State Convergence, Acta Polytechnica Hungarica, Vol. 8, No. 14, 2017, pp. 7-26

[16] J. M. Azorin, O. Reinoso, R. Aracil, M. Ferre: Generalized Control Method by State Convergence of teleoperation Systems with Time Delay, Automatica, Vol. 40, No. 9, 2004, pp. 1575-1582

[17] J. C. Tafur, C. Garcia, R. Aracil, R. Saltaren: Control of Nonlinear teleoperation System by State Convergence, Proc. IEEE International Conference on Control and Automation, 2011, pp. 489-494

[18] R. Kubo, T. Shimono, K. Ohnishi: Flexible Controller Design of Bilateral Grasping Systems Based on a Multilateral Control Scheme, IEEE Transactions on Industrial Electronics, Vol. 56, No. 1, 2009, pp. 62-68

[19] S. Katsura, T. Suzuyama and K. Ohishi: A Realization of Multilateral Force Feedback Control for Cooperative Motion, IEEE Transactions on Industrial Electronics, Vol. 54, No. 6, 2007, pp. 3298-3306

[20] B. Khademian and K. Hashtrudi-Zaad: A Framework for Unconditional Stability Analysis of Multimaster/Multislave teleoperation Systems, IEEE Transactions on Robotics, Vol. 29, No. 3, 2013, pp. 684-694

[21] M. Shahbazi, S. F. Atashzar, H. A. Talebi, R. V. Patel: Novel Cooperative teleoperation Framework: Multi-Master/Single-Slave System, IEEE Transactions on Mechatronics, Vol. 20, No. 4, 2015, pp. 1668-1679

[22] D. Sun, F. Naghdy, H. Du: Stability Control of Force-Reflected Nonlinear Multilateral teleoperation System under Time Varying Delays, Journal of Sensors, Vol. 2016, pp. 1-17

[23] S. Katsura, T. Suzuyama, K. Ohishi: A Realization of Multilateral Force Feedback Control for Cooperative Motion, IEEE Transactions on Industrial Electronics, Vol. 54, No. 6, 2007, pp. 3298-3306

[24] F. Hashemzadeh, M. Sharifi, M. Tavakoli: Nonlinear Trilateral teleoperation Stability Analysis Subjected to Time Varying Delays, Control Engineering Practice, Vol. 56, 2016, pp. 123-135

[25] A. Ghorbanian, S. M. Rezaei, A. R. Khooger, M. Zareinejad, K. Baghestan: A Novel Control Framework for Nonlinear Time Delayed Dual-Master/Single-Slave teleoperation, Vol. 52, 2013, pp. 268-277

[26] Z. Li, Y. Xia, F. Sun: Adaptive Fuzzy Control of Multilateral Cooperative teleoperation of Mutiple Robotic Manipulators under Random Network Induced Delays, IEEE Transactions on Fuzzy Systems, Vol. 22, No. 2, 2014, pp. 437-450

[27] U. Farooq, J. Gu, M. El-Hawary, M. U. Asad, J. Luo: An Extended State Convergence Architecture for Multilateral Teleoperation Systems, IEEE Access, Vol. 5, 2017, pp. 2063-2079

Development of the Information and Analytical System in the Control of Management of University Scientific and Educational Activities

Kumargazhanova Saule, Uvaliyeva Indira, Baklanov Aleksander, Zhomartkyzy Gulnaz

East Kazakhstan State Technical University Faculty of Information Technology and Power Engineering
A. K. Protazanov Str. 69, 070004, Ust-Kamenogorsk, Kazakhstan
e-mail: {Saule.Kumargazhanova, IUvalieva, ABaklanov, GZhomartkyzy}@ektu.kz

Mamykova Zhanl

Al-Farabi Kazakh National university, 71 al-Farabi Avenue, 050040 Almaty, Kazakhstan

Ipalakova Madina

International Information Technology University, 34A, Manas Street, 050040 Almaty, Kazakhstan

György Györök

Óbuda University, Alba Regia Technical Faculty Budai út 45, H-8000 Székesfehérvár, Hungary; gyorok.gyorgy@amk.uni-obuda.hu

Abstract: In the article a concept of the result-oriented management is presented. The concept is based on the methodology of the indicative planning of the university scientific and educational activities and presented as formalized procedures. Particular attention is paid to the system of indicators, their formalization and algorithms to design the analytics of the educational system functioning. Moreover, the incentive rating model for the scientific and educational activities of the university staff is considered. The model contains the indicators that agree with the university indicative plans. In addition, in the article the structure scheme of the management of the information flows in the information and analytical system in the contour of the university management is described. The agent-oriented approach to the management of the scientific and educational activities of the university is considered. The rule base for the evaluation of the indicators state is described. It allows determining the state of the indicator regarding the achievement of the desired state of the scientific and educational activities and formalizing the dataset for the evaluation of the attainability of the university development plan. The information and analytical system in the contour of the management of the scientific and educational

activities of the university is presented as a tool for the management of the university business-processes.

Keywords: indicative planning; rating assessment; information systems; information and analytical system; strategic planning; operational planning; scientific and educational activities of a university

Introduction

The relevance of the research topic is high, because higher education institutions play an important role in the market economy [1]. They have a right to determine the development directions, goals and methods to achieve them on their own.

Universities as independent structures should apply work methods and management models that are used at the national level, develop alternatives to their future behavior depending on changes of the outside environment, i.e. apply a strategic approach to the regulation of scientific and educational activities (SEA) [2]. One such strategic approach is result-oriented management (ROM), which is based on the strategic plan of the university development.

Management of the university under modern conditions requires an integrated solution of many problems caused by both external and internal factors. Requirements of the university management are increasing, which leads to the inclusion of information systems in the control loop [5]. The information system in the control loop of scientific and educational activities of the university should not only provide to the administration of the university information about the current and future state, but also identify problem areas of the university SEA functioning and develop corrective actions to strengthen work in this direction [6].

The subject of this research is the methods and models of the information support of the result-oriented management processes [7].

The basic idea of the work is the application of modern information technologies to the implementation of the university research and education planning system as a purpose-program management system that is oriented to accessibility of final results of the development plan and uses indicative planning as a management tool for the research and education activities [8].

The goal of the research is the development of an information and analytical system, which is based on the result-oriented management concept and provides sustainable development of the university business processes.

The novelty of the proposed approaches is in use of modern ICT and indicative plans. They are based on the models of sustainable development of the scientific and educational system, as well as on the monitoring of educational resources, which are aimed at reaching the high level of quality of education or educational processes.

The scientific significance of the project is in the development of integrated technology of university management based on the midterm indicative planning of the university SEA and the creation of the incentive system based on this technology.

The research positions and their novelty are the following:

- the conceptual model of ROM, which is aimed at the information support of planning processes and management of the university business processes, and makes it possible to link task goals and current social and science important results of the university SEA development;
- the information support method of indicative planning of the university SEA based on a purpose-program approach; system of indicators, which characterizes the development clusters of the university SEA; and monitoring system that allows detecting «bottlenecks» at the planning process;
- the model of the incentive rating system, which is connected with university development indicative plan and implements the control function of its execution;
- the rule base for the evaluation of the attainability of the university development plan; the plan is presented as a decision bank and formalized by the agent-oriented technology for the design of intellectual management systems;
- the information and analytical system in the contour of management of the university SEA; the system supports the processes of planning and management at a medium term perspective, monitoring and analysis of the operating control for the corrective actions formulation, which when combined focuse on achieving the goals and tasks of education system development.

1 Planning and Assessment Methods and Models of Scientific and Educational Activities of the University

1.1 Conceptual Management

The information content of the conceptual *result-oriented management* (ROM) model is to bring the university to the desired criteria of the SEA development. The activities are determined by each owner of the business process within operational, strategic plans and education system policy. Such policy is intended to link decisions concerning the development and functioning of the university SEA and their efficiency and effectiveness for the university and the education system as a whole [9, 10].

Schematic description of the conceptual model of ROM is shown in the Fig. 1. As seen from the figure, the planning process of SEA in the mid-term is based on the iterative approach, thereby characterizing the principle of the «sliding» planning.

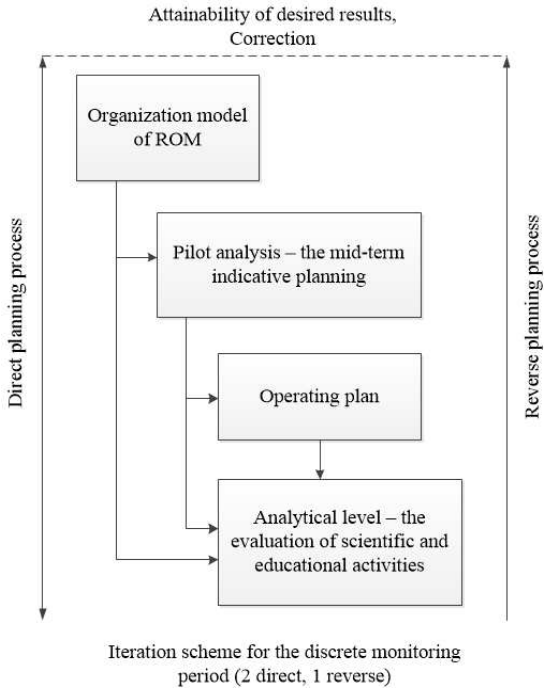

Figure 1
Schematic description of the conceptual model of ROM

The *methodology of the results-oriented management* is designed to link decisions concerning the development and functioning of the university SEA and their efficiency and effectiveness for the university and the education system as a whole. This ROM methodology is designed for the university business process management through the development of strategic indicative plans.

A university as a complex system has a main management contour (Fig. 2). It is a strategic indicative midterm plan of the university development that obeys its own law of behavior (regulatory documents, criteria for national accreditation systems, rankings of world universities, etc.). The subject of management is administrative management. It controls the scientific, educational, administrative and financial university activities based on the ROM concept according to the midterm strategic indicative university plan. The plan must correspond to the university mission and vision, which are depicted as a vector of driving influences $\vec{Z}$.

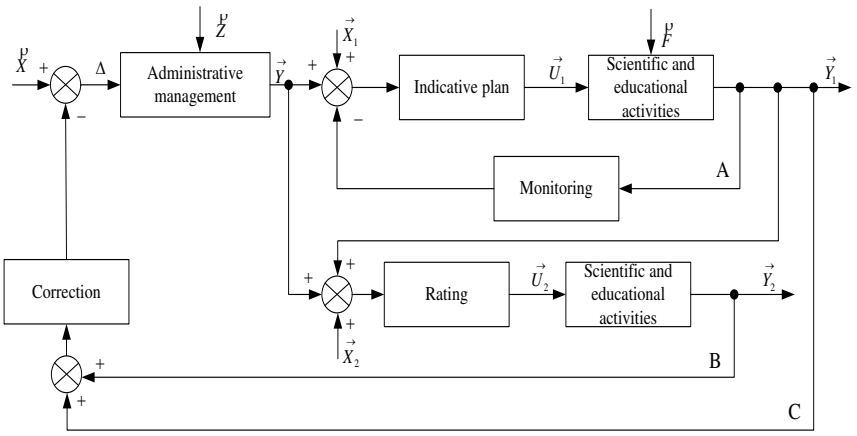

Figure 2
Structure scheme of the management of the university SEA based on the indicative planning and rating

The input ($\vec{X}$) of the system is various indicators of university activities, the state of the resources (intellectual, educational and financial). The vector $\vec{Y}$ is an output of the system and it allows for judging the whole of the universitys activities.

On the scheme there are three contours of university SEA management: A – indicative planning, B – rating system, C – adjustment.

In the A contour the input ($\vec{X}_1$) is the indicators of indicative plans, which are realized according to the main strategic directions of the university development. The output of this contour ($\vec{Y}_1$) characterizes university SEA. SEA are affected by driving influences $\vec{F}$. The indicative planning performs the management ($\vec{U}_1$) of SEA at the beginning of the academic year and each term it monitors the results of plan execution.

The input of the B contour is the rating indicators ($\vec{X}_2$) and the results of the indicative planning ($\vec{Y}_1$) of the A contour. The rating system performs the management ($\vec{U}_2$) that implements the incentive mechanism of objects of the educational business process of the university.

The C contour contains A and B contours. It implements the feedback to the administrative management in order to adjust the system by corrective actions. The adjustment of university SEA allows reconsidering and creating the corrective actions in the implementation of the university strategic indicative plan in the

ROM model. In this way the *flexible management* of the university educational business process is performed.

1.2 Information Support Method of the Indicative Planning of the SEA

The *information support method of the indicative planning of the SEA* is a procedure for information support of the planning process.

The first stage: the development of the information base of the SEA characteristics defined in the form of information resources: goal-setting system (strategic directions of SEA development, targets and tasks); hierarchical system of indicators (target indicators, integrated indicators, criteria and an index passport); strategic indicative plans and ratings checklists corresponding to the in-house hierarchy (faculties, departments, ATS).

The second stage: data acquisition depending on the level of compliance with targets and tasks of the indicative plan through the information interaction interface; activation of the system with the automated monitoring of the realization of strategic indicative plans at control points of time.

The third stage: the first step: information and analytical processing of monitoring results (activation of system procedures with the automated monitoring of indicators) by evaluation of the index of goal achievement (IGA) for each indicator according to the formula:

$$\text{IGA} = I_{nm}\left(i_{mr}^{n}\right) = \frac{I_{nm}\left(i_{mr}^{n}\right)_{fact}}{I_{nm}\left(i_{mr}^{n}\right)_{plan}} \cdot 100\% \quad (1)$$

where $I_{nm}\left(i_{mr}^{n}\right)$ is the integrated indicator m, which characterizes the basic indicator n; in brackets there is a simple index r, which expresses an integrated indicator, i.e. IGA will be determined both for integrated indicators and for simple indicators of the entire plan.

Such evaluation of indicative plans indicators allows determining «bottlenecks» in the management, i.e. making management problems «recognizable», thereby indicating the main task of the system with the automated monitoring. Second step: formation of the analytics of the university SEA and definition of qualitative and quantitative evaluation of the educational process according to the control statistics reports. Third step: analysis of the plans indicators, whose IGA is less than 50%, for decision making on the level of an administrative unit (dean, vice-rector, rector). Fourth step: development of the final information reports on the monitoring of the scientific and educational activities.

Fourth stage: general evaluation of the attainability of the university SEA development plan (activation of the rule base), providing recommendations for correction of the rating system indicators and strategic plans indicators for the next planning period.

1.3 The Model of the Incentive Rating System for the Cadre Personnel of ATS

The composition of rating lists is performed in correspondence with the accepted systems of indicators. They allow measuring the volume, quality and efficiency of the work done based on the scoring system. The total score of a lecturer is calculated as a sum of points for all indicators, which later are summarized into group indicators. The total scores for each type of SEA are generated using sums of group indicators. And the resulting score is a sum of indicator of each type of activity:

$$\begin{cases} R_{\sum} = \sum_{i=1}^{3} R_i \\ R_i = \sum_{j=1}^{m} r_j \\ r_j = \sum_{l=1}^{n} p_l \end{cases}, \tag{2}$$

where RS – the total score; R_i – the points that are obtained for i-th type of SEA; r_j – the points for j-th group indicator; p_l – the points for l-th indicator.

According to the ROM concept the rating indicators are approved annually. They are derived from the strategic indicative plans of the university in general and each department in particular. In this way, the rating indicators reflect the level of goals achievement and the development objectives on the current academic year. In this regard, each employee of the university including heads of all departments and deans makes a personal contribution to the overall strategic development of a department, faculty and the university in general by creation and implementation of his/her own individual indicative plan.

The creation of the internal rating system to evaluate the university SEA and the incentive mechanism based on it allows the university to manage efficiently the scientific and educational process in the context of strategic management and planning (Fig. 3).

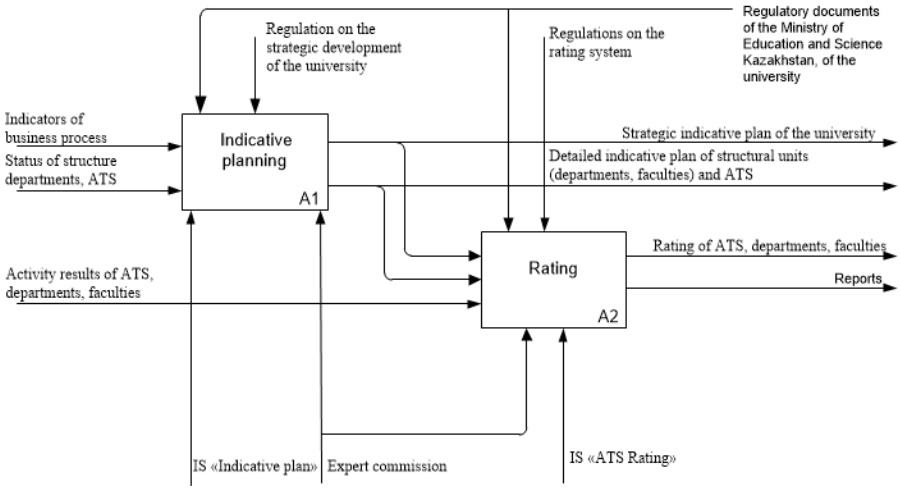

Figure 3
Scheme of the indicative planning and rating interaction

The driving influences on «Indicative planning» and «Rating» are regulated by the documents of Ministry of Education and Science of the Republic of Kazakhstan, documents about university strategic development plan and about rating system. The input parameters for the «Indicative planning» system are indicators of business processes, status of structure departments and ATS. The output of the system is the university strategic plan, indicative plan of structural units (departments, faculties) and ATS, which in their turn are the input parameters for the «Rating» system. Apart from those, the input parameters for the «Rating» system are the results of ATS, departments and faculties activities. The output of the «Rating» system is the ratings of ATS, departments, faculties, as well as various other reports. These systems are implemented in the information systems «Indicative planning» and «ATS Rating».

2 The Usage of Agent-oriented Approach to Management of the University SEA

The structure scheme of the information management in the information and analytical system within the university management (IASUM) consists of such components as (Fig. 4): storage is a module with the information about main university resources; handler is a module to forecast, analyze and compare the indicators of the medium-term planning results; programmer is a module to plan the indicators for the medium-term period and to establish the incentive program as rating points for the specific type of activity; regulator is a module to account

and evaluate the indicators of the university activities; corrective module to correct the development strategy, which implies the correction of indicators of different aspects of the university activities.

The agent-oriented approach to the management of the university SEA allows answering the three important questions: where is the organization now (monitoring); in what direction, according to the senior management's view, it should develop in future (planning); how is it going to achieve the state, where the senior management want to see it (correction, stimulation).

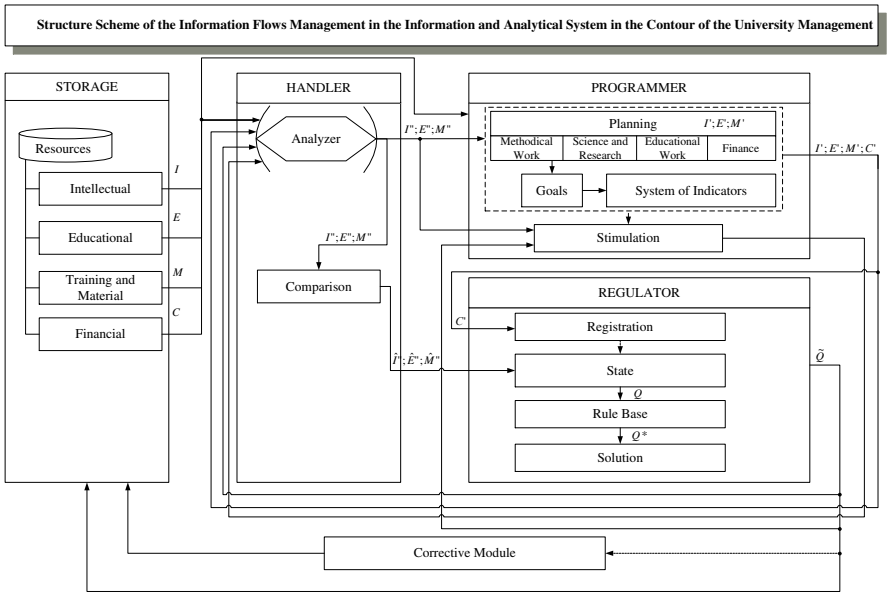

Figure 4

Structure scheme of the information flows management in the information and analytical system in the contour of the university management

An *agent* of the IASUM of the SEA is an intellectual management mechanism. Its functionality provides evaluating the internal state of the university SEA and making recommendations to university management. They are aimed at eliminating problem spots within the strategy of the university development, thereby, characterizing the problems «recognition». The agent model of the IASUM of the SEA can be represented as a set of values, which describe the process of the agent functioning:

$$A(P,F,O,U), \tag{3}$$

where P is the indicators of the SEA development, which characterize the desired state of the university development for the planning period; F is the actual state of the university SEA, which is expressed as the actual realization of the

development indicators at the control point of the evaluation of the university development; *O* is the indicators of the agent performance; they are the marks of the evaluation of the university SEA development plan, which characterize the efficiency of the development strategy and recommendations on the correction measures for achieving the development plan; *U* is a bank of the control parameters; they are the rating indicators, which are determined annually to stimulate the university staff; it is necessary for the analysis of the development of the SEA directions and for the strengthening the indicators of the problem spots in order to eliminate them.

According to the classification, the agent is a *model of agent based on the goal*. Its functioning requires not only the knowledge about the current state, but about the goal as well, which describes the desirable situations of the university SEA development.

The Fig. 5 presents the technological scheme of the agent work. Its principle is that after each checkpoint the monitoring of the SEA is performed by comparing the actual values of the indicators of the SEA development with the planned ones.

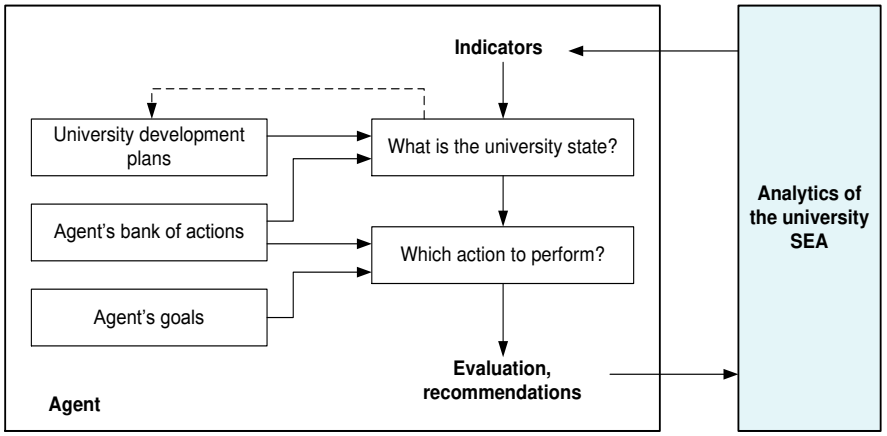

Figure 5
Technological scheme of the agent work

The evaluation of the current indicators of the development plan allows answering the question «What is the university state?». The answer is formed from the bank of agent actions with indicators of the agent performance. The indicators of performance are rules. A set of such rules is a *rule base of the agent actions*. Based on these rules, it is possible to judge about the value of an indicator with respect to the achieving of the desired state. It is formulated in such terms as not effective, satisfactory, effective.

After the current state of the university SEA is known, it is necessary to determine «Which action to perform?». For this, from the bank of actions the agent selects the coefficients to correct the points of the rating indicators according to the

recommendations, which were obtained after the analysis of the university SEA. When choosing a model of the rating indicators correction the agent goals are taken into account. They are expressed by the simple law as achieving the desired state of the SEA development. Thereby, the result of the agent's work is the determination of the evaluation of the plan effectiveness and the development of corrective actions. The chosen measures in the form of recommendations and correction coefficients are transferred to the executive mechanisms of the agent. In this way, the connection with the subsystem «ATS Rating» is realized. In it the recalculation of the rating points will be made, after a decision maker (DM) confirms those corrective actions.

The actions bank of the agent is a rule base with a structure shown in the Fig. 6. The production model was used as a knowledge representation model.

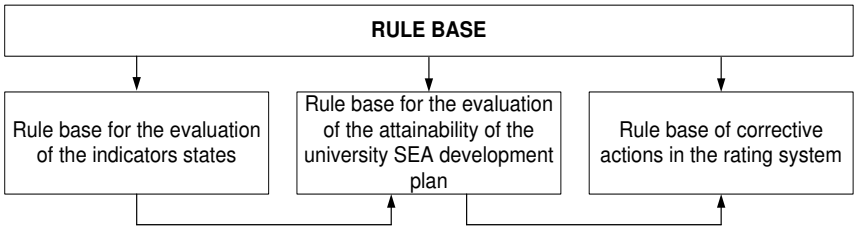

Figure 6
Structure scheme of the agent rule base

The rule base for the indicators evaluation allows checking the indicator state regarding the achievement of the desired state of the SEA development and formalizing a dataset for the evaluation of the attainability of the university development plan (Fig. 7).

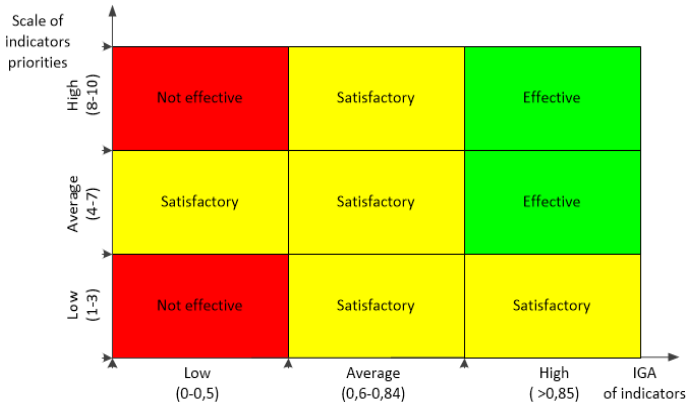

Figure 7
Structure scheme of the rule base for the evaluation of the indicators state

The graphic interpretation of the rule base is presented in the Fig. 7. An example of production has the following notation:

$$IF\ \Pr(i_r) \in \langle high \rangle\ AND\ \ IGA(i_r) \in \langle medium \rangle$$

$$THEN\ \ Indicator\ state \in \langle satisfactory \rangle$$

Table 1 presents the rules, which evaluate the attainability of the university SEA development. It can be read in a following way:

$$IF\ \ (\ Indicator\ priority \in \langle high \rangle\ OR\ Indicator\ priority \in \langle average \rangle\ )$$

$$AND\ Indicator\ state \in \langle satisfactory \rangle\ AND\ Quantity > 75$$

$$THEN\ Plan\ evaluation \in \langle satisfactory \rangle$$

Table 1

Rule base to evaluate the plan effectiveness and recommendations

№	Operation	Indicator priority	Indicator state	Quantity (%)	Plan evaluation	Recommendations
1	AND	high average	effective	> 75	effective	
2	AND	high average	satisfactory	> 75	satisfactory	To correct the indicators in the rating
3	AND	high average	not effective	> 75	not effective	To reconsider the plan entirely
4	AND	average low	effective	> 75	satisfactory	To correct the indicators in the rating
		high	not effective	25		
5	AND	high average	effective	50-75	satisfactory	To correct the indicators in the rating
		high average	satisfactory			
6	AND	high average	satisfactory	50-75	not effective	To reconsider the plan entirely
		high average	not effective			
7	AND	high average	effective	50-75	not effective	To reconsider the plan entirely
		high average	not effective			

8	AND	high	effective	< 50	not effective	To reconsider the plan entirely
		average				
		high	satisfactory			
		average				
9	AND	high	satisfactory	< 50	not effective	To reconsider the plan entirely
		average				
		high	not effective			
		average				

Based on the recommendations made a model of correction coefficients is activated, while the points of the rating indicators are determined, according to the following rule:

IF the plan indicators are needed to be corrected
IF the indicators are in the rating THEN the rating points multiply by the coefficient 0,3
ELSE include the indicators into the rating AND assign the highest priority.

In such a way, the feedback model was created to evaluate the attainability of the university SEA development plan and to work out corrective actions, which are aimed to decrease the deviation of real values of the development indicators from the planned ones. Thereby, the result-oriented management is performed.

3 Development of the Information System in the Control Loop of the Scientific and Educational Activities of the University

The analysis of modern information systems of university management shows that the process of informatization is mainly oriented on automation of educational process, functioning of educational portals and distance learning. The blocks of planning, monitoring and analytical processing of results of the university SEA based on the strategic plan exist only in a few Kazakhstani universities and are closed resources [14-18].

The information and analytical system in the contour of the management of the university SEA has a modular structure (Fig. 8). Each module is connected with the information database of the university. The database is an information source for all types of management; the database elements are available almost for all the university departments according to their access privileges.

The modules of the indicative planning, incentive system, analytical processing and the intellectual module were developed.

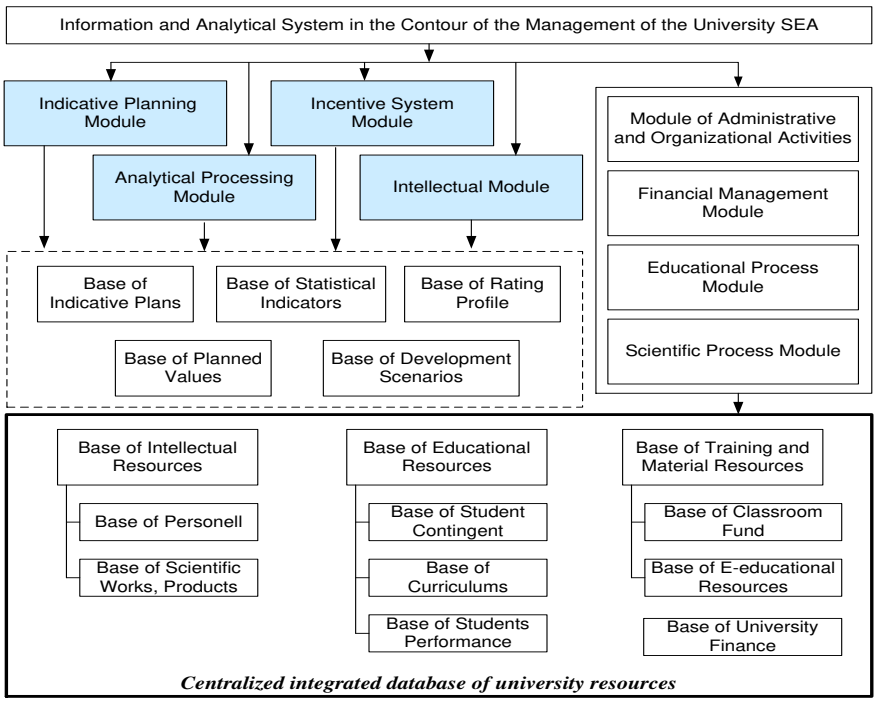

Figure 8
Structure of the IASUM of the university SEA

The created IASUM of the SEA is implemented according to the client-server architecture. The server side consists of the database server (MS SQL Server 2014) and web-server (IIS). The client side is realized as a web-application (.NET Framework) with the functions of data entry and editing. For the data access the ADO.NET technology was used, which simplifies the process, in particular, in distributed Internet applications. The structure of the subsystems of the IASUM of the SEA is presented in the Fig. 9.

IASUM is a system that is composed of two main subsystems – «Indicative planning» and «ATS Rating» which provide:
– the automated calculation of the integrated indicators of the indicative plan and the cumulative scores for the rating questionnaire;
– the monitoring and the analytical processing of data for estimation of level of indicative plans execution and rating lists formation;
– the flexible management of the structure and content of the indicative plan;
– the values of indicators by request;
– the authorized user access to indicative plans and rating questionnaires;
– the centralized administration of the group access rights;
– the automation data conversion and data export to the given format.

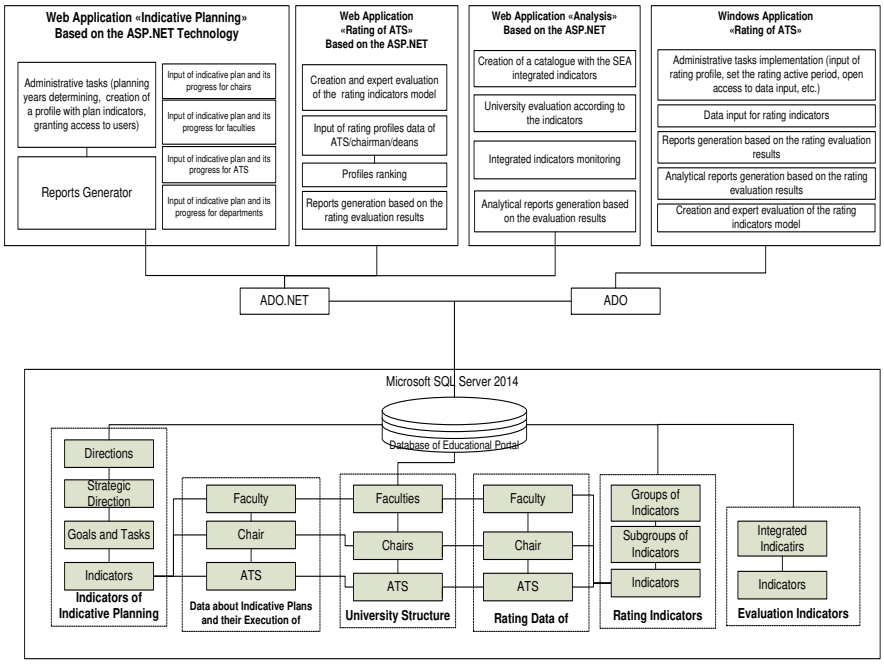

Figure 9

Structure of the subsystems of the IASUM of the university SEA

The subsystem «Indicative Plan» (Fig. 10) provides an automated process of the mid-term indicative planning of the university and analyzes the effectiveness of the plan.

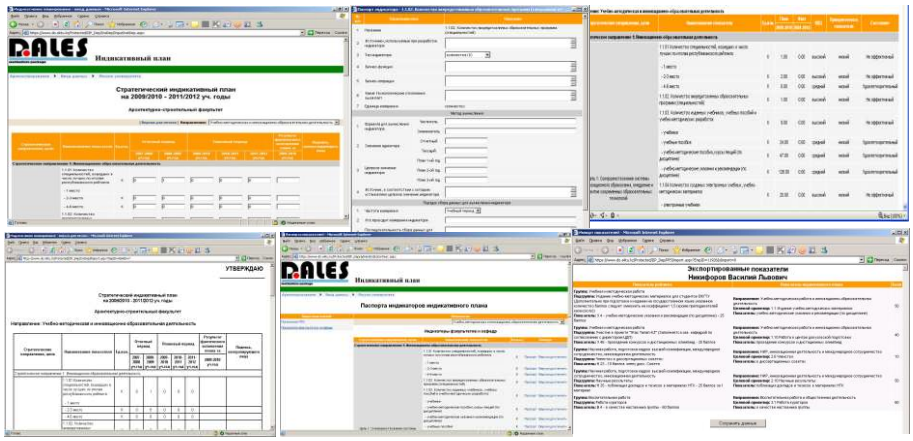

Figure 10

Interface of the «Indicative Plan» subsystem

The subsystem «ATS Rating» is designed to evaluate the SEA of the university professors according to their main activity directions. Key indicators, which determine the evaluation, are exported from the subsystem «Indicative Plan».

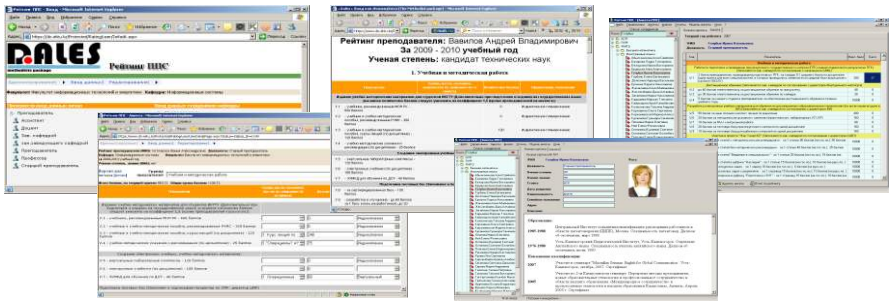

Figure 11
Interface of the « ATS Rating » subsystem

Conclusion

It can be concluded that the practical results obtained in the experiment confirm the feasibility and usefulness of the theoretical developments, which together with the information system present a work tool for the management and planning of the university SEA.

According to the results of the study, the following conclusions can be made.

A conceptual model of the result-oriented management was developed, aimed at information support of planning and university business processes management, which allows linking targets and current socially and scientifically significant results of the development of the university scientific and educational activities.

A method was developed for the information support of the indicative planning of the scientific and educational activities, based on the result-oriented approach; the indicators system that characterizes clusters of the development of the university scientific and educational activities, and the monitoring system, which allows identifying «bottlenecks» in the management process.

All the indicators of the scientific and educational activities were systematized. Based on them a system of indicators was proposed, which consist of two levels: integrated indicators and indices. The integrated indicators show the state of the SEA, they meet the main accreditation criteria to evaluate the system of higher education.

The rating model was developed to stimulate university employees, which is integrated with the indicative planning system, for flexible regulating of ATS employees activities through rating parameters.

A rule base was created to evaluate the attainability of the university development plan. It is a set of solutions of the management intellectual mechanism of the information and analytical system, which is formalized by the agent-oriented technology for the design of intellectual management systems.

The information system was developed in the control loop of the university scientific and educational activities, supporting the process of planning and management in the mid-term, monitoring and analysis of the operational management for the development of corrective actions intended to the achievement of goals and tasks of the educational system.

References

[1] Jones G. A.: An introduction to higher education in Canada, In Higher Education across Nations, Publishing: Delhi, India, 2014, Vol. 1, pp. 1-38

[2] Aksenov, K. A., Klebanov, B. I. and Goncharova, N. V. (2004) Primeneniye sredstv imitatsionnogo modelirovaniya v sisteme strategicheskogo upravleniya vuzom. Universitetskoye Upravleniye, 2(31) 54-57

[3] Uskenbayeva R., Kurmangaliyeva B., Mukazhanov N.: Development of multidimensional model of data for information and analytical decision-making support system, Computer Modelling & New Technologies, 2014, 18(2), pp. 170-174

[4] Mutanov, G. M., Mamykova, ZH. D. and Kumargazhanova, S. K. (2010) Upravleniye, oriyentirovannoye na rezul'tat, na primere obrazovatel'noy sistemy. Ust-Kamenogorsk: EKSTU

[5] Uvalieva I., Garifullina Z., Soltan G., Kumargazhanova S.: Distributed information-analytical system of educational statistics. Proceedings of 6th International Conference on Modelling, Simulation and Applied Optimization. Istanbul, Turkey, 2015, pp. 1-6

[6] Ales Popovic, Ray Hackney, Pedro Simoes Coelho, Jurij Jaklic: How information-sharing values influence the use of information systems: An investigation in the business intelligence systems context, The Journal of Strategic Information Systems, Vol. 23, Issue 4, 2014, pp. 270-283

[7] Khalyasmaa A. I., Dmitriev, E S. A.. Kokorin L. and Valiev R. T.: Information and analytical system for power system life cycle management, Proceedings of 57th International Scientific Conference on Power and Electrical Engineering of Riga Technical University (RTUCON), Riga, 2016, pp. 1-6, doi: 10.1109/RTUCON.2016.7763124

[8] D. Kassymkhanova, D. Kurochkin, N. Dinissova, S. Kumargazhanova, A.Tlebaldinova. Majority voting approach and fuzzy logic rules in license plate recognition process // The 8th International Conference on Application

of Information and Communication Technologies (AICT 2014), Astana, 2014, pp. 155-159

[9] Mamykova, ZH. D., Denisova, O. K. and Kumargazhanova, S. K. (2010) Organizatsionnyy podkhod k sozdaniyu sistemy strategicheskogo i operativnogo planirovaniya v vysshem uchebnom zavedenii. Tranzitivnaya Ekonomika, 3, 72-78

[10] Mutanov, G. M. (2008) Education. Science. Innovation. Ust-Kamenogorsk: EKSTU

[11] Bieler A.; McKenzie M.: Strategic Planning for Sustainability in Canadian Higher Education. Sustainability, 2017, 9, p. 161

[12] Mutanov, G. M. and Kumargazhanova, S. K. (2009) Reytingovaya model' otsenki deyatel'nosti prepodavateley VKGTU im. D. Serikbayeva. Regional'nyy Vestnik Vostoka, 4(44), 6-10

[13] Vlasova V., Kirilova G.: Matrix Classification of Information Environment Algorithms Application in the Educational Process, Mathematics Education, 2016, 11(1), pp. 165-171

[14] The Kazakh National Research Technical University after K.I. Satpaev www.kaznitu.kz (05.01.2018)

[15] M. Kozybayev north kazakhstan state university: www.nkzu.kz (05.01.2018)

[16] Karaganda Economic University of Kazpotrebsouz: www.keu.kz (05.01.2018)

[17] Sarsen Amanzholov East Kazakhstan State University: www.vkgu.kz (05.01.2018)

[18] Al-Farabi Kazakh National university: www.kaznu.kz (05.01.2018)

Synthesis of an Automatic Obstacle overcoming Control Module, dedicated for Manual Wheelchairs

Jarosław Szrek, Artur Muraszkowski

Wroclaw University of Science and Technology, Faculty of Mechanical Engineering, Department of Biomedical Engineering, Mechatronics and Theory of Mechanisms, Łukasiewicza 7/9, 50-371 Wrocław, Poland
jarosław.szrek@pwr.edu.pl, artur.muraszkowski@pwr.edu.pl

Abstract: This article presents the concept of an automatic overcome obstacle control module, dedicated to a wheelchair for everyday use. The module consists of a mechanical system which has front and rear lift mechanisms for the wheelchair and drive that performs displacement while the main wheels of the wheelchair are raised. We also discusses the electronics and particularly the control system with all necessary sensors. Two algorithms are proposed to overcome obstacles. The prototype module has been built and tested under laboratory conditions. The paper also presents the results of experiments involving overcoming obstacles with manual control and in automatic mode.

Keywords: wheelchair; overcoming obstacles; automation

1 Introduction

One of the many transport problems with which people with disabilities have to struggle, are architectural barriers. The most common obstacles that people in wheelchairs can meet on their way are thresholds, curbs and stairs. In many cases, the environment is friendly for people with disabilities – sidewalks and walkways are built with ramps or lowered curbs, buildings have elevators, doors are automatically opened [1, 2]. Currently, facilities for the disabled are required by law, but there are still many obstacles present.

The design of a mobility enhancement wheelchair systems are often taken into account at research centers. In the current articles, solutions that allow easier usage and mobility in a wheelchair are presented [3]. Some solutions are based on devices supporting the control of a wheelchair [4], others focus on avoiding, overcoming obstacles, including stairs [5, 6]. An example of a device that facilitates control, especially for people with upper limb dysfunction, is the

application of head or chin controls as alternatives to a joystick [7]. In this type of solution, the motors of an electric powered wheelchair are activated by chin or head movements [8]. Sip-and-Puff devices are another solution [9]. In this case, the wheelchair is controlled by air pressure via dedicated mouthpiece, placed on the frame near the mouth. These types of devices are dedicated for people with upper limb paresis.

A very important element in moving, in a wheelchair, is overcoming obstacles like curbs, thresholds or stairs, in cases where they cannot be avoided. To overcome this type of obstacle, the wheelchair must be equipped with special climbing mechanisms [10]. Devices having such features are practically mobile robots [12, 13] equipped with complex sensory systems, including level stabilization algorithms [14, 15].

An undoubted drawback of complicated devices is their high cost, which translates into their availability. Therefore, researchers are looking for less complex solutions, that have the function of overcoming obstacles. The presented module is such a solution. To deal with selected obstacles, one only need equip the wheelchair with a simple mechatronic system [11].

This article presents the concept of an automatic obstacle control module, dedicated to a wheelchair for everyday use. The module consists of a mechanical system which is built into the front and rear lift mechanisms of the wheelchair and function, sensing displacement, when main wheels of the wheelchair are raised. We also present the electronics, in particular, the control system, with the necessary sensors and control algorithms. Additionally, the device automatically executes the process of overcoming obstacles, without significant user involvement.

2 The Overcoming Obstacles Module

The module for overcoming obstacles, for manual wheelchairs, has been developed on the basis of the module for overcoming obstacles with a manual control system [10]. Kinematic structures of the device has been developed using conventional and author developed methods of synthesis [16]. In comparison to the previous lifting system, minor modifications were made to improve the system, the size of the wheels has been changed, rear-wheel drive has been modified and all motors have been equipped with sensors.

The general concept, necessary components and the wheelchair with lifts mechanisms is shown in Fig. 1. Two identical linear actuators (M1 and M2) are used for lifting. The rear wheel lift system is equipped with an additional motor (M3) to ensure the wheelchair moves when the main wheels are raised. The maximum lifting height of the wheelchair can be adjusted by selecting the actuator

stroke (M1, M2) and the attachment points (B and E) of the lifting mechanism to the wheelchair. The development of the electronic modules, including the selection of sensors (Front-S1, Rear-S2), control modules and implementation of algorithms has been designed and constructed for the purpose of described system of automation of overcoming obstacles process.

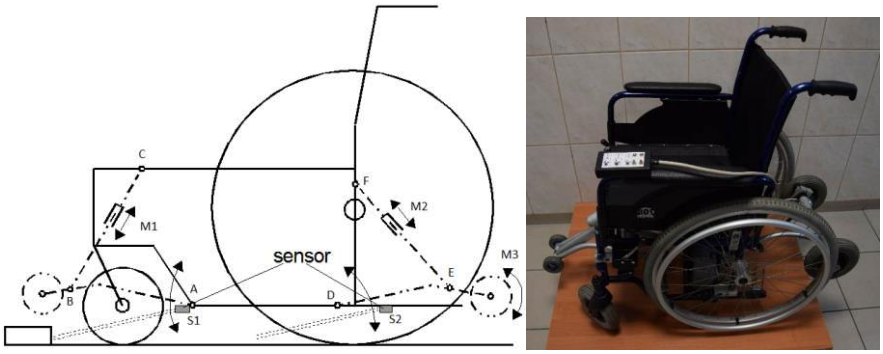

Figure 1
Kinematic scheme of the lifting system and overview of the mechatronic wheelchair

Operation of the system requires minimal user participation at initiation of the process and then the rest of the process is done automatically. The developed device, along with the obstacles algorithm, has been implemented and verified experimentally.

1.1 The Control System Unit

The Central Processing Unit of the control system is a RBC-4242 [17] module with STMF103 microcontroller with an ARM Cortex M3 core. The User Control Panel is connected to the general purpose digital inputs, where the change of the voltage sets the control value of drives individually and is used to select the automatic mode.

Distance measurement is carried out with the IR sensors, whose output is connected to a block of analog-to-digital converter (ADC) of the microcontroller. Motor movement is realized through motor controllers RbMD vnh3sp30-DUAL, built with integrated H bridges, with which drives are connected. Control is performed by giving the input motor driver a PWM signal and two digital signals defining the direction. The distance sensors are placed in the front and rear of the truck. A front sensor determines the height of rise of the front of the chair and is set in an appropriate orientation to detect the edge of the threshold, during the lift process. The rear sensor is directed downward in the vertical axis. It is used to measure the distance from the ground and the detection of the passage over the threshold. In addition, rotary incremental encoders are mounted into drives, which provide information about their movement. As a result, the control module is able

to determine the absolute position and motor velocity. The block structure of the control system is shown in Fig. 2.

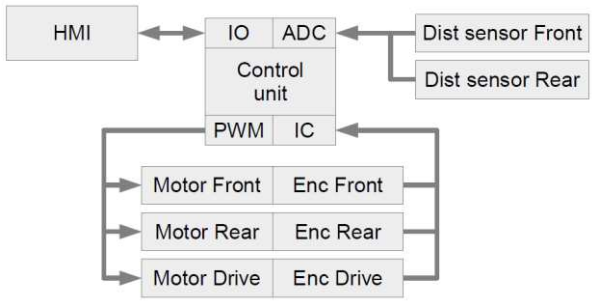

Figure 2
Block diagram of control system

The device can operate in three modes: manual, automatic time and automatic sensory (distance). In all these modes, the process of overcoming obstacles occurs in a very similar way. First, it is necessarily to drive the wheelchair to the obstacles ahead, so that the front wheels were not more than 4 cm from the obstacle.

In manual mode, the user through the control panel shown in Fig. 3, is capable of independently control each of the drives.

Figure 3
Control panel

There are three toggle switches for this purpose that triggers the individual drives in the order: moving the front lift, rotation of the rear wheels, moving the rear lift. The switches are three-position momentary type. Switching one of them forward, results in extension of the actuator (forward rotation of the wheels) and switching back, results in shortening of the actuator (backward rotation of the wheels). With the appropriate control signals, the user can, while sitting in a wheelchair, overcome an obstacle by themself.

1.2 Algorithms of Control

Auto modes allow overcoming an obstacle with minimal involvement of the user, in the form of initiating the whole process by pressing a button, when the wheelchair is in front of an obstacle. The only thing the user need do is, drive the wheelchair to the obstacles so that the front wheels touch the obstacle, then press the automatic mode button. Depending on whether the button is pressed once or twice, different algorithm will run.

1.2.1 The "Time" Control Algorithm

Pressing once starts the time control mode. During operation of this algorithm (block diagram shown in Fig. 4) each drive is operated for a specified length of time.

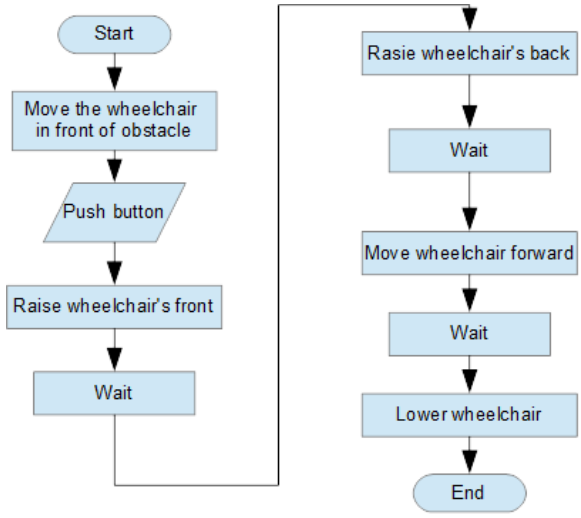

Figure 4
Block diagram of time control algorithm

The time constants are selected so that the wheelchair can overcome the highest possible threshold. The maximum height of the threshold is determined by the geometry of the mechanical system. At the beginning, the front lift is lowered (Fig. 5) so that the front wheels of wheelchair rise over the threshold (Fig. 6). Then the rear lift is lowered so that the large wheels of wheelchair rise above the obstacle (Fig. 7). Next the drive of the wheels attached at the end of the rear lift starts to rotate them. The wheelchair moves forward until the big wheels of wheelchair will go beyond the threshold (Fig. 8). At the end, front and rear lifts rise to the initial positions and the wheelchair is ready to proceed (Fig. 9).

Figure 5
Wheelchair during overcoming threshold, phase 1. lowering front support

Figure 6
Wheelchair during overcoming threshold, phase 2. raise front of the wheelchair

Figure 7
Wheelchair during overcoming threshold, phase 3. raise rear of the wheelchair

Figure 8
Wheelchair during overcoming threshold, phase 4. moving wheelchair over threshold

Figure 9
Wheelchair during overcoming threshold, phase 5. The return of supports to their initial positions

1.2.2 The "Distance" Control Algorithm

Pressing the button twice starts the last run mode of operation, which is based on the use of signals from the optical distance sensors (block diagram shown in Fig. 10). Observing the wheelchair from the outside, the process looks analogous to the previous mode. The movement is made up of the same phases but the start and stop phase conditions, are different, due to the active sensors.

To start, the front lift is lowered until the front distance sensor indicates equal or higher reading than a preset value. The setting of this sensor is, such as to be able, to measure the distance to the front wall of threshold. This value changes slightly while lifting the front of the wheelchair until the distance from the threshold is measured. At this time, the measure line of the sensor is above the edge of the threshold, the indicated value begins to increase rapidly. This is the signal to stop the lowering of the front lift. Then the rear part of the wheelchair rises by lowering the rear lift. The actuator operates as long as the rear sensor indicates a sufficient distance from the ground. Next, the drive of the wheels on the rear lift begins to operate and the wheelchair begins to move forward.

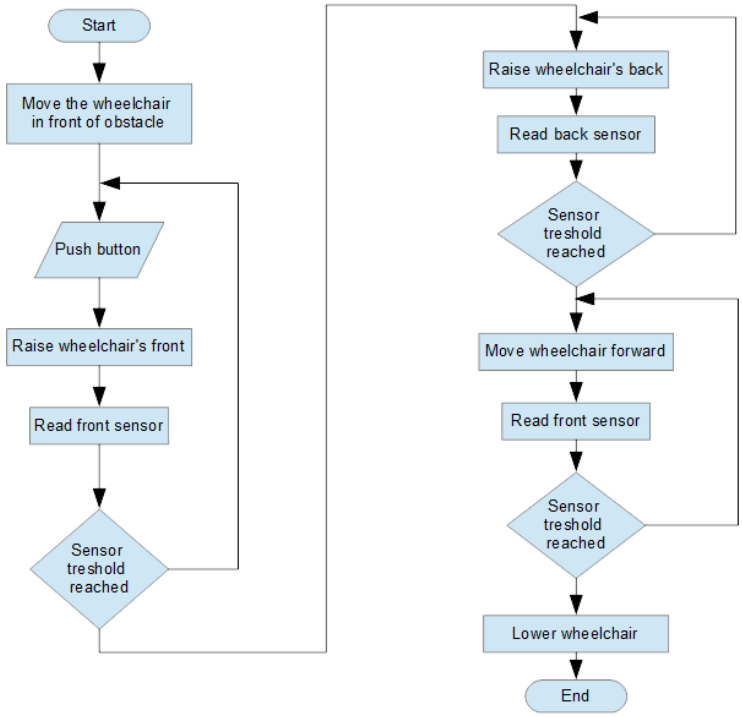

Figure 10
Block diagram of distance sensors control algorithm

This phase is performed as long as the controller registers a rapid decrease in the value measured by the rear sensor, which means exceeding the threshold edge. The vehicle stops, front and rear lifts are lifted to the initial positions. The wheelchair is then ready for further operations.

3 Experiments and Results

Experiments were performed under laboratory conditions. For this purpose a platform with a sill height of 10 cm has been constructed, which is shown in Fig. 5. The position was evenly lit by fluorescent lighting. The task of the wheelchair was to drive onto the platform while overcoming the threshold. All three modes for overcoming obstacles were tested: manual control, automatic time control and automatic, using optical distance sensors.

In manual mode, all of the movements of the mechanism were initiated and completed by the operator. The ergonomics of the control panel are adapted for

mounting to one of the armrests and allows control with one hand. Therefore, during tests, the panel was operated with one hand and each drive was handled individually. In this mode, periods of time for individual movements of the drives were very different during subsequent attempts. This was due to manual control, in which the operator was starting and stopping the actuators in the moments that subjectively considered appropriate. Fig. 11 shows the characteristics of the positions of individual drives, for the sequence of movements, so that the wheelchair could overcome obstacles, in the shortest time for manual mode.

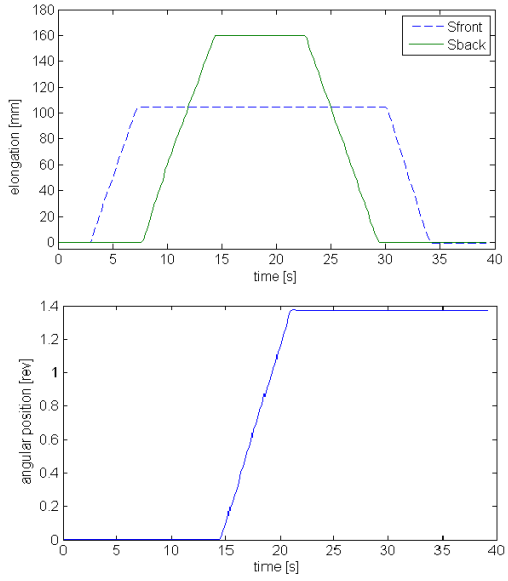

Figure 11

Displacement characteristics of overcoming obstacles module drives in manual mode

In the next tested mode, individual movements of the drives were programmed to have constant period of time operation. In order to overcome steps of varying sizes, the mechanism must be programmed for the greatest possible obstacle, because it does not use any information about the object being negotiated. Therefore, the main advantage of this mode is that it requires no sensors. The characteristics are shown in Fig. 12. The advantages of this solution are a simple construction and a low cost as well as, fewer components and wires that can be damaged. The disadvantage of this solution is the duration of the process, which is adapted to the greatest obstacles.

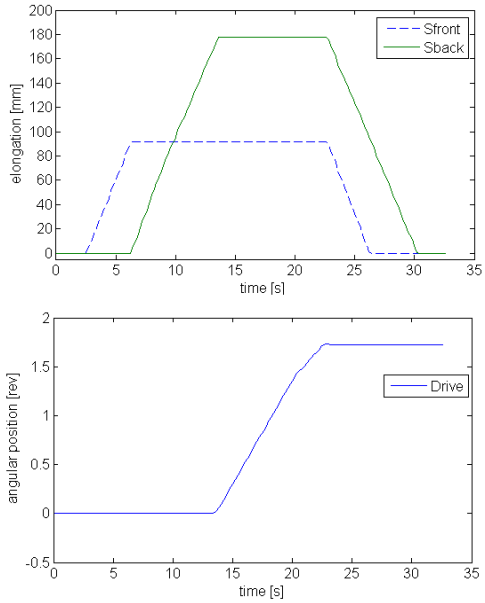

Figure 12

Displacement characteristics of overcoming obstacles module drives in automatic time control mode

Overcoming a small threshold takes as much time as for the greatest obstacle. A further disadvantage of this method is, that it has constant preset value for moving each of the drive, but for proper realization of the task actuators has to operate for a different period of time, which is dependent on the actual load. As a result, this translates into different lengths of extension actuators or rotation of the wheels. Therefore, parameters of this automatic mode must be preset for each user individually.

The characteristics of the last tested algorithm, which is the automatic mode using optical distance sensors, are shown in Fig. 13. In this mode, the system detects a threshold height and adapts the duration of drive operation time, which is the equivalent of the actuator length, so as not to perform unnecessary motions. Furthermore, the second sensor detects movement when the wheelchair large wheels are passing over the threshold and stops the vehicle at the right time. The disadvantage of this solution is the greater cost of the device. Moreover, cheaper sensors are more susceptible to external noise such as fluorescent lamps in the room or the sun's rays in an open space. The biggest problem with this arrangement is the selection of appropriate sensors that can operate under different conditions simultaneously.

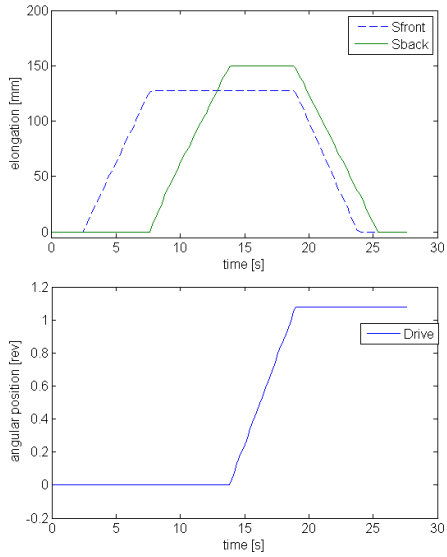

Figure 13
Displacement characteristics of overcoming obstacles module drives in automatic distance sensors control mode

This study shows that both modes of automatic control work correctly, in stable external conditions. A big impact on the quality of automatic control using sensors is the type of used measuring elements and the influence of external conditions. During the test of the automatic mode using the sensors, proper operation was affected by disruption, such as fluorescent lights and shadows cast by the wheelchair components, which cause erroneous distance measurements and stop the actuators at improper positions. Due to the fact that, when determining the displacement of the actuators, sensors data are used to get the information about current position relative to the obstacle, there are no unnecessary movements made, as it happens, in the time control mode. Therefore, in testing this mode, it has proven to be the fastest in overcoming obstacles. Automatic time mode, in addition to increased operating time, as compared to the previously described, is impaired by an error, that comes from the varying dimensions of obstacles and loads (weight of different users, carrying additional cargo). It consists in that the drive working under different loadings running at different speeds. When periods of operation time are set constant, the actuator performs various lengths. Sometimes, the process ended in an unsuccessful attempt to overcome the obstacles. Manual operation was the slowest because of the fact that there was an assumption that the panel has to be operated with one hand, resulting in one drive is driven at the same time. Despite these problems, there was no situation in which the operator of the wheelchair was exposed to a fall.

4 Summary

The automatic obstacle control module correctly realizes the task of overcoming thresholds during stable conditions. The tested algorithms are working correctly within the predicted conditions. Emerging errors were formerly anticipated. The device, during the test, ran in a stable fashion, it did not create any new bugs. Even during a malfunction, the wheelchair acted within the limits of safe use and did not tip, fall or experience any major shocks.

The mechanism now requires further testing under "real world" conditions. Both time control and the use of optical sensors, requires further improvements, algorithms modifications and possible changes of sensors. Furthermore, there were no tests done concerning the possibility of using these other sensors, including a variety of configurations that can be applied to the task of overcoming obstacles. Future studies will include the use of encoders mounted on the motors, in order to determine the instantaneous configuration of mechanisms to overcome thresholds and inertial sensors. They will be progressively tested in future work in order to find the optimal cost solution. Additionally, the platform will be developed for further improvements, such as an auto-leveling wheelchair seat while overcoming obstacles.

References

[1] Felicetti T., Barriers to Community Access: It's About More Than Curb Cuts, The Case Manager, Vol. 16, pp. 70-72, 2005

[2] Deepan C. Kamaraj, Brad E. Dicianno, Rory A. Cooper.: A Participatory Approach to Develop the Power Mobility Screening Tool and the Power Mobility Clinical Driving Assessment Tool. Hindawi Publishing Corporation BioMed Research International Volume 2014, Article ID 541614, 15 pages http://dx.doi.org/10.1155/2014/541614

[3] Tzafestas S. G.,: Autonomous Robotic Wheelchairs in Europe, IEEE Robotics and Automation Magazine, Vol. 8, March 2001, pp. 4-6

[4] Narayanan V. K., Pasteau F., Marchal M., Krupa A., and Babel M.: Vision-based adaptive assistance and haptic guid-ance for safe wheelchair corridor following. Computer Vision and Image Understanding, Vol. 149, pp. 171-185, 2016

[5] Chatzidimitriadis S., Oprea P., Gillham M. Sirlantzis K.: Evaluation of 3D obstacle avoidance algorithm for smart powered wheelchairs. 2017 Seventh International Conference on Emerging Security Technologies (EST), Canterbury, 2017, pp. 157-162, doi: 10.1109/EST.2017.8090416

[6] Zondervan DK, Secoli R, Darling AM, Farris J, Furumasu J, Reinkensmeyer DJ: Design and Evaluation of the Kinect-Wheelchair Interface Controlled (KWIC) Smart Wheelchair for Pediatric Powered

Mobility Training. Assist Technol. 2015 Fall;27(3):183-92. doi: 10.1080/10400435.2015.1012607

[7] Rabhi Y., Mrabet M. and Fnaiech F. :Intelligent control wheelchair using a new visual joystick, Journal of Healthcare Engineering, Vol. 2018, Article ID 6083565, 20 pages, 2018

[8] Kondori F. A., Yousefi S., Liu L., and Li H.,: Head operated electric wheelchair. Southwest Symposium on Image Analysis and Interpretation, pp. 53-56, San Diego, CA, USA, April 2014

[9] Mougharbel I., El-Hajj R., Ghamlouch H. Monacelli E.: Comparative study on different adaptation approaches concerning a sip and puff controller for a powered wheelchair, 2013 Science and Information Conference, London, 2013, pp. 597-603

[10] Murray L., Takashi T.: Design of a robotic-hybrid wheelchair for operation in barrier present environments. Proceedings - 20th Annual International Conference - IEEE/EMBS Oct. 29 - Nov. 1, 1998, Hong Kong

[11] Bałchanowski J., Szrek J., Wudarczyk S: Wheechairl mechanism for negotiating obstacles, The Archive of Mechanical Engineering, Vol. LVI 2009, Warszawa, Vol. 56, No. 3, pp. 251-261

[12] Carlson, T., Demiris, Y.: Collaborative control for a robotic wheelchair: Evaluation of performance, attention, and workload. IEEE Transactions on Systems, Man, and Cybernetics. Part B, Cybernetics: A Publication of the IEEE Systems, Man, and Cybernetics Society, 42(3), 876-888, doi:10.1109/TSMCB.2011.2181833 (2012)

[13] Daveler B1, Salatin B, Grindle GG, Candiotti J, Wang H, Cooper RA.: Participatory design and validation of mobility enhancement robotic wheelchair. JRRD Volume 52, Number 6, 2015, pp. 739-750, doi: 10.1682/JRRD.2014.11.0278

[14] Bałchanowski J.: Modelling and simulation studies on the mobile robot with self-leveling chassis. Journal of Theoretical and Applied Mechanics. 2016, Vol. 54, No. 1, pp. 149-161, http://dx.doi.org/10.15632/jtam-pl.54.1.149

[15] Candiotti J., Sundaram S. A., Daveler B., Gebrosky B., Grindle G., Wang H., Cooper R. A.: Kinematics and Stability Analysis of a Novel Power Wheelchair When Traversing Architectural Barriers. Topics in Spinal Cord Injury Rehabilitation: Spring 2017, Vol. 23, No. 2, pp. 110-119

[16] Szrek J.: Wheel-legged suspension system of a wheelchair, Bio-Eng-Young -2nd Students' Scientific Conference of Biomedical Engineering, Szklarska Poręba, str. 37-38, 2006

[17] http://robosystem.pl/files/RbC-4242.pdf

Electric Parameters Determination of Solar Panelby Numeric Simulations and Laboratory Measurements during Temperature Transient

István Bodnár

Univesity of Miskolc, Faculty of Mechanical Engineering and Informatics, Institute of Electrical and Electronic Engineering, H-3515 Miskolc-Egyetemváros, vegybod@uni-miskolc.hu

Abstract: The efficient operation of a solar panel is influenced by several factors. Someof these factors are the intensity and the spectral composition of illumination as well as the ambient temperature together with the temperature and contamination of the solar panel and the atmosphere. This study presents the voltage, amperage, and power change of a commercially available solar panel caused by the temperature transient, by the help of numeric simulations and laboratory measurements. Temperature transient investigations allow us to know more about cooled and non-cooled solar panel behavior, in case of constant intensity of illumination. During the measurements, we have concluded that the temperature increase decreases the maximum power of the solar panel. Compared to the simulation results we experienced good tendential similarity.

Keywords: efficiency; temperature dependence; temperature transient; solar panel; simulation; laboratory measurement

1 Introduction

In today's fast-paced world, people's energy consumption has become enormous. Over the last century, the energy demand of an ordinary person has grown by about fivefold, which is attributed to the spread of machinery and electronics. In order to avoid the excessive consumption of our energy carriers, both in energy production and consumption the increase of efficiency became important. The operating efficiency of the solar panel is influenced by the installation environment and the weather conditions. Among these factors, the intensity of illumination, the temperature of the solar panel's surface and its ambient temperature together with the surface pollution of the solar panel and its shadow effect are the most significant. During the research, I present the effect of solar panel surface temperature on its electrical parameters.

The main goal of the research is to establish a correlation between the surface temperature of the solar panel and its electrical parameters. The correlations were determined by laboratory measurements and numerical simulations.

Numerous literature deals with measurements and simulations at constant temperatures, but the present paper contains measured and simulated results in the transition state, which is the novelty content of the research work.

2 The Operation of Solar Panel

To understand the operation of solar panel, we examine a p-n junction semiconductor cell, which is the base of most solar panel constructions. If the energy of photons, coming from the sun is higher than the E_g , energy of the prohibited line, photons generate electron-hole pairs. The voltage, generated inside of the p-n junction disparts the electrons and holes and also prevents the recombination. Electrons move toward to the n-side, while holes move toward to the p-side. So if the energy of photons is high enough, then a so-called photo-current appears inside of the solar panel. This generated photo-current flows in the same direction as the dark current [1].

During the process we can measure the Open Circuit voltage (U_{OC}) between the poles of the solar panel and in case of shorting the solar panel, the Short Circuit current (I_{SC}) too. If we connect electrical load to the solar panel, we experience U voltage and I current, which are always lower than the U_{OC} and I_{SC}, measured in case of an unloaded solar panel. The I current is the difference between the I_{ph} photocurrent and I_D diode current, which is described by *Formula 1.* [1, 5, 9]:

$$I = I_{ph} - I_D = I_{ph} - I_s \left[exp\left(\frac{eU}{kT}\right) - 1 \right]. \quad (1)$$

The I_D diode current can be defined by the help of the I_s diode saturation current, depending on the voltage and constants.

The simplified electronic model of the solar panel, ignoring all the resistive and capacitive natured elements, consists of a diode and a current generator. The produced current of the current generator depends on the intensity of illumination [5, 12, 13]. *Figure 1.* contains this model together with the mentioned I, I_D, I_{ph} current directions.

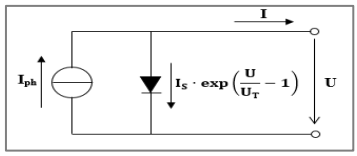

Figure 1
Model of the ideal, unloaded solar panel

By substituting U=0 and I=0, the short circuit current *(2)* and the open circuit voltage *(3)* can be defined easily [5, 9, 10, 12, 13]:

$$I_{SC} = I_{ph}, \tag{2}$$

$$U_{OC} = \frac{k \cdot T}{e} \cdot ln\left(\frac{I_{ph}}{I_s} + 1\right) = U_T \cdot ln\left(\frac{I_{ph}}{I_s} + 1\right), \tag{3}$$

where: $U_T = \frac{k \cdot T}{e}$ the thermic voltage.

It can be seen that the short circuit current is directly proportional to the strength of illumination, as the photocurrent increases with the light intensity increase and *Formula 2.* shows that the photocurrent equals to the short circuit current. From *(3)* we can see that the open circuit voltage logarithmically depends on the light intensity, measured on the surface and is directly proportional to the thermic voltage. The U_T thermic voltage represents the voltage change caused by the temperature. By knowing the open circuit voltage and the short circuit current, the *U-I* graph can be drawn. *Figure 2.* shows the *U-I* characteristics in case of different light intensities. It can be seen that if the intensity decreases, the short circuit current decreases much more than the open circuit voltage. Therefore, we can say that the intensity does not affect the open circuit voltage as it only decreases by a few Volts [1, 5, 9, 10, 12, 13].

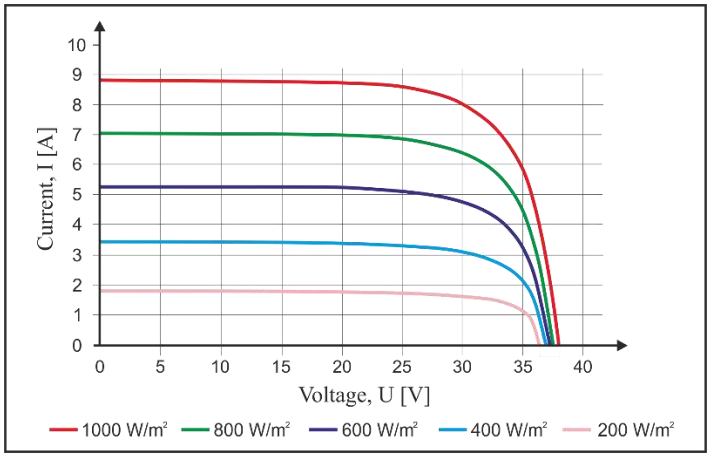

Figure 2

The U-I curves of the solar panel in case of different light intensities

In the following, consider the electric model of the solar panel without neglecting the losses. Both internal and wire resistance is represented by an ohmic resistance in this case. A capacitor can also be connected in parallel to the diode, representing the parasitic capacitance between the two poles of the diode, but because of its value, it is negligible. According to these, the mentioned equations need to be modified. *Figure 3.* shows this model [1, 5, 12, 13, 33].

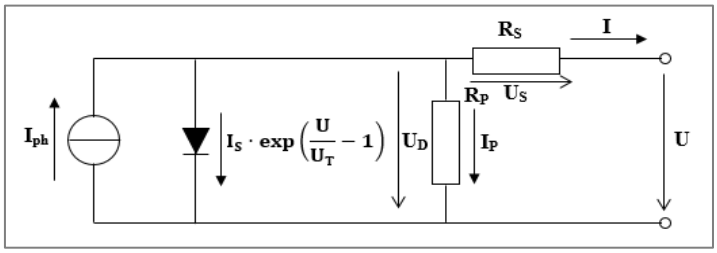

Figure 3
The real circuit model of the solar panel

This more realistic model modifies the equations too. The currents and voltages are the following [5, 9, 10, 12, 13, 33]:

$$I = I_{ph} - I_D - I_P, \tag{4}$$

$$I_D = I_s \left[exp\left(\frac{e \cdot U_D}{n \cdot k \cdot T \cdot N_s}\right) - 1 \right], \tag{5}$$

$$I_P = \frac{U_D}{R_p} = \frac{U + I \cdot R_S}{R_p}, \tag{6}$$

$$U = U_D - U_s. \tag{7}$$

Ideally $R_p \approx \infty$ and by shorting the circuit means: $R_D \gg R_s (R_{Cp} \gg R_s)$ [5].

3 Mathematical Determiantion of Solar Panel's Electrical Parameters

3.1 Power of the Solar Panel

The efficient P power of the solar panel can be counted by the multiplication of the I amperage and U voltage, measured on the R resistance. According to the simplified model [5, 7, 33]:

$$P = I \cdot U = I_{SC} \cdot U - I_s \cdot U \cdot exp\left(\frac{U}{U_T} - 1\right). \tag{8}$$

The maximum power of the solar panel can only by reached if we suit the load resistance. To find the extreme value of relation *(8),*we partially derive the function by U and look for the solution of the $\frac{\partial P}{\partial U} = 0$ equation. From this, the amperage *(9)* and the voltage *(10)* of the operating point can be expressed, while producing the maximum power [5, 7, 9, 10, 12, 13, 33].

$$I_M = I_{ph} - \frac{U_M}{U_T} \cdot I_s \cdot \exp\left(\frac{U_M}{U_T}\right) \approx I_{ph} \cdot \left(1 - \frac{U_T}{U_M}\right), \tag{9}$$

$$U_M = U_{OC} - U_T \cdot ln\left(1 + \frac{U_M}{U_T}\right). \tag{10}$$

The value of the optimal R_M load resistance can be determined *(11)* according to Ohm's law, from equation *(9)* [5, 9, 10, 12, 13, 32, 33]:

$$R_M = \frac{U_M}{I_M} = \frac{U_T}{I_s \cdot exp\left(\frac{U_M}{U_T}\right)} = \frac{U_T}{I_M + I_s + I_{ph}}. \tag{11}$$

The ideal value of the load resistance equals to the internal resistance of the solar panel. If this is true in practice, then the solar panel is operating in maximum power point (MPP) [5, 7]. The maximum power point can be found with the help of a maximum power point control unit. MPPT controllers use different algorithms, the two main types of which are True Maximum Point Seeking (TMPS) and Non-true Maximum Point Seeking (NMPS) maximum point seekers. The most common are the climbing and oscillating algorithms. To achieve maximum power, the load on the solar panel must be changed dynamically. Similar algorithms are used by Precup et al.[22] and Ürmös et al. [23] and Shams et al. [24].

The so-called φ fill factor shows how the multiplication of U_M voltage and I_M amperage of the operating point relates to the multiplication of U_{OC} open circuit voltage and I_{SC} amperage *(12)* [5, 7, 14, 17, 32]:

$$\varphi = \frac{P}{P_{th}} = \frac{U_M \cdot I_M}{U_{OC} \cdot I_{SC}}. \tag{12}$$

We can see in *Figure 4.,* how the rectangle area of the maximum power (grey rectangle, $I_M \cdot U_M$) relates to the theoretical power (multiplication of $I_{SC} \cdot U_{OC}$) determined rectangle area [12, 13, 14, 32, 33].

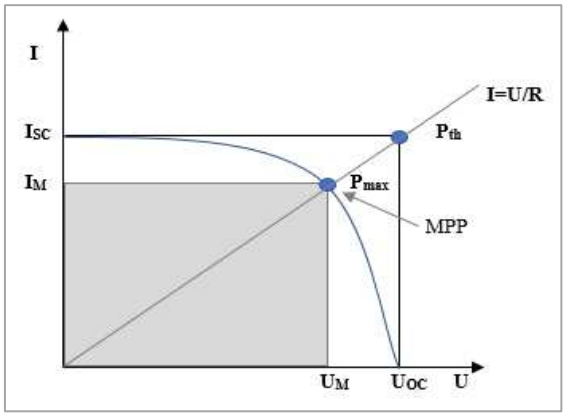

Figure 4
The operating point of the maximum power on the U-I curve

The value of the φ fill factor depends on the structure of the solar panel and on the chosen operating point. The value of φ, in case of solar panel used in practice is

between 0.75 and 0.85. However, its value significantly decreases during its aging. The older the solar panel, the lower the value of the fill factor is, which results in a reduction of efficiency [5, 7, 9, 10, 32].

3.2 The Efficiency of the Solar Panel

The maximum power point efficiency η_{max} of the solar module can be counted by dividing the P_{max} maximum power of the solar panel with the P_{light} light power, measured on the effective surface *(13)* [6, 14, 15, 16, 27, 32, 33]:

$$\eta_{\max}(T) = \frac{P_{max}(T)}{P_{light}} = \frac{I_M \cdot U_M(T)}{P_{light}} = \frac{\varphi \cdot P_{th}(T)}{P_{light}} = \frac{\varphi \cdot I_{SC} \cdot U_{OC}(T)}{P_{light}}. \quad (13)$$

Since the power output of the solar panel is dependent on the temperature, its efficiency is also a function of temperature. The function has a maximum that gives the maximum efficiency of the solar panel. It should be noted here that the solar panel operates with maximum efficiency when the intensity of illumination is low and its temperature is colder [28, 39]. The maximum power and maximum efficiency at the same time can be guaranteed if the solar panel is cooled during the operation while the load is dynamically optimized. Guo et al. [37] and Farshchimonfared et al. [38] shows opportunities for this purpose, where they combine solar panels with solar collectors.

The energy magnitude of the prohibited band E_g is an important parameter during the determination of the solar panel's efficiency. If the energy of the incoming photon E_{photon} is lower than the energy of the prohibited band, then the potential electron is not able to leave the valence band and to enter the conducting band, so photocurrent can not be formed. Therefore, the creation of prohibited band width above the photon's energy is necessary to generate charge carriers. The extra energy (E_{foton} - E_g) transforms into heat [4, 5, 28].

3.3 The Effect of Temperature and Intensity on the Current and Voltage

The T_S operating temperature of the solar panel can be expressed by equation *(14)*:

$$T_S = (T_N - T_A) \cdot \frac{E_{ill}}{E_{STC}} + T_A, \quad (14)$$

where: T_N – the nominal temperature of the solar panel (K),
T_A– the ambient temperature (K),
E_{ill} – the intensity of illumination (W/m^2) [3, 4, 17, 18, 26].

Taking these into account, the photocurrent can be determined as a function of temperature [3, 4, 17, 18, 25, 26, 33]:

$$I_{ph} = I_{SCN} \cdot [1 + \mu_{ISC} \cdot (T_S - T_A)] = I_{SCN} + K_{ISC} \cdot (T_S - T_A), \quad (15)$$

where: μ_{Ir} – the percentage coefficient of the short-circuit current (%/K),
K_{ISC} – the coefficient of the short-circuit current (A/K),
$E_{int\ standard}$ – the intensity of standard illumination (1.000 W/m^2).

If the intensity also changes, the photocurrent value can be written as follows [3, 4, 17, 18, 25, 26, 33]:

$$I_{ph} = \frac{E_{int}}{E_{int\ sztenderd}} \cdot I_{SCN} \cdot [1 + \mu_{Ir} \cdot (T_S - T_A)] =$$

$$\frac{E_{int}}{E_{int\ sztenderd}} \cdot I_{SCN} + K_{ISC} \cdot (T_S - T_A). \quad (16)$$

According to *correlation (16),* the intensity of the illumination and the temperature change also linearly influence the amperage. It can be concluded that if the intensity of the illumination and/or the temperature of the solar panel increases, the voltage drops, so the efficiency of the solar panel decreases.

The saturation current value, as a function of temperature can be calculated based on the two diode models [3, 4, 9, 10, 12, 13, 17, 18, 25, 30, 33]:

$$I_S = \frac{I_{ph}}{\left[exp\left(\left(\frac{e \cdot U_{OC}}{n \cdot k \cdot T \cdot N_S}\right) \cdot (1 + \mu_{UOC} \cdot (T_S - T_A))\right)\right] - 1}, \quad (17)$$

where: μ_{UOC} – the percentage coefficient of the idling voltage (%/K).

The temperature dependence of idle voltage [3, 4, 17, 18, 25, 26, 33]:

$$U_{OCT} = U_{OCN} \cdot [1 + \mu_{UOC} \cdot (T_S - T_A)] = U_{OCN} + K_{UOC} \cdot (T_S - T_A), \quad (18)$$

where: K_{UOC}– the coefficient of idle voltage (V/K).

The power of the solar panel and its efficiency can be determined by the voltage. Amperage can be determined depending on the power (8) and efficiency (13) of the solar panel. All the results of the literature show that the increase in both the temperature and the intensity of illumination results in a decrease in the efficiency of the solar panel [8, 11].

4 The Measurement Compilation and Description of the Measuring Process

4.1 The Sun Simulator

The design of the appropriate lighting conditions was a very important part of constructing the measuring compilation. Simulating the light of nature is an extremely difficult task. Attention should be paid to the intensity of the light, the uniformity of its distribution and to the similarity of the light spectrum of the

illumination and sunlight. According to the *IEC 60 904-9* (Sun Simulator Performance Requirements) the lighting can be classified into different classes according to the homogeneity of the light intensity distribution. For the worst, C-type devices, the ± 10% difference is allowed. Thus, based on the naturally occurring maximum 1,000 W/m^2 light intensity, the value of light intensity can move between 900−1,100 W/m^2 with standard illumination [19, 20, 26]. The reflectors at my disposal did not allow me to meet the criteria prescribed by the standard Therefore, spectral energy density divergences were taken into account by a constant factor. At present, I am working on developing a new kind of simulator for accurate measurements. The intensity distribution of the Sun simulator is shown in *Figure 5*.

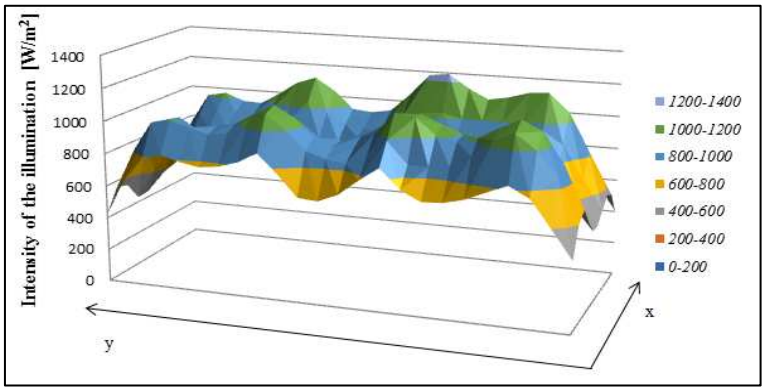

Figure 5
Reflector layout with the associated light intensity distribution

The inhomogeneity of illumination is described in (19) [21]:

$$\Delta E = \frac{E_{max} - E_{min}}{E_{max} + E_{min}} \cdot 100\%, \tag{19}$$

where: ΔE– the degree of inhomogeneity of the illumination [%];
E_{max}– the maximum light intensity value $\left[\frac{W}{m^2}\right]$;
E_{min}–the minimum light intensity value $\left[\frac{W}{m^2}\right]$.

In the measurement setup: E_{max} = 1,245 W/m^2, E_{min} = 407 W/m^2 and ΔE = 50.73%. The median: 874 W/m^2, the modus: 1,000 W/m^2. The light power is: 490.48 *W*.

The significant inhomogeneity determined on the basis of (19) is caused by the drastic reduction of the light intensity on the corners of the illuminated surface. However, if we look at the light intensity distribution shown, it is clear that this surface is a very small fraction of the effective surface. Therefore, the homogeneity of the light intensity distribution is more satisfactory for the remainder of the solar panel.

The value of the average light intensity per solar panel (integrated mean value) can be calculated by means of *formula (20)* from the previously determined real light intensity distribution matrix elements [19].

$$E_{average} = \left(\sum_{i=1}^{10}\sum_{j=1}^{24}(E_{ij} \cdot A_{cell})\right) \cdot \frac{1}{A_{solar\ module}}, \qquad (20)$$

where: $E_{average}$–the value of the average light intensity per solar panel W/m^2;
E_{ij}–the value of the light intensity per cell W/m^2;
A_{cell}– area of one cell (A_{cell} = 0.0025 m^2);
$A_{solar\ module}$–the size of the solar panel's surface ($A_{solar\ module}$ = 0.5695 m^2).

In the measurement setup: $E_{average}$= 861.267 W/m^2. This is slightly below the maximum 1,000 W/m^2 in nature. This light intensity value corresponds to the value of light intensity on a slightly cloudy day. However, due to the shift of the spectral energy of the halogen reflector from the natural light, according to the Vienna law, we have to consider a constant [8, 11, 19, 26, 28]. *Figure 6.* illustrates different light source spectral compositions. It can be observed that the spectral composition of the Sun simulator used differs significantly from the sunlight's.

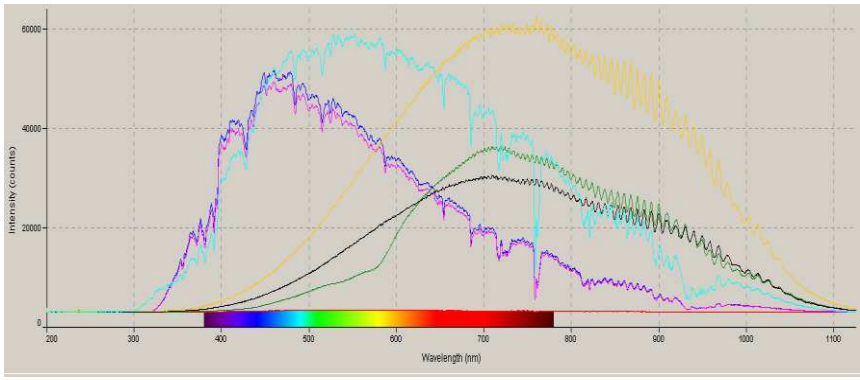

	Blue sky		Blue sky
	Direct sunlight		Regular bulb
	Sun simulator direct		Sun simulator scattered

Figure 6
Spectral composition of different light sources

4.2 The Compiled System and its Components

For the measurements, I used a KS-85 monocrystalline solar panel, created by korax solar. The solar panel was placed on a same sized table az its own size, and 50 *mm* thick wooden slats were placed under the solar panel to lift it, and to create a flow channel between the back of the solar panel and the table. The cool air, to cool the solar panel, was given by an *Orion CSHP 9001 C4* typed mobile climate system. The cold air outflow from the climate was driven by a plastic film to the

already mentioned flow channel. This plastic film worked as a buffer and made the flow sufficiently even. Preliminary temperature examinations proved that the reverse side of the solar panel heats up the same as the absorber surface. According to these, it is possible to withdrawal thermal energy from the reverse side of the solar panel too, so this kind of cooling proved to be functional. The basic assumption is that applying a cooling system increases the power of the solar panel. The compiled system can be seen in *Figure 7.*

Figure 7
The measurement layout

A *YC-747D* typed, four channel digital thermometer was applied to measure the temperature of the solar panel. The four sensors were placed to different parts of the solar panel (Figure 8). in the following, the average temperature of the four points was considered to be the temperature of the solar panel. The sensors were fastened to the surface of the solar panel by the use of good thermal conductive aluminum tape to ensure the accuracy of the results, making sure that the shielded surface is negligibly small.

The temperature of the illuminated and non-cooled solar panel reached 80 °*C*. With applying this cooling, I was able to decrease this temperature by 15 °*C*. To further cool, I tried to extract heat from the absorber surface of the solar panel with the use of a *TT 150* type pipe fan. The flow channel between the reflector and the fan was also created by using plastic film. This solution widened the flow area, so a larger surface of the solar panel could be cooled. It is important to mention that this solution decreases the speed of the flow. When the air conditioner and the fan were used together, the average temperature of the solar panel had decreased by 40 °*C*. Then, the air flowing out of the fan outlet was directed to the surface of the solar panel, so I did not use the previously mentioned deflector. In this case, the speed of flow did not decrease and a further 10 °*C* decrease was achieved. So

using both the climate system and the fan this way means a 50 °*C* temperature decrease. The average temperature in this case was 30 °*C*.

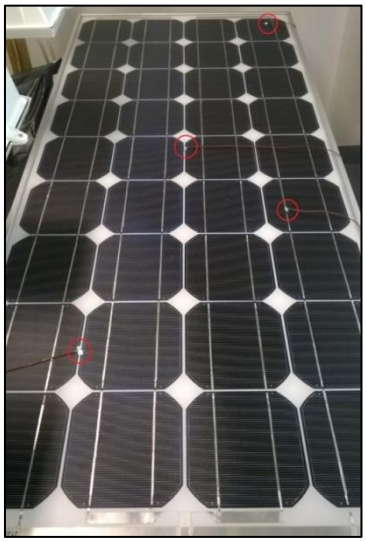

Figure 8
Placing the four sensors on the absorber surface on the solar panel

The load resistance of the solar panel was modelled by a high powered potmeter. The resistance of this potmeter could be set between 0.7 and 7.2 Ω, according to measurements. I used a *Protek DM-301* and a *METEX M-365OD* type digital multimeter to measure the voltage and amperage of the solar panel at the same time.

The purpose of the measurement was to find out the processes during temperature transient. According to the literature, it can be said that the open circuit voltage of the solar panel decreases significantly, while its short circuit amperage slightly increases by the temperature increase. The voltage decreases more than the amperage increases, so the power of the solar panel decreases too in case of higher temperature.

4.3 Constants and Baseline Data Considered during the Simulation

The numerical simulations were made using the equation system of the two-diode model mentioned in the previous chapters. During the simulation, I started from the simplified circuit model of the solar panel. Table 1 contains the constants used during the simulation, while the electrical parameters of the solar panel can be seen in Table 2.

Table 1

Constant parameters [5, 19, 20, 25, 30]

Parameter	Symbol and measurements	Value
The solar irradiation intensity at standard test conditions	E_{STC} [W/m^2]	1,000
Intensity of illumination	E_{ill} [W/m^2]	861
Diode reverse bias saturation current (according to the two diode model)	I_s [A/cm^2]	$1 \cdot 10^{-11}$
Electron charger	e [C]	$1.60 \cdot 10^{-19}$
Boltzmann constant	k [J/K]	$1.38 \cdot 10^{-23}$
Diode ideality factor	n [-]	2
Constant of the light spectral composition	C [-]	0.532

Table 2

Electrical parameters of the solar panel

Parameter	Symbol and measurements	Value
Year of manufacture	-	2008
Peak Power	P_{max} [W]	85
Max. power current	I_M [A]	4.88
Max. power voltage	U_M [V]	17.45
Short circuit current	I_{SC} [A]	5.40
Open circuit voltage	U_{OC} [V]	21.20
Nominal fill factor	φ [-]	0.74
Serial resistance	R_s [Ω]	0.0035
Parallel resistance	R_P [Ω]	10,000
Number of serial connected cells	N_S [piece]	18
Number of parallel connected cells	N_P [piece]	2
Temperature co-efficient for P_{max}	K_{PM} [W/°C]	-0.391
Temperature co-efficient for I_{sc}	K_{ISC} [A/°C]	0.001674
Temperature co-efficient for U_{oc}	K_{UOC} [V/°C]	-0.073776
Percentage Temperature co-efficient for P_{max}	μ_{Pm} [%/°C]	-0.460
Percentage Temperature co-efficient for I_{sc}	μ_{Isc} [%/°C]	0.031
Percentage Temperature co-efficient for U_{oc}	μ_{Uoc} [%/°C]	-0.348
Efficiency (maximal power)	η [%]	12.75
Nominal operating temperature	T_N [°C]	25

During the simulation, I had the following considerations and ommisions:

- I reduced the solar module to one cell,
- I omitted the serial and parallel resistance,
- I took the integrated mean of the intensity of the illumination,
- I calculated with the help of the open circuit voltage, short circuit current and temperature constant, which were given by the manufacturer,
- I considered the difference between the spectral composition (spectral energy density) of the halogen and the sunlight as a constant [5, 9, 10, 12, 13, 25].

4.4 The Modified Model

The modified model uses the temperature constants, determined with the help of the measurement results. It does take the open circuit voltage and short circuit current, given by the manufacturer into account. The temperature constant from the measurements are given in Table 3.

The simulation with the modified model aims to estimate the deterioration of efficiency, caused by the aging of the solar panel. Aging examinations provide more accurate data if the intensity is constant and the temperature is varied. The measurements should be done at different intensities and then average the results with statistical methods.

Table 3

Thermal constants derived from the measurements

Parameter	Symbol and measurements	Value
Temperature co-efficient for P_{max}	K_{PM} [W/°C]	-0.5255
Temperature co-efficient for I_{sc}	K_{ISC} [A/°C]	0.000594
Temperature co-efficient for U_{oc}	K_{UOC} [V/°C]	-0.08692
Percentage Temperature co-efficient for P_{max}	μ_{pm} [%/°C]	-0.459
Percentage Temperature co-efficient for I_{sc}	μ_{Isc} [%/°C]	0.011
PercentageTemperature co-efficient for U_{oc}	μ_{Uoc} [%/°C]	-0.410

Table 4

The ratio of theoretical (catalogue) and counted (measured) temperature constants

	Catalog $\left[\frac{\%}{°C}\right]$	**Measurement** $\left[\frac{\%}{°C}\right]$	**Ratio**[%]
$\boldsymbol{\mu_{pm}}$	-0.46	-0.459	99.78
$\boldsymbol{\mu_{Isc}}$	0.031	0.011	35.48
$\boldsymbol{\mu_{Uoc}}$	-0.348	-0.41	117.82

Thermal constant of the open circuit voltage, derived from the measurements approximates the value given by the solar panel manufacturer. This proves the accuracy of my measurement. The deviation may be caused by the inaccuracy of the measurement and the aging of the solar panel may also affect this value (the year of manufacture of the solar panel I used was: 2008).

Instead of this, the value of the thermal constant of the short circuit current differs greatly from the catalog data. This may by caused also by the inaccuracy of the measurement and the properties of the illumination because the light conditions produced in my case were not the same as those that were used during the qualification of the solar panel. If we consider the difference of the illumination's spectral composition, then the thermal constant of the short circuit current from the measurement results is 0.0207 %/°C, which means 66.77% of the one, which is given by the manufacturer.

5 Comparasion ofMeasurement and Simulation Results

5.1 Transient Examination in Case of Unloadid Solar Panel

I made transient examinations by using an unloaded solar panel at first. In this case, I turned the illumination and the cooling system at the same time. I measured the temperature at four places in every minute for 20 minutes. I also measured the open circuit voltage, generated by the cells, and the short circuit current (Section 1). After this, I turned the cooling system off, and resumed sampling at 10 measuring points for 10 minutes (Section 2). After the solar panel temperature stabilized, it had been cooled down to the initial temperature, by inserting the previously described cooling fan (Section 3). The temperature-time graph is shown in Figure 9. It can be observed that the surface temperature of the solar panel changes exponentially while applying the cooling system. I show the results as a function of the temperature, however, a scale still indicates a lapse of one minute, so the temperature and time function can be written simultaneously.

Without cooling, the temperature of the solar panel, determined by the average of the four sensors, seemed to remain constant at 74.88 *°C*. The temperature, defined by equation (14) is 76.66 *°C*, so the value is 2.38% higher than the measured value.

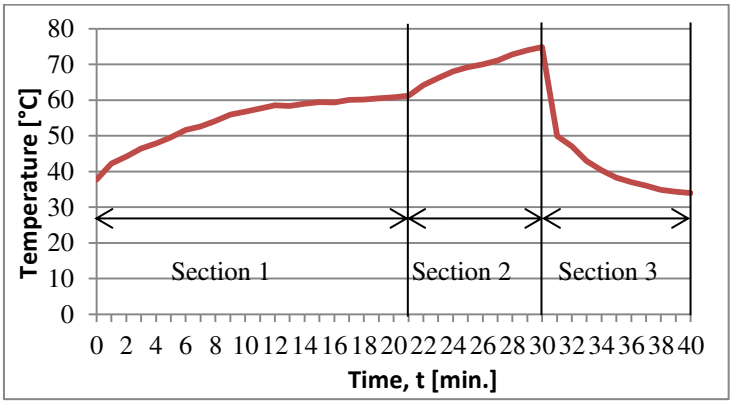

Figure 9
The time function of the temperature of the solar panel's surface

The short circuit current value, as a function of the temperature can be seen in Figure 10. It can be observed that the current-temperature (time) curve outline in the measurement results follows the curve outlined on the basis of numerical simulations based on catalog data. The time-averaged difference is 4.14%, while the difference created with the help of the modified model is 1.38%. So the modified model gives a more accurate approximation overall, but the outlined curve is less similar to the measured curve. For each curve it can be said that depending on the temperature, the expected amperage-change occurred. The amperage increased without cooling, while it decreased with cooling. The same tendency can be seen in some similar publications, such as Singh et al. [28] and Malik et al. [31].

The temperature dependence of the open circuit voltage can be seen in Figure 11. It can be noticed that the modified model had produced nearly coincident results with the measured results during lightly cooling the solar panel. The model is more similar to the basic model in the case of non-cooling or strong cooling. The modified model overestimates the measured results in time-average by 2.52%, while this percentage is 5.98%, in case of the basic model. These results are very similar to the results which were obtained by many other studies, such as Singh et al. [28], Chantana et al. [29] and Malik et al. [31].

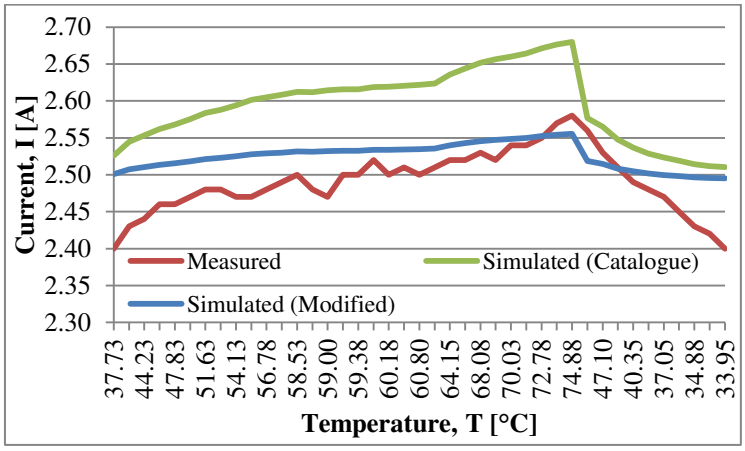

Figure 10

The short circuit current of the solar panel, depending on the temperature (time)

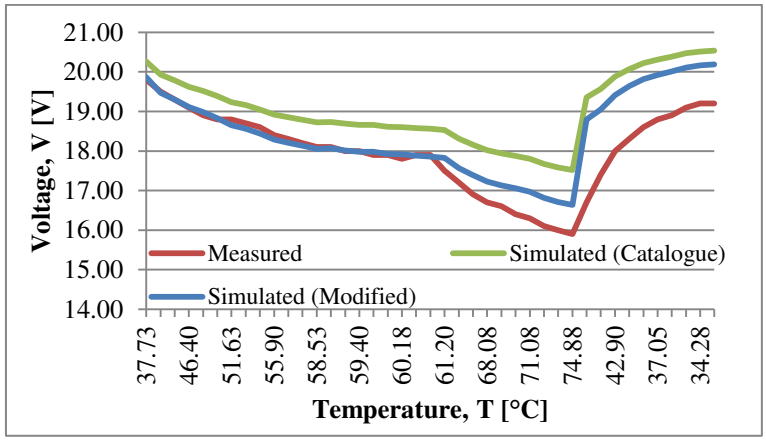

Figure 11

Temperature (time) dependence of the solar panel's open circuit voltage

The theoretical power graphs can be seen in Figure 12. It can be clearly stated that the theoretical power decreases due to the increase in the solar panel's temperature. This was assumed, based on the theoretical power calculation (1). The reason of the decrease is that the voltage of the solar panel decreases more than its amperage increases with the temperature increase. The simulation basic model estimated the theoretical power by 10.34%, while the modified model estimated it by 3.92%.

Based on numerical simulations using catalog data, it can be said that the theoretical power (and efficiency) of the solar panel 9.32%, while in case of the simulation with the modified model is 3.7% less than in case of its new state. The

modified model calculates with temperature constants determined from the measurement results, but it considers the open circuit voltage and short circuit current, given by the manufacturer. Therefore, the decrease in power caused by the aging of the solar panel can be attributed to this value. The 3,7% drop in power and efficiency deterioration can approximate better the real value.

Overall, it can be said that the temperature increase causes a decrease in the open circuit voltage, while the short circuit amperage only slightly increases, and the multiplication of these amounts, so the power of the solar panel decreases too. In the reverse case, if the solar panel cools down, the voltage and the power increases, while the amperage decreases. The experiments proved that the phenomenon, described in the literature is correct.

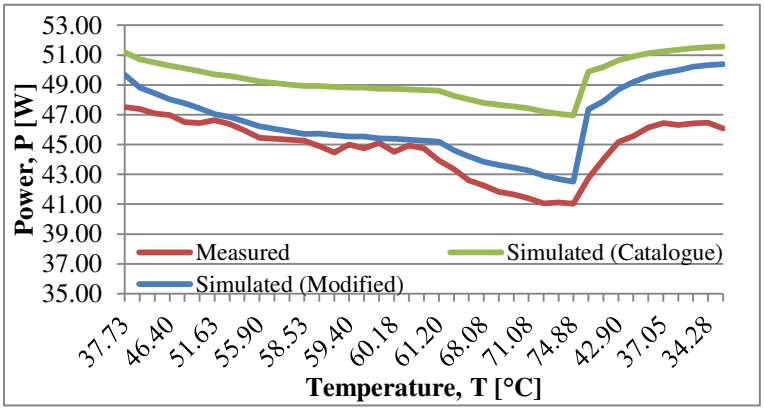

Figure 12

Temperature (time) dependence of the solar panel's theoretical power

Table 5 summarizes statistical data for differences between simulation and measured results, during transient analyzing in the case of an unloaded solar panel. It can be observed that the largest difference between simulation and measurement of open circuit voltage and theoretical power is greater than 10% for both the catalog and the modified model. There is no repeat (modus) in the deviations.

Table 5

Statistical data for the difference between the simulated and measured results.

	Simulated (Catalog)				**Simulated (Modified)**			
	Min [%]	Max [%]	Median [%]	Avarage [%]	Min [%]	Max [%]	Median [%]	Avarage [%]
I_{SC}	0.66	5.84	4.59	4.14	-1.71	4.20	1.31	1.38
U_{OC}	2.20	15.92	4.52	5.98	-0.87	12.58	0.63	2.52
P	6.60	16.68	9.91	10.34	0.66	10.77	2.93	3.92

5.2 Transient Examination inCase of Loaded Solar Panel

Temperature transient analyzes were made in case of a loaded solar panel in two cases. I connected a 4.2 ohm resistor to the terminals of the solar panel. In the first case, the solar panel was non-cooled, while in the other case the cooling was continuous. I measured the terminal voltage, the amperage and the temperature of the solar panel every minute. The purpose of this measurement was to reveal the change in electrical parameters of a chilled and a non-cooled solar panel, operating at the same temperature. The temperature-time curves in both cases can be seen in Figure 13. It can be observed that the temperature in both cases increased by time.

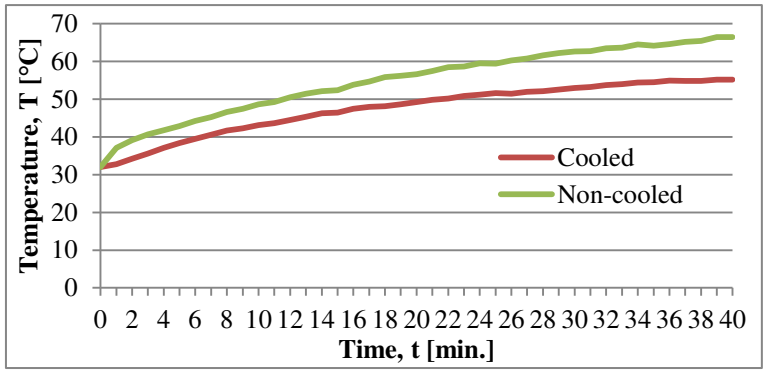

Figure 13
The time function of the temperature of the loaded solar panel's surface in chilled and non-cooled cases

Figure 14. shows the amperage. In both the simulations and the curves from the measurement it can be seen that with time (temperature increase) the chilled and non-cooled curves are merged. The time-average difference between the simulation and the measurement results for the chilled solar panel is 2.67%, and this is 3.85% without cooling. Many other researchers received similar results, for example Singh et al. [28] and Malik et al. [31].

In Figure 15 the voltage, as the function of time (temperature) can be seen. It can be observed in both the simulation and the measurement results, the curves of the chilled and non-cooled solar panel cross each other, just like in case of other researches: Singh et al. [28],Chantana et al.[29] and Malik et al. [31]. The time-averaged difference in cooled case is 4%, while without cooling it is 4.03%.

Figure 16 shows the power of the solar panel. It can be seen, that the curves from the simulation and measurement show the same characteristics. The characteristics of both the chilled and the non-cooled solar panel cross each other in case of simulation and measurement too. The time-average difference in case of cooled solar panel is 6.79%, while it is 8.04% without cooling.

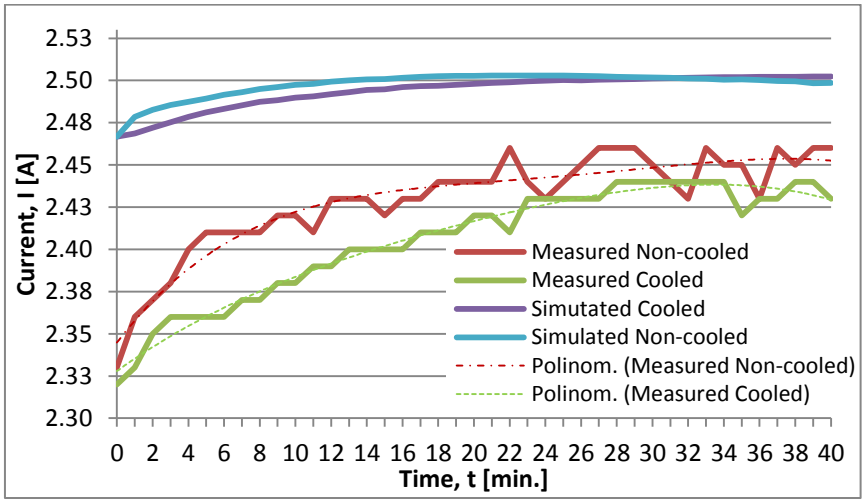

Figure 14

The time function of the loaded solar panel's current in chilled and non-cooled cases

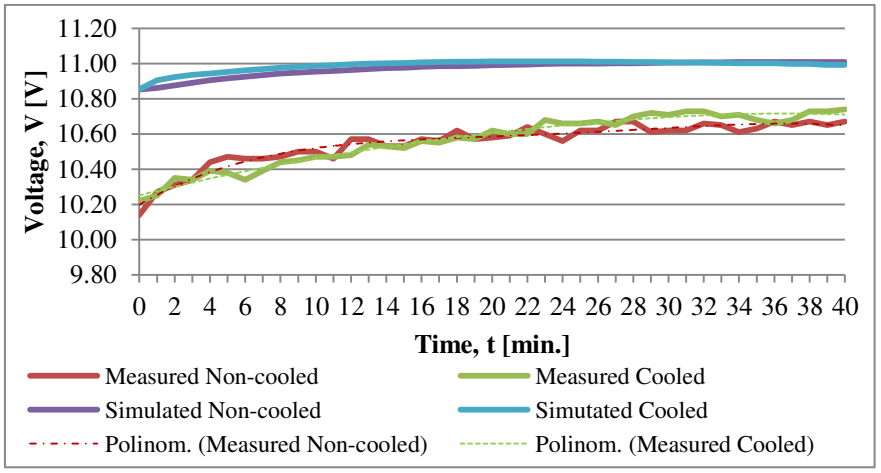

Figure 15

The time function of the loaded solar panel's voltage in chilled and non-cooled cases

During the transient analyzation of the loaded solar panel, the results from the measurements approach the simulation results more closely. The curves nature exactness is best seen in terms of power.

Table 6 summarizes the statistical data of differences between simulated and measured results, during transient analyzes in case of loaded solar panel, in both chilled and non-cooled cases. It can be observed that the largest difference between simulation and measurement of power is greater than 10% in both chilled and non-cooled cases. There is no repeat (modus) in the deviations.

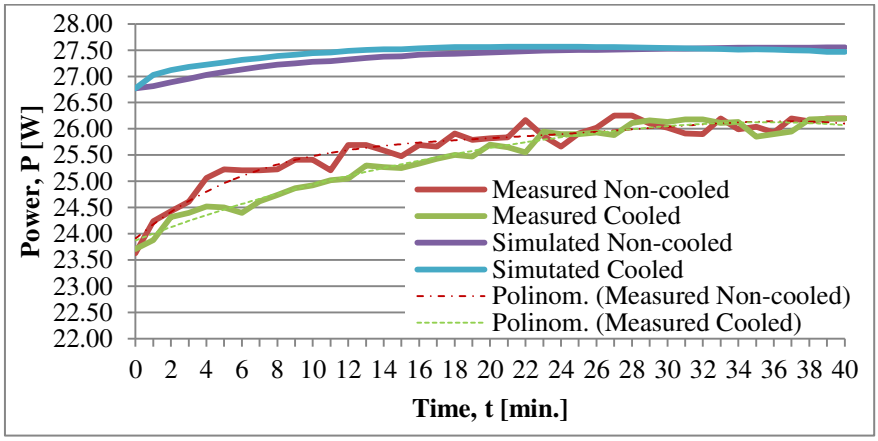

Figure 16
The time function of the loaded solar panel in chilled and non-cooled cases

Table 6
Statistical data of difference between simulated and measured results

	Cooled				Non-cooled			
	Min [%]	Max [%]	Median [%]	Avarage [%]	Min [%]	Max [%]	Median [%]	Avarage [%]
I	1.58	5.87	2.55	2.67	2.40	6.37	3.82	3.58
U	3.11	7.04	3.78	4.00	2.36	6.39	3.90	4.03
P	4.80	11.30	6.34	6.79	4.83	13.18	7.89	8.04

Conclusions

The open circuit voltage and short circuit amperage values were close to the values described in the literature. The measurement results approached the values from the numerical simulation well. In case of the loaded solar panel, during the transient analyzes, the voltage increased, while the current decreased almost the same, due to the temperature decrease. Cooling increased the P_{th} theoretical power. So the main goal of the cooling is to improve the solar panel's energetic efficiency and to increase its lifetime. The results of the experimental and simulation examinations clearly reflect that the cooling changes the solar panel power in a positive direction, so the basic assumption is correct.

After comparing the measurement results with the simulation results, the conclusion can be drawn that the efficiency of the solar panel decreased compared to its new state. However, it should be not be ignored that the results are significantly dependent on the inaccuracy of the instruments and the measurement method, the measurement errors. So, the resulting percentage deviations can also be tracked back to these.

Inaccuracies and many other things may cause the difference between measured and calculated data. The illumination I used, did not reproduce the natural light enough (smaller, and not sufficiently homogeneous light intensity, different wavelength structure). During the aging of the solar panel, efficiency degradation is experienced, which results in a decrease in power.

The manufacturer warrants that the efficiency of the solar panel will not decrease more than 10% in the first 10 years. The solar panel I used during the examinations was 7 years old. The efficiency decrease of the solar panel was about 4%, which was calculated from the simulation and measurement results.

It is important to note that each solar panel manufacturer gives the maximum power and efficiency of the solar panel, measured with STC (Standard Test Conditions). The value of the light intensity is 1,000 W/m^2 in that case, the temperature of solar cells is 25 $°C$ and the value of air density is AM 1.5. These conditions can only be realized in an ideal case. The temperature value differs from those actually experienced. Based on these, it can be said that the power of the solar panel in majority of cases is less than the maximum power given by the manufacturer. During the examinations I made, the lowest cell temperature was about 30$°C$, so it did not meet the STC temperature criteria. This also contributed to the difference between the measured and the maximum power from the catalog. Some manufacturers correct this and give so-called electrical parameter values valid on NOCT (Normal Operating Cell Temperature). These values are closer to the real values. The NOTC means 800W/m^2 light intensity, 20 $°C$ temperature and 1 *m/s* air flow speed, and the manufacturer gives the temperature value of the module during the operation. This value moves between 33 $°C$ and 58 $°C$ in practice [19, 20, 21].

References

[1] Hersch, P.: Basic photovoltaic principles and methods. United States Department for Energy. USA, 1982. p. 55

[2] King, L. D., Kratohvil, A. J., Boyson, E. W.: Temperature Coefficients for PV Modules and Arrays: Measurement Methods, Difficulties, and Results, 26th IEEE Photovoltaic Specialists Conference, Anaheim, California, 1997. pp. 1183-1186

[3] Dubey, S., Sarvaiya, J. N., Seshadri, B.: Temperature Dependent Photovoltaic (PV) Efficiency and Its Effect on PV Production in the World-A Review. Energy Procedia 33. 2013. pp. 311-321

[4] Singh, P., Singh, S. N., Lal, M., Husain, M.: Temperature dependence of I-U characteristics and performance parameters of silicon solar cell. Solar Energy Materials and Solar Cells. Vol. 92. No. 12. 2008, pp. 1611-1616

[5] Szász, Cs.: Optimal control of Photovoltaic Modules Energy Efficiency. Journal of Computer Science and Control Systems. Vol. 10, No. 1, 2017, pp. 29-34

[6] Zerhouni, Z. F., Zerhouni, H. M., Zegrar, M., Benmesseaoud, T. M., Stambouli, B. A., Midoun, A.: Prosed methods to increase the output efficiency of a photovoltaic (PV) system. Acta Polytechnica Hungarica. Vol. 7, No. 2, 2010, pp. 55-70

[7] Makhloufi, M. T., Khireddine, M. S., Abdessemed, Y., Boutarafa, A.: Maximum power point tracking of a photovoltaic system using a fuzzy logic controller on DC/DC boost converter. International Journal of Computer Science. Vol. 11, No. 3, 2014, p. 12

[8] Kádár, P., Varga, A.: Measurement of spectral sensitivity of PV cells. 2012 IEEE 10th Jubilee International Symposium on Intelligent Systems and Informatics. 2012, pp. 549-552

[9] Chan, D. S. H., Phang, J. C. H.: Analytical methods for the extraction of solar-cell single- and double-diode model parameters from I-V characteristics. IEEETransactions on Electron Drives. Vol. 34, No. 2, 1987, pp. 286-293

[10] Ishaque, K., Salam, Z., Taheri, H.: Simple, fast and accurate two-diode model for photovoltaic modules. Solar Energy Materials and Solar Cells, Vol. 95, No. 2, 2011, pp. 586-594

[11] Chegaar, M., Ouennoughi, Z., Hoffmann, A.: A new method for evaluating illuminated solar cell parameters. Solid-State Electronic, Vol. 45, No. 2, 2001. pp. 293-296

[12] Kurobe, K., Matsunami, H.: New two-diode model for detailed analysis of multicrystalline silicon solar cell. Japanese Journal of Applied Physics, Vol. 44, 2005, pp. 8314-8321

[13] Ishaque, K., Salam, Z., Taheri, H., Syafaruddin: Modelling and simulation of photovoltaic (PV) system during partial shading based on a two-diode model. Simulation Modelling Practice and Theory, Vol. 19, No. 7, 2011, pp. 1613-1626

[14] Malik, A. Q., Damit, S. J. B. H., Outdoor testing of single crystal silicon solar cells. Renewable Energy 28, 2003, pp. 1433-1445

[15] Nagy, D., Rácz, E., Varga, A. Ruf, H., Neuchel, E., R.: Comparison of electric current – voltage, characteristics and maximal power point values of differently and artificially aged solar panels. Proceedings of the 13th IEEE International Symposium on Applied Computational Intelligence and Informatics. 2016, pp. 295-300

[16] Varga, A., Libor, J., Rácz, E., Kádár, P.: A small laboratory-scale experimental method and arrangement for investigating wavelength dependent irradiation of solar cells. Proceedings of the 11th IEEE International Symposium on Applied Computational Intelligence and Informatics. 2014, pp. 137-141

[17] Radziemska, E.: The effect of temperature on the power drop in crystalline silicon solar cells. Renewable Energy. Vol. 28, No. 1, 2003. pp. 1-12

[18] Skoplaki, E., Palyvos, J. A.: On the temperature dependence of photovoltaic module electrical performance: A review of efficiency/power correlations. Solar Energy. Vol. 83, No. 5, 2009, pp. 614-624

[19] Siddiqui, R., Kumar, R., Jha, K. G., Morampudi, M., Rajput, P., Lata, S., Agariya, S., Nanda, G.,Raghava, S. S.: Comparison of different technologies for solar PV (Photovoltaic) outdoor performance using indoor accelerated aging tests for long term reliability. Energy. Vol. 107, No. 15, 2016, pp. 550-561

[20] Munoz-Garcia, M. A., Marin, O., Alonso-García, M. C., Chenlo, F.: Characterization of thin film PV modules under standard test conditions: Results of indoor and outdoor measuremnets and the effects of sunlinght exposure. Solar Energy. Vol. 86, No. 10, 2012, pp. 3049-3056

[21] Földváry, Á.: Napelemeklaboratórium. Budapest University of Technology and Economics. Performance materials. 2015, p. 32

[22] Precup, R. E., Preitl, S., Korondi, P.: Fuzzy Controllers With Maximum Sensitivity for Servosystems. IEEE Transactions on Industrial Electronics, Vol. 54, No. 3, 2007, pp. 1298-1310

[23] Ürmös, A., Farkas, Z., Farkas, M., Sándor, T., Kóczy, L.T., Nemcsics, Á.: Application of self-organizing maps for technological support of droplet epitaxy, Acta Polytechnica Hungarica, Vol. 14, No. 4, 2017, pp. 207-224

[24] Shams, M., Rashedi, E., Dashti, S.M., Hakimi, A.: Ideal gas optimization algorithm. International Journal of Artificial Intelligence. Vol. 15, No. 2, 2017, pp. 116-130

[25] Pareja-Aparicio, M., Pelegrí-Sebastia, J., Sogorb, T., Llario, V.: Modeling of Photovoltaic Cell Using Free SoftwareApplication for Training and Design Circuit inPhotovoltaic Solar Energy. INTECH World's largest Science,Technology & MedicineOpen Access book publisher. Chapter 6, 2013, p. 21

[26] Kandil, M. K., Altouq, M. S., Al-asaad, A. M., Alshamari, L. M., Kadad, I. M., Ghoneim, A. A.: Investigation of the Performance of CIS Photovoltaic Modules under Different Environmental Conditions. Smart Grid and - Renewable Energy. No. 2, 2011, pp. 375-387

[27] Mishima, T., Taguchi, M., Sakata, H., Maruyama, E.: Development status of high-efficinecy HIT solar cells. Solar Energy Materials and Solar Cells. Vol. 95, 2011, pp. 18-21

[28] Singh, P., Ravindra, N.M.: Temperature dependence of solar cell performance – an analysis. Solar Energy Materials and Solar Cells. Vol. 101, 2012, pp. 36-45

[29] Chantana, J., Kato, T., Sugimoto, H., Minemoto T.: Time-resolved photoluminescence of Cu(In,Ga)(Se,S)2 thin films and temperature dependent current density-voltage characteristics of their solar cells on surface treatment effect. Current Applied Physics. Vol. 17, No. 4, 2017, pp. 461-466

[30] Ashi, S., Teranishi., H., Kusaki, K., Kaizu, T., Kita, T.: Two-step photon up-conversion solar cell. Nature Communitacions. 2017, p. 9

[31] Malik, A. Q., Ming, L. C., Sheng, T. K., Blundel, M.: Influence of Temperature on the Performance of Photovoltaic Polycrystalline Silicon Module in the Bruneian Climate. AJSTD Vol. 26, No. 2, 2010, pp. 61-72

[32] Yadav, P., Pandey, K., Bhatt, V., Kumar, M., Kim, J.: Critical aspects of impedance spectroscopy in silicon solar cell characterization: A review. Renewable and Sustainable Energy Reviews. Vol. 76, 2017, pp. 1562-1578

[33] Altermatt, P., Reinders, A., Verlinden, P., van Sark W.,Freundlich A.: Numerical Simulation of Crystalline Silicon Solar Cells. Photovoltaic Solar Energy. 2017, p. 682

[34] Sundarabalan, C. K., Selvi, K., Sakeenathul Kubra, K.: Performance Investigation of Fuzzy Logic Controlled MPPT for Energy Efficient Solar PV Systems.Power Electronics and Renewable Energy Systems. Vol. 326, 2014, pp. 761-770

[35] Verma, D., Nema, S., Shandilya, A. M., Soubhagya Dash, K.: Maximum power point tracking (MPPT) techniques: Recapitulation in solar photovoltaic systems. Renewable and Sustainable Energy Reviews. Vol. 54, 2016, pp. 1018-1034

[36] Gobhinat, S., Ram Abhinav, P. S., Gowtham, V., Lokesh, S.: A Prototype Development of MPPT Algorithm based Solar Photovoltaic Charging System. International Journal of Engineering and Management Research (IJEMR). Vol. 6, No. 2, 2016, 139-143

[37] Guo, J., Lin, S., Bilbao, J. I., White, S. D., Sproul, A. B.: A review of photovoltaic thermal (PV/T) heat utilisation with low temperature desiccant cooling and dehumidification. Renewable and Sustainable Energy Reviews. Vol. 67, 2017, pp. 1-14

[38] Farshchimonfared, M., Bilbao, J. I., Sproul, A. B.: Full optimisation and sensitivity analysis of a photovoltaic–thermal (PV/T) air system linked to a typical residential building. Solar Energy. Vol. 136, 2016, 15-22

[39] Koós, D., Szaszák, N., Bodnár, I., Boldizsár, Cs.: Temperature Dependance of Solar Cell's. ActaTechnicaCorviniensis- Bulletin of Engineering. Vol. 9, No. 2, 2016, pp. 107-110

Gradient-based Image Quality Assessment

Boban Bondzulic[1], Vladimir Petrovic[2], Milenko Andric[1], Boban Pavlovic[1]

[1] Military Academy, University of Defence in Belgrade, Generala Pavla Jurisica Sturma 33, 11000 Belgrade, Serbia

[2] Faculty of Technical Sciences, University of Novi Sad, Trg Dositeja Obradovica 6, 21000 Novi Sad, Serbia

e-mails: boban.bondzulic@va.mod.gov.rs, v.petrovic@manchester.ac.uk, milenko.andric@va.mod.gov.rs, boban.pavlovic@va.mod.gov.rs

Abstract: An objective measure for image quality assessment based on a direct comparison of visual gradient information in the test and reference images is proposed. A perceptual model is defined to provide local estimates of gradient preservation and investigate perceptual importance pooling of such local quality estimates by using the lowest scores. The proposed perceptual pooled measure is validated using extensive subjective test results. Results indicate that the proposed measure is perceptually meaningful in that it corresponds well with the results of subjective evaluation and can outperform actual objective metrics.

Keywords: gradient magnitude; gradient orientation; image quality assessment

1 Introduction

Recent years have seen tremendous growth in visual information representation and communication applications whose performance depends greatly on the quality of output images. Subjective trials and mean opinion scores (MOS) are the most relevant way of assessing image quality but they are inconvenient, slow, and expensive for most real applications. Objective image quality metrics predict perceived image quality computationally.

Objective image and video quality assessment measures have been used in numerous applications. Most of the applications relate to situations where it is necessary to evaluate the quality of a modified version of the reference (original, source) image or they have been used in situations where a comparison is converted into something that is not the signal quality, such as a set of measured data or decisions [1]. Thus, image and video quality assessment measures have

been used in the following applications: steganography, digital image watermarking, image fusion quality assessment, noise removal, image enhancement, the assessment of the success of super-resolution techniques, assessing the quality of the resolution degraded images, dynamic range image conversion, coding, remote sensing, video surveillance, object identification, object tracking, classification, analysis of quality of service, etc.

This paper explores the feasibility of a gradient preservation framework, successfully applied to image fusion evaluation [2], in the domain of objective full-reference image quality assessment. The proposed method is a customized and linearized version of the initial framework and is tested on well known, publicly available subject-rated image databases with different distortion types and levels of distortion [3-7]. The performance is compared with actual image quality assessment measures: peak signal-to-noise ratio (PSNR), structural similarity index (SSIM) [8], as well as its relatives – universal image quality index (UIQI) and multi-scale structural similarity (MS-SSIM) [9], visual information fidelity (VIF) [10], visual signal-to-noise ratio (VSNR) [11], most apparent distortion (MAD) [12] and edge preservation measure (Q^{AB}) [13].

Image gradient has, in recent years, been used in an increasing number of ways in assessing image quality [14-24]. In the largest number of objective measures, the gradient magnitude of the original and test image is evaluated, mostly using Roberts, Sobel, Scharr or Prewitt filters, after which the magnitude comparison is performed in similar manner to the SSIM index [14-16]. In addition to image gradient magnitude, different methods often use additional features. Thus, in [17], in addition to the gradient magnitude, phase congruency was used as a measure of the significance of the local structure and as a complementary feature in the local quality assessment. In [18], gradient magnitude is combined with a visual saliency map, which has a dual role – as a feature to determine local quality of the test image and as a weighting function when pooling local quality scores into a global one. A reliable objective measure from [19], in addition to determining the similarity of the gradient magnitudes, also uses chromaticity similarity to measure color distortions. In [20] gradient magnitude and color similarity maps in contour regions, edge-extension regions and slowly-varying regions are pooled by two complementary aspects: visual saliency and visual masking effect.

Apart from a full reference assessment of test image quality compared to the original signal, gradient magnitude has also been used for reduced-reference [21], and no-reference image quality estimation [22, 23]. The method in [21] exploits natural image statistics and shows that log histogram of natural image gradients obeys a specific distribution. No-reference image quality assessment model from [22] utilizes joint statistics of the normalized gradient magnitude map and the Laplacian of Gaussian response. Another blind image quality assessment approach from [23] extracts features in both the spatial (point-wise statistics) and gradient (neighboring gradient magnitude statistical features) domains. While mostly using complimentary approaches, all these studies agree on the fact that gradient

information is key to estimating objective image quality and is particularly useful in comparing structures between original and test images. In this context however only gradient magnitude is used and directional gradient information is ignored.

In this paper an objective, full reference image quality metric based on the preservation of gradient information from the original signal is proposed. Our contribution is to explore and use gradient orientation information as a complementary feature to gradient magnitude as well as new effective methods for pooling of local quality scores obtained using gradient information. The application of gradient orientation has not been fully explored in the context of image quality assessment, with very few studies available in the literature [13, 24]. We show that using gradient orientation can improve the results, increase the correlation with subjective scores of objective image quality assessment based solely on gradient magnitude. We also shown that the correct selection of local quality scores can additionally increase the degree of agreement between subjective and objective quality scores. The performance of the proposed measure is consistent and stable with five publicly available subject-rated image datasets.

2 Theory

Image gradient plays a very important role in human understanding of visual signals, effectively serving to carry structural scene information. As such it is a vital feature in the development of objective quality assessment measures that largely base their measurement on the preservation of this information from the original image into the test image. Different types of degradations lead to a gradient changes, with changes in contrast graded by changes in gradient magnitude, and structural changes evident in changes to gradient orientation. Using estimates of both local gradient magnitude and orientation, local quality of reproduction of the information from the original image can be determined as a direct measure of displayed image quality. In this manned both the contrast and shape distorting effects of various degradations to image quality can be measured.

Gradient preservation framework is based on the idea that only successful transfer of image structures from the reference into the test image constitutes good quality and that structural information can be captured by looking at local intensity gradients. The method extracts gradient information and uses a perceptual change model to compare them in between reference and test images to obtain local estimates of gradient preservation. These effectively local quality estimates are combined using a more advanced perceptual pooling method into an overall objective quality score.

Initially, local x and y gradients are extracted from the reference and test images, R and T, using Sobel templates. Gradient (edge) magnitude, g, and orientation, α,

are easily obtained for each pixel (n,m) from the Sobel responses s^x and s^y according to:

$$g_R(n,m) = \frac{\sqrt{s_R^x(n,m)^2 + s_R^y(n,m)^2}}{g_{\max}} \tag{1}$$

$$\alpha_R(n,m) = \arctan\left(\frac{s_R^y(n,m)}{s_R^x(n,m)}\right) \tag{2}$$

where $g_{\max}$ is maximum magnitude, taken as $g_{\max}$=4.472, for 8-bits/pixel grayscale images. Both parameters are thus bounded, $g \in [0,1]$ from none to maximum contrast, and orientation $\alpha \in [-\pi, \pi]$.

It is assumed that an input edge is perfectly represented only if both its magnitude and its orientation are unchanged in the test image. When a loss of contrast exists between R into T, gradient magnitude change, Δ_g, is observed, and is defined as:

$$\Delta_g(n,m) = \begin{cases} \dfrac{g_T(n,m)+C}{g_R(n,m)+C}, g_R(n,m) > g_T(n,m) \\ \dfrac{g_R(n,m)+C}{g_T(n,m)+C}, g_R(n,m) \le g_T(n,m) \end{cases} \tag{3}$$

where the constant C (C=1/64) is included to avoid instability when the denominator in Eq. (3) is very close to zero.

Orientation α however, is cyclic, i.e. values at the two extremes ($-\pi$, and π) are in fact equivalent and change in orientation in T with respect to R, Δ_α, measuring structural similarity can be defined as:

$$\Delta_\alpha(n,m) = \frac{\left|\left|\alpha_R(n,m) - \alpha_T(n,m)\right| - \pi\right|}{\pi} \tag{4}$$

For a total of NxM pixels, the overall success of gradient preservation is obtained as a mean value of local gradient preservations:

$$\Delta_i^{RT} = \frac{1}{NM}\sum\nolimits_{\forall n,m} \Delta_i(n,m)\,,\ i \in \{g,\alpha\} \tag{5}$$

This model in effect quantifies perceived visual information loss with respect to changes in gradient parameters, broadly changes in contrast (magnitude), Δ_g^{RT}, and shape/structure (orientation), Δ_α^{RT}. Gradient magnitude and orientation preservations, Δ_g^{RT} and Δ_α^{RT}, are combined into a single gradient preservation measure Δ^{RT}:

$$\Delta^{RT} = \sqrt{\Delta_g^{RT} \cdot \Delta_\alpha^{RT}} \tag{6}$$

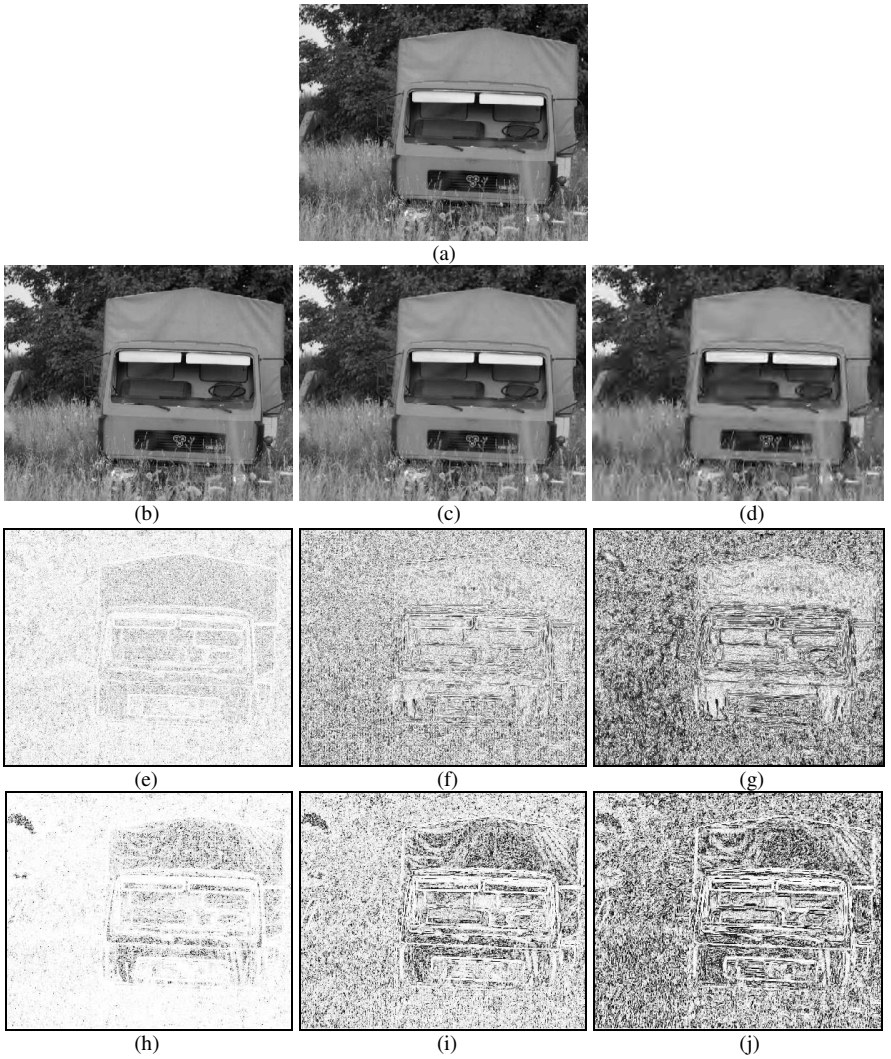

Figure 1

(a) reference image, (b) (c) (d) distorted (test) images (created by JPEG2000 compression), (e) (f) (g) gradient magnitude preservation maps computed using Eq. (3), and (h) (i) (j) gradient orientation preservation maps computed using Eq. (4)

A pixel-domain full-reference example is shown on Figure 1, where the goal is to evaluate the quality of test images, (b), (c) and (d), with a given perfect-quality reference image (a) (images are from the VCL@FER database [5]). The resulting gradient magnitude and orientation information preservation maps are shown below the test images – the brighter indicates better quality (larger local Δ_g^{RT} and Δ_α^{RT} values). The gradient information preservation maps reflect the spatial

variations of the perceived image quality. The careful inspection shows that the coarse quantization in JPEG2000 algorithm results in smooth representations of fine-detail regions in the image (e.g. the trees and the grass in (c) and (d)).

Table 1 provides subjective (MOS) and objective values for test images on Fig. 1. Objective measures deliver good consistency with perceived quality measurements. Notice from Table 1 that for high-quality Figure 1(b) image, MAD technique, which uses a simple spatial-domain model of local visual masking, provides the value of 0 (lower is better). It means that there are no visible distortions on Figure 1(b).

Table 1
Subjective (MOS) and objective evaluations for the test images shown on Figure 1

Image	MOS	PSNR	MS-SSIM	VIF	VSNR	MAD	Q^{AB}	Δ_g^{RT}	Δ_α^{RT}	Δ^{RT}
Fig. 1(b)	75.72	43.89	0.99	0.98	42.15	0	0.91	0.95	0.94	0.94
Fig. 1(c)	52.44	31.68	0.98	0.51	33.15	31.86	0.56	0.78	0.79	0.78
Fig. 1(d)	31.59	26.85	0.89	0.18	19.62	69.79	0.31	0.66	0.66	0.66

3 Perceptual Importance Pooling

Image quality assessment is most often carried out in two phases. In the first phase, the quality is determined at the local level, while in the second phase, the integration of local quality scores is performed to determine a single global quality score for the entire test image. The second phase, considered in this chapter focuses on the observation that human observers do not base their impressions of quality on the entire visible signal. Furthermore, the influence different locations in the signal have on their subjective scores varies highly [25, 26] and in order to predict subjective quality scores, this effects needs to be modeled effectively. In addition to the most obvious average pooling of all local quality scores, different techniques for the association of local quality scores have been proposed: deviation based pooling, region-based pooling, pooling using the lowest quality scores, ... [26].

Summations in Eq. (5), effectively represent a linear spatial pooling where each pixel has an equal influence on the overall quality score. It is an established fact however, that humans tend to attach more importance to regions of poor quality in images [25, 26]. Perceptual importance approach by pooling over only the lowest Δ_g and Δ_α scores, i.e. only regions with poor quality, is investigated. Specifically, quality maps Δ_g and Δ_α are found using Equations (3) and (4), then the values are arranged in ascending order. A mean score is calculated from the lowest $p\%$ of these values ($\Delta_g^{p\%}/\Delta_\alpha^{p\%}$). Pixels that fall outside this percentile range are rejected.

Driven by the experience of probabilistic systems where a single low value biases a global score obtained using a product rule (e.g. Eq. (6)), a simpler, additive framework as an alternative to Eq. (6), combined with optimal quality guided lowest percentile pooling is investigated:

$$AM\text{-}\Delta^{RT} = w_g \Delta_g^{p_g\%} + (1-w_g)\Delta_\alpha^{p_\alpha\%} \tag{7}$$

where, w_g and $(1\text{-}w_g)$ are the relative importance of the magnitude and orientation components, $w_g \in [0,1]$. Two questions remain – what percentile should be used and what weight to assign to each of the two components?

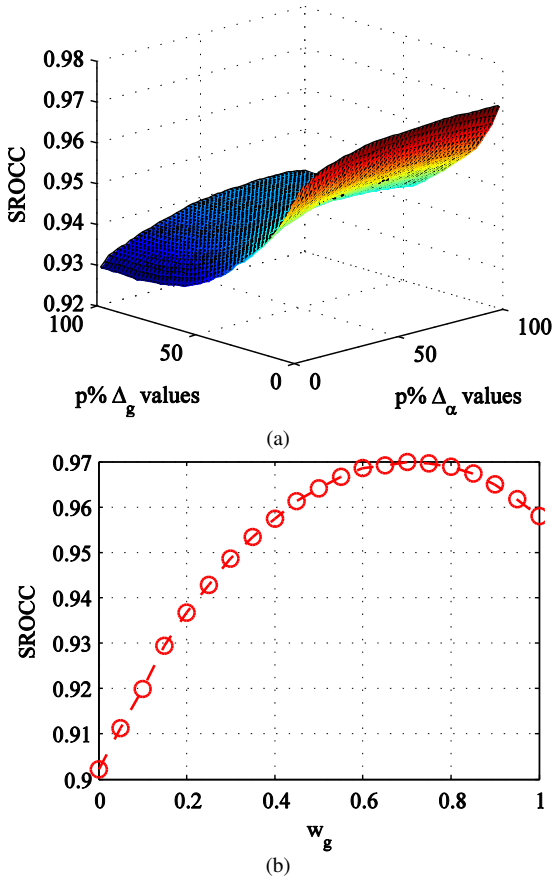

Figure 2

(a) SROCC as a function of the lowest $p\%$ scores for Δ_g and Δ_α (in p=2% increments and for optimal w_g=0.7 value), and (b) training set SROCC of $AM\text{-}\Delta^{RT}$ (Eq. (7)) as function of w_g (in 0.05 increments and for optimal p_g=2% and p_α=78% values)

In order to determine the optimal values for p_g, p_α and w_g, an exhaustive optimization on LIVE image quality assessment database [3] was performed. Fifteen reference images and their distorted versions were selected for training (374 images) and parameters that produce optimal Spearman's rank-order correlation coefficient (SROCC) for the proposed AM metric were sought. Optimum values that were obtained are p_g=2%, p_α=78%, and w_g=0.7. A p_g–p_α section of the 3D optimization surface for AM-Δ^{RT} at w_g=0.7, is illustrated on Figure 2(a). Low p_g values provide the most relevant quality measurements while the robust performance is observed over the entire p_α range. The effect of weight distribution between the Δ_g and Δ_α channels is illustrated on Figure 2(b) showing SROCC for AM-Δ^{RT} as function of w_g (w_α=1-w_g) at p_g=2% and p_α=78% values. Optimally, contrast measure Δ_g is marginally more important than local structure Δ_α, 0.7 vs. 0.3.

4 Results

To demonstrate the performance of the proposed measure, the rest of LIVE image quality assessment database [3] – fourteen reference images and their distorted versions for testing (405 images), CSIQ [4], VCL@FER [5], MCL-JCI [6] and JPEG XR [7] image quality assessment databases were used.

Table 2 provides the comparison of the used, publicly available databases. Databases have different numbers of reference images (6-50), distorted (rated) images (180-866), distortion types (1-6), distortion levels (3-9), number of human observers, ratings and stimulus method. Viewing conditions (e.g. display resolution and viewing distance) are different also.

Subjective tests where average human observers are displayed series of test, and optionally corresponding original images and their quality impressions of those images collected as simple scalar ratings have long been considered as the most reliable way to obtain ground truth evaluation of perceptual image quality. Individual subjective quality scores (opinions) are usually sumarised in the form of mean opinion values of the scores, MOS/DMOS/SQF, and confidence intervals about those scores for each evaluated image. Subjective trials are usually conducted in strictly controlled environmental conditions and involve large user samples to render statistical relevance to their results, making them time and effort consuming and impractical for any routine use in imaging applications. The goal of objective metrics has always been accurate prediction of such scores that could be obtained without the complex practical procedure involved in organizing subjective trials. Subjective studies conducted so far have mostly been inconclusive in terms of identifying a single optimal objective metric [4-7] with various metrics exhibiting optimal performance for different sets of subjectively evaluated data.

Table 2
Comparison of the public databases

	LIVE	CSIQ	VCL@FER	MCL-JCI	JPEG XR
Year	2006	2009	2011	2016	2009
Display	CRT, 21"	Sceptre 24", X24WG LCD	N/A	65"	Eizo CG301W LCD
Display resolution	1024x768	1920x1200	N/A	3840x2160	2560x1600
Viewing distance	2-2.5 SH[!]	70 cm	N/A	2 m (~1.6 SH)	1 SH
Reference images	29	30	23	50	10 (4 for training and 6 for testing)
Image resolution	~768x512	512x512	~768x512	1920x1080	1600x1280
Distortion types	JPEG, JPEG2000, additive Gaussian noise, blurring, fast fading	JPEG, JPEG2000, blurring, contrast decrements, additive pink noise, additive Gaussian noise	JPEG, JPEG2000, blurring, additive Gaussian noise	JPEG	JPEG, JPEG2000 (two configurations), JPEG XR (two implementations)
Distortion levels	5-9	4-5	6	3-7	6
Method	Single Stimulus (with hidden reference)	Categorical Subjective Image Quality	Single Stimulus	two images (side by side)	Double-Stimulus Continuous Quality Scale
Data	DMOS[%]	DMOS	MOS	SQF[&]	MOS
Observers	161	35	118	>150	16
Number of ratings per image	20-29	5-7	16-36	30	16
Test images	779	866	552	243	180
Format	**BMP**	**PNG**	**BMP/JPG**	**BMP**	**BMP**

N/A = Not Available [!] SH = Screen Height
[%] DMOS = Difference MOS [&] SQF = Stair Quality Function [6]

The performance of objective metrics was evaluated over three aspects of their ability to estimate subjective image quality [27]: (i) prediction accuracy, measured using linear correlation coefficient (LCC), mean absolute error (MAE), and root mean squared error (RMSE); (ii) prediction monotonicity, measured using the SROCC; and (iii) prediction consistency, quantified using the outlier ratio (OR).

A comparison over five performance measures of several objective metrics on LIVE test images is summarized in Table 3 (three best methods are in bold). *AM-*Δ^{RT} outperforms other objective measures. In contrast to some prior studies [28],

significant gains in performance can be obtained using the right pooling strategy, compare the Δ^{RT} and $AM\text{-}\Delta^{RT}$ scores. The significance in using both gradient magnitude and orientation information can be seen in the difference between complete metrics Δ^{RT} and $AM\text{-}\Delta^{RT}$ on one side and $\Delta_g{}^{RT}$ and $\Delta_\alpha{}^{RT}$ on the other.

Table 3
Performance comparison on LIVE test images (405 images) [3]

Method	LCC	SROCC	MAE	RMSE	OR (%)
PSNR	0.8784	0.8852	10.1182	13.0942	9.8765
UIQI	0.8982	0.8925	9.3335	12.0433	6.9136
SSIM	0.9008	0.9107	9.2729	11.8967	7.6543
MS-SSIM	0.9443	0.9596	7.2996	9.0185	2.7160
VIF	**0.9623**	**0.9662**	**6.0976**	**7.4502**	**0.2469**
VSNR	0.9265	0.9320	7.9889	10.3109	4.1975
MAD	**0.9648**	**0.9652**	**5.5983**	**7.2002**	**0.4938**
$\mathbf{Q^{AB}}$	0.9405	0.9418	7.5332	9.3083	2.9630
$\mathbf{\Delta_g{}^{RT}}$	0.9190	0.9235	8.3077	10.8030	4.6914
$\mathbf{\Delta_\alpha{}^{RT}}$	0.9235	0.9150	8.4850	10.5109	3.2099
$\mathbf{\Delta^{RT}}$	0.9403	0.9443	7.3584	9.3216	2.7160
$\mathbf{AM\text{-}\Delta^{RT}}$	**0.9692**	**0.9709**	**5.4455**	**6.7419**	**0.2469**

Table 4
Performance comparison on CSIQ images [4]

Method	LCC	SROCC	MAE	RMSE	OR (%)
PSNR	0.7999	0.8057	0.1195	0.1576	34.2956
UIQI	0.8289	0.8092	0.1127	0.1469	34.4111
SSIM	0.8151	0.8368	0.1161	0.1521	33.4873
MS-SSIM	0.8666	**0.8774**	**0.0972**	0.1310	**27.7136**
VIF	**0.9252**	**0.9194**	**0.0753**	**0.0996**	**22.7483**
VSNR	0.8018	0.8132	0.1152	0.1569	30.1386
MAD	**0.9502**	**0.9466**	**0.0636**	**0.0818**	**17.8984**
$\mathbf{Q^{AB}}$	0.8556	0.8520	0.1039	0.1359	31.1778
$\mathbf{\Delta_g{}^{RT}}$	0.8459	0.8690	0.1052	0.1400	30.1386
$\mathbf{\Delta_\alpha{}^{RT}}$	0.7792	0.7147	0.1332	0.1646	40.9931
$\mathbf{\Delta^{RT}}$	0.8605	0.8621	0.1018	0.1338	29.4457
$\mathbf{AM\text{-}\Delta^{RT}}$	**0.8847**	0.8616	0.0986	**0.1224**	29.9076

Tables 4–7 provide further objective metric performance results on CSIQ [4], VCL@FER [5], MCL-JCI [6], and JPEG XR [7] databases ($AM\text{-}\Delta^{RT}$ uses parameters determined on the LIVE training set). Combined magnitude/orientation models achieve better results than individual preservation models ($\Delta_\alpha{}^{RT}$ and $\Delta_g{}^{RT}$). The additive combined model, Eq. (7), outperforms the

multiplicative, Eq. (6), and achieves performance near the top of the tested metrics (MS-SSIM, VIF and MAD).

Table 5
Performance comparison on VCL@FER images [5]

Method	LCC	SROCC	MAE	RMSE	OR (%)
PSNR	0.8321	0.8246	10.2335	13.6204	53.8043
UIQI	0.7965	0.7983	11.5681	14.8495	62.5000
SSIM	0.8742	0.8677	9.3849	11.9244	54.8913
MS-SSIM	**0.9183**	**0.9227**	**7.7862**	**9.7238**	**49.0942**
VIF	0.8922	0.8866	8.8811	11.0905	53.9855
VSNR	0.8805	0.8754	8.9194	11.6415	**52.1739**
MAD	**0.9051**	**0.9061**	**8.2371**	**10.4450**	**49.6377**
$\mathbf{Q^{AB}}$	0.8694	0.8692	9.6409	12.1358	59.9638
$\mathbf{\Delta_g^{RT}}$	0.8819	0.8723	9.0247	11.5790	53.8043
$\mathbf{\Delta_\alpha^{RT}}$	0.8055	0.8039	11.2442	14.5545	61.0507
$\mathbf{\Delta^{RT}}$	0.8898	0.8879	8.9453	11.2091	56.1594
AM-$\mathbf{\Delta^{RT}}$	**0.9036**	**0.8978**	**8.3128**	**10.5201**	52.3551

Table 6
Performance comparison on MCL-JCI images [6]

Method	LCC	SROCC	MAE	RMSE
PSNR	0.4721	0.4486	0.1907	0.2288
UIQI	0.5746	0.5713	0.1742	0.2124
SSIM	0.6053	0.5898	0.1676	0.2066
MS-SSIM	0.8340	0.8139	0.1102	0.1432
VIF	**0.8884**	**0.8791**	**0.0909**	**0.1191**
VSNR	0.6441	0.6337	0.1608	0.1985
MAD	**0.8713**	**0.8668**	**0.0984**	**0.1274**
$\mathbf{Q^{AB}}$	0.7879	0.7863	0.1223	0.1598
$\mathbf{\Delta_g^{RT}}$	0.8246	0.7959	0.1138	0.1468
$\mathbf{\Delta_\alpha^{RT}}$	0.6567	0.6466	0.1551	0.1957
$\mathbf{\Delta^{RT}}$	0.8318	0.8229	0.1091	0.1440
AM-$\mathbf{\Delta^{RT}}$	**0.8603**	**0.8462**	**0.1020**	**0.1323**

Table 7
Performance comparison on JPEG XR images [7]

Method	LCC	SROCC	MAE	RMSE	OR (%)
PSNR	0.7819	0.7980	12.8737	16.5360	35.5556
UIQI	0.8621	0.8186	9.5605	13.4404	23.3333

SSIM	0.8744	0.8435	9.6144	12.8684	23.8889
MS-SSIM	0.9309	0.8930	7.0745	9.6863	14.4444
VIF	**0.9389**	**0.9130**	**6.8067**	**9.1278**	13.3333
VSNR	0.8765	0.7803	10.1065	12.7692	23.3333
MAD	**0.9466**	**0.9406**	**6.2598**	**8.5498**	**11.1111**
$\mathbf{Q^{AB}}$	0.9269	0.8995	6.8809	9.9561	**11.6667**
$\mathbf{\Delta_g^{RT}}$	0.9246	0.9071	7.4744	10.1074	12.7778
$\mathbf{\Delta_\alpha^{RT}}$	0.9034	0.8685	7.8474	11.3751	16.1111
$\mathbf{\Delta^{RT}}$	**0.9339**	**0.9117**	**6.5091**	**9.4860**	**9.4444**
AM-$\mathbf{\Delta^{RT}}$	0.9277	0.9089	7.3250	9.9039	12.7778

It is worth noting that no single metric performs best on all the datasets, which is an indication of the sensitivity of the metrics to test data content. The proposed gradient preservation metric with alternative quality guided pooling method *AM*-Δ^{RT} exhibits consistently high performance. Except for the LIVE dataset, gradient magnitude preservation model Δ_g^{RT} provides significantly better results than gradient orientation preservation model Δ_α^{RT}. Hence, it is expected that with improvements of the orientation comparison model, proposed method will improve too.

Furthermore, *AM*-Δ^{RT} is a very well behaved metric with a smooth relationship between objective and subjective scores across the entire range, as shown on the scatter plots on Figure 3.

Since all databases contain JPEG distortion, the performance of objective quality metrics on the JPEG subsets of the five databases was analyzed in more detail. Figure 4 presents subjective-objective agreement (LCC and SROCC) for the eight objective measures on the JPEG subsets (LIVE – 92 images, CSIQ – 150 images, VCL@FER – 138 images, MCL-JCI – 243 images, and JPEG XR – 30 images).

As expected from previous research [29], the performance of quality metrics exhibits similar behavior for the five publicly available databases (extended sets of objective quality measures, databases, and images here were analyzed). The differences over databases, particularly the decrease of performance on MCL-JCI for all objective measures might be explained by a new methodology for perceptual quality measurement – subjective results are given through the stair quality functions (SQF), which are obtained by analysis and post-processing of the raw just noticeable difference (JND) data [6, 30]. Additionally, MCL-JCI dataset contains images with higher spatial resolution than standard datasets used in image quality assessment (see Table 2).

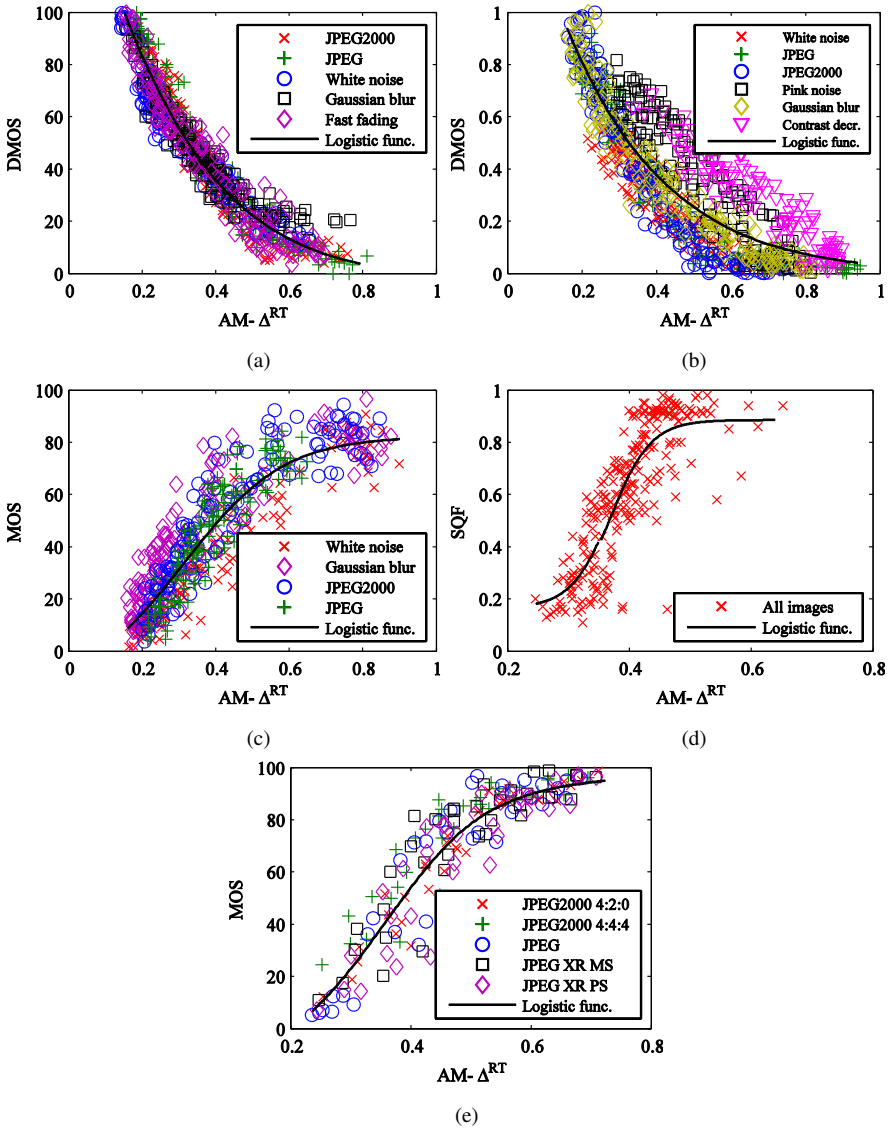

Figure 3
Subjective (DMOS/MOS/SQF) scores versus *AM*-Δ^{RT} model predictions for data from: (a) LIVE, (b) CSIQ, (c) VCL@FER, (d) MCL-JCI and (e) JPEG XR image databases

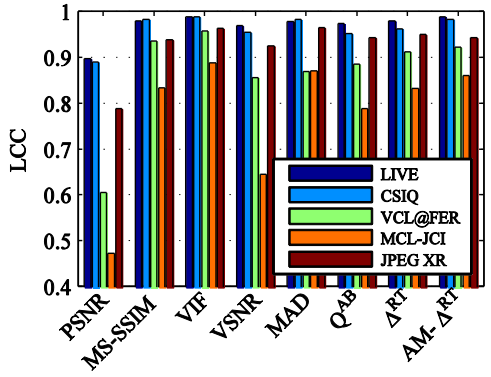

(a)

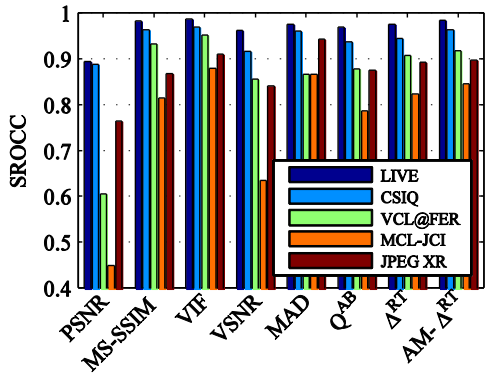

(b)

Figure 4

Subjective-objective agreement on the JPEG subsets of the five databases: (a) linear correlation coefficient (LCC), and (b) Spearman's rank-order correlation coefficient (SROCC)

Conclusions

This paper described a novel, gradient-based, full-reference image quality assessment measure, explicitly incorporating gradient orientation information from test signals. Different gradient formulations were investigated, as well as, different spatial score pooling strategies on a variety of subjectively evaluated datasets.

The addition of the gradient orientation information, as a complementary feature to gradient magnitude, is shown to directly improve objective metric performance. Improvement is obtained for all datasets tested in the range 1–3% which is particularly significant in the critical top 15% to the theoretical maximum of the linear correlation range (>0.85).

In contrast to prior studies, it was found that perceptual importance pooling strategy can further improve metric correlation with subjective judgment in a range typically ~3% of linear and rank correlation. Experimental results show that the proposed method achieves consistently high levels of performance, with correlation levels up to 97% and above 85% on all datasets, outperforming many similarly complex metrics and reaching the level of much more complex metric formulations such as VIF and MAD.

Finally, we confirmed a significant variability of metric performance levels on different subjective databases. Significant performance level differences were confirmed to exist in JPEG image subsets. This leads to the conclusion, that metric evaluation on a single subject-rated database is generally insufficient.

In future work, the existing gradient-based assessment approach will be expanded to explore and include explicit formulations for temporal gradient, with the aim of evaluating quality of dynamic, video signals. These studies will also include a critical comparison of the types of gradient assessment models required for static and dynamic imagery.

Acknowledgement

This research has been a part of the project No. VA-TT/1-17-19 supported by the Ministry of Defence, Republic of Serbia.

References

[1] Wang, Z., Bovik, A. C.: Mean squared error: love it or leave it? A new look at signal fidelity measures. *IEEE Signal Processing Magazine*, 2009, Vol. 26, No. 1, pp. 98-117. DOI: 10.1109/MSP.2008.930649

[2] Petrovic, V. S., Xydeas, C.: Objective evaluation of signal-level image fusion performance. *Optical Engineering*, 2005, Vol. 44, No. 8, pp. 087003-(1-8). DOI: 10.1117/1.2009764

[3] Sheikh, H. R., Wang, Z., Cormack, L., Bovik, A. C.: *LIVE image quality assessment database release 2*. [Online] Cited 2010-11-17. Available at: http://live.ece.utexas.edu/research/

[4] Larson, E. C., Chandler, D. M.: *The CSIQ image database*. [Online] Cited 2015-11-17. Available at: http://vision.okstate.edu/?loc=csiq

[5] Zaric, A., Tatalovic, N., Brajkovic, N., et al.: VCL@FER image quality assessment database. *Automatica*, 2012, Vol. 53, No. 4, pp. 344-354, DOI: 10.7305/automatika.53-4.241

[6] Jin, L., Lin, J. Y., Hu, S., et al.: Statistical study on perceived JPEG image quality via MCL-JCI dataset construction and analysis. In *Proceedings of the IS&T International Symposium on Electronic Imaging – Image Quality and System Performance XIII*. San Francisco (CA, USA) 2016, IQSP-222.1-IQSP-222.9

[7] De Simone, F., Goldmann, L., Baroncini, V., Ebrahimi, T.: *JPEG core experiment for the evaluation of JPEG XR image coding*. [Online] Cited 2016-06-17. Available at: http://mmspg.epfl.ch/iqa

[8] Wang, Z., Bovik, A. C., Sheikh, H. R., Simoncelli, E. P.: Image quality assessment: from error visibility to structural similarity. *IEEE Transactions on Image Processing*, 2004, Vol. 13, No. 4, pp. 600-612, DOI: 10.1109/TIP.2003.819861

[9] Wang, Z., Simoncelli, E. P., Bovik, A. C.: Multi-scale structural similarity for image quality assessment. In *Proceedings of the 37th Asilomar Conference on Signals, Systems and Computers*. Pacific Grove (CA, USA), 2003, pp. 1398-1402, DOI: 10.1109/ACSSC.2003.1292216

[10] Sheikh, H. R., Bovik, A. C.: Image information and visual quality. *IEEE Transactions on Image Processing*, 2006, Vol. 15, No. 2, pp. 430-444, DOI: 10.1109/TIP.2005.859378

[11] Chandler, D. M., Hemami, S. S.: Vsnr: a wavelet-based visual signal-to-noise ratio for natural images. *IEEE Transactions on Image Processing*, 2007, Vol. 16, No. 9, pp. 2284-2298, DOI: 10.1109/TIP.2007.901820

[12] Larson, E. C., Chandler, D. M.: Most apparent distortion: full reference image quality assessment and the role of strategy. *Journal of Electronic Imaging*, 2010, Vol. 19, No. 1, pp. 011006-1-011006-21

[13] Bondzulic, B., Petrovic, V.: Edge-based objective evaluation of image quality. In *Proceedings of the IEEE International Conference on Image Processing*. Brussels (Belgium) 2011, pp. 3305-3308, DOI: 10.1109/ICIP.2011.6116378

[14] Liu, A., Lin, W., Narwaria, M.: Image quality assessment based on gradient similarity. *IEEE Transactions on Image Processing*, 2012, Vol. 21, No. 4, pp. 1500-1512, DOI: 10.1109/TIP.2011.2175935

[15] Zhang, X., Feng, X., Wang, W., Xue, W.: Edge strength similarity for image quality assessment. *IEEE Signal Processing Letters*, 2013, Vol. 20, No. 4, pp. 319-322, DOI: 10.1109/LSP.2013.2244081

[16] Xue, W., Zhang, L., Mou, X., Bovik, A.C.: Gradient magnitude similarity deviation: a highly efficient perceptual image quality index. *IEEE Transactions on Image Processing*, 2014, Vol. 23, No. 2, pp. 684-695, DOI: 10.1109/TIP.2013.2293423

[17] Zhang, L., Zhang, L., Mou, X., Zhang, D.: FSIM: a feature similarity index for image quality assessment. *IEEE Transactions on Image Processing*, 2011, Vol. 20, No. 8, pp. 2378-2386, DOI: 10.1109/TIP.2011.2109730

[18] Zhang, L., Shen, Y., Li, H.: VSI: a visual saliency-induced index for perceptual image quality assessment. *IEEE Transactions on Image Processing*, 2014, Vol. 23, No. 10, pp. 4270-4281, DOI: 10.1109/TIP.2014.2346028

[19] Nafchi, H. Z., Shankolaei, A., Hedjam, R., Cheriet, M.: Mean deviation similarity index: efficient and reliable full-reference image quality

evaluator. *IEEE Access*, 2016, Vol. 4, pp. 5579-5590, DOI: 10.1109/ACCESS.2016.2604042

[20] Shi, Z., Zhang, J., Cao, Q., Pang, K., Luo, T.: Full-reference image quality assessment based on image segmentation with edge feature. *Signal Processing*, 2018, Vol. 145, pp. 99-105, DOI: 10.1016/j.sigpro.2017.11.015

[21] Cheng, G., Huang, J., Liu, Z., Lizhi, C.: Image quality assessment using natural image statistics in gradient domain. *AEU – International Journal of Electronics and Communications*, 2011, Vol. 65, No. 5, pp. 392-397. DOI: 10.1016/j.aeue.2010.05.007

[22] Xue, W., Mou, X., Zhang, L., Bovik, A. C.: Blind image quality assessment using joint statistics of gradient magnitude and Laplacian features. *IEEE Transactions on Image Processing*, 2014, Vol. 23, No. 11, pp. 4850-4862, DOI: 10.1109/TIP.2014.2355716

[23] Jia, H., Sun, Q., Ji, Z., Wang, T., Chen, Q.: No-reference image quality assessment based on natural scene statistics and gradient magnitude similarity. *Optical Engineering*, 2014, Vol. 53, No. 11, pp. 113110-(1-9), DOI: 10.1117/1.OE.53.11.113110

[24] Liu, L., Hua, Y., Zhao, Q., Huang, H., Bovik, A. C.: Blind image quality assessment by relative gradient statistics and adaboosting neural network. *Signal Processing: Image Communication*, 2016, Vol. 40, pp. 1-15, DOI: 10.1016/j.image.2015.10.005

[25] Moorthy, A. K., Bovik, A. C.: Visual importance pooling for image quality assessment. *IEEE Journal on Selected Topics in Signal Processing*, 2009, Vol. 3, No. 2, pp. 193-201, DOI: 10.1109/JSTSP.2009.2015374

[26] Bondzulic, B., Petrovic, V.: Additive models and separable pooling, a new look at structural similarity. *Signal Processing*, 2014, Vol. 97, No. 4, pp. 110-116, DOI: 10.1016/j.sigpro.2013.10.020

[27] ITU-T Telecommunication Standardization Bureau: *Objective Perceptual Assessment of Video Quality: Full Reference Television*. Geneva, Switzerland, 2004

[28] Wang, Z., Shang, X.: Spatial pooling strategies for perceptual image quality assessment. In *Proceedings of the IEEE International Conference on Image Processing*. Atlanta (GA, USA) 2006, pp. 2945-2948 DOI: 10.1109/ICIP.2006.313136

[29] Tourancheau, S., Autrusseau, F., Parvez Sazzad, Z. M., Horita, Y.: Impact of subjective dataset on the performance of image quality metrics. In *Proceedings of the IEEE International Conference on Image Processing*. San Diego (CA, USA) 2008, pp. 365-368, DOI: 10.1109/ICIP.2008.4711767

[30] Lin, J. Y., Jin, L., Hu, S., et al.: Experimental design and analysis of JND test on coded image/video. In *Proceedings of SPIE 9599, Applications of Digital Image Processing XXXVIII*. San Diego (CA, USA) 2015, pp. 95990Z. DOI: 10.1117/12.2188389

Multi-Project Optimization with Multi-Functional Resources by a Genetic Scheduling Algorithm

Tibor Dulai, György Dósa, Ágnes Werner-Stark
University of Pannonia, Egyetem u. 10, H-8200 Veszprém, Hungary
dulai.tibor@virt.uni-pannon.hu
dosagy@almos.uni-pannon.hu
werner.agnes@virt.uni-pannon.hu

Abstract: In this paper we show how a genetic scheduler algorithm can be applied to solve a hard multi-project optimization problem with shared resources. The resources work in multiple operation modes, so they can substitute each other (but with different efficiency). We consider processes which have quite complex structure, i.e., it allows the existence of parallel sub-processes. This problem is extremely complex, there is no chance to get the optimal solution in reasonable time. The proposed algorithm intends to find a near-optimal solution, where the goal of the optimization is the minimization of the makespan of the schedule. We present the genetic operations of the algorithm in detail. We fill the pool of populations only with feasible solutions, but making possible the discovery of the whole search space. The feasibility of a schedule is ensured by excluding time-loops regarding the sequence of the tasks both in their process and in the queue of their resource. We executed several tests for determining the (hopefully) optimal parameters of the algorithm regarding the number of generations, the population size, the crossover rate and rate of the mutation. We applied the algorithm for many problem classes where the parameters of the input are fixed or randomly chosen from some interval.

Keywords: multi-project scheduling; genetic algorithm; multi-purpose machines

1 Introduction

Scheduling is a widespread research area of operations research. The classes of the problem differs, e.g. in the number of the resources (machines) or in the properties of the tasks to schedule. Two important versions of the problem are the flow-shop problem [5, 10] and the job-shop problem. [2, 11]

As the basic scheduling problem – called job-shop scheduling problem (JSP), where a set of jobs have to be scheduled on a set of machines regarding certain criterion(s) – is NP-hard [6], heuristics and more effective meta-heuristics are often used for real-life sized problems instead of exact solution methods. An

effective meta-heuristic is genetic algorithm (GA), in [15] Zhang et al. reviewed some of GA applications for flexible JSP and introduced their own problem representation and genetic operators. It was followed by the presentation of their computational results on common benchmark data sets. Next to GA other heuristics like tabu search [7] or simulated annealing [9] are also popular methods.

The application area of different scheduling problems has a wide spectrum. In computer architecture and parallel software planning tasks have to be scheduled on processors (e.g. on CPU and GPU), in industrial or business applications workflow elements have to be assigned to resources and scheduled in time, while, e.g. in software project scheduling project-tasks have to be scheduled mainly on a human-based resource set usually in a dynamic manner. The different application areas differ in their requirements and have their own specialities.

Nevertheless, the complexity of the basic problem remains, what necessitates the usage of heuristics. Votava [14] simulated two heuristic algorithms (named HEFT and CPOP) for task scheduling in a networking subsystem. Alba and Chicano [1] shown that GA is an appropriate tool for project scheduling and can be applied efficiently for automated task assignment. Chang et al. [4] - extending their former work [3] - presented a GA with improved representation and parameters, which took into account more human resource factors. Moreover, as the representation introduced a timeline axis as a third dimension (next to tasks and resources), it made possible the suspension and resumption of tasks and the reassignment of resources.

Sadegheih used simulated annealing for determining the effect of GA parameters on the schedule [13]. In his work he dealt with 8-jobs and 7-machines problems and found the importance of mutation rate and not significant effect of crossover rate.

Joo et al. [8] dealt with multi-project scheduling with multimode resources and applied activity splitting and simulated annealing. In this paper, a genetic algorithm for scheduling in multi-project environment is presented, where resources may have multiple functions, so they can substitute each other. The representation of a schedule is shown, the developed crossover and mutation genetic operators are introduced. The algorithm is able to cover the whole feasible search space during its operation. The paper emphasizes the method for guarantying the feasibility of the schedule by eliminating possible time loops what could arise after applying genetic operators.

Pongcharoen et al. [12] dealt with similar sized problem as ours (similar number of resources and tasks), too, however, their problem had not such a complex structure. They investigated population size, generation number, mutation and crossover rates. While determining optimal parameters of GA they also described how they face and eliminate time-loop (they called it deadlock). If they got an infeasible schedule, they swapped the problematic action with a random one. In our paper we handle this problem in other way.

In Section 2 the model of the problem is introduced and described formally. Section 3 presents the genetic algorithm and its operators we applied. In Section 4 we summarize the computational results, while Section 5 concludes our work.

2 The Example Processes and the Model of the Problem

2.1 The Basic Example Processes

This subsection introduces the problem we worked on, for illustrative purposes. In our simulations we used two kinds of processes: the tested production of 15 pieces of sensor type I and 20 pieces of sensor type II. Altogether, it means that we deal with 35 processes, parallel. The processes of producing one of each types of these products are illustrated in Figure 1.

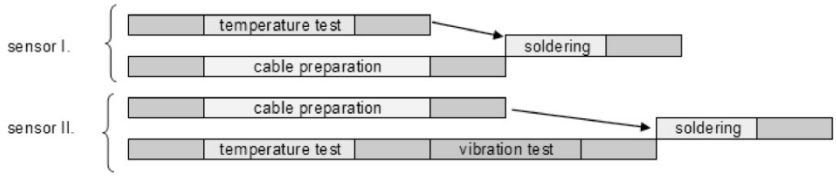

Figure 1
The two types of our example processes

In the figure we can see the sequence of tasks in processes. Tasks without caption are transportation tasks from one resource to another. The initial and final destination is the depot. The duration time of each task depends on the resource which operates, as Table 1 shows. In the table Tr. marks transportation task, Tr.d. holds for a transportation device followed by the abbreviated places of work phases (moreover d stands for the depot). In our example all the transportation devices have to get back to their starting place if we want to reuse them, and it takes the same time as to carry the materials to a place of work. For example, a transportation device can transfer a material from the depot to the place of temperature test in 3 time units, however, we have to wait 6 time units if we want to reuse it. The table also contains how many pieces of the different resources are available at all.

In our example we apply setup time only in case of temperature chamber and vibration chamber. If they change their operation mode between temperature test and vibration test, symmetrical setup times are used. For temperature chamber we defined 5 time units as setup time and for the vibration chamber we determined the setup time as 6 time units.

Table 1

Duration time of each task related to its resource usage /in time units/

	Tr. d-t	Temp. test	Tr. t-s	Solde-ring	Tr. s-d	Tr. d-c	Cab-ling	Tr. c-s	Tr. t-v	Vibr. test	Tr. v-s
Temperature chamber (3 pieces)	-	6	-	-	-	-	-	-	-	10	-
Cable producer (2 pieces)	-	-	-	-	-	-	6	-	-	-	-
Vibration chamber (1 piece)	-	10	-	-	-	-	-	-	-	6	-
Solderer (2 pieces)	-	-	-	4	-	-	-	-	-	-	-
Tr.d. d-t (1 piece)	3	-	-	-	-	-	-	-	-	-	-
Tr.d. d-c (1 piece)	-	-	-	-	-	5	-	-	-	-	-
Tr.d. t-s (1 piece)	-	-	4	-	-	-	-	-	-	-	-
Tr.d. t-v (1 piece)	-	-	-	-	-	-	-	-	3	-	-
Tr.d. c-s (1 piece)	-	-	-	-	-	-	-	3	-	-	-
Tr.d. v-s (1 piece)	-	-	-	-	-	-	-	-	-	-	5
Tr.d. s-d (1 piece)	-	-	-	-	4	-	-	-	-	-	-
Tr: transport; Tr.d.: transportation device; d: depot; c: cable producing; t: temperature test; v: vibration test; s: soldering											

An example for a schedule can be seen in Figure 2 for a scenario where 3 processes exist: 2 of them test and produce sensor type I and 1 of them tests and produces sensor type II. In the figure (Figure 2) each rectangle of a task contains its process ID. Moreover, empty boxes represent the duration while a transportation device reaches back to its start place.

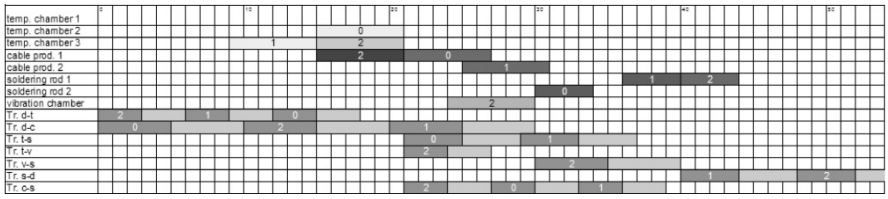

Figure 2

A simple schedule as a result of our algorithm

Several similar problems – with the same process structure, conditions and constraints – can be found in real-life practice (e.g. producing and packing a

porcelain in a manufacture requires parallel execution of tasks packaging material preparation and creation of the porcelain). There can be orders that require pure sculpted porcelain, while other orders necessitate paint. Human resources of the manufacture are specialized: there are potters and painters. Painters are better (and quicker) in paint and potters are better in sculpting. However, they can execute the task of the other specialists, too, but significantly slower. When both the porcelain and the packaging material are ready, the porcelain has to be packaged by a third type of specialist of the company.

Next to this second example, other industrial/business processes may have the same characteristics.

2.2 Difficulties of the Problem

The complexity of the algorithm showed in this paper origins from the properties of the problem that we intend to solve. The problem class is a scheduling problem where resources have to be allocated to carry out the tasks of a process and the allocations have to be ordered in the time domain. However, as common practical scheduling problems, the basic problem has some other properties:

- we deal with multiple processes parallel, which may share in the resources they use,
- each process can include parallel substructure(s) of tasks instead of a fully sequential order of its ingredient tasks,
- resources can operate in different operation modes. There are tasks, which can be carried out by more than one resources (usually with different parameters like operation time), and there are resources, which are able to do different tasks. It results in resource-substitution possibilities.

These properties make the problem extremely complex, e.g. related to the common NP-hard $P_m||C_{max}$ problems.

2.3 Notations

The input is given as follows:

- $P = \{p_1, ..., p_n\}$ is the set of processes.
- $T_i = \{t_{i,1}, ..., t_{i,m}\}$ is the set of tasks of process p_i.
- $T = \cup^{n}_{i=1} T_i$ is the set of the tasks of all processes.
- $Pre(t_{i,j}) \subset T_i$ is the subset of the tasks of process p_i (what can be an empty set) which are direct prior tasks to task $t_{i,j}$ in process p_i. This set may have

more than one element because of the possible parallel structure of processes.

- *allPre($t_{i,j}$) C Ti* is the subset of the tasks of process p_i (what can be an empty set) which are prior tasks to task $t_{i,j}$ in process p_i. E.g. if $t_{i,b} \in Pre(t_{i,c})$ and $t_{i,a} \in Pre(t_{i,b})$ then $t_{i,a} \in allPre(t_{i,c})$.
- $R = \{r_1, ..., r_o\}$ is the set of resources.
- *capable: R x T → {0,1}* is a function which describes whether a resource is able to carry out a task.
- $dur(t_{i,j}, r_k) \in N$shows the duration time of carrying out task $t_{i,j}$ by resource r_k, where $capable(r_k, t_{i,j}) = 1$.

The schedule-related variables are:

- $allocatedRes(t_{i,j}) \in R$ is the resource which is assigned by the scheduler to task $t_{i,j}$.
- $start(t_{i,j}) \in N$ is the start time of task $t_{i,j}$ of process p_i.
- $end(t_{i,j}) \in N$ is the end time of task $t_{i,j}$ of process p_i.
- $makespan(P) = max(end(t_{i,j})) - min(start(t_{k,l}))$ for all $t_{i,j}, t_{k,l} \in T$.

2.4 Constraints

The constraints for determining $start(t_{i,j})$ and $end(t_{i,j})$ for all $ti,j \in T$ are:

$$allocatedRes(t_{i,j}) \neq \emptyset, \forall t_{i,j} \in T \quad (2.1)$$

So, each task has to be carried out by a resource.

$$end(t_{i,j}) = start(t_{i,j}) + dur(t_{i,j}, allocatedRes(t_{i,j})), \forall t_{i,j} \in T \quad (2.2)$$

The above constraint represents the connection between the start and finish time of a task regarding the related operation time.

$$start(t_{l,m}) \geq end(t_{i,j}) or\ end(t_{l,m}) \leq start(t_{i,j}), \forall t_{i,j}, t_{l,m} \in T, if\ t_{i,j} \neq t_{l,m}\ and\ allocatedRes(t_{i,j}) \equiv allocatedRes(t_{l,m}) \quad (2.3)$$

This constraint specifies that the tasks allocated to the same resource can not overlap each other.

$$end(t_{i,a}) \leq start(t_{i,b}), \forall 1 \leq i \leq n, \forall t_{i,a}, t_{i,b} \in T_i, if\ t_{i,a} \in allPre(t_{i,b}) \quad (2.4)$$

The final constraint describes that a task of a process can not start before its prior tasks of the same process are not finished.

We look for a schedule where all constraints 2.1-2.4 are satisfied and the *makespan(P)* is minimal.

3 The Genetic Algorithm

The scheduling of real workflows – especially in multi-project environment – requires more and more computational power regarding the increasing of the number and complexity of the processes. It is the reason for preferring heuristics to exact solvers for solving them. This paper presents a genetic algorithm which was developed for scheduling workflows/processes even if they have the properties introduced in Section 2.

Genetic Scheduler (GS):

The GS has the following steps:

Step 1. An initial population is filled up by random instances.

Step 2. Evaluation of the instances of the initial population (a fitness value is calculated for each of the instances of the population).

Step 3. Applying elitism the best x percent of the generation is copied into the new generation.

Step 4. The remaining instances of the new generation are selected and copied randomly from the previous generation.

Step 5. We apply crossover genetic operator to the new generation: a randomly selected instance of the new generation will be replaced by the resulted child instance.

Step 6. We apply mutation genetic operator to the instances of the new generation.

Step 7. Fitness value is calculated for each of the instances of the new generation.

Step 8. While the desired generation number is not reached: GOTO Step 3.

The details of the algorithm are presented in the following subsections.

3.1 Representation

The genetic algorithm requires a solution – a schedule – to be represented by a coding technique that results a coded instance, on what, it is easy to apply the genetic operators and what is unambiguous. Since an instance is unambiguously described by the resource-assignment and the sequence of the tasks at each of the resources – what clearly defines the timing of the task as we intend to minimize the makespan so start each task as soon as possible –, it is enough only to store these data as an instance representation. We chose a two dimensional data structure (*PS*) for this type of representation: the first dimension represents the resources while the second dimension shows the sequenced tasks assigned to the resources.

PS is a pseudo-instance of a schedule, where

$$PS_i C\ T\ and\ allocatedRes(t_{k,l}) = r_i\ \forall t_{k,l} \in PS_i, \forall 1 \leq i \leq o$$
$$and\ PS_i \neq PS_j\ if\ i \neq j,$$

moreover $PS_{i,j} \in T$ means that this task is assigned to resource r_i and is the j^{th} ordered element among the tasks assigned to r_i.

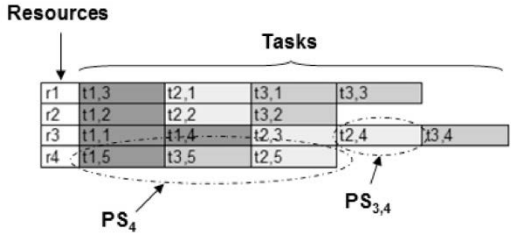

Figure 3
The representation of an instance

Figure 3 illustrates a simple instance as an example for the coding we apply. As we have introduced, $t_{i,j}$ signs the j^{th} task of the i^{th} process. For the sake of perspicuity, we used for the illustration of the tasks which belong to the same process the same color. As the coding schema shows, the representation includes only sequences, it has not exact timing data neither task duration.

3.2 Population

We create the initial population of the genetic algorithm populated by instances presented in subsection 3.1. The cardinality of the population is determined by an a priori set variable (*populationSize*).

All of the instances are created as follows:

Step 1. Select randomly one of the unscheduled processes until there exist at least one of them.

Step 2. For each task of the selected process, starting from the first one taking into account the sequence of the tasks, do the followings:

Step 2.1. Collect all the resource which are capable to carry out the task.

Step 2.2. Select randomly one of these resources.

Step 2.3. Select a random feasible position between the ordered tasks of the selected resource.

Step 2.4. Place the task at the selected position (update the instance.)

Step 3. GOTO Step 1.

The result of the algorithm is an instance. The number of the instances to create is shown by the population size parameter of the genetic algorithm.

However, step 2.3 is critical: the generated instance has to be feasible. By selecting a nonlegal position for the task to insert a time-loop may evolve. It can happen in two ways:

A In the ordered sequence of the tasks of a resource a later task of a process has the position with a smaller index than an earlier task of the same process. A simple example for it can be seen in Figure 4.

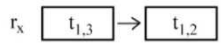

Figure 4
Time-loop related to one resource

B Time-loops may occur involving more than one resource, too. Figure 5 illustrates this kind of time-loop related to two resources, however, the number of the affected resources and tasks can be higher. Since, on one hand task $t_{2,1}$ is executed by resource r_x later than task $t_{1,3}$, on the other hand task $t_{2,2}$ - what has to be executed after task $t_{2,1}$of the second process had been finished - is carried out earlier by resource r_y than task $t_{1,2}$. Although task $t_{1,3}$ should have been processed after task $t_{1,2}$ regarding the sequence of the tasks of the first process. If the insertion of a task triggers a situation similar to this, a time-loop occurs.

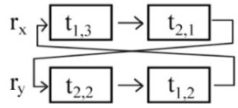

Figure 5
Time-loop related to one process

After the creation of the initial generation whose population is filled up by random, feasible instances, further generations are generated by using genetic operators on the actual generation. The number of generations is also given by the preset value of a variable.

3.3 Fitness Function

For being able to decide which instances are better, we have to qualify them by a numeric value. In our case the fitness value of an instance is the makespan. It shows how does it take to do all the tasks of the schedule, starting from the beginning of the earliest task until the finishing of the latest one. In this work we deal only with time aspects, however, other parameters also can be involved into the creation of the fitness functions, e.g. the cost of the applied resources, creating a multi-objective problem. For calculating the fitness value of an instance it is important to know that the instance describes the order of the tasks for each resource. This sequence and the knowledge about process-related constraints and the operation times, determine the optimal timing unambiguously. We have to

know the start and finish time of all the tasks for calculating the makespan – the fitness value of a schedule.

For timing three basic ideas have to be followed:

- Each task as to be started as early as possible.
- A task cannot be started until its direct prior task in the queue of the resource is not finished and the resource has not been transferred to the state in which it is ready for doing the new task (the latter duration is called setup time).
- A task can not be started until all of its prior tasks in its process have not been finished.

Keeping these constraints – which result a greedy scheduling – all the tasks are timed. After that the makespan can be calculated, obtaining the fitness value of the instance.

3.4 Elitism

The use of elitism on a generation of the genetic algorithm depends on a parameter of our algorithm, see subsection 3.7. When elitism is applied, then the best instances – instances with the lowest makespan – of the previous generation are copied to the next generation. The quantity of the instances which are handled as elites are set by a parameter of the algorithm. As the cardinality of a generation is unchanged, the remaining part of the new generation has to be filled up by random instances of the previous generation. In our case, other parameter signs whether any member – also the elites – can be selected during this random fill up without return.

3.5 Crossover

After the initial instances of the new generation are determined, our algorithm applies crossover genetic operation on the instances with a priori set probability. If crossover is applied, another parameter shows how percent of the population is created by crossover. Supposing that the value of this parameter is c, the following steps are iterated c times:

Step 1. Select two different instances randomly from the new generation (*parent1* and *parent2*)

Step 2. There is a parameter of the algorithm which shows what percent of the processes are inherited from *parent1* and how much from *parent2*. Based on the value of this parameter:

Step 2.1. Select randomly so many processes from *parent1* that it meets the value of the parameter.

Step 2.2. Create a new instance, where the resource assignment for each task of the selected processes is the same as in *parent1*. The position of the tasks in the row of their resources is random, but taking care of avoiding the creation of time-loops.

Step 2.3. The resource assignment of the tasks of the remaining processes is the same as in *parent2*. The position of these tasks in the row of their resources is also random, but prevents the creation of time-loops.

The created *c* pieces of child instances are first put into a temporary storage, then randomly selected instances of the generation is replaced by these children, taking care of not to select an instance which was put into the generation in this phase as a child. There is a parameter of the algorithm that controls whether an elite can be replaced by a child who was created by crossover.

3.6 Mutation

After the possible crossover over the new generation, mutation genetic operator can be applied on the population of the new generation. There is a parameter which shows the probability of whether applying mutation on this generation. If it is applied, another parameter determines the probability of using mutation for each instance of the generation, separately.

Mutating an instance covers the following steps:

Step 1. Select a process randomly from the schedule.

Step 2. Delete all of the tasks of the selected process from the instance.

Step 3. Do the following steps for each task of the process - starting from the first task of the process and processing them in order:

Step 3.1. Collect all the resources which are able to carry out the task.

Step 3.2. Select randomly one from these resources.

Step 3.3. Insert the task into a random, but feasible position of the row of the selected resource.

After all of these operations, the finalized population of the new generation is created. The fitness value of each created instance has to be calculated for qualifying the instances of the new generation and being able to inherit more generations based on the presented rules.

3.7 Parameters of the Algorithm

The developed genetic algorithm has several parameters. These are:

- The size of a population (*sizeofPopulation*).

- The number of the generations.
- The percent of the instances of a population obtained by elitism (*elites*).
- When selecting the other *(1-elites)*sizeofPopulation* instances, whether we can reselect elites, too?
- The possibility for applying crossover on a generation.
- How percent of a generation should be resulted by crossover?
- How percent of the processes origins from the first parent in case of crossover?
- Whether only the instances with the worst fitness values should be replaced by the results of the crossover or any random instances?
- The possibility for applying mutation for a generation.
- The possibility for mutation in case of an instance of a generation which lets mutation to be applied.
- Whether crossover and mutation can influence elites, too?

In our work the execution of the algorithm always happens as long as the parameter of the generation number indicates and does not stop even if it realizes convergence of the results before the preset generation number is reached.

4 Results

The presented algorithm was applied for two kinds of problems. Both of them were based on the problem presented in subsection 2.1, but differ in the definiteness of the process number and the operation time. The first problem realizes exactly the same problem as subsection 2.1 presents. The second one applies stochastic operation time and process number.

4.1 Results for the Deterministic Problem

First, we run several times the algorithm for exactly the same problem presented in subsection 2.1 (with 35 processes) with the following parameter settings:

- *sizeofPopulation*: 60.
- The number of the generations: 400.
- *elites*: 0.2.
- When selecting the other instances, we can reselect elites, too.
- The possibility for applying crossover on a generation: 1.
- The percent of a generation should be resulted by crossover: 0.7.
- The percent of the processes origins from the first parent in case of crossover: 0.5.
- Only the instances with the worst fitness values should be replaced by the results of the crossover.
- The possibility for applying mutation for a generation: 1.

- The possibility for mutation in case of an instance: 0.18.
- Crossover and mutation can not influence elites.

Some of the parameters – e.g. 0.18 mutation rate – were based on the values Pongcharoen et al. [12] found to be optimal.

Figure 6 shows that even in case of 400 generation the results (the best makespan) differ significantly.

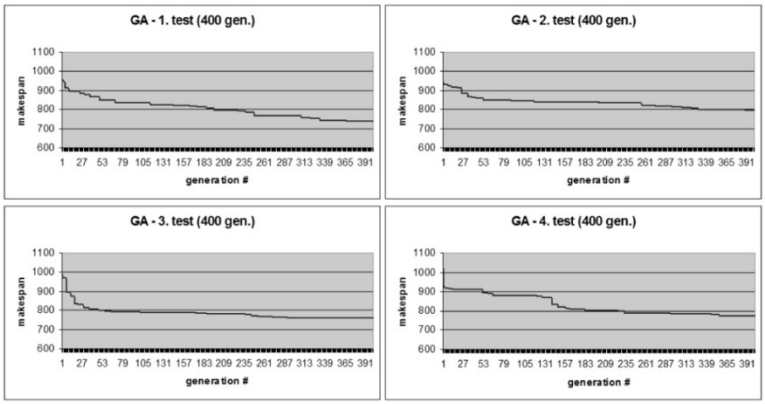

Figure 6
Some results in case of the deterministic problem, applying GA with 400 generation and 60 population size

After we found this fact, we intended to analyze the effect of the other important parameters both on the makespan of the resulted solution and the convergence of the results we obtained.

In the next step, we changed the value of the population size while all the other parameters of the genetic algorithm stayed unchanged. The results are illustrated in Table 2.

Table 2
Makespan results for the genetic scheduler with variable population size /in time units/

generation: 400, crossover rate: 0.7, mutation rate: 0.18, population size: p									
	p:10	p:20	p:30	p:40	p:50	p:60	p:80	p:100	p:150
Test 1.	857	802	832	802	780	740	770	790	734
Test 2.	854	796	779	796	767	796	743	779	760
Test 3.	834	812	797	844	803	799	775	756	732
Test 4.	876	823	824	792	774	799	761	732	752
Test 5.	829	818	826	804	782	758	808	762	744
The best	829	796	779	792	767	740	743	732	732
Avg.	850	810.2	811.6	807.6	781.2	778.4	771.4	763.8	744.4
Deviation	16.96	9.97	20.26	18.70	12.09	24.69	21.30	19.96	10.61

Table 3
Makespan results for the genetic scheduler with variable crossover rate /in time units/

generation: 400, population size: 100, mutation rate: 0.18, crossover rate: c				
	c: 0.7	c: 0.5	c: 0.3	c: 0.1
Test 1.	790	708	723	684
Test 2.	779	689	660	710
Test 3.	756	711	683	720
Test 4.	732	708	688	704
Test 5.	762	718	684	700
The best	732	689	660	684
Avg.	763.8	706.8	687.6	703.6
Deviation	19.96	9.62	20.24	11.89

As it can be seen, the higher the cardinality of the population is the better the results we got for the same generation number, however after population size 100 the best makespan does not improve.

In the followings, we fixed the value of the population size 100 and investigated the effect of smaller crossover rates. We collected the results in Table 3.

The results show that crossover rate 0.3 resulted the best makespan and the best average makespan, too. For our further investigation we fixed crossover rate at value 0.3. At this point, we found the importance of well determined crossover rate, unlike in paper by Pongcharoen et al. [12]. The difference may origin from the difference of the design of the genetic operators. The final important parameter we dealt was the mutation rate. Its effect on the efficiency of the genetic algorithm is illustrated in Table 4.

Table 4
Makespan results for the genetic scheduler with variable mutation rate /in time units/

generation: 400, population size: 100, crossover rate: 0.3, mutation rate: m					
	m: 0.08	m: 0.18	m: 0.28	m: 0.38	m: 0.48
Test 1.	887	723	692	678	682
Test 2.	751	660	674	648	648
Test 3.	707	683	680	676	692
Test 4.	708	688	736	672	674
Test 5.	698	684	692	661	675
The best	698	660	674	648	648
Avg.	750.2	687.6	694.8	667	674.2
Deviation	70.83	20.24	21.75	11.17	14.59

The results show that a higher mutation rate (0.38) has positive effect on the genetic algorithm. Its reason can be that it makes the algorithm jump out of local

optimum more often, but the construction of the algorithm does not let it to leave a better part of the search space for the worse part of that.

4.2 Results for Stochastic Problem

Based on the parameters we determined in the previous subsection, we applied our genetic algorithm on a problem, where operation time and process number are stochastic. The problem includes the same type of processes presented in subsection 2.1. However, the number of processes was changed as follows: the problem produces x pieces of sensor type I where $x \in [10,20]$ and y pieces of sensor type II where $y \in [15,25]$. For different executions we selected x and y from their interval based on uniform distribution.

Moreover, the operation times are also stochastic variables, following uniform distribution from the interval presented in Table 5.

Table 5

Duration time selection interval of each task /in time units/ in case of the stochastic problem

	Tr. d-t	Temp. test	Tr. t-s	Solde-ring	Tr. s-d	Tr. d-c	Cab-ling	Tr. c-s	Tr. t-v	Vibr. test	Tr. v-s
Temperature chamber	-	**[4,8]**	-	-	-	-	-	-	-	**[8,12]**	-
Cable producer	-	-	-	-	-	-	**[4,8]**	-	-	-	-
Vibration chamber	-	**[8,12]**	-	-	-	-	-	-	-	**[4,8]**	-
Solderer	-	-	-	**[3,5]**	-	-	-	-	-	-	-
Tr.d. d-t	**[2,4]**	-	-	-	-	-	-	-	-	-	-
Tr.d. d-c	-	-	-	-	-	**[3,7]**	-	-	-	-	-
Tr.d. t-s	-	-	**[3,5]**	-	-	-	-	-	-	-	-
Tr.d. t-v	-	-	-	-	-	-	-	-	**[2,4]**	-	-
Tr.d. c-s	-	-	-	-	-	-	-	**[2,4]**	-	-	-
Tr.d. v-s	-	-	-	-	-	-	-	-	-	-	**[3,7]**
Tr.d. s-d	-	-	-	-	**[3,5]**	-	-	-	-	-	-
Tr: transport; Tr.d.: transportation device; d: depot; c: cable producing; t: temperature test; v: vibration test; s: soldering											

We applied our genetic algorithm with the following parameter settings:

- *sizeofPopulation*: 100.
- The number of the generations: 400.

- *elites*: 0.2.
- When selecting the other instances, we can reselect elites, too.
- The possibility for applying crossover on a generation: 1.
- The percent of a generation should be resulted by crossover: 0.3.
- The percent of the processes origins from the first parent in case of crossover: 0.5.
- Only the instances with the worst fitness values should be replaced by the results of the crossover.
- The possibility for applying mutation for a generation: 1.
- The possibility for mutation in case of an instance: 0.38.
- Crossover and mutation can not influence elites.

For this problem the random selected values of 6 test cases are represented in Table 6 and the results of our algorithm for these cases are shown in Table 7.

Table 6

Random selected process numbers and operation time of the resources (the latter in time units, related to their actions, which are illustrated in Table 5 in case of the 6 presented stochastic examples)

	1. test	2. test	3. test	4. test	5. test	6. test
sensor type I (pieces)	17	16	13	14	13	18
sensor type II (pieces)	17	23	21	22	15	21
Temperature chamber (temp./vibr. test)	8/11	6/10	6/10	8/12	5/9	6/11
Cable producer	10	11	12	10	11	9
Vibration chamber(temp./vibr. test)	5/6	4/7	4/6	5/7	4/5	3/6
Solderer	2	4	4	2	2	2
Tr.d. d-t	5	5	5	4	5	3
Tr.d. d-c	4	5	4	3	4	3
Tr.d. t-s	3	3	5	3	4	4
Tr.d. t-v	4	7	4	8	6	6
Tr.d. c-s	2	2	4	4	4	2
Tr.d. v-s	2	2	2	4	4	3
Tr.d. s-d	7	6	3	6	4	4
Tr: transport; Tr.d.: transportation device; d: depot; c: cable producing; t: temperature test; v: vibration test; s: soldering						

The velocity of convergence of the algorithm for our tests is illustrated in Figure 7.

As the tables show, we got reasonable results. The makespan we got for the stochastic cases where the average values are the same as in case of the original problem, are around the values that we got for the original problem. Moreover, it can be seen that the results depend on the input values.

It is almost impossible to carry out sensitivity analysis for heuristic methods. However, we investigated how small changes in the input values influence our genetic algorithm. We chose an initial input, then we changed one-by-one only one operation time from the possible 8 (transportation operation times were treated together). Results are presented in Table 8. It can be realized that changes of originally higher values have bigger impact on the makespan.

Table 7

Makespan results for the genetic scheduler applied for the stochastic problem /in time units/

generation: 400, population size: 100, crossover rate: 0.3, mutation rate: 0.38	
Test 1.	567
Test 2.	700
Test 3.	724
Test 4.	658
Test 5.	529
Test 6.	630

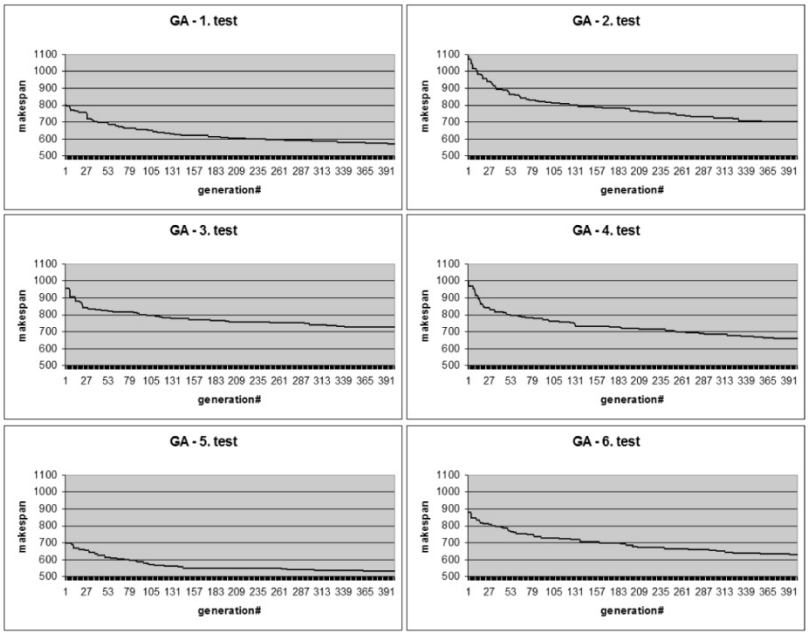

Figure 7

Some results in case of the stochastic problem, applying GA with the determined parameter values

Table 8

Makespan results for the genetic scheduler for small changes in input values /in time units/

init.	1.	2.	3.	4.	5.	6.	7.	8.
580	566	583	553	550	573	562	619	732

init: initial parameter values 1. cabling: 8→7 2. soldering: 4→5 3. temp.test by temp. chamber: 8→7 4. temp.test by vibr. chamber: 9→10	5. vibr.test by vibr.chamber: 4→5 6. vibr.test by temp.chamber: 10→9 7. transportation from depot to temperature test: 3→4 8. each transportation is increased by 1 time unit

Conclusions

In this paper we introduced a genetic algorithm-based scheduler, which is able to handle multiple projects with shared resource. These resources can be multi-functional. The processes to schedule can have parallel structured parts. The genetic operators were created to result only feasible schedule.

We found that in case of our model problem, minimum 400 generations, about 100 instances of a population is needed, and both the crossover rate and the mutation rate have important role. Our test results for the static problem were the best with crossover rate 0.3 and mutation rate 0.38 by applying coarse resolution. When the problem was changed to be a stochastic one by using variables for operation times and process number – taking care for being their average value the same as in case of the static problem – the results indicated that the algorithm parameters have the same impact. Future works can determine in more detail how the results depend on the input.

Acknowledgement

The authors wish to thank Prof. Katalin M. Hangos from Computer and Automation Research Institute, Budapest, Hungary, for her advice during the creation of this paper. We acknowledge the financial support of Széchenyi 2020 under the EFOP-3.6.1-16-2016-00015. We are also thankful for the helpful comments of the referee.

References

[1] Alba, E. and Chicano, J. F.: Software project management with GAs, InformationSciences, 177 (2007) No. 11, pp. 2380-2401

[2] Brucker, P.: Scheduling Algorithms, Springer-Verlag New York, Inc., Secaucus, NJ, USA, 2001, 3rd edn

[3] Chang, C., Christensen, M., and Zhang, T.: Genetic algorithms for project management, Annals of Software Engineering, 11 (2001) No. 1, pp. 107-139

[4] Chang, C. K., Jiang, H.-y., Di, Y., Zhu, D., and Ge, Y.: Time-line based model for software project scheduling with genetic algorithms, Inf. Softw. Technol., 50 (2008) No. 11, pp. 1142-1154

[5] Chen, P., Wen, L., Li, R., and Li, X.: A hybrid backtracking search algorithm for permutation flow-shop scheduling problem minimizing makespan and energy consumption, in: 2017 IEEE International Conference on Industrial Engineering and Engineering Management (IEEM) 2017, pp. 1611-1615

[6] Garey, M. R., Johnson, D. S., and Sethi, R.: The complexity of flowshop and jobshop scheduling, Mathematics of Operations Research, 1 (1976) No. 2, pp. 117-129

[7] Glover, F.: Tabu search-part i, ORSA Journal on computing, 1 (1989) No. 3, pp. 190-206

[8] Joo, B. J. and Chua, P. C.: Multimode resource-constrained multi-project scheduling with ad hoc activity splitting, in: 2017 IEEE International Conference on Industrial Engineering and Engineering Management (IEEM) 2017, pp. 2261-2265

[9] Kirkpatrick, S., Gelatt, C. D., and Vecchi, M. P.: Optimization by simulated annealing, Science, 220 (1983) No. 4598, pp. 671-680

[10] Pavol, S. and Vladimír, M.: A comparison of constructive heuristics with the objective of minimizing makespan in the flow-shop scheduling problem, Acta Polytechnica Hungarica, 9 (2012) No. 5, pp. 177-190

[11] Pinedo, M. L.: Scheduling: Theory, Algorithms, and Systems, Springer Publishing Company, Incorporated, 2008, 3rd edn.

[12] Pongcharoen, P., Hicks, C., Braiden, P. M., and Stewardson, D. J.: Determining optimum genetic algorithm parameters for scheduling the manufacturing and assembly of complex products, International Journal of Production Economics, 78 (2002) No. 3, pp. 311-322

[13] Sadegheih, A.: Scheduling problem using genetic algorithm, simulated annealing and the effects of parameter values on GA performance, Applied Mathematical Modelling, 30 (2006) pp. 147-154

[14] Votava, O.: A network simulation tool for task scheduling, Acta Polytechnica, 52 (2012) No. 5, pp. 112-119

[15] Zhang, G., Gao, L., and Shi, Y.: An effective genetic algorithm for the flexible job-shop scheduling problem, Expert Syst. Appl., 38 (2011) No. 4, pp. 3563-3573

Attitudes of European Consumers towards Digital Shadow Economy: Lithuanian and Spanish Cases

Ligita Gasparėnienė[1], Rita Remeikienė[2], Romualdas Ginevičius[3]

[1,2] Mykolas Romeris University, Ateities st. 20, LT-08303 Vilnius, Lithuania, e-mails: ligitagaspareniene@mruni.eu, rita.remeikiene@mruni.eu

[3] Vilnius Gediminas Technical University, Saulėtekio al. 11, LT-10223 Vilnius, Lithuania, e-mail: romualdas.ginevicius@vgtu.lt

Abstract: The article is aimed at complementation of the theory of shadow economy with consumers' attitudes towards the concept, determinants and channels of digital shadow economy at the international level. The results of the empirical research have enabled to define the phenomenon of digital shadow economy leaning on evaluations of the consumers from two different states, identify the main determinants of consumers' participation in digital shadow economy, and disclose the channels that are commonly employed for acquisition of goods/services from digital shadow markets. Although the states, which were selected for the research, differ by their geographical location, size and population's mentality, the results lead to the conclusion that consumers from both of them have a clear perception of the phenomenon of digital shadow economy, and are able to point out the main factors that motivate their participation in it. The research has also disclosed the lack of consumers' tax morale in both of the states.

Keywords: digital shadow economy; consumers; Lithuania; Spain; features of digital shadow economy; concepts of digital shadow economy

1 Introduction

Globalisation and digitalisation have dramatically changed the ways of how people work, communicate, and even make their purchase decisions. All across Europe, consumers widely use modern communication technologies for their daily activities. With reference to the report of the global management consulting firm *AT Kearney* (2013), more than 6 out of 10 mobile phone users own smart phones that provide connectivity to any website anytime, anywhere. High degree of mobility as well as availability of the Internet connection and a wide variety of products and services traded online promote a rapid spread of so-called "digital consumption". A today's consumer may visit several websites of retailers,

compare the prices, and then make an online purchase by his/her smart phone or home computer.

With the access to a huge number of potential suppliers, modern consumers demand for convenience and low prices across the purchase channels. However, they rarely care about a supplier's license to provide particular goods or services, and occasionally have their purchases properly documented. In other cases, consumers' choice to make a purchase from an unknown agent in an online forum or a social network is deliberate, mainly driven by an offer of a lower price. The examples above show that although the issues of shadow economy and digital shadow economy are basically analysed from a supplier's position (i.e. suppliers are considered the main agents of shadow economy and digital shadow economy since they provide goods and services for shadow and digital shadow markets, and deliberately conceal their income from public authorities), the role of consumers cannot be underestimated because consumers are the agents that generate the demand – an engine of any economic activity.

Thus far, the studies on consumers' participation in digital shadow economy mainly covered the research of e-fraud (Blackledge, Coyle 2010; Akintoye, Araoye 2011; Vlachos *et al.* 2011, etc.), digital piracy (Williams *et al.* 2010; Ho, Weinberg 2011; Belleflamme, Peitz 2010; Camarero *et al.* 2014; Yu *et al.* 2015, etc.), and the determinants of consumer's involvement in illegal activities online (Shang *et al.* 2008; Higgins *et al.* 2008; Williams *et al.* 2010, Yu *et al. 2015*, etc.). However, consumers' attitudes towards the phenomenon of digital shadow economy, including its concept, determinants, channels, and types of goods/services acquired by these channels, have hardly been analysed in complex. Minding the role of consumers as generators of demand in digital shadow markets, the research of this type would allow to complement the theories of shadow economy and digital shadow economy with new data, and in the future could contribute to the improvement of the measures of shadow economy estimation and prevention.

The purpose of this article is to research consumers' attitudes towards the concept and features of digital shadow economy in Lithuania and Spain, and conduct a comparative analysis of the results. Thereby, complementing the theory of shadow economy with new findings of the empirical study.

For the fulfillment of the defined aim, the following **objectives** have been raised: 1) to review the theoretical concepts and interpretations of digital shadow economy; 2) to review the literature on the features of digital shadow economy, including its determinants and channels; 3) to select and present the methodology of the research; 4) to introduce and compare the results of the empirical research on Lithuanian and Spanish consumers' attitude towards digital shadow economy.

The methods of the research include systematic and comparative analysis of the scientific literature, snowball data sampling method, consumer survey, Pearson correlation and multiple regression analysis.

2 What is Digital Shadow Economy?

As it was noted by Holz *et al.* (2009), a rapid advance of IT conditions a relatively complicated and perplexing understanding of digital shadow economy. The definition of digital shadow economy can be derived from the concept of traditional shadow economy. In the scientific literature, shadow economy is known by a multitude of names such as „non-observed economy", "informal economy", "undeclared economy", "black economy", "underground economy", "hidden economy", "cash-in-hand economy" and others (Barros 2005; Williams 2006; Feige, Urban 2008; Herley, Florencio 2010; Dion 2011; Feige 2012; Schneider *et al.* 2015, etc.). Nevertheless, despite the variety of the terms, there is a strong consensus on how to understand the phenomenon of shadow economy in its broad sense. Shadow economy refers to all legal production and provision of goods and services that are deliberately concealed from public authorities to avoid payment of taxes, social security contributions, or to escape compliance with particular legal standards (e.g. minimum wages, minimum and maximum working hours, vacation benefits, etc.) and administrative procedures (e.g. business registration, establishment of labour contracts, etc.) (European Commission 2005; Schneider, Buehn 2013; Schneider *et al.* 2015).

Leaning on this general definition of traditional shadow economy, and minding the fact that digital activities are the activities performed exceptionally in electronic space (in other words, e-space or digital space) (Holz *et al.* 2009; Herley, Florencio 2010; Yip *et al.* 2012; Feige 2012; Gaertner, Wenig 2012, etc.), it can be proposed that digital shadow economy in general refers to all legal production and provision of goods and services online, when the agents deliberately conceal their activities from public authorities to avoid tax payment or to bypass particular legal standards and/or administrative procedures.

Scientific literature contains a variety of definitions that stress different aspects of digital shadow economy. Some authors are inclined to reveal the underlying nature of digital shadow economy by interpreting it as an unregistered (hidden) profit-driven operation online (Moore *et al.* 2009; Herley, Florencio 2010; Yip *et al.* 2012, etc.), while others highlight online agents' strive to bypass established business standards and regulations (Schneider, Buehn 2013; Arango, Baldwin-Edwards 2014; Schneider *et al.* 2015, etc.) or avoid payment of taxes and/or social security contributions (Feige 2007; Feige 2012; Gaertner, Wenig 2012; Schneider, Buehn 2013, etc.) rather than concentrate on purely economic benefits (cash flows, revenue, profit). The term "digital unrecorded economy" refers to a deliberate concealment of online operations in the sense that neither operations themselves nor their results are properly captured in business accounting documents and/or reports (Karanfil 2008; Feige, Urban 2008). Finally, digital shadow consumption can be interpreted as one of the forms of cybercrime, in particular concerning e-fraud (i.e. consumers' activities of obtaining money illegally using the Internet (Vlachos *et al.* 2011; Amasiatu, Shah 2014; *McMillan*

Dictionary 2015, etc.), digital piracy (i.e. an illegal or unauthorized copying/downloading of particular copyrighted content (Castro *et al.* 2009; Camarero *et al.* 2014, etc.) or dysfunctional consumer behaviour online (i.e. consumers' actions on the Internet that violate the generally accepted norms of conduct in trade (Reynolds, Haris 2009; Harris, Daunt 2013). Although the majority of authors (Williams 2006; Feige 2012; Gaertner, Wenig 2012; Schneider, Buehn 2013; Schneider *et al.* 2015, etc.) are inclined to distinguish between digital shadow economy and cybercrime since the latter is a criminal offence rather than a type of economic activity, it is purposeful to find out whether the same attitudes are shared by consumers.

Hence, the analysis of the scientific literature has enabled to identify the following main characteristics of digital shadow economy that are considered while formulating theoretical definitions of this phenomenon:

- Digital shadow economy is a profit-driven online trade or service provision;
- Digital shadow economy is a global network of e-crimes;
- Digital shadow economy is provision of particular commodities or services in a remote space without any formal registration or appropriate capture of operations and their results in accounting documents or reports;
- Digital shadow economy is an illegal operation online that generates money flows for traders/service providers;
- Digital shadow economy is a trade or service provision in e-space without paying taxes to the state budget.

Since the aim of this article is to find out European consumers' attitudes towards the phenomenon of digital shadow economy, it is purposeful to research how European consumers perceive digital shadow economy. Additionally, whether they distinguish between the concepts of digital shadow economy and criminal activities in e-space (cybercrime). For this purpose, considering the above-mentioned characteristics of digital shadow economy, the following definitions of digital shadow economy were developed:

- Digital shadow economy is a part of shadow economy, when illegal profit-driven online trade or service provision is performed. The activities of digital shadow economy have the trend to be of repeated or non-repeated nature with or without changing IP addresses/computer networks;
- Digital shadow economy refers to global networks emerging in closed Internet forums and promoting chains of e-crimes, including bank attacks, payment card crimes, identity steals and other Internet intrusions;
- Digital shadow economy refers to (un)interrupted, financial gain driven provision of particular commodities or services in the remote space, performed without activity registration and causing damage to an officially registered subject, who provides similar commodities or services;
- Digital shadow economy is an illegal operation in the Internet space, which generates illegal money flows for commodity/service providers or

purchasers, and deprives legal traders/service providers from the revenue that could be officially accounted, calculated and declared;
- Digital shadow economy refers to the trade in e-space, performed without paying any taxes to the state budget, excluding purely criminal activities such as drug trafficking, prostitution).

The proposed definitions of digital shadow economy were presented for evaluation of Lithuanian and Spanish consumers in order to clarify their perceptions of the researched phenomenon.

3 The Features of Digital Shadow Economy

While analysing the features of digital shadow economy, it is purposeful to find out which motives drive the agents to get involved in digital shadow markets, and identify the basic channels through which goods and services from digital shadow markets are delivered to consumers. Scientific literature contains a large number of studies to research the determinants of agents' participation in shadow activities online, and the results of these studies show that individuals can be driven by different motives, starting from the general economic situation in their countries, and ending with particular personal (or ego) characteristics.

Economic determinants (i.e. lack of attractive forms of legal activities, unfavourable economic situation in a country, economic opportunities, low costs of data storage online, cost reduction and development of financial innovations) are considered to be the most important determinants of agents' participation in digital shadow economy (Williams *et al.* 2010; Schneider *et al.* 2010; Putninš, Sauka 2014; Lithuanian Free Market Institute (LFMI) 2014, etc.). Accessibility of attractive economic activities (LFMI 2014), reduction of unemployment rate (Williams *et al.* 2010; LFMI 2014), increased wages (Schneider *et al.* 2010; Putninš, Sauka 2014; LFMI 2014), and other similar factors of economic welfare in a country contribute to the growth of personal income (Williams *et al.* 2010; LFMI 2014) and make legal activities more attractive than illegal ones. Hence, favourable economic conditions in a country serve as a favourable environment for legal commerce. What is more, increased economic opportunities (e.g. an ability of a person to own a computer or a smart phone) as well as low costs of digital data storage serve as extra motives to get involved in digital activities (Ho, Weinberg 2011; Sirkeci, Magnusdottir 2011). The attractiveness of e-commerce is even further increased by lower prices of products and services online (Ho, Weinberg 2011; Williams *et al.* 2010; Yu *et al.* 2015). The development of financial innovations (e.g. access to fast credits online or via smart phones) also have a significant impact on consumers' purchase habits since they are always sure to get extra funding for spontaneous shopping (Šukytė 2010).

Low-level of consumers‘ tax morale (arising from the low-level of the general tax morale in society) alongside stereotypical negative society’s opinion about public authorities (citizens, especially in developing countries, often consider a country‘s government and public institutions under supervision of the government to be an evil pumping out their hard-earned money) make digital activities online look justifiable, and consumers do not mind making purchases without the requirement of any confirmation documents. According to Williams (2014), and Williams and Horodnic (2015), low tax morale alongside with low-level of public self-consciousness are important determinants of social acceptability of any shadow activities, including the ones online.

In the group of legal determinants, weak legal framework of e-commerce regulation, and poor regulation of the IT sector to the minimum reduce the fear that any unreported operation online can be detected, and punishments for unreported activities can be imposed (Waterman *et al.* 2007; Ho, Weinberg 2011). Apart from disadvantages of a legal framework itself, the problems with appropriately trained staff are also extremely topical. Law enforcement institutions feel the lack of officials with the skills to detect shadow activities online, which reduces the risk of being caught even further (Waterman *et al.* 2007; Ho, Weinberg 2011; Bossler, Holt 2012).

Finally, consumers’ inclination to acquire products/services in digital shadow markets is determined by the advantages of the IT age (e.g. variety of available products and services, easy and convenient access to information, electronic communication with a product seller or service supplier, sales promotions, convenient return policies, convenience of an acquisition channel, short payment terms, and customer maintenance promote digital shadow consumption) (Mikalajūnas, Pabedinskaitė 2010; Šukytė 2010; Sirkeci, Manusdottir 2011; Ho, Weinberg 2011), lack/absence of a particular product or service in the local market (which is typical of smaller-town markets), and an opportunity to save time which would have been spent going to a traditional shop (Šukytė 2010; Hafezieh *et al.* 2011; Levi, Williams 2013, etc.). More specifically, some scientific studies found that participation in e-commerce generates higher customers‘ satisfaction by providing quicker service, demand for less effort to buy a product or service, and lower business cost compared to a business run without the use of information technology (IT) (McLeod, Schell 2001). Also, as it was noted by Laudon and Laudon (2000), suppliers in e-commerce deal with advanced technical facilities to run their business smoothly, which very much appeals to potential consumers.

After identification of the main theoretical determinants of consumers‘ involvement in digital shadow economy, it is important to have more information about the channels through which goods and services from digital shadow markets are delivered to consumers. The analysis of the scientific literature (Hafezieh *et al.* 2011; Levi, Williams 2013; Amasiatu, Shah 2014; Vlachos *et al.* 2011; Dion 2011; Smith 2015, etc.) has disclosed, despite the category of a customer (i.e. a

natural entity, legal entity, multinational enterprise or business network), the channels employed for acquisition of goods/services from digital space are similar (see Table 1).

Table 1
The channels of digital shadow economy employed by different categories of consumers

Category of a consumer	Channels of digital shadow economy
Natural entities	Internet network, online forums, platforms for anonymous operation, online retail stores, online service provision websites, social networks, e-auction sites
Legal entities	E-advert sites, e-auction sites, platforms for anonymous operation
MNEs	E-advert sites, e-auction sites, platforms for anonymous operation
Business networks	Global networks, Internet network, remote spaces, servers, platforms for anonymous operation

As it can be seen from the information in Table 1, unlike legal entities, MNEs and business networks, natural entities more often employ online forums, online retail stores and social networks (e.g. Facebook, Twitter, etc.) for their purchases in digital markets (Hafezieh *et al.* 2011; Levi, Williams 2013; Amasiatu, Shah 2014), although in some cases they also visit e-advertisement or e-auction sites (e.g. for purchase of secondhand cars or other valuable assets) (Dion 2011; Smith 2015). Legal entities and MNEs give preference to the search of goods/services in e-advert sites, e-auction sites and Internet platforms developed for anonymous operation (it should be noted that legal entities and MNEs commonly act via agents or representatives). Finally, business networks, if we consider them as consumers in e-commerce, also act via agents, but the channels of their interest more often cover remote spaces and Internet servers (Holz *et al.* 2009; Hafezieh *et al.* 2011; Levi, Williams 2013).

Summarising, the determinants of consumers' participation in digital shadow economy fall into the groups of economic, psychological, legal and other factors. Economic determinants mainly cover lack of attractive forms or legal activities, unfavourable economic situation in a country, wider economic opportunities conditioned by higher income of population, low costs of data storage online, cost reduction, and development of financial innovations. Psychological determinants cover low-level of consumers' tax morale, and their stereotypical negative opinion about governmental and public authorities. The impact of legal determinants is observed through the emergence of such motivators as low risk of detection on an illegal behaviour online, weak legal framework of e-commerce regulation, lack of public officials with the skills to detect unreported activities online, and poor regulation of IT sector. The other influential determinants include advantages and conveniences of the IT age, lack/absence of a particular product/service in the local market, and time saving. The channels employed by different categories of consumers for acquisition of goods/services from digital space include online retail shops, social networks and platforms, online trade/service provision

websites, e-advert and e-auction sites. In the empirical part of the research, we will identify the main features of digital shadow economy, including its determinants and channels, from consumers' point of view in Lithuania and Spain.

4 The Methodology of the Research

In order to have a deeper insight in the attitudes of European consumers towards the phenomenon of digital shadow economy, two European countries – Lithuania and Spain were selected for the research. With reference to the estimations made by Schneider and Buehn (2016), both Lithuania and Spain are attributed to the category of the states with the scopes of shadow economy that exceed the average of the EU, which currently amounts to 17.6 percent of GDP. In 2016, the scope of shadow economy in Lithuania amounted to 24.9 percent of GDP, while in Spain it composed 17.9 percent of GDP (Schneider, Buehn 2016). The second criterion of selection was a similar level of development of both of the states (as of 2013, GDP in current prices amounted to 24.500 PPS (Purchasing Power Standard per inhabitant) in Spain, and 19.100 PPS in Lithuania (*Eurostat* 2016). In 2016, the Word Bank attributed Lithuania and Spain to the category of the states with high income per capita (*The World Bank* 2016).

In this research "mixed methods design refers to the use of two (or more) research methods in a single study, when one (ore more) of the methods is not complete in itself" (Morse, Niehaus, 2016). So we define, mixed methods as the incorporation of one or more techiques into a single research study in order to reach the main aim.

In order to fulfill the aim of the research, i.e. to compare and assess consumers' attitudes towards the phenomenon digital shadow economy in Lithuania and Spain, "snowball" data sampling method was selected. This method was employed considering its ability to provide the access to target population groups. Employment of "snowball" data sampling method for surveys of hidden population groups is recommended by Atkinson and Flint (2001). The questionnaire for the survey was composed of three structural parts: the first part was developed to establish demographic characteristics of consumers who operate in digital shadow markets; the second part covered the concepts of digital shadow economy proposed for consumers' evaluation in Likert scale; finally, the third part was developed to establish the determinants of acquisition of goods/services from digital shadow markets, to identify the acquisition channels, and find out what categories of goods/services are most commonly acquired via these channels.

The sample was estimated by engaging the *Internet survey system calculator,* which covers the variables of confidence level (expressed as a percentage and representing how often the true percentage of the population who would pick an

answer lies within the confidence interval), confidence interval (a marginal error), and population (in our case, 66 percent of 3 million people in Lithuania makes 1980000 people). To ensure 5 percent error rate under 95 percent confidence level, 384 respondents needed to be surveyed. However, the real number of the respondents, available for the survey, composed 368 people, which determined a slight increase in the error rate up to 5.11 percent. The research was carried out from August 2015 to October 2016 by employing the tools of e-survey.

The sample of the respondents in Spain was estimated leaning on the following criteria: with reference to the data of Eurostat (2016), population of Spain, aged from 15 to 64, composes 30808.47 people, 79 percent of whom have an access to the Internet; hence, the sample of the research should make 24338.69 people; with survey reliability rate of 95 percent, and survey error rate of 7 percent, it is enough to involve 194 respondents. The survey in Spain was carried out from September to October, 2016. The main condition of inclusion of the respondents in the survey was at least once purchase of a good/service in e-space.

Additionally, in order to establish which determinants had the impact on the scope of shadow economy in Lithuania and Spain over 2005-2015, the methods of Pearson regression analysis and multiple regression analysis were employed.

The collected data was processed with SSPS and Microsoft Excel software.

5 The Comparative Analysis of Consumers' Attitudes towards Digital Shadow Economy in Lithuania and Spain

For comparison of the attitudes of Lithuanian and Spanish consumers towards digital shadow economy, at first it is purposeful to analyse which determinants had impact on the scopes of shadow economy in both states over 2005-2015. In order to substantiate expedience of the assessment of the impact of economic and political determinants on the scopes of shadow economy in Lithuania and Spain, the authors verified whether there exists any correlation between *the Freedom from Corruption Index, tax paying (in numbers), profit tax (percent), business start-up costs (percentage from the income per capita), GDP per capita (EUR), exports of goods and services (percentage of GDP), imports of goods and services (percentage of GDP), unemployment rate (percentage of the total labour force), inflation (annual, in consumption prices, percent), crediting of private sector (percentage of GDP), total tax rate (percentage of commercial profits) and size of shadow economy in Lithuania and Spain over the period 2005-2015.* The results have been presented in Table 2.

Table 2

The values of Pearson correlation coefficient

No.	Determinants	Pearson correlation coefficient	
		Lithuania	Spain
X1.	The Freedom from Corruption Index	**0.864** (p = 0,001)	**0.759** (p = 0.007)
X2.	Protit tax (percent)	**0.795** (p = 0.003)	0.223
X3.	Tax paying (numbers)	0.182	**-0.826** (p = 0.002)
X4.	Total tax rate (percentage of commercial profits)	**0.795** (p = 0.003)	0.223
X5.	Business start-up costs (percentage of income per capita)	**0.884** (p = 0.000)	**0.605** (p = 0.049)
X6.	Exports of goods and services (percentage of GDP)	**-0.741** (p = 0.009)	**-0.629** (p = 0.038)
X7.	Imports of goods and services (percentage of GDP)	**-0.688** (p = 0.019)	-0.104
X8.	Inflation (annual, in consumption prices, percent)	0.466	0.438
X9.	GDP per capita (EUR)	0.142	0.275
X10.	Unemployment rate (percentage of total labour force)	-0.279	-0.556
X11.	Crediting of private sector (percentage of GDP)	0.407	0.111

The results in Table 2 show that statistically significant determinants (i.e. the ones with p lower than 0.05, and coefficient *r* higher than 0.6) of the size of shadow economy in Lithuania and Spain over 2005-2015 were as follows: X1 – the Freedom from Corruption Index (r = 0.864); X2 – Profit tax, percent (r = 0.795); X4 – Total tax rate, percentage of commercial profit (r = 0.795); X5 – Business start-up costs, percentage of income per capita (r = 0.884); X6 – Exports of goods and services, percentage of GDP (r = -0.741); X7 – Imports of goods and services, percentage of GDP (r = -0.688).

Further in the research, only the variables with values $p < 0.05$ were included in the multiple regression model. The following equation was developed: $Y_{Lithuania} = 22.348+0.178*X1+0.259*X4$. The value of the standardised Beta coefficient (-0.612) shows that coefficient X1 has a greater impact on variable Y (shadow economy) than coefficient X4.

In Spanish case, the determinants with statistically significant values that have the impact on the size of shadow economy are as follows: X1 – the Freedom from

Corruption Index; X3 – Tax paying, numbers; X5 – Business start-up costs, percentage of income per capita; X6 – Exports of goods and services, percentage of GDP.

The following multiple regression equation was developed: Y_{Spain} = 35.372-1.828*X3.

Summarising the mathematical estimations, it can be stated that the size of shadow economy is determined by different factors in Lithuania and Spain: over the period under research, the size of shadow economy in Lithuania was to the greatest extent determined by the Freedom from Corruption Index and total tax rate, while the size of shadow economy in Spain was to the greatest extent determined by tax paying. Nevertheless, taxes (regardless of their expression in numerical values or percentage of commercial profits) had a significant impact on the size of shadow economy in both of the states.

The answers to the questions of the first part of the questionnaire have enabled to specify demographic characteristics of the respondents:

- ***By age,*** the most active participants of e-commerce in both Lithuania and Spain are young people aged from 16 to 29 (69.8 percent of the total number of Lithuanian respondents, and 95.9 percent of the total number of Spanish respondents). The groups of population aged from 30 to 49 composed 23.4 percent of the total number of the respondents in Lithuania, and 2 percent – in Spain. The rest part (i.e. 2.7 percent) of the respondents in Lithuania belonged to the group of population over 50.
- ***By profession,*** the largest part of the respondents was composed of students (46.7 percent of all Lithuanian survey participants, and 87.8 percent of all Spanish survey participants). Professionals composed the second significant group of the respondents in Lithuania (18.2. percent of all survey participants), while entrepreneurs – in Spain (6.1 percent of all survey participants). The survey involved 7.6 percent IT professional from Lithuania, and 2 percent – from Spain. The number of employees amounted to 7.9 percent of the total number of the respondents in Lithuania, and 4.1 percent in Spain.
- ***By income,*** the group of the people with no personal income composed 21.2 percent in Lithuania, and 67.3 percent in Spain. Such distribution of the respondents can be explained minding the fact that a large number - 46.7 percent of the respondents from Lithuania, and 87.8 percent of the respondents from Spain - were students, who do not earn any personal income for living. The largest part (25.5 percent) of Lithuanian respondents were attributed to the group of people whose income reach 501 – 1000 Eur per month, while only 2 percent of Spanish respondents fall into the same group. Distribution of the other respondents by their income was as follows: 8.4 percent of Lithuanian and 10.2 percent of Spanish respondents indicated that their monthly income makes under 100 Eur; 14.1 percent of Lithuanian

and 6.1 percent of Spanish respondents declared earning from 101 to 300 Eur per month; 18.8 percent of Lithuanian and 8.2 percent of Spanish respondents declared earning from 301 to 500 Eur per month; finally, 7.9 percent of the respondents from Lithuania and 6.1 percent of the respondents from Spain indicated that their monthly income is over 1001 Eur.

- ***By education,*** the largest parts of the respondents in both countries indicated having higher education (i.e. 45.9 percent of Lithuanian and 83.7 percent of Spanish respondents). Slightly smaller parts of the respondents (i.e. 39.4 percent of Lithuanian and 16.3 percent of Spanish respondents) indicated having secondary or vocational education.
- ***By gender,*** the survey involved 31.3 percent of Lithuanian and 38.8 percent of Spanish male, while the share of female composed 63 and 59.2 percent in Lithuania and Spain respectively.

The value of *Cronbach alpha* coefficient, estimated for the second part of the questionnaire titled "The concept of digital shadow economy," amounted to 0.6, which proposes that the questions of the survey reflect the target dimension with appropriate accuracy. The marginal value of *Cronbach alpha* coefficient, fixed for this research, is equal to 0.6.

At first, we will analyse how consumers from both states interpret the phenomenon of digital shadow economy. The values of *Kendall's coefficient* of concordance for this group of questions were equal to 0.061 and 0.053 for Lithuania and Spanish respectively, and values p were equal to 0.000, which, in turn, proposes that congruence of the respondents' opinions is weak, but statistically significant (see Table 3).

Table 3

Mean ranks estimated for different concepts of digital shadow economy: attitudes of Lituanian and Spanish consumers

No.	Proposed concepts of digital shadow economy	Mean ranks (Lithuanian consumers)	Mean ranks (Spanish consumers)
1.	Digital shadow economy is a part of shadow economy, when illegal profit-driven online trade or service provision is performed. The activities of digital shadow economy have the trend to be of repeated or non-repeated nature with or without changing IP	3.48	2.93
2.	Digital shadow economy refers to global networks emerging in closed Internet forums and promoting chains of e-crimes, including bank attacks, payment card crimes, identity thefts and other Internet intrusions	3.19	2.86
3.	Digital shadow economy refers to (un)interrupted, financial gain driven provision of particular	3.78	2.77

	commodities or services in the remote space, performed without activity registration and causing damage to an officially registered subject, who provides similar commodities or services.		
4.	Digital shadow economy is an illegal operation in the Internet space, which generates illegal money flows for commodity/service providers or purchasers, and deprives legal traders/service providers from the revenue that could be officially accounted, calculated and declared	3.83	3.31
5.	Digital shadow economy refers to the trade in e-space, performed without paying any taxes to the state budget, excluding purely criminal activities such as drug trafficking, prostitution, etc.	3.53	3.02

For this research, it was established that the proposed concepts of digital shadow economy with mean ranks over 3 should be treated as understandable and acceptable to consumers. The concepts with mean ranks under 2.9 points are considered as poorly reflecting consumers' perception of digital shadow economy.

The data in Table 3 shows that regardless of their citizenship, consumers are inclined to interpret the phenomenon of digital shadow economy as *an illegal operation in the Internet space, which generates illegal money flows for commodity/service providers or purchasers, and deprives legal traders/service providers from the revenue that could be officially accounted, calculated and declared* (mean ranks 3.83 and 3.31 for Lithuania and Spain respectively). While evaluating the other concepts of digital shadow economy, the opinions of Lithuanian and Spanish respondents significantly varied. Spanish respondents found the concept proposing that *digital shadow economy refers to the trade in e-space, performed without paying any taxes to the state budget, excluding purely criminal activities such as drug trafficking, prostitution, etc.* comparatively acceptable, while the concepts marked as 1-3 in Table 2 were found poorly reflecting the core of the researched phenomenon.

Unlike Spanish respondents, consumers from Lithuania found all the concepts of digital shadow economy comparatively acceptable (with mean ranks over 3). The concept proposing that digital shadow economy refers to *(un)interrupted, financial gain driven provision of particular commodities or services in the remote space, performed without activity registration and causing damage to an officially registered subject, who provides similar commodities or services* took the second position (with mean rank equal to 3.78) among all other concepts, which were presented for consumers' evaluation.

The systematised results of the empirical research lead to the conclusion that **both Lithuanian and Spanish consumers are inclined to differentiate between cybercrime (drugs, prostitution, steals of credentials, smuggling, etc.) and digital shadow activities, which, by their nature, are unreported economic activities online that violate legal regulations of a state. Performance of**

unreported activities generates unreported cash flows to illegally acting agents and allows to evade payment of particular taxes.

The value of *Cronbach alpha* coefficient, estimated for the third part of the questionnaire titled "The features and channels of digital shadow economy", amounted to 0.823, which proposes that the questions of the survey reflect the target dimension with appropriate accuracy. The values of *Kendall's coefficient* of concordance for this group of questions were equal to 0.133 and 0.093 for Lithuania and Spain respectively, and values p were equal to 0.000, which proposes that congruence of the respondents' opinions is weak, but statistically significant. Incongruence of the respondents' opinions can be explained by employing different presumptions: firstly, each respondent leans on his/her personal experience in e-commerce; secondly, the respondents may have different perceptions concerning the phenomenon of digital shadow economy, which thus far has not been universally defined either in scientific or in legal sources; finally, the issue of digital shadow economy remains insufficiently researched, which makes the concept of this phenomenon seem completely new. The determinants of consumers' participation in digital shadow economy and evaluations of the influence of these determinants on consumers' decision to acquire products/services from digital shadow markets have been presented in Table 4.

Table 4

The determinants of consumers' participation in digital shadow economy: comparative analysis of the attitudes of Lithuanian and Spanish consumers

Determinant group/Determinant	Mean rank (Lithuanian consumers)	Mean rank (Spanish consumers)
Economic determinants		
1. The lack of availability of economic activities	3.02	3.02
2. Unfavourable economic situation in the country (high unemployment, low salary)	***3.67***	***3.46***
3. Economic potential (internet access, hardware and software quality, reasonable smart phone and computer costs)	***3.66***	***3.02***
4. Reasonable digital data storage costs	3.45	3.07
5. Lower price	***4.08***	***3.52***
6. Development of financial innovations (availability of short-term credits online)	3.26	3.11
Psychological determinants		
7. Low tax morality level	3.45	3.17
8. Prevailing stereotypical negative opinion about governmental institutions and public authorities	3.38	2.75
Legal determinants		
9. Low possibility of detection of a purchase from legally non-existent entity without paying VAT	3.26	2.95

10. Weak legal framework which could help to control the scopes of cybercrime	3.32	2.71
11. Lack of professionals with the skills to investigate cybercrimes; as a result, agents in digital shadow markets are not afraid to be caught or punished	3.37	2.57
12. Poor regulation and control of the IT sector	3.42	2.67
Other determinants		
13. Advantages of the IT age (convenience of shopping without leaving home at any time, anonymity, etc.)	***4.03***	***3.02***
14. Lack/absence of desired goods/services in the local market	***3.83***	***3.34***
15. Time saving when purchasing goods/services online	***3.95***	***3.36***

The values of mean ranks are interpreted as follows: if a mean rank is over 3.5, it is considered that the factor with this mean rank is a strong motivator for consumers to acquire goods/services from digital shadow markets; if a mean rank falls into the interval from 3.49 to 3.00, the factor with this mean rank is considered less influential; finally, if a mean rank is under 2.99, the factor with this rank is considered unimportant for the decision of a consumer to acquire goods/services from digital shadow markets.

In the group of *economic determinants*, consumers from both states indicated **lower price** as the most influential factor that determines acquisition of goods/services from digital shadow markets (mean rank for Lithuanian consumers was equal to 4.08, and for Spanish consumers – to 3.5 points). **Unfavourable economic situation in the country** (with mean rank equal to 3.67 for Lithuanian consumers, and 3.56 – for Spanish consumers) was acknowledged as the second influential factor. Economic opportunities (e.g. access to the Internet, possession of a PC or a smart phone, low costs of acquisition of technologies, etc.) was pointed out as influential by Lithuanian consumers (mean rank equal to 3.66), while their Spanish counterparts attributed it to the group of less influential factors.

The other determinants, such as ***advantages of the IT age*** (mean rank equal to 4.03), ***lack/absence of a desired good/service in the local market*** (mean rank equal to 3.83), and ***time saving*** (mean rank equal to 3.95) were indicated as influential only by Lithuanian consumers, while Spanish consumers treated them as less influential.

Summarising the results of the survey, the following trends can be observed: a consumer regardless of the country of his/her origin, gives priority to an opportunity to acquire a good/service at a lower price. This determinant is complemented with the unfavourable economic situation in the country (following the statistical data, high-level (20.5 percent) of unemployment has remained one of the most topical problems of Spanish economy in 2016, while Lithuania is facing the problems of wages that are considered among the lowest in the EU (the average wage in Lithuania amounted to 380 Eur in 2016)). The other influential

determinants, such as the advantages of the IT age, time saving, and lack of a desired good/service in the local market, could be attributed to the group of the determinants of e-commerce in general, but consumers indicated them as motivators to acquire goods/services from suppliers operating in digital shadow markets. The remained groups of the proposed determinants of digital shadow economy (i.e. psychological and legal determinants) were indicated as less influential or not influential for acquisition of goods/services from digital shadow markets.

In order to identify the channels, which are most commonly employed by consumers for acquisition of goods/services from e-space, the respondents were asked to indicate and evaluate them (see Fig. 1).

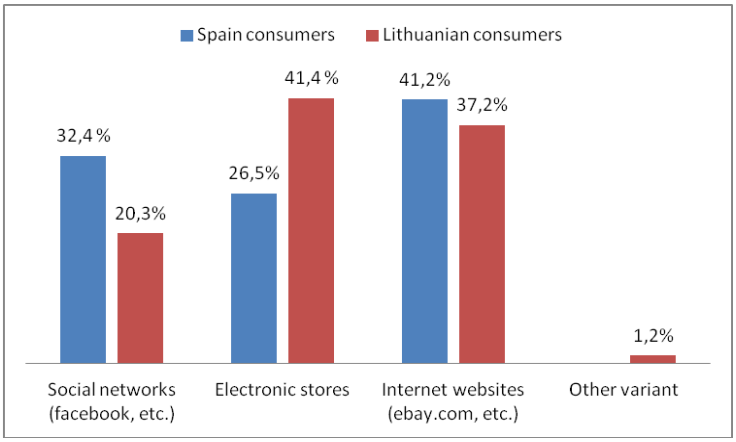

Figure 1

The channels commonly employed for acquisition of goods/services from e-space, percent

Systematisation of the survey results has revealed that Spanish consumers are inclined to acquire goods/services from various Internet websites (as it was indicated by 41.2 percent of Spanish respondents), while Lithuanian consumers prefer electronic stores (as it was pointed out by 41.4 percent of Lithuanian respondents). What is more, consumers from both states admitted acquiring goods/services from social networks. Hence, the results of the survey propose that the above-mentioned channels appeal to both Spanish and Lithuanian consumers, which serves as a strong motive for suppliers to advertise their goods/services in these channels in order to reach a potential consumer. Another interesting fact is that 30.4 percent of Lithuanian, and 20.4 percent of Spanish consumers have never required for any purchase confirmation documents (e.g. invoices, bills, checks, etc.). 37.2 percent of Lithuanian, and 36.7 percent of Spanish respondents not always require for such documents, but the vast majority of the respondents who ask for confirmation a status of an online trader (i.e. 57.7 percent of Lithuanian, and 42.9 percent of Spanish respondents) do this for the following reasons: trying

to escape the risk to acquire a poor quality product/service or following recommendations of friends or acquaintances. Lithuanian consumers more than their Spanish counterparts pay attention to reliability and guarantees of a good/service. The issues of tax morale were not indicated as significant in this respect.

Summarising, the empirical research has disclosed the following consumers' attitudes towards digital shadow economy:

- Both Lithuanian and Spanish consumers interpret the phenomenon of digital shadow economy as *an illegal operation in the Internet space, which generates illegal money flows for commodity/service providers or purchasers, and deprives legal traders/service providers from the revenue that could be officially accounted, calculated and declared.*
- The main determinants of digital shadow economy from consumers' point of view are lower price and unfavourable economic conditions. In addition, the advantages of the IT age, lack/absence of a desired good/service in the local market, and time saving serve as extra motivators for Lithuanian consumers to participate in digital shadow economy, while Spanish consumers treat these factors as less influential. Legal and psychological determinants do not have any significant impact on the decision of consumers from both states to acquire goods/services from digital shadow markets.
- Consumers are not inclined to require for any purchase confirmation documents from online suppliers of goods/services (this tendency was confirmed by similar distribution of the answers provided by the respondents from both of the states) or require for such documents only trying to escape the risk to acquire a poor quality product/service, to have more guarantees or following the recommendations of friends or acquaintances. However, the principle of tax morale is not considered.
- The main difference between the habits of Lithuanian and Spanish consumers relevant to their participation in digital shadow economy is selection of the channels for acquisition of goods/services from e-space. The results of the survey have disclosed that Lithuanian consumers prefer electronic stores, while Spanish consumers choose various Internet websites. These findings could be the reason for state tax inspectorates to monitor the activities of the above-mentioned channels of e-commerce with higher accuracy.

Conclusions

The comparative analysis of Lithuanian and Spanish consumers' attitudes towards the phenomenon of digital shadow economy has enabled to complement the theory of shadow economy with the concept, determinants and channels of digital shadow economy from consumers' position. The results of the research have revealed that consumers from the states with the similar level of economic development interpret the phenomenon of digital shadow economy as an illegal

operation in the Internet space, which generates illegal money flows for commodity/service providers or purchasers, and deprives legal traders/service providers from the revenue that could be officially accounted, calculated and declared. In other words, digital shadow economy is an unregistered commercial operation in electronic space, when unregistered suppliers earn income, but evade payment of taxes to the state budget. Economic determinants (e.g. lower prices of goods/services provided online or unfavourable economic situation in the country) are the main determinants that motivate consumers to acquire goods/services from the Internet, usually without verification of a status of a supplier. The spread of digital shadow economy in European level is not highly determined by psychological (tax morale, negative society's attitudes towards public authorities) or legal factors (e.g. poor regulation of the IT sector, low risk of detection, etc.). Hence, the results of the research propose that in order to reduce consumers' motivation to participate in digital shadow economy, first of all, it would be purposeful to increase consumers' awareness by improving conditions for legal business conduct, reducing unemployment rate, and employing educational measures (since leaning on the results of the survey, consumers hardly consider the issues of tax morale when making purchases from illegal suppliers online; what is more, they occasionally require for any purchase confirmation documents). The future research on this topic could be aimed at clarification which measures would be efficient to discourage consumers from participation in digital shadow economy.

Acknowledgement

This work was supported by the Research Council of Lithuania [grant number MIP-15642]

References

[1] Akintoye, K. A.; Araoye, O. E.: Combating e-fraud on electronic payment system, International Journal of Computers 25(8), 2011, pp. 48-53

[2] Amasiatu, C. V.; Shah, M. H.: First party fraud: a review of the forms and motives of fraudulent consumer behaviours in e-tailing, International Journal of Retail & Distribution Management 42(9) 2014, pp. 805-817

[3] Arango, J.; Baldwin-Edwards, M.: Immigrants and the informal economy in Southern Europe, 2nd ed., Frank Cass, London, 2014

[4] AT Kearney: The shadow economy in Europe, 2013 [online] [cited 06 November 2016] Financial Institutions, 2013, retrieved from: https://www.atkearney.com/financial-institutions/featured-article/-/asset_publisher/j8IucAqMqEhB/content/the-shadow-economy-in-europe-2013/10192

[5] Atkinson, R.; Flint, J.: (2001) Accessing hidden and hard-to-reach populations: snowball research strategies [online] [cited 25 November

2016] University of Surrey, 2001, retrieved from http://sru.soc.surrey.ac.uk/SRU33.pdf

[6] Barros, C. P.: Performance measurement in tax offices with a stochastic frontier model, Journal of Economic Studies 32, 2005, pp. 497-510

[7] Belleflamme, P.; Peitz, M.: Digital piracy: theory economy [online] [cited 06 November 2015] CESifo Working Paper Series No. 3222, 2010, retrieved from: http://papers.ssrn.com/sol3/papers.cfm?abstract_id=1698618

[8] Blackledge, J. M.; Coyle, E.: E-fraud prevention based on the self-authentication of e-documents, Digital Society 10, 2010, pp. 329-338

[9] Bossler, A. M.; Holt, T. J.: Patrol officers' perceived role in responding to cybercrime, Policing 35(1) 2012, pp. 165-181, http://dx.doi.org/10.1108/13639511211215504

[10] Camarero, C.; Anton, C.; Rodriguez, J.: Technological and ethical antecedents of e-book piracy and price acceptance: evidence from the Spanish case, The Electronic Library 32(4) 2014, pp. 542-566, http://dx.doi.org/10.1108/EL-11-2012-0149

[11] Castro, D.; Bennett, R.; Andes, S.: Steal these policies: strategies for reducing digital piracy [online] [cited 18 November 2016] The Information Technology and Innovation Foundation, 2009, retrieved from: www.itif.org/files/2009-12-15.DigitalPiracy.pdf

[12] Dion, M.: Corruption, fraud and cybercrime as dehumanizing phenomena, International Journal of Social Economics 38(5) 2011, pp. 466-476, http://dx.doi.org/10.1108/03068291111123156

[13] European Commission: Feasibility study of a direct survey of undeclared work in Europe, Brussels, 2005

[14] Eurostat: Your key to European statistics. [online] [cited 4 December 2016] Eurostat Database, 2016, retrieved from: http://ec.europa.eu/eurostat/data/database

[15] Feige, E. F.; Urban, I.: Measuring underground (unobserved, non-observed, unrecorded) economies in transition countries: can we trust GDP?, Journal of Comparative Economics 36(2) 2008, pp. 287-306

[16] Feige, E. L.: The underground economies – tax evasion and information distortion, 2nd ed, Cambridge University Press, Cambridge, 2007

[17] Feige, E. L.: New estimates of U.S. currency abroad, the domestic money supply and the unreported economy, Crime, Law and Social Change 57(3) 2012, pp. 239-263

[18] Gaertner, W.; Wenig, A.: The economics of the shadow economy, 1st ed., Springer-Verlag, Berlin, 2012

[19] Hafezieh, N.; Akhavan, P.; Eshraghian, F.: Exploration of process and competitive factors of entrepreneurship in digital space: a multiple case study in Iran, Education, Business and Society: Contemporary Middle Eastern Issues 4(4) 2011, pp. 267-279

[20] Harris, L. C.; Daunt, K. (2013). Managing customer misbehaviour: challenges and strategies // Journal of Services Marketing 27(4): 281-293

[21] Herley, C.; Florencio, D.: Nobody sells gold for the price of silver: dishonesty, uncertainty and the underground economy [online] [cited 28 November 2016] Springer Link, 2010, retrieved from: http://link.springer.com/chapter/10.1007%2F978-1-4419-6967-5_3#page-1

[22] Higgins, G. E.; Wolfe, S. E.; Markum, C. D.: Digital piracy: an examination of three measurements of self-control, Deviant Behaviour 29(5) 2008, pp. 440-461

[23] Ho, J.; Weinberg, C. B.: Segmenting consumers of pirated movies, Journal of Consumer Marketing 28(4) 2011, pp. 252-260

[24] Holz, T.; Engelberth, M.; Freiling, F.: Learning more about the underground economy: a case-study of keyloggers and dropzones [online], [cited 28 November 2016] Springer Link, 2009, retrieved from: http://link.springer.com/chapter/10.1007%2F978-3-642-04444-1_1#page-1

[25] Karanfil, F.: Energy consumption and economic growth revisited: does the size of unrecorded economy matter?, Energy policy 36(8) 2008, pp. 3029-3035

[26] Laudon, K. C.; Laudon, J. P.: Management information systems: organisation and technology in networked enterprise, Prentice Hall, New Jersey, 2000

[27] Levi, M.; Williams, M. L.: Multi-agency partnerships in cybercrime reduction, Information Management & Computer Security 21(5) 2013, pp. 420-443, http://dx.doi.org/10.1108/IMCS-04-2013-0027

[28] Lithuanian Free Market Institute: Lietuvos šešėlinė ekonomika [Lithuanian shadow economy] [online] [cited 23 November 2016] Free Market Institute, 2014, retrieved from: http://files.lrinka.lt/Seseline_ekonomika/LSE3.pdf

[29] McLeod, R.; Schell, G. P.: Management information systems. Prentice Hall, New Jersey, 2001

[30] McMillan Dictionary: The term of e-fraud economy [online], [cited 20 November 2016] McMillan Online Dictionary, 2015, retrieved from: http://www.macmillandictionary.com/dictionary/british/e-fraud

[31] Mikalajūnas, A.; Pabedinskaitė, A.: Elektroninio verslo plėtra Lietuvoje [Development of electronic business in Lithuania] [online] [cited 10 October 2016] BME conferences, 2010, retrieved from:

http://leidykla.vgtu.lt/conferences/BME_2010/005/pdf/Art-Mikalajunas_Pabedinskaite.pdf

[32] Moore, T.; Clayton, R.; Anderson, R.: The economics of online crime, Journal of Economic Perspectives 23(3) 2009, pp. 3-20

[33] Morse, J. M., Niehaus, L. (2016) Mixed Method Design. Principle and procedures. Routledge

[34] Putninš, T. J.; Sauka, A.: Shadow economy index for the Baltic countries 2009-2013 [online] [cited 15 March 2016] The Centre for Sustainable Business at Stockholm School of Economics in Riga, 2014, retrieved from: http://www.sseriga.edu/en/centres/csb/shadow-economy-index-for-baltics/

[35] Reynolds, K. L.; Haris, L. C.: *Dysfunctional customer behavior severity: an empirical examination,* Journal of Retailing 85(3) 2009, pp. 321-335

[36] Schneider, F.; Buehn, A.: Estimating the size of the shadow economy: methods, problems and open questions [online] [cited 10 November 2016] The Institute for the Study of Labor, 2013, retrieved from: http://www.economics.jku.at/papers/2013/wp1320.pdf

[37] Schneider, F.; Buehn, A.: Estimating the size of the shadow economy: methods, problems and open questions [online] [cited 10 November 2016] The Institute for the Study of Labor, 2016, retrieved from http://ftp.iza.org/dp9820.pdf

[38] Schneider, F.; Buehn, A.; Montenegro, C.: New estimates for the shadow economies all over the world, International Economic Journal 24(4) 2010, pp. 443-461

[39] Schneider, F.; Raczkowski, K.; Mróz, B.: Shadow economy and tax evasion in the EU, Journal of Money Laundering Control 18(1) 2015, pp. 34-51, http://dx.doi.org/10.1108/JMLC-09-2014-0027

[40] Shang, R.; Chen, Y.; Chen, P.: Ethical decisions about sharing music files in the P2P environment, Journal of Business Ethics 80(2) 2008, pp. 349-365

[41] Sirkeci, I.; Magnusdottir, L. B.: Understanding illegal music downloading in the UK: a multi-attribute model, Journal of Research in Interactive Marketing 5(1) 2011, pp. 90-110

[42] Smith, G. S.: Management models for international cybercrime, Journal of Financial Crime 22(1) 2015, pp. 104-125

[43] Šukytė, R.: Elektroninės komercijos vystymosi tendencijos Lietuvoje ir kitose ES šalyse [The tendencies of the development of electronic commerce in Lithuania and other EU states] [online] [cited 11 November 2015] Northern Lithuania College, 2010, retrieved from: http://www.slk.lt/studentukonferencijos/2010/articles/PDF/15_VVs_SLK_R.%20Sukyte.pdf

[44] The World Bank: Doing business [online] [cited 11 November 2016] World Bank Information Base, 2016, retrieved from http://www.doingbusiness.org/rankings

[45] Vlachos, V.; Minou, M.; Assimakopouos, V.; Toska, A.: The landscape of cybercrime in Greece, Information Management & Computer Security 19(2) 2011, pp. 113-123

[46] Waterman, D.; Ji, S. W.; Rochet, L. R.: Enforcement and control of piracy, copying and sharing in the movie industry, Review of Industrial Organisation 30(4) 2007, pp. 255-289

[47] Williams, C. C.: Evaluating the magnitude of the shadow economy: a direct survey approach, Journal of Economic Studies 33(5) 2006, pp. 369-385

[48] Williams, C. C.: Confronting the shadow economy: evaluating tax compliance behaviour and policies, 2nd ed., Edward Elgar, Cheltenham, 2014

[49] Williams, C. C.; Horodnic, I. A.: Evaluating the prevalence of the undeclared economy in Central and Eastern Europe: an institutional asymmetry perspective, European Journal of Industrial Relations 21(4) 2015, pp. 389-406

[50] Williams, P.; Nicholas, D.; Rowlands, I.: The attitudes and behaviours of illegal downloaders, Aslib Proceedings 62(3) 2010, pp. 283-301

[51] Yip, M.; Shadbolt, N.; Tiropanis, N.; Webber, C.: The digital underground economy: a social network approach to understanding cybercrime [online] [cited 28 October 2016] University of Southampton, 2012, retrieved from: http://eprints.soton.ac.uk/343351/4/yip_de2012.pdf

[52] Yu, C. P.; Young, M. L.; Ju, B. C.: Consumer software piracy in virtual communities: an integrative model of heroism and social exchange, Internet Research 25(2) 2015, pp. 317-334

The „Phantom" Delta Robot
A New Device for Parallel Robot Investigations

János Somló, Gábor Dávid Varga, Márk Zenkl, Balázs Mikó

Bánki Donát Faculty of Mechanical and Safety Engineering, Óbuda University,
Népszínház u. 8, H-1081 Budapest, Hungary
E-mail: somlo@uni-obuda.hu; miko.balazs@bgk.uni-obuda.hu

Abstract: A new device is proposed for parallel robot investigations. Basically, a robot with equilateral basic and working triangles, driving arm and parallelogram connection is considered, which is called Clavel's Robot. This device is constructed in a way that the sizes of elements may be changed in certain regions. In doing so, different robots can be realized with the reconfiguration of the same device and different accuracy, stiffness, compliance, and force characteristics, etc. can be studied. For example: accuracy maps can be prepared. Through changing the constructional elements (principle, shape, strength, etc.) the effect of these changes may be estimated. We remark that the Phantom Robot may be used not only for the investigation of Clavel's but also, proposed by us the General Triangle Parallel Robot.
The presented device is devoted to construction studies. Works can be extended further to the investigation of drives and controls. We considered it necessary to summarize, and give somewhat new directions, for the solutions of inverse and direct transformation problems.
The realized device proved very suitable. The rather simple and cheap measurements were realized at the usual university laboratory level. The first experiments proved a good performance.

1 Introduction

Parallel robots are more and more promising in the solution of recent application problems of robotics technology. Parallel robot applications own several outstanding features which make them more preferable than the use of serial robots:

- They are cheap compared to serial robots of the same class.
- The motors that move the parallel arms can be allocated together, on the same platforms, close to each other. Their relative positions have much less restrictions than the same for serial robots.
- The constructional elements of parallel robots are simpler than those for serial robots.

- The service is simpler, the replacements are cheaper.
- The solution of inverse and direct kinematics problems are of the same difficulty class as those for serial robots. That is, these can effectively be solved without any difficulty.
- Sometimes, parallel robots promise a better solution for special application tasks than the serial ones. Sometimes the solutions are, at least, equivalent.
- Frequently, the application of a parallel robot is easier than serial one.
- The force (moment) characteristics of the parallel robots are better than those for serial ones. This is due to the parallel actions of arms. For example, the static force acting on a serial arm can be distributed to three forces in parallel robot cases giving less deformation and providing more accuracy.

The present paper deals with the topic of the design of the parallel robots mechanical part. This part provides the basic task of manipulation of the objects by the machine elements and parts.

In this work the questions concerning the drives, the control systems, instrument units, etc., are not taken into consideration. Of course, the above aspects have significant effect on systems performances, but those are the topics of other investigations.

We proposed and built a so-called "PHANTOM" Delta Robot which makes it possible to investigate the practical performances of Delta robots in general, and which covers quite a wide class of possible robot constructions. We performed as much research and experimental investigations as possible with the help of the given device.

Concerning the history of parallel robots here we give only a short review. A rather detailed picture may be obtained from Bonev [3] and others. The intensive development of the Delta robots may be contacted with the works of R. Clavel [1, 2]. The Delta robot idea and the most popular constructions are those which are proposed in the above works.

Monograph of J.-P.Merlet [4] is a summary of most important results. A picture of how wide the choice of parallel robots is today can be obtained from the material provided by ParalleMIC (the Parallel Mechanism Information Center). Recently, more than 26 companies are producing parallel robots [3].

The constructions of the variants of the parallel robots are very wide. But the dominant variant is the Delta robot. This robot uses DC or AC servo driven motors rotating the thing-rods (motor arms) which move the (shin) parallelograms (or Cardan mechanisms) moving a point of the work triangles. The motors are mounted on the upper platforms (basic triangles). The parallelograms move the lower platform points (joints) to realize the working motions.

Development of the Delta robots began at the end of the 80s, during the last century. Solutions for the inverse and direct kinematics problems were found which were necessary for them to work. A number of publications are available regarding this topic. New, rather sophisticated results were obtained by Murray [5, 6]. Based on his results software for direct and inverse problem's solutions were developed which are widely available [7].

2 Constructionof the "Phantom" Robot

Figure 1 shows a Delta robot construction. This is very similar to the construction given in R. Clavel's US Patent description [1].

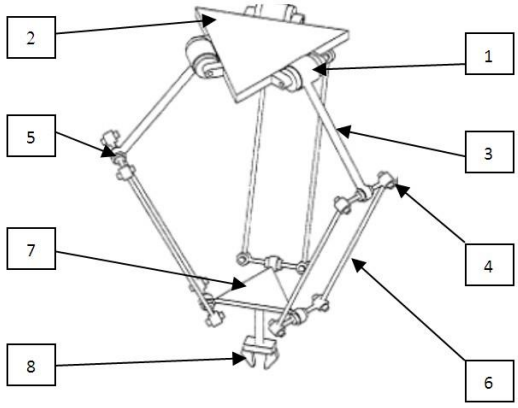

Figure 1
The Delta robot construction

Where:

1- the driving motor arm coupling joint
2- upper platform (basic triangle)
3- driving arm (thing-road)
4- Parallelogram joint
5- Driving arm, parallelogram joint
6- Parallelogram arm (shin)
7- Lower platform (working triangle)
8- Tool

In industrial Delta Robot constructions all the above elements have fixed quantities. In case of a presented device some of the mechanical elements may be easily changed. This device is named "Phantom Delta" robot. The device is designed by considering easy modification of shape and size. In the Phantom Robot many elements may have different and/or adjustable sizes. Figure 2 shows the adjustable elements of the investigated Phantom Delta robot. These elements are the distance of rotation point from the centre of basic triangle, the rotation arm lengths, and the distance of driven point on the working triangle from the centre of this triangle.

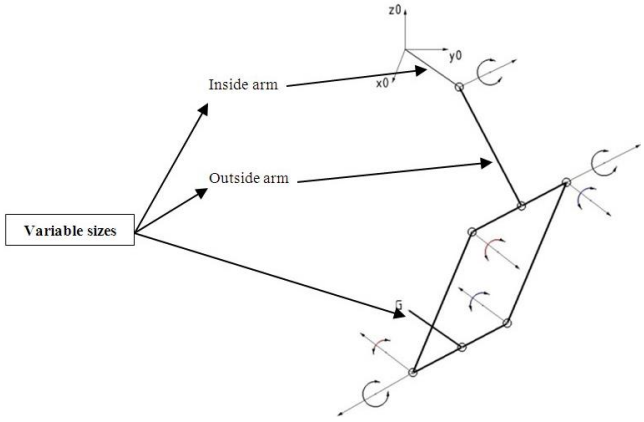

Figure 2
The adjustable elements of the „Phantom" Delta robot

In the present work the size of the parallelogram is kept constant. It has practical reasons (availability): in the future we plane to change the size of parallelogram, too.

The parameters of the Phantom Delta robot should be close to the same as of the robots intensively used in industry. For this goal the Table 1 was created to helpmake a proper choice.

Table 1
Robot arms sizes

	Insidearm [mm]	Outsidearm[mm]	Proportion
AdeptQuattro s650H	373	825	2,2
ABB FlexPicker IRB 360-1/1600	524	1244	2,4
FANUC M-1iA/0.5S	100	270	2,7
Fantom Delta Robot	**100-125-150**	**332**	**2,2-2,7-3,3**

The intensive research, development and design work in the field of parallel robots was reviewed in diploma work of M. Zenkl [8]. The Phantom Robot has been built according to the constructional schema shown in Figure 3.

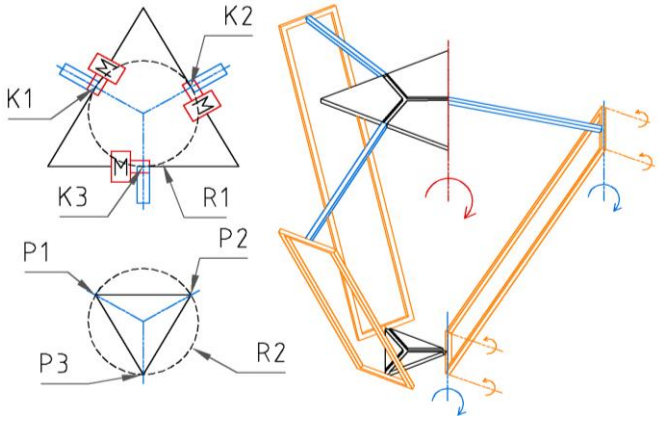

Figure 3
Constructional schema of the Phantom Robot

Where:

- K1, K2, K3 are the basic triangle driving arm rotation centres
- P1, P2, P3 are the working triangle joints rotation centres
- R1 is the driving arm rotation centres allocation radius
- R2 is the working joints centres allocation radius

In Zenkl's work [8], among others, the following problems were solved.

The basic triangle construction

After analysing a number of variants, a final version of basic triangle was developed. This is shown in Figure 4.

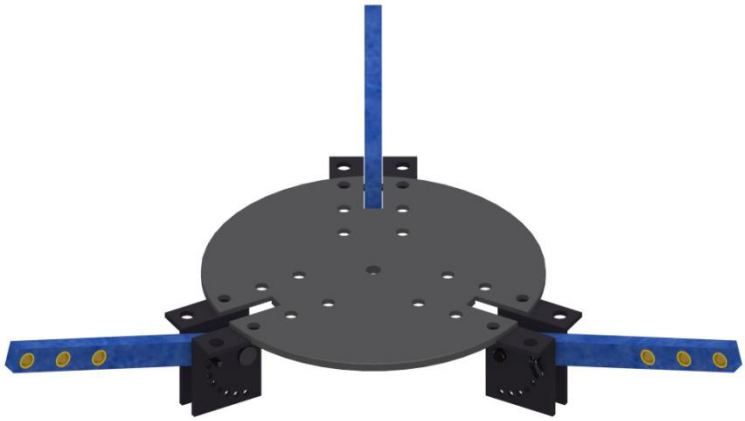

Figure 4
Basic triangle

Robot arm, parallelogram joints construction

Analysing a number of variants, the one on Figure 5 was accepted. A simple sliding bearing is applied made from bronze. Ball bearings and spherical joints were rejected. The given construction is very easy to implement. Nevertheless, it could be applied very effectively.

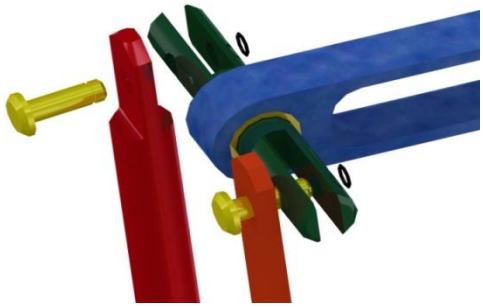

Figure 5
Driving arm, parallelogram joints

The working triangle joints construction

The working triangle joints were designed as shown in Figure 6. The parallelogram connections were produced as shown in Figure 5.

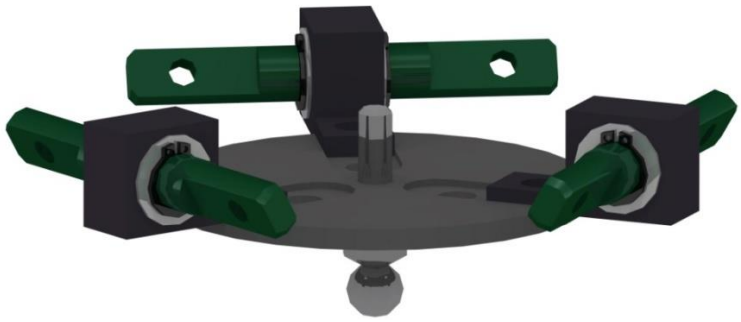

Figure 6
The working triangle joints construction

Elements fixing the driving arms in fixed position

The Phantom Delta Robot has no electrical drives. The arms are taken to some given position by hand and are fixed with bolts. With the given construction a discrete points realisation was chosen. As it is demonstrated in Figure 7, an element is introduced for each arm which has 7 holes located to realize a 15 degrees angle change. So, 7*7*7=343 position can be investigated.

Figure 7
Elements fixing the driving arms in fixed position

The presented mechanism was developed for estimating the opportunity of simple and effective build of Delta Type Parallel Robots. Namely, to analyse how the accuracy changes, force characteristics, etc. in function of geometric size. (Without developing a new robot) The way of realizing the above may be: accept robot parameter values which are the closest to the realized version of the Phantom Robot; solve the direct and inverse transformation problems. Then, compare the measurement results with the theoretical ones to get characteristics.

Below, a treatment of the direct and inverse transformation problems for Delta Robots will be given, slightly different in interpretation of the results from the published ones.

3 Inverse and Direct Transformation of Delta Robots

As it has been outlined in the Introduction the inverse and direct transformation problems for Delta robots are solved. Several variants of the solutions are available. Here, for the sake of completeness, we give some details of the approaches used in the present work.

3.1 Inverse Transformation

The task formulated for robot working process is usually formulated in the world coordinate systems. In the case analysed in the present work translation motions are considered. Three degree of freedom Delta robots are used.

The inverse transformation task is formulated in the way that three world coordinates values x_0, y_0, z_0, are given and the robot's joint coordinates values q1, q2, q3 realizing those are to be determined.

Let us allocate one of the parallel robot legs driving arm (central line) as is shown in Figure 8. That is, this central line coincides with axis y when the joint coordinate value q1 is zero. The axis z is allocated in point x=y=0. The positive direction of z is downward.

For more details we refer to Figures 2 and 3.

We use q1, q2 and q3 for the joint coordinates of the robots. These, are the motor driven arm's angular positions. The q1, q2 and q3 have zero values at the horizontal positions of the driving arms.

The Delta robot quantities necessary for inverse transformation are shown in Fig. 8.

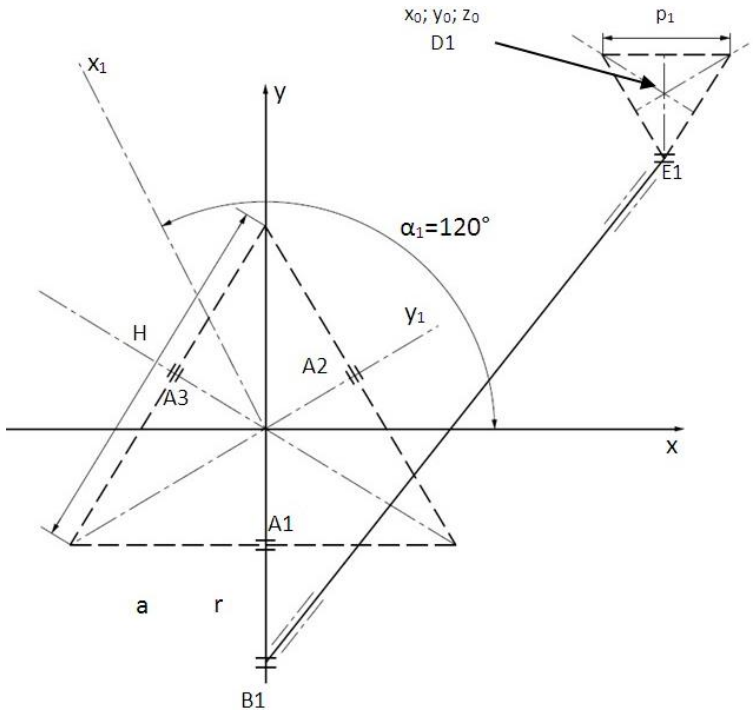

Figure 8
Robot arm quantities necessary for inverse transformation

Let us deal with the first arm. (Later the results will be extended to the second and third arms, too) This arm is allocated in the coordinates system as shown in Figure 8. The driving arm (central line) is in axis y. The axis of rotation of the driving arm there is in the point A1. This point's distance from the origin is "a". The arm rotation radius is "r". Point B1 is the arm-parallelogram rotation reference point. E1 is the parallelogram-working triangle rotation reference point. The length of the central line of the parallelogram is "d". The central point of the work triangle is D1. The distance D1E1=e.

The basic triangle size is "H", $a=\frac{\sqrt{3}}{6}H$.The working triangle size is "h", $e=\frac{\sqrt{3}}{3}h$.

According to Figure 8:

E1=(x0; y0 –e; z0).

The goal is to determine the B1 point coordinate values. Then, the solution of the inverse problem is:

$$q1 = \text{arctang}\frac{z_{B1}}{y_{B1}-y_{A1}} \quad (1)$$

The point B1 is the intersection of a circle in plane yz with centreA1 and with radius "r" and a sphere with centre E1 and radius "d".

That is:

$$(y_{B1}\text{-}y_{A1})^2 + (z_{B1}-z_{A1})^2 = r^2 \quad (2)$$

and

$$(x_{B1}-x_{E1})^2 + (y_{B1}-y_{E1})^2 + (z_{B1}-z_{E1})^2 = d^2 \quad (3)$$

Because

$x_{B1=0}$ and $x_{E1}=x_0$ ($y_{E1}=y_0-e$; $z_{E1}=z_0$)

$$(y_{B1} - y_{E1})^2 + (z_{B1} - z_{E1})^2 = d^2 + x_0^2 \quad (4)$$

Equation (4) is the equation of the circle in which the sphere crosses the yz plane.

Solving equations (2) and (4) (the solutions are the intersection points of the two circles) we obtain the solution of the inverse kinematics problem for the first arm.

(The determination of the crossing points of two circles is a simple task of elementary mathematics.)

This way of the solution of the inverse transformation problem is called the Two Circle Algorithm (TCA).

Concerning the other two arms, we call attention to the following. If we rotate the xy axes by angle α1, we reach a situation similar to the original, with the only difference that the allocation of the working point is related to the new axes change.

That is, the computations for the other two arms are exactly the same as for the first arm with the difference that instead of x_0, and y_0 new values x_1 and y_1 should be substituted ($z_1=z_0$).

Let us consider as second arm the one rotated by $\alpha 1 = -120^o$ in negative direction. The new x,y axes are indicated in Figure 7 as x1 and y1.

The x_1 and y_1 values may be obtained by homogeneous transformation as

$$\begin{pmatrix} x_1 \\ y_1 \\ z_1 \\ 1 \end{pmatrix} = \bar{\bar{H}}_{-\alpha 1} \begin{pmatrix} x_0 \\ y_0 \\ z_0 \\ 1 \end{pmatrix} \quad (5)$$

$$\bar{\bar{H}}_{-\alpha 1} = \begin{pmatrix} \cos(-120°) & -\sin(-120°) & 0 & 0 \\ \sin(-120°) & \cos(-120°) & 0 & 0 \\ 0 & 0 & 1 & 1 \\ 0 & 0 & 0 & 1 \end{pmatrix} \quad (6)$$

In the case of the third arm the approach is the same. The rotation is to: -240^o.

Based on the above one can get:

$x_1 = x_0\cos(-120°) - y_0\sin(-120°)$

$y_1 = x_0\sin(-120°) + y_0\cos(-120°)$ (7)

In similar manner

$x_2 = x_0\cos(-240°) - y_0\sin(-240°)$

$y_2 = x_0\sin(-240°) + y_0\cos(-240°)$ (8)

The Two Circles Algorithm (TCA) is demonstrated in Figure 9.

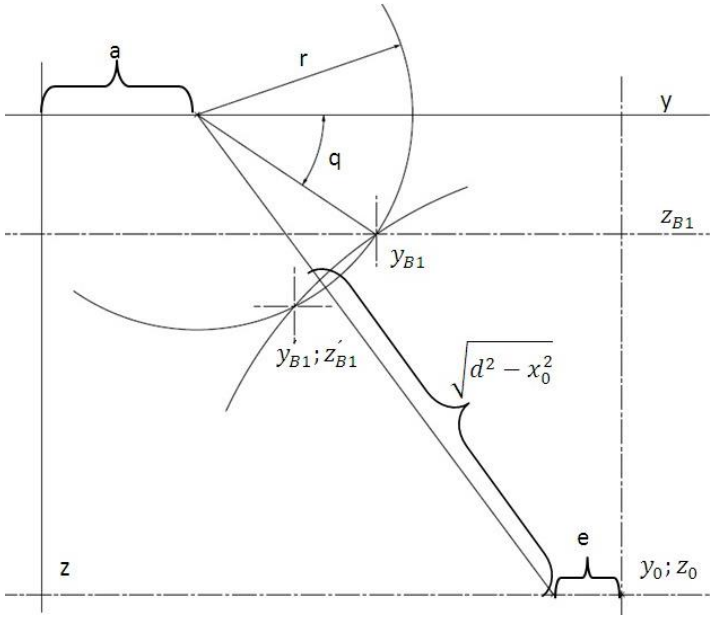

Figure 9
Demonstration of the Two Circle Algorithm

3.2 Direct Transformation

The solution of inverse problem makes it possible to solve motion planning problems and it has the most important role in application planning. The solution of direct kinematics problems may have importance in accuracy, force (moment) management, etc. problems.

As it was outlined in the above section the individual arms may be treated separately at the solution of inverse problem. The situation is different at the solution of the direct problem.

The direct transformation problem may be solved using the following idea.

Figure 10 (similar to those proposed by Williams [9]) shows that a virtual parallelogram may be introduced to each of the driving arms which allows to reduce the motions of the parallelograms working point straight to the working point of the robot. Point P may move only along a sphere with radius "d" around point "B" at any motion. Virtual points B1v, B2v, B3v are introduced in such a way that virtual parallelograms B*i*P*i*B*iv*D(i=1,2,3) are constructed. The B*i*B*iv* vectors are parallel with the PiD vectors (i=1, 2, 3). When looking for the solution of the direct kinematics problems we should consider points obtained by the motions of parallelograms central line end points (Pi) on a sphere with radius "d" which has the central point in Bi (i=1, 2, 3). At the same time points Di also move along a sphere with radius "d" and centre Biv. The solution of the direct kinematics problem is when the three arms have one common D1=D2=D3=D point. That is the solution is the common (intersection) point of the three spheres.

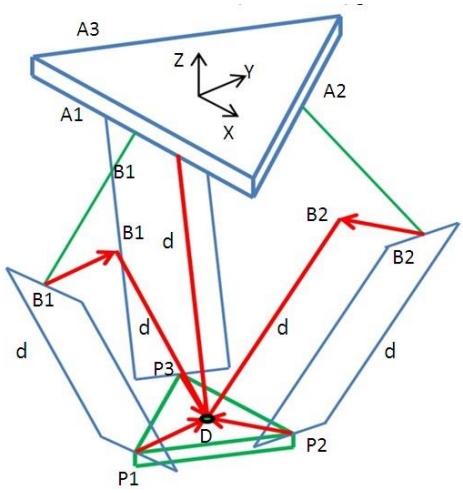

Figure 10
Direct transformation

Now, let us determine the coordinates of the virtual points B1v, B2v and B3v.

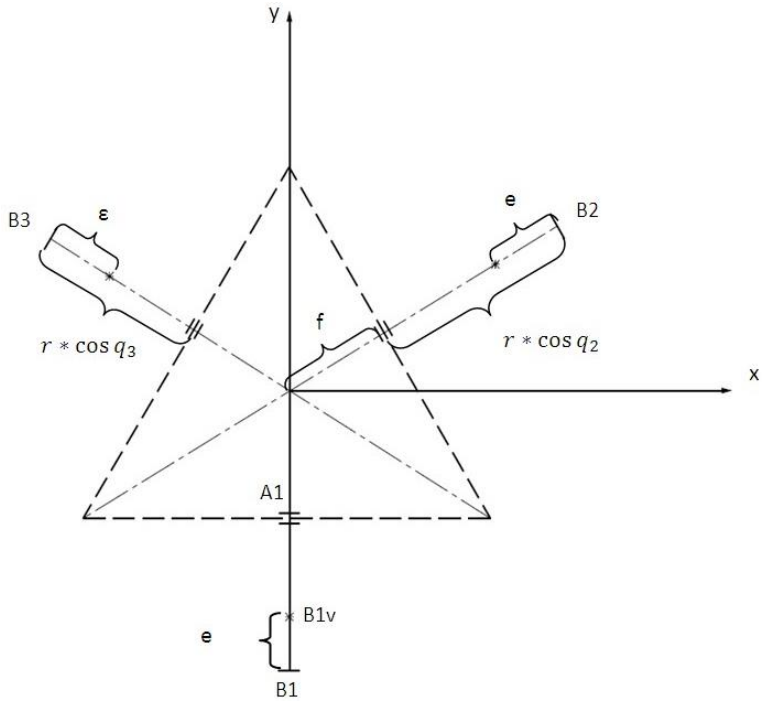

Figure11
Determination of virtual points

According to Figure 11:

$$\overline{B1}_v = \begin{pmatrix} 0 \\ -f - r * \cos q_1 + e \\ r * \sin q_1 \end{pmatrix} = \begin{pmatrix} x_{B1_v} \\ y_{B1_v} \\ z_{B1_v} \end{pmatrix}$$

$$\overline{B2}_v = \begin{pmatrix} (f + r * \cos q_2 - e) * \cos 30° \\ (f + r * \cos q_2 - e) * \sin 30° \\ r * \sin q_2 \end{pmatrix} = \begin{pmatrix} x_{B2_v} \\ y_{B2_v} \\ z_{B2_v} \end{pmatrix}$$

$$\overline{B3}_v = \begin{pmatrix} -(f + r * \cos q_2 - e) * \cos 30° \\ (f + r * \cos q_2 - e) * \sin 30° \\ r * \sin q_3 \end{pmatrix} = \begin{pmatrix} x_{B3_v} \\ y_{B3_v} \\ z_{B3_v} \end{pmatrix} \quad (9)$$

The three spheres equations are:

$$(x_0 - x_{\mathrm{B1v}})^2 + (y_0 - y_{\mathrm{B1v}})^2 + (z_0 - z_{\mathrm{B1v}})^2 = d^2$$

$$(x_0 - x_{\mathrm{B2v}})^2 + (y_0 - y_{\mathrm{B2v}})^2 + (z_0 - z_{\mathrm{BvV}})^2 = d^2$$

$$(x_0 - x_{\mathrm{B3v}})^2 + (y_0 - y_{\mathrm{B3v}})^2 + (z_0 - z_{\mathrm{B3v}})^2 = d^2 \quad (10)$$

The Equations should be solved for x_0, y_0, z_0.

The direct transformation problem may be solved by determining the intersection point of the three spheres $x_{0,}$ $y_{0,}$ $z_{0.}$. An algorithm for the solution is given in Williams [9].

The algorithm is named Three Sphere Intersection Algorithm (TSIA). This gives x_0 , y_0 , z_0 : having the data: $x_{Biv.}y_{Biv}$, z_{Biv} (i=1, 2, 3) and "d".

The solution of direct transformation task is:

- The robot hardware data are introduced (a, e, r, d; (a is the basic triangle side; f=$\frac{\sqrt{3}}{6}$a

  e=$b * \sqrt{3}$; b is the working triangle side).
- Having q1, q2, q3
- $x_{Biv.}y_{Biv}$, z_{Biv} (i=1, 2, 3) are determined according to Eq. (9)
- TSIA is applied
- x_0 , y_0 , z_0 is obtained

4 Investigations Using the Phantom Robot

A draw of the final version of the Phantom robot is given in Figure12. In the thesis work of Varga [10] a number of investigation studies are described, and some of the results are reviewed below.

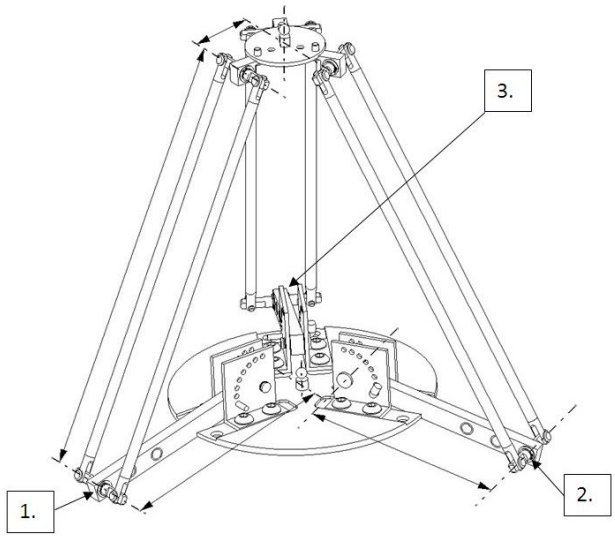

Figure 12
Accepted parameters

4.1 Accuracy Studies

The studies were directed to the investigation of accuracy and repetition. A construction variant was chosen characterized by data of Table 2.

Table 2
Sizes and accepted values for the computations

	a[mm]	**b**[mm]	**c**[mm]	**d**[mm]
1	39,98	332,32	209,74	149,62
2	39,05	332,55	213,54	149,14
3	39,51	331,9	215,122	149,16
Accepted values	39	332	205	149

Computation of the theoretical values of the working points was performed using the equations of the direct kinematics. The graphics of the working points are given in Figure 13.

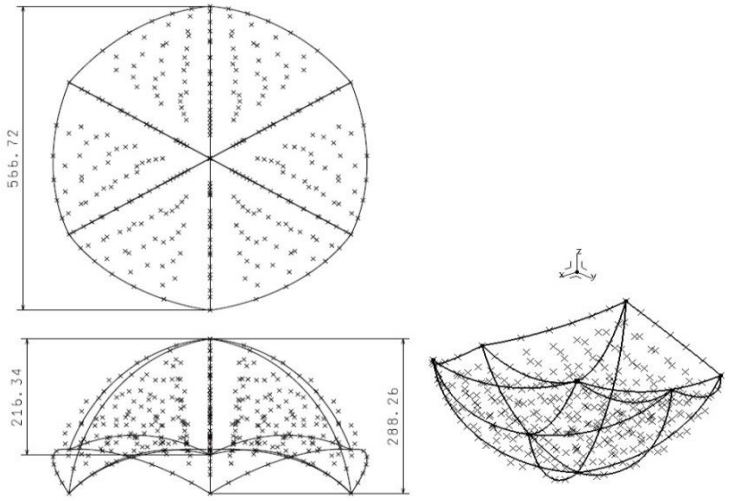

Figure 13
Working points

Besides the working points the work space is given on Figure 13, too.

We performed the measurement of all experimental points. We got pictures that were much similar to Figure 13 in shape. But for example the size 566,72 mm on computed picture was 530,12 mm. The same in measurement was 288,26 mm the "high's" of the computed was 273,72 mm.

The results are summarized in Figure 14, where on the horizontal axes the absolute value of accuracy is shown.

$$\Delta\epsilon = \sqrt{(\Delta x_\epsilon)^2 + (\Delta y_\epsilon)^2 + (\Delta z_\epsilon)^2}$$

The difference of the computed and measured values where: $\Delta x_\epsilon; \Delta y_\epsilon; \Delta z_\epsilon$

This diagram very well characterizes the accuracy of the device.

But these results are given only for the demonstration of investigation opportunities. This is only an example of showing that a certain robot configuration may result in inappropriate characteristics.

Changing the shapes the sizes, etc. similar measurements can be performed for better and better understanding of the parallel robot features.

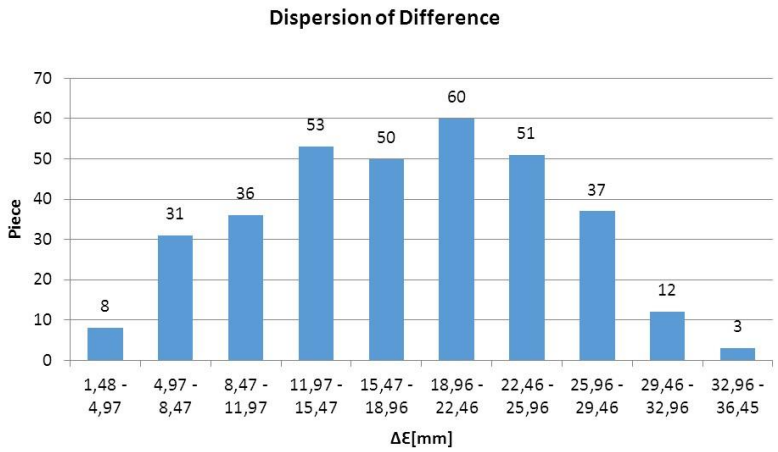

Figure 14
Dispersion of Difference

The investigations were performed using the coordinate's measurement machine of the measuring technology lab of Óbuda University. Photography of the phantom robot is shown in Figure 15.

4.2 The Use of Parallel Robot as Leg of Exoskeletons

In the above the accuracy of Phantom robot was analysed. It should be emphasized that the accuracy may be increased using very simple means. Nevertheless, there are applications where the provided accuracies are enough for satisfying the requirements. For example: the parallel robot can be used as one of the leg of exoskeletons. Such research is on at Óbuda University [11].

Figure 15
Measurement

5 Summary

The developed delta robot has variable size and no drive in order to investigate the geometric properties of different constructions. It was named Phantom Delta Robot. This made possible to investigate features not available for existing (in given construction) robots. This opens new ways to develop robots which are reconfigurable, accurate, stiff and compliant.

References

[1] Clavel, R. (1990) U.S. Patent No. 4,976,582. Washington, DC: U.S. Patent and Trademark Office

[2] Clavel, R. (1991) Conceptiond'un robot Parallelerapide 4degre's de Liberte. Ph.D. thesis EPFL Laussane, Switzerland

[3] Bonev, I. (2014) Delta Parallel Robot, The Story of Success, The Parallel Mechanisms Information Center, (http://www.parallemic.org)

[4] Merlet, J. P. (2012) Parallel robots (Vol. 74) Springer Science & Business Media

[5] Zsombor-Murray, P. J. (2004) Descriptive geometric, kinematic analysis of Clavel's "Delta" Robot; Centre of Intelligent Machines, McGill University

[6] Zsombor-Murray, P. J. (2009) An improved approach to the kinematics of Clavel's DELTA robot. Intelligent Machines, McGill University

[7] Marginally Clever Software (2012) Delta robot, Forward/InverseKinematics,www.marginallyclever.com/other/samples/fkik-test.html

[8] M. Zenkl, Design of Phantom Delta Robot Construction 2017, Budapest, BSc Thesis Work, Óbuda University

[9] Robert L. Williams II, Ph.D., The Delta Parallel Robot: Kinematics Solutions Mechanical Engineering, Ohio University, October 2016

[10] D. Varga, Fantom Delta Robot Precision Measurement 2017, Budapest, BSc Thesis Work, Óbuda University

[11] Somló J., Paniti I., Rudas I. (2016) Léptetőszerkezet humanoid robothoz (Stepping device for humanoid robots), Presented for Hungarian Intellectual Property Office, P1600241, unpublished

Predictive Power of the ZEW Sentiment Indicator: Case of the German Automotive Industry

Lubor Homolka, Drahomíra Pavelková

Tomas Bata University in Zlín, Faculty of Management and Economics, Mostní 5139, 760 01 Zlín, Czech Republic

homolka@fame.utb.cz, pavelkova@fame.utb.cz

Abstract: This paper presents an analysis of German automotive industry and its connection to the market sentiment indicator ZEW. The analysis spans a period of the last decade and is divided into Pre-Crisis, Crisis and Post-Crisis periods. Research questions related to the predictive power of ZEW indicator on macro level indicators (composite DAX and GDP), sector indicator (technology-oriented companies TecDAX) and a selected automotive manufacturer (BMW) were answered. We found that ZEW index had foreseen the economic crisis starting in the March 2008 three months ahead of its start, but failed to see an upcoming economic recovery. We fit two models to estimate whether ZEW index can be used as a standalone forecasting instrument or whether inclusion of lagged values of other variables improves forecasting ability. We conclude that predictions from the ZEW-only models are worse in the test sample than those of the more complex model. We provide further evidence in form cross-correlations and causality analysis in the Granger sense. The study concludes with Impulse Response Function analysis. This analysis found that reaction of TecDAX on change of ZEW is strongest amongst studied variables.

Keywords: market sentiment; automotive industry; ZEW; DAX; VAR; Granger causality

1 Introduction

To efficiently utilise all available information is amongst the most challenging tasks in any analytical process. Those who are uncovering the fundamental value of a company must be concerned about the complete environment in which a company operates. Although it's clear that companies operate within a sector and a general macroeconomic framework, there is no clear link between macroeconomic variables' effects on a single company's performance. Many factors, mostly idiosyncratic, complicate the problem. How fast change in CPI translates into a change of interest rates of some financial instrument that company uses? Idiosyncratic effects represent a significant problem as they hide

or completely neglect theoretical explanations and expectations. Creating a model based on a pool of similar companies, say, within an industry, to predict a single-company performance might work only in a limited way. This does not mean that single-company analysis is impossible. The analysis must be tailored to the specific case. There are approaches which mitigate this problem. For example, in the portfolio theory, idiosyncratic risks are removed through the process of diversification.

In this paper, an attempt of connecting a macro-level indicator to a single-company performance is made. Macroeconomic conditions are frequently described in terms of GDP growth, unemployment rate, inflation and other indicators. Peiró [1] highlights differences between macroeconomic research conducted in the US and in Europe. He concludes that changes in production and interest rates are the determinants of stock returns on the French, German and United Kingdom stock markets. These indicators explain about half of stock returns.

As a proxy the general economic condition can be also used as a latent indicator – market sentiment. Sentiment does not only reflect a current state of the economy but is also forward-looking.

For this paper, a macro-level indicator is considered an indicator of general economic conditions. We note that this is not exactly a fundamental analysis; as a proxy for company's performance are used stock price returns. In a real world, returns subject to many factors other than changes in fundamentals, such as speculative or inside trading. Moreover, given the rather low free float of European companies, the price of share might differ significantly in the case of full free float companies.

Finter et al. [2] divide sentiment measures to *implicit* and *explicit* sentiment proxies. *Implicit* proxies rely on market data. Baker and Wurgler [3] have developed composite indicator relying on six market variables: i) the total number of initial public offerings (IPO), ii) the average first-day returns of IPOs, iii) the dividend premium, iv) the close and fund discount, v) New York Stock Exchange turnover, and vi) the equity share in new issues. They adjusted this indicator by macroeconomic indicators to make the index comparable throughout the business cycle by regressing original sentiment values to the growth of industrial production, the real growth of goods and services growth. Shen at al. [4] expanded this model by adding total productivity, current inflation growth and market expectations, term and default premiums, aggregate market volatility and market excess returns and labour income growth. Lux [5] points to other less-frequent market indicators, such as the ratio of equity put to call trading volume or number of advancing to declining issues. A novel approach is provided in [6]. Sentiment indicator is decomposed to the rational (regression on economic indicators) and irrational parts. The irrational part contains residuals from the first regressions. Both parts have a predictive power on the near-term returns.

Survey-based indicators belong to the category of explicit proxie. Consumers and investors are being asked about their expectations related to either general economic conditions or stock index performance (market consensus released by rating agencies or other financial companies). ZEW Germany Expectation of Economic Growth Index (ZEW) belongs to the first category. ZEW index was chosen from available explicit proxies.

This paper aims to evaluate the forecasting power of ZEW. Last similar analysis was conducted by Spiwoks [7]. Our analysis is made on updated data sample ranging from 2005 to 2016. Time series are further divided according to the business cycle phases into three parts. We have designed two models which should provide a better estimation of the ZEW's predictive power. Predictive power is also assessed by Granger causality tests. First, is the simple model with only lagged explanatory variable of itself. The second model is the Vector Autoregressive model. We propose a dynamic prediction (rolling MSE) as the model's quality indicator.

2 Theoretical Framework

Companies operate in a larger framework described by macroeconomic or financial theory (e.g., Keynesian economics, Efficient market theory), represented by macroeconomic variables (e.g. inflation) and measured by macroeconomic indicators (e.g. Consumer Price Index). An information content of such indicators faces ongoing criticism for low validity and reliability. Researchers and practitioners are creating methodologies and tools to describe and summarise multidimensional nature of the reality [8]. From the practical side, some indicators, such as GDP growth, are usually released quarterly, while CPI is released on monthly basis.

Research directions of market sentiment can be categorised into two groups. The first concerns testing of theory. As Lux [5] states, under the Efficient Market Theory, publicly released sentiment measures should be reflected in the prices and should not, therefore, have any predictive power on prices. However, Lux also provides a literature review on "noise trader risks" which explains why some traders (non-fundamental traders) can make a profit in a long-term by following such indicators. The second group utilises sentiment as a predictor for other time-series or entity behaviour. This group relates to valuation and portfolio modelling. According to Baker and Wurgler [3, p. 1652] “market sentiment may cause systematic patterns of mispricing”.

Expected performance of any economy closely relates to the phase of the business cycle. Sentiment of market participants can provide another explanation why some companies and sectors exhibit different performance throughout the business cycle. Shen et al. [4] concluded that high-risk portfolios tend to earn more in the

low sentiment periods than low-risk portfolios. Reverse works in the high sentiment periods. Yu and Yuan [9] analyse behaviour of sentiment traders and test the mean-variance relation in different periods. They conclude that in the low-sentiment period expected market returns positively relate to the conditional variance. This does not necessarily hold true in the high sentiment periods when the relation is weak. Stambaugh et al. [10] analyses market-wide sentiment and its influence on mispricing of financial assets.

AsFinter, Niessen-Ruenz&Ruenzi [2] point, market movers can be retail or institutional investors. The first is more common in the US, whereas the latter in the UK or Germany. Transferability of research results can be problematic as the investors' responses to shocks differ. Behaviour of smaller market participants was analysed Chackley et al. [11]. Main source of the data was content of micro-blogging sites. They analysed relations between sentiment and stock price, volatility and traded volume on a short trading frame. Extensive literature review on application of text mining tools in market prediction was conducted by Nassirtoussi et al. [12]. They provide a deep discussion about approaches to non-traditional sources of data, such as social networks to assess an instantaneous mood of the market.

3 Methodology of Research

German automotive industry for the empirical study was selected. Germany was selected for (i) its developed financial market, (ii) availability of sentiment indicators and (iii) a high importance of automotive industry, which is a central topic of the project this paper contributes to.

3.1 Data Selection

This study deals with macro, sector and individual company performance and its relation to the sentiment indicator ZEW. Data was acquired from the period of 2005 to 2016. This period is divided into three periods: Pre-Crisis, Crisis (March 2008 - June 2009) and Post-Crisis.

GDP and composite DAX index were selected to track the general economy. The technological sector index TecDAX was selected from available indexes tracked by Deutsche Börse. Its performance is based on the performance of the 30 largest companies from the technological industry listed on the Frankfurt Stock Exchange. On the company level, car manufacturer Bayerische Motoren Werke AG (BMW) was chosen. Selection of companies is explained in a dedicated paragraph.

Germany went through the whole economic cycle during analysed period. Grey areas in Figure 1 indicate short Crisis period. Left window of Figure 1 tracks

development of BMW and Continental AG. Performance of both titles surpasses growth of the economy. The quarter growth of GDP [13], composite index DAX and TecDAXexhibit similar development. Time series were scaled to have index value 1 in 2005 as they differ in levels.

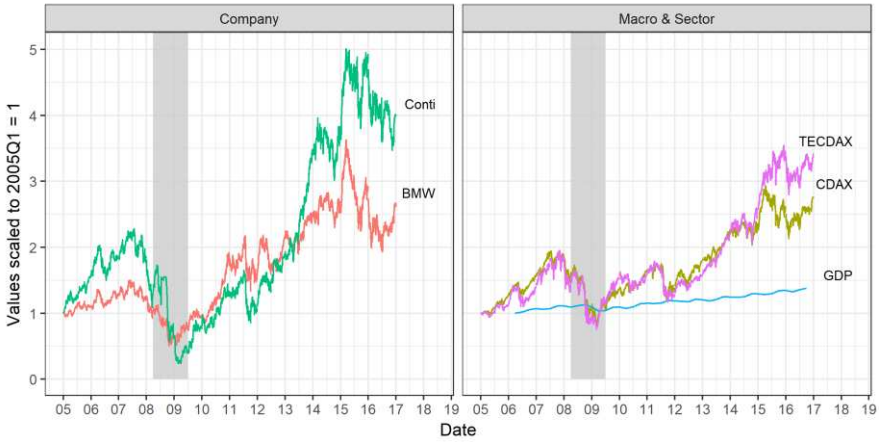

Figure 1
Development of performance of BMW, Continental AG, GDP, composite DAX and TecDAX.
Source: Own processing

In the initial research design, three car manufacturers were considered - BMW, Daimler (DAI) and Volkswagen (VOW). Looking at the development of the share prices we see a similar pattern in both BMW and Daimler. Three panels in Figure 2 reveal different paths of three major car producers throughout the analysed period. During the Crisis period Volkswagen (VOW) made a large acquisition and other changes in governance of the company which cannot be reflected in the general economic indicator immediately.

Volkswagen took a different path, especially during the crisis year. This was caused by extraordinary events, such as the acquisition by and of Porsche and following restructuring processes [14]. In the 2016 “Dieselgate” affair harmed the price, too. These company-related events would lead to unreliable outcomes as they cannot be depicted in the economic indicator designed to measure general condition. Therefore, we only analyse BMW in this paper. An inclusion of other sectors important for German’s economics, such as finance or energy, would require special treatment (such as seasonality adjustments), and is, therefore, omitted.

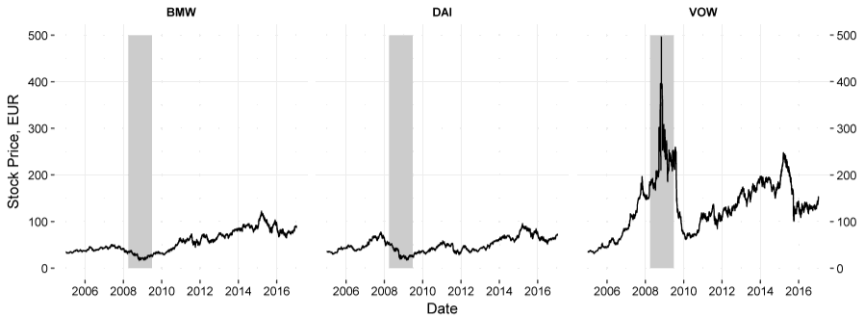

Figure 2

Development of stock prices of BMW, DAI and VOW during analysed period Source: Own processing

ZEW is a top-level indicator of expected Germany's economic performance. It is constructed as a composite indicator of views of 350 experts from various sectors. The experts are asked to express their opinions about general economic conditions during upcoming 6 months. Negative values indicate negative outlook. ZEW indicator is usually released in the middle of the month.

Huffner et al. [15] compared ZEW to other sentiment indicators, such as IfoExpectations. They concluded that for longer predictive horizons (3-12 month) ZEW-based models beat predictions of naive models and models based on the Ifo indicator. We consider the start of the foreseen three-months-period the first day of the month after the release.

We investigate whether sentiment index ZEW has had a good predictive power during the period 2006-2016. To assess the predictive ability, two research questions (RQ) were asked:

RQ 1: How did the ZEW Index predict BMW share price changes in the Pre- and Crisis periods?

RQ 2: How many false alarms did ZEW send to investors in the Post-Crisis period?

The first two research questions investigate whether ZEW index warned of Crisis before it had started and whether it predicted the end of the Crisis in time.

Next three research question focus on the Post-Crisis period and usefulness of ZEW as a standalone and complementary indicator in econometric models:

RQ 3: How good is a predictive ability of a model with only lagged ZEW values on DAX, TecDAX and BMW variables in the Post-Crisis period?

RQ 4: Does inclusion of lagged values of GDP, ZEW and modelled variable improve forecasting model (from RQ3) in the Post-Crisis period?

RQ 5: How does a change of ZEW value translate into the change of DAX, TecDAX and BMW values in the Post-Crisis period in the extended model from RQ4?

To answer the RQ1, visualisation of ZEW values and price returns computed using Equation 1 will be done. An indication of a good predictive power would be if combinations of ZEW values and returns with the same sign appear more often than combinations with mismatching signs.

Visual representation of time series may provide important insight although it does not provide any inferential test. It is, however, possible to assess predictive ability by looking at confusion matrix which summarises combinations of growth expectations and true values of growth. This approach was used by [16] in a 2x2 contingency table case (up-down) and further expanded in [17] to 4x4 case (Peak-Through-Upward-Downward tendency). Given the limited number of observations in the "Crisis period" Fisher Exact test was used to assess predictive power. Monte Carlo simulation with 2000 replications will be performed to estimate p-value. ZEW indicator will have a predictive ability if the positive association is found. RQ2 will be answered from the 2x2 confusion table described above.

Price analysis is based on logarithmic daily returns defined as:

$$\boldsymbol{R_t} = \ln(\boldsymbol{P_t}) - \ln(\boldsymbol{P_{t-1}}) \tag{1}$$

Difference between P_t and $P_{t-1}$is 1 trading day. Maximum difference between two trading days was 6 weekdays.

For the predictive model suggested in the RQ4 we use indicators that are released monthly. GDP, which is released quarterly, was smoothed by third polynomial spline to interpolate missing values. This imputation introduces autocorrelated values, which will be handled later in the Vector Autoregressive model.

Two models will be fitted and the predictive ability will be assessed by comparing mean squared error (MSE) on the test sample. Models will be trained on the period 7/2008 – 12/2015 + month ω. Prediction will be computed on the period 12/2015 + month ω to 12/2015 + month ω + p. Average value of the MSE values on all predicted periods will decide the model's quality. We have 12 growth values to be predicted in 2016. If the best model has$p = 3$ we will have first MSE for period 1/2016 – 3/2016. The second model will be trained on data from 7/2008 – 1/2016 and predictive period on which second MSE will be computed is 2/2016 – 4/2016. Best model will be found as an average of 10 MSE values.

First model (RQ 3) is a lagged model of form:

$$\boldsymbol{y_t} = \boldsymbol{\alpha_0} + \boldsymbol{\alpha_1 x_{t-1}} + \cdots + \boldsymbol{\alpha_p x_{t-p}} + \boldsymbol{\epsilon_t} \tag{2}$$

Where$y_t$is a value of an endogenous variable. As stated in RQ3, those endogenous variables will be DAX, TecDAX and BMW. For each variable a separate model will be created.

Second model (RQ 4) will take a form of Vector Autoregressive Model (VAR). Matrix representation of the model:

$$\mathbf{y_t} = \mathbf{v} + \mathbf{A_1 y_{t-1}} + \mathbf{A_p y_{t-p}} + \mathbf{D} + \boldsymbol{\epsilon_t} \quad (3)$$

where y_t is a $m \times 1$ dimensional random vector of m variables. A_k are coefficient matrices for $k = 1, \dots, p$ of size $m \times m$. Matrix D contains seasonal dummy variables multiplied by corresponding seasonal coefficients. To test RQ4 we select ZEW, GDP and one of DAX, TecDAX or BMW variables. Therefore, in our model $m = 3$. [18]

A value of maximum lag$p$ will be estimated automatically by optimisation rule based on AIC as described in [19]. Theory-based selection might not lead to the best predictive model. This does not represent a problem as RQ4 asks about prediction and is not concerned about real-world meaning of the parameters.

Correlations between variables will be analysed by means of cross-correlation up to lag ± 12 ($\pm$one-year period). Statistical testing of correlations is highly influenced by the underlying nature of the time series. The analysis will be done on detrended values. Time series can be considered as independent if the cross-correlations are centred around lag 0. [20]

Predictive power will be used to assess causality of time series on another in the Granger's sense (whether an addition of predictor's lagged values in addition to lagged values of original series improves predictions). As some of the original time series are non-stationary, an adjusted version of the Granger test based on Wald's test developed by Toda and Yamamoto [21] will be computed.

Effect of change of endogenous variable (RQ 5) in the model from RQ 4 will be estimated by Impulse Response Function (IRF). IRF measures reactions of modelled variables on the change of the selected variable over the $t + j$ predictive horizon. IRF is used to estimate response reaction only. It shall not be interpreted as a cause-effect analysis as a change of ZEW does not affect change of BMW prices or GDP growth.

To ensure that VAR model is estimated correctly and the IRF is meaningful, time-series will be transformed to be covariance-stationary. Augmented Dickey-Fuller test will be used to test for the presence of stochastic trend (unit root). Tests will be conducted for in three settings, i) unit root tests only, ii) unit root and bias (drift) test and iii) as a combination of unit root, bias and trend.

4 Results

To answer the RQ1 Figure 3 was constructed. In this figure the relation between values of ZEW index and mean values of returns is depicted. Mean value is computed on the three months period starting after the ZEW value is released. To emphasize varying uncertainty of the daily returns, point size shows standard deviation of returns in the corresponding period. Larger size means higher uncertainty as the prices were more volatile.

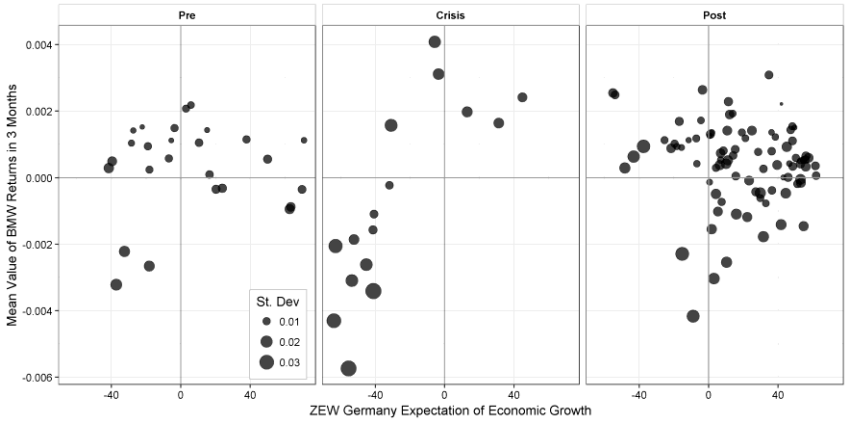

Figure 3

Three windows contain scatter plots of ZEW-Returns variables. Source: Own processing

Visual inspection reveals that lower ZEW values are associated witha higher variance of returns. Table 1 summarises expected direction of BMW's returns in the period of positive/negative ZEW value. There were 13 months with positive ZEW values in the Pre-Crisis period. Out of those releases, 8 following three months periods resulted in positive growth. Conversely, there were 13 months with negative ZEW figure but in 10 months turned to have positive returns. This error represents an upside risk. It expresses higher pessimism of the general market conditions than the actual performance of the stock price.

This erroneous evaluation during the Pre-Crisis period can be attributed to the foreseen crisis. As can be seen from the Figure 4, an expectation of BMW price drop was wrongly timed. The first point in Figure 4 labelled as 2006 corresponds to the late December value of 2005 and is considered as a starting value for the first year. The first point after 2006 summarises values achieved in January 2006 or in the period starting from January (bottom panel). Inspection of the upper panel of monthly returns does not provide much evidence for price-drop in the Crisis period. Returns oscillated around value 0. Reading the second panel, ZEW started losing from February 2006 on the value 69.8. Such a high value was not reached since then.ZEW rose for the first time after ten months in December 2005, when it was already in negative values. Despite the sharp rise in 6 consecutive months in the Crisis period, only in three months positive returns were achieved (top panel). Yet, average returns on the three months predictive window were all positive (bottom panel). When the ZEW reached local maximum in May 2007, future returns were below zero. Since this time to one month before Crisis period, ZEW was steadily decreasing and returns we rather negative across the period. Lowest values of returns were not predicted at all as they occurred in the same month ZEW was released (see the lowest values of the first and second panel).

Table 1
Prediction of the returns' trend in relation to absolute value of ZEW in the Pre-Crisis, Crisis and Post-Crisis periods

	ZEW					
	Pre-Crisis		Crisis		Post-Crisis	
Returns	Negative	Positive	Negative	Positive	Negative	Positive
Negative	3	5	10	0	2	22
Positive	10	8	3	3	16	47

Source: Own processing

Although ZEW started growing since November 2008, the first value indicating positive market sentiment has appeared in April 2009. By this time, monthly returns were positive, so the future returns. If the analyst would not be interested only in the absolute value, but also about the rate of change of ZEW, future positive returns in the upcoming recovery would be discovered sooner. From the economic perspective, positive change in negative ZEW values is a sign of improvement but should be interpreted as the negative consequences will bear lower costs than in the previous period. However, it still talks about expected costs rather than profit. BMW recovered faster than ZEW expected, as the last six points in the bottom window of Crisis period confirm (from those only three months reached positive ZEW values). These results show that ZEW index warned before declination of prices, but (perhaps) too early and did not recognise the price recovery. In the After-Crisis period, ZEW valueswere mostly positive, except of two periods in the end of 2012 and second quarter of 2013.

Formally, three Fisher tests were performed. Inconclusive results were reached in the Pre-Crisis period (sample odds-ratio of $t = 0.493$ on the sample size 26 values is not strong evidence enough to reject null of true odds $\theta = 1$ which indicates no association (p-value is 0.678). In Post-Crisis period $t = 0.27$, p-value=0.1363). Since there is a cell in the confusion matrix in the Crisis period which contains 0 combinations, odds ratio of the sample is not computed. We can, however, provide a p-value, which is derived from marginal sums. This p-value=0.0357 leads to rejection of the null hypothesis on standard $\alpha = 0.05$ level.

Qualitative analysis in Table 1 answers the RQ2. Contingency table suggests that 3 months ahead predictive power was reasonably strong in the Post-Crisis period. From the 63 periods with positive returns, 47 (75%) reference ZEW values were positive. Remaining 25% represent False alarm rate. Economic conditions were expected to be negative while the returns in the forecasted period were positive.

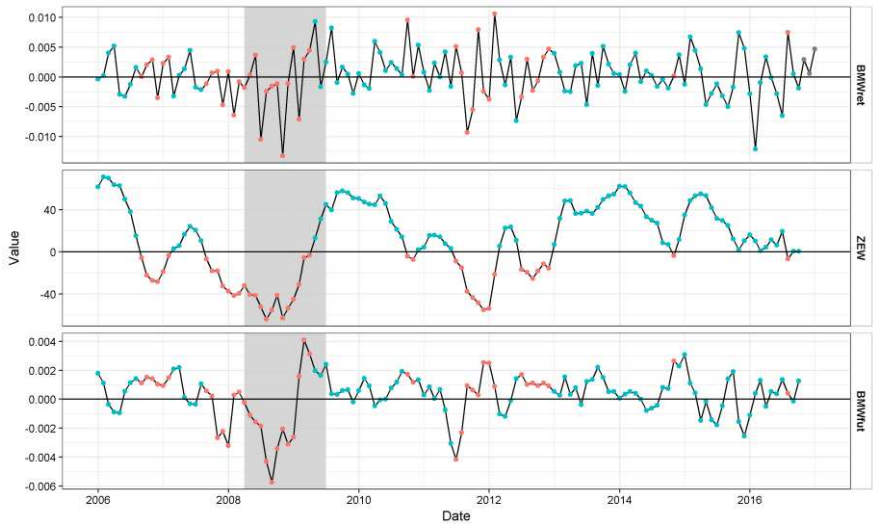

Figure 4

Three windows provide comparison of monthly returns (upper), ZEW value and mean value of future returns (bottom). Colour of the point indicates whether ZEW value was positive. Source: Own processing

Another perspective on usefulness ZEW indicator provides single-variable model defined in Equation 2. Model was estimated on integrated data to allow comparison of VAR models' MSE. These models need to be estimated on stationary times series as the IRF was computed in the last step. To achieve the stationarity, first differences were computed, see Figure 5. Visual inspection suggests that TecDAX is heteroscedastic. This might negatively affect predictive ability of the VAR model.

Stationarity was checked by ADF test with lag up to 3 months. Results of τ, the test statistics of unit-root stationarity, are provided in Table 2. Tau values indicate whether integrated time series do not contain a unit root. Stochastic trend column contains results of ADF test which was based on lag one value. The last column identifies whether time series is stationary after drift and trend are removed. In all differenced time series drift and trend were missing. The last row presents critical values for test on the given the time series length.

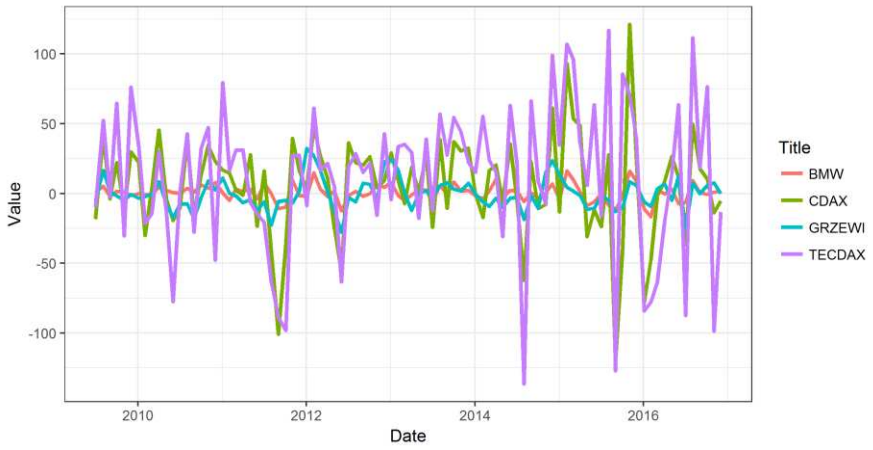

Figure 5

Values of differenced time series. Values of TecDAX are more volatile in the end of the analysed period. This might negatively affect predictive ability of the variable. Source: Own processing

Table 2

Results of ADF test. Presence of stochastic trend (unit root test), drift and deterministic trend was tested

	Lag	Unit root (UR)	UR+Drift	UR+Drift+Trend
TecDAX	1	-5.13	-5.53	-5.57
	2	-3.85	-4.22	-4.26
	3	-3.56	-3.92	-4.00
CDAX	1	-7.43	-7.68	-7.63
	2	-5.49	-5.79	-5.76
	3	-4.47	-4.75	-4.72
BMW	1	-7.85	-7.89	-7.97
	2	-6.11	-6.18	-6.33
	3	-5.27	-5.36	-5.54
GRZEWI	1	-5.07	-5.06	-5.03
	2	-5.28	-5.26	-5.24
	3	-5.14	-5.13	-5.11
Crit. Val 5 pct		-1.95	-2.89	-3.45

Source: Own processing

Figure 6 shows predicted values of the single model with $p = 3$. As expected, the worst performance was achieved on TecDAX index which has the highest variability in the training sample. Data points are scattered manually on to demonstrate differences on forecasted models in both plots. These models were identified on different sample sizes, depending on the valueω.

All predicted time series were mean-reverting. Model which utilised only one lagged value as a predictor performed the best on the DAX series. This can be seen in Figure 6 where the predicted values are copying the latest development of the time series, change of DAX. In case of TecDAX lagged values turned to have only a limited predictive power and the forecasting trajectory fluctuates around long-term mean value of change.

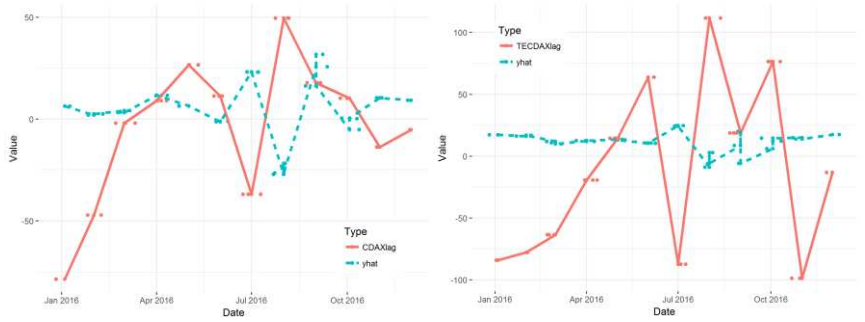

Figure 6

Predicted values from simple lagged model. Dashed lines are predictions based on the past data of lag 3. Solid line shows real value of time series. Composite DAX and Technological DAX are plotted. BMW is not plotted as shows similar pattern as TecDAX. Source: Own processing

Relation of ZEW to other time series is described by cross-correlation plots (with 5% significance bounds). This analysis was conducted on the Post-Crisis period due to the data availability.

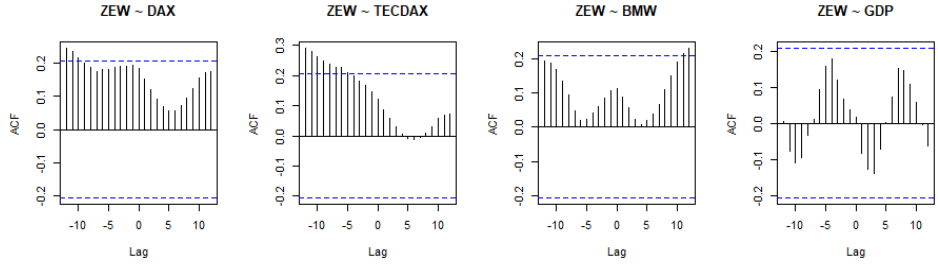

Figure 7

Cross correlations spanning periods of 24 months. Although DAX and TECDAX exhibit similar growth patterns throughout the whole Post-crisis period, shape of correlogram differs. Source: Own processing

Symmetry (based on visual inspection) in the windows of Figure 7 is reached only in case of BMW. If the ZEW takes above average values, BMW tends to have above average returns 12 months later. For both DAX and TECDAX ZEW is a leading indicator. Statistically significant lags start near the lag 6. This corresponds with the aim of the ZEW indicator to capture future trends occurring half a year after issuing. In the last window, ZEW and GDP exhibit a strong

seasonal pattern. This confirms our decision to include seasonal dummy variables in VAR models.

Granger test based on the Wald test with an adjusted number of parameters [21] were conducted on models with two variables. Tests were conducted for all pairs of variables with the lag length of 3 and 6 months and with the option of monthly seasonality. ZEW does not Granger-cause (and is not Granger-caused) by any variable except GDP. The strongest evidence is for GDP granger causes ZEW on the 3 months lag model ($\chi^2 = 11.85$, p-value=0.01) and ZEW is Granger causing GDP on the 6 lags ($\chi^2 = 15.16$, p-value=0.02).

Whether the inclusion of lagged values of GDP and a dependent variable itself improves predictive power was investigated by using VAR model, specified in Equation 3. For all VAR models lag $p = 1$ minimised information criterions. Such parsimonious models were more successful than long-lagged models. The quality of forecasts is in Table 3. VAR models were more accurate than simple univariate models. Trailing MSE of a simple model was about 14% higher in the DAX and 17% in the TecDAX case. Interestingly, simple model outperformed VAR in the BMW series. Values in the table refer to an average value of test-sample MSE on updated models. Value of BMW is substantially lower due to different scale [EUR], whereas DAX and TecDAX are measured in points.

Table2

Comparison of prediction quality on the test sample

	Simple lag model (RQ:2)	Vector Autoregressive Model (RQ:3)
DAX	1486	1304
TecDAX	5755	4913
BMW	55	58

Source: Own processing

Table presented above does not convey the whole message. It only evaluates distance from point estimate to the actual values. Following figure contains a probabilistic assessment of a predictive uncertainty in fan charts [22]. The darkest line is a point estimate similar to those that were computed above. The difference is that point estimates in Figure 8 are computed on the whole training period and on the predictive horizon of 12 months. In the detailed analysis, VAR model was re-estimated when new information about remaining two indicators appeared. Moreover, predictive horizon was set to 3 months. All figures revert to the mean value of the integrated time series. As expected, time series with higher volatility has wider 90% intervals.

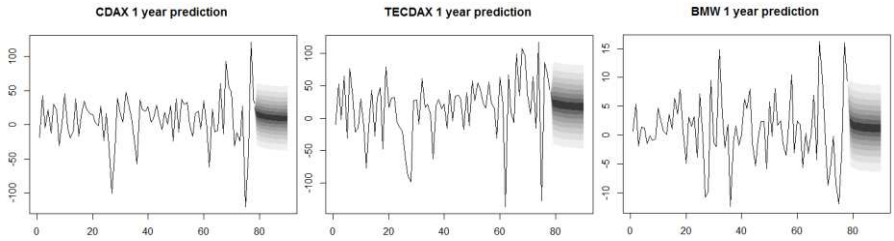

Figure 8

Estimated values of change in the last 12 months. This forecast covers the whole test period. Range covers interval with probability 0.1 to 0.9 (lightest range). Source: Own processing

Outcomes of Impulse Response functions are shown in Figure 9. All variables follow a similar pattern. There is a large change in the first month after the ZEW index is increased. The largest shock is caused to technological companies. Usually, when ZEW increases, TecDAX is increasing by 21 points in the first month. This ZEW's change is also associated with changes in following months, but with the lower magnitude.

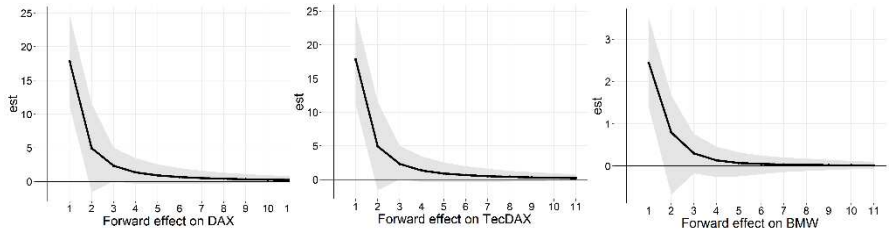

Figure 9

Plots of IRF functions for DAX, TecDAX and BMW (grey area indicates 95% confidence interval of the forward effect). Source: Own processing

Discussion and Conclusions

Five research questions were asked to analyse predictive power of selected sentiment. Answer to *RQ1* revealed that ZEW index warned before declination of prices, but (perhaps) too early. On the other hand, ZEW failed to recognise price recovery in time. Both outcomes are based on absolute value of ZEW. If analysis of changes would be considered, forecasters would discover changing momentum earlier for future returns declinations and recoveries.

RQ2 aimed at predictive power in the Post-Crisis period. Although returns of BMW were positive in 73% of all forecasting periods, relying on ZEW would lead to losses caused by both expecting better market conditions (in 31% of all cases when ZEW presented positive outlook). Performance of ZEW indicator as a standalone predictor has improved in the Post-Crisis period compared to previous periods. False alarm rate reached 25%. One third of three-month forecasted periods were expected to be negative, but BMW price returns were positive.

RQ3 concerned simple univariate models with lagged values. As the best performing models were identified models with lag 1. The importance of lagged variable differed. Its importance in composite DAX time series was higher than in remaining two.

Sentiment indicator ZEW can be considered as a good predictive indicator when accompanied by other indicators, such as lagged values of GDP. Although ZEW indicator is designed as 6 months-ahead indicator, it showed good classification accuracy of the trend direction in the Crisis period on the3-months prediction window. As assigned in *RQ4*, we have quantified the performance difference. Our setup on the rolling MSE on the test sample of the year 2016 showed that in market indexes VAR model outperformed univariate lagged model on the test sample. This does not apply to BMW returns where training MSE was almost identical. Although VAR model is more accurate, provided predictions are quite uncertain. This uncertainty was visualised in fan charts. The price volatility of BMW resulted in the widest range of predictive intervals relative to the scale.

An answer to the last research question *RQ5* provided a sensitivity analysis of shocks in time series. We see diminishing effect of shocks over time in all series. The largest shock is caused to technological companies. Shock in ZEW is associated with changes in other variables for upcoming 3-4 months. This is consistent with design of ZEW indicator which foresees economic sentiment in a short term.

This study has several limitations. Proposed models necessarily suffer from an omitted variable problem as they were intended to demonstrate the usefulness of ZEW indicator. More sophisticated models can be constructed by including more time series and implicit sentiment indicators, interactions or better error-variance handling. For the future research, other sentiment indexes, sectors and companies might be considered.

Acknowledgement

The authors are thankful to the Czech Science Foundation (GA CR), project No. 16-25536S: “Methodology of Developing a Predictive Model of Sector and Company Performance in the Macroeconomic Context”, for financial support of this research.

References

[1] Peiró, A. (2016) Stock prices and macroeconomic factors: Some European evidence. *International Review of Economics & Finance*, 41, 287-294. doi:10.1016/j.iref.2015.08.004

[2] Finter, P., Niessen-Ruenzi, A. &Ruenzi, S. (2012) The Impact of Investor Sentiment on the German Stock Market. *Zeitschriftfür Betriebswirtschaft,82*(0), 133-163, doi:10.2139/ssrn.1650164

[3] Baker, M. & Wurgler, J. (2006) Investor Sentiment and the Cross-Section of Stock Returns. *The Journal of Finance, 61*(4), 1645-1680. doi:10.1111/j.1540-6261.2006.00885.x

[4] Shen, J., Yu, J. & Zhao, S. (2017) Investor sentiment and economic forces. *Journal of Monetary Economics, 86*, 1-21. doi:10.1016/j.jmoneco.2017.01.001

[5] Lux, T. (2010). Sentiment dynamics and stock returns: the case of the German stock market. *Empirical Economics, 41*(3), 663-679, doi:10.1007/s00181-010-0397-0

[6] Verma, R. & Soydemir, G. (2006) The Impact of U.S. Individual and Institutional Investor Sentiment on Foreign Stock Markets. *Journal of Behavioral Finance, 7*(3), 128-144. doi:10.1207/s15427579jpfm0703_2

[7] Spiwoks, M. (2004) Die Verwendbarkeit der ZEW-Aktienindex-Prognosenfür active Portfoliomanagement-Strategien / The Usefulness of ZEW Stock Market Forecasts for Active Portfolio Management Strategies. *Jahrbücher fü rNationalökonomie und Statistik, 224*(5) doi:10.1515/jbnst-2004-0503

[8] Zhong, X., &Enke, D. (2017) Forecasting daily stock market return using dimensionality reduction. Expert Systems with Applications, 67, 126-139, doi:10.1016/j.eswa.2016.09.027

[9] Yu, J. & Yuan, Y. (2011) Investor sentiment and the mean–variance relation. *Journal of Financial Economics, 100*(2), 367-381, doi:10.1016/j.jfineco.2010.10.011

[10] Stambaugh, R., Yu, J. & Yuan, Y. (2012) The Short of It: Investor Sentiment and Anomalies. *Journal of Financial Economics* (104) 288-302, doi:10.1016/j.jfineco.2011.12.001

[11] Checkley, M., Higón, D. A., &Alles, H. (2017) The hasty wisdom of the mob: How market sentiment predicts stock market behavior. *Expert Systems with Applications*, 77, 256-263, doi:10.1016/j.eswa.2017.01.029

[12] Nassirtoussi, A. K., Aghabozorgi, S., Wah, T. Y., & Ngo, D. C. (2014) Text mining for market prediction: A systematic review. *Expert Systems with Applications*, 41(16), 7653-7670, doi:10.1016/j.eswa.2014.06.009

[13] Germany GDP, Current Prices: Eurostat, Gross Domestic Product for Germany© [CPMNACNSAB1GQDE] retrieved from FRED, Federal Reserve Bank of St. Louis; https://fred.stlouisfed.org/series/CPMNACNSAB1GQDE, Febr. 17, 2017

[14] Akpinar, M. & Vincze, Z. (2016) The dynamics of coopetition: A stakeholder view of the German automotive industry. *Industrial Marketing Management, 57*, pp. 53-63, doi:10.1016/j.indmarman.2016.05.006

[15] Hüfner, F. P., &Schröder, M. (2002) Prognosegehalt von ifo-Geschäftserwartungen und ZEW-Konjunkturerwartungen: EinökonometrischerVergleich / Forecasting German industrial Production: An Econometric Comparison of ifo- and ZEW-Business Expectations. *Jahrbücher für Nationalökonomie und Statistik,222*(3) doi:10.1515/jbnst-2002-0303

[16] Schnader, M. H. &Stekler, H. O. (1990) Evaluating Predictions of Change. *The Journal of Business, 63*(1), 99-107, doi:10.1086/296486

[17] Tsuchiya, Y. (2016) Do production managers predict turning points? A directional analysis. *Economic Modelling, 58*, 1-8, doi:10.1016/j.econmod.2016.05.019

[18] Pfaff, B. (2008a) *Analysis of integrated and cointegrated time series with R*. New York: Springer, doi:10.1007/978-0-387-75967-8

[19] Pfaff, B. (2008b) VAR, SVAR and SVEC Models: Implementation Within R Package vars. *Journal of Statistical Software, 27*(4) doi:10.18637/jss.v027.i04

[20] Dean, R. T., & Dunsmuir, W. T. (2015) Dangers and uses of cross-correlation in analyzing time series in perception, performance, movement, and neuroscience: The importance of constructing transfer function autoregressive models. *Behavior Research Methods*, 48(2), 783-802, doi:10.3758/s13428-015-0611-2

[21] Toda, H. Y., & Yamamoto, T. (1995) Statistical inference in vector autoregressions with possibly integrated processes. *Journal of Econometrics*, 66(1), 225-250, doi:10.1016/0304-4076(94)01616-8

[22] Britton, E., Fisher, P., & Whitley, J. (1998) The Inflation Report projections: understanding the fan chart. *Bank of England Quarterly Bulletin*, 38:30-37

Wavelet-based Optimization of Surface Reconstruction

Péter Kocsis, Petra Balla and Ákos Antal

Department of Mechatronics, Optics and Mechanical Engineering Informatics,
Budapest University of Technology and Economics
Műegyetem rkp. 3, 1111 Budapest, Hungary

E-mail: petra.balla@mogi.bme.hu, antal.akos@mogi.bme.hu

Abstract: By the development of artificial Intelligence – whether unintentionally – we are constantly trying to mimic the human senses. Biomimicry, as the starting point, is an engineering approach to emulate nature's well working patterns and strategies. Our goal is to create a standalone artificial system which can respond adequately to various environmental impacts without human intervention. In order to detect these influences over the accuracy of human limitations, the most advanced sensors are needed both in software and hardware. The development in computing power highlights some forgotten algorithms, which were neglected because their complexity made them inefficient on early computers. One of these methods is the Wavelet-Transform Profilometry (WTP) of which successful application is demonstrated in this paper. WTP is a three-dimensional profilometric surface reconstruction algorithm in which orthogonal trajectories are used for high-level signal processing of huge datasets. Our goal was to find a high-precision solution for surface reconstruction by replacing the processing software with advanced mathematical methods rather than use more expensive optical systems.

Keywords: profilometry; Wavelet; reconstruction; machine vision

1 Introduction

Accurate surface reconstruction plays an important role in the field of non-destructive measurement technology that is why the concept of human eye can be only a starting point. There are two main parts of these systems, which can be improved: the optics and the processing algorithm. With the development of computing power the price gap between them became wider and wider. Therefore, we should focus on complex mathematical methods to reach higher-level precision, like Hilbert-, S-, Gábor-, Fourier- or Wavelet-transform. The industrial usage of three-dimensional scanners requires less noise sensitive methods because the machines are continuously vibrating in most places. The advantage of the

complex orthogonal methods is that the entire spatial analysis needs only one image and by increasing the number of the pixels of the image the function of frequency and the accuracy itself will be significantly improved. The first successful use of the one-dimensional Fourier-transformation was published in 1982 by M. Takeda [1], [2] and in 1982 Bone applied the two-dimensional algorithm successfully as well [3]. The method evolved since then and its use of scale became wider, making it possible to be able to reconstruct three-dimensional surfaces with it. In this paper, you can read a short presentation of the field of structured light techniques and profilometry, then Fourier- and Wavelet-transformations are presented as a sequel to our former research [4]. After, the main part Wavelet-transformation profilometry, the laboratory tests, the functional tests and the results will be presented. Finally, the conclusions and the development opportunities will follow.

2 Imaging Methods with Structures Lights

In machine vision the datasets are containing a two-dimensional matrix as an image. To obtain the depth value we can use density distribution (MRI, CT) or traditional surface analysis, in which the information is stored in given scaled scale values, or colour values by using vectors calculated with RGB (red-green-blue). The most common method is to project structured light on the surface with a projector, modulated illuminant by spatial light or laser matrix and capture the reflection with a detector. Each pixel of the digitally processed image has a matrix element and $\{I_{ij} = (i,j), i = 1,2,\dots,I; j = 1,2,\dots,J\}$ is characterizing the intensity, where (i, j) is the (x, y) coordinate of the projected pattern. The distorted image contains deformed patterns, which from; we can extract the depth information. Two main groups of methods can be distinguished by their dynamics, depending on the number of images the algorithm needs. The first one is a sequential, so called multi-shot method, in which we capture multiple images and the additional information can be calculated from the differences between them. We can use binary- and Graycode, phase shift method or a hybrid one. The more images means higher amount of data. Therefore, the method is very precise, but can be only used on static objects. Thanks to the colour information or the specific encoding schemes we can use single-shot methods to reconstruct surfaces from only one image. For this we can use constantly changing patterns like the 3D rainbow camera, band indexing procedures like colour codes, grayscale patterns, De Brujin series or special 2D grid indexing with pseudo-random binary array and colour-coded grids [5].

Figure1
De Brujin series

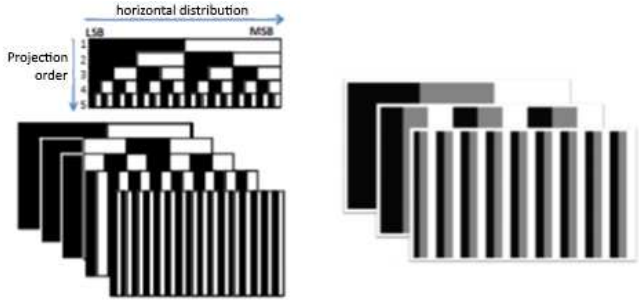

Figure 2
Binary and Gray coding [5]

3 Profilometry

Profilometry is one of the most researched fields of the last decade, although it has relatively short existence and it is also called Fringe Projection Technique. The name came from the fact that the base of this method is to create a specific projection pattern, which is projected and deforms on the surface. The layout is similar to the deflectometric and the triangulation methods, the main units are:

1.) Test object

2.) Projector

3.) Image capture unit (Camera)

4.) Image processing unit (Computer)

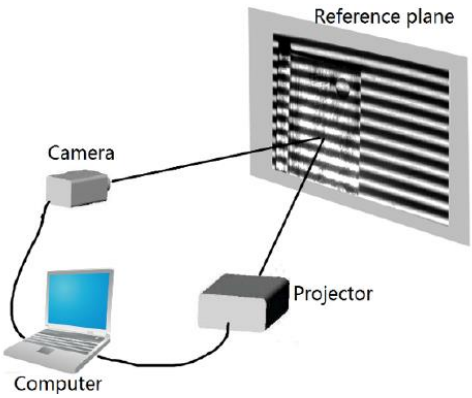

Figure 3
Fringe Projection Technique layout [6]

The method comprises the following steps: First, we select a periodically structured signal, project it on the object and record the distorted image from the surface. This signal is usually a sinusoidal pattern with known phase, the recording device is a camera, but in special cases we can use a system with image capture card. We read the image and process it with a chosen algorithm, then calculate the phase modulation and unwrap the phase. To manage this, we used MATLAB to store the scanned image in a three-dimensional colour matrix, which was reduced to two-dimensional with black and white transformation. The algorithm is mostly a Fourier-transformation or its modification, like the interpolating- or regressive Fourier-transformation, dilated Gabor-transformation, discrete cosine-transformation, S-transformation and Hilbert-transformation, or what we used is one- and two-dimensional Wavelet transformation. Finally, we are mapping the unwrapped values and perform phase- and depth conversion. The unwrapping is performed with a built-in unwrapping algorithm that we present in Sec. 6.

4 Fourier-Transform Analysis

Image processing is just one of the many options that Fourier-transform algorithm is capable of [7]. The three-dimensional surface reconstruction needs to capture of the deformed surface$(g(x,y))$, and a reference sample$(g_0(x,y))$ in the following ways:

$$g(x,y) = r(x,y)\sum_{n=-\infty}^{\infty} A_n e^{j(2\pi f_0 x + n\varphi(x,y))} \tag{1a}$$

$$g_0(x,y) = r_0(x,y)\sum_{n=-\infty}^{\infty} A_n e^{j(2\pi f_0 x + n\varphi(x,y))} \tag{1b}$$

where $\mathrm{r}(\mathrm{x},\mathrm{y})$ and $\mathrm{r}_0(\mathrm{x},\mathrm{y})$ are the concurrent components of the non-uniform reflections, A_n is the weighting factor, f_0 is the carrier frequency, $\varphi(x,y)$ and $\varphi_0(x,y)$ are the value of the phase. The spectrum is the Fourier-transform of the sum, which from we can filter and define the required components. The difference between the modulated signal and the reference signal can be calculated with inverse Fourier-transform:

$$\bar{g}(x,y) = A_1 r(x,y) e^{j(2\pi f_0 x + \varphi(x,y))} \tag{2a}$$

$$\bar{g}_0(x,y) = A_1 r_0(x,y) e^{j(2\pi f_0 x + \varphi(x,y))} \tag{2b}$$

The disadvantage of the procedure is that only frequency domain analysis is performable with it because it approximates the signal with sinusoidal harmonics. Therefore, the analysis does not have temporal localization properties and the time function cannot determine the examined frequency components. Due to the breakdown of the signal into plane waves, if the signal changes in one coordinate its Fourier-transform will change as well, that is why we cannot define the place of change. On the other hand, the overlapping can occur signal analysis errors because the sinusoidal signals cannot be ended in the block borders. We can eliminate these errors by using Wavelet-transform analysis [8].

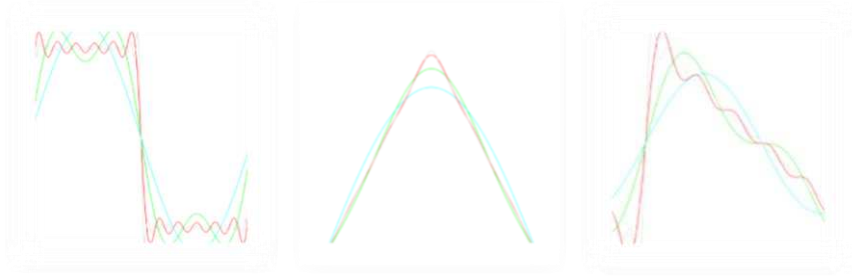

Figure 4
a) square wave approximation, b) Saw wave approximation, c) Triangle wave approximation

5 Wavelet-Transform Analysis

This spectral resolution method has been known since the beginning of the 20th Century, but became internationally known from the late 1980s thanks to Y. Meyer's and Stephane Mallatt's work [7], [9]. The advantage of this algorithm is that WTA divides the signals into so-called mother wavelets instead of sinusoidal, which have limited length and zero mean value. These properties eliminate the errors of FTA because the sharp changes in the frequency spectrum and their coordinates can be determined at the same time. So, time analysis – in our case spatial analysis – is also feasible with it.

Correspondingly to the Fourier-transform the additional information can be obtained from the difference between the signal under test (u) and the test function (v) using internal multiplying mathematical tools:

$$< u, v \geq |u||v| \cos(\theta) \tag{3}$$

If u and v is a unit, then the cosine of the angle between them determines the result, so it is limited into the $[-1, 1]$ interval. The harmonics of the sine function are regular and smooth while in case of Wavelet-transform analysis they are irregular and asymmetric, that is why the sharp and sudden changes can be detected easier. [10]

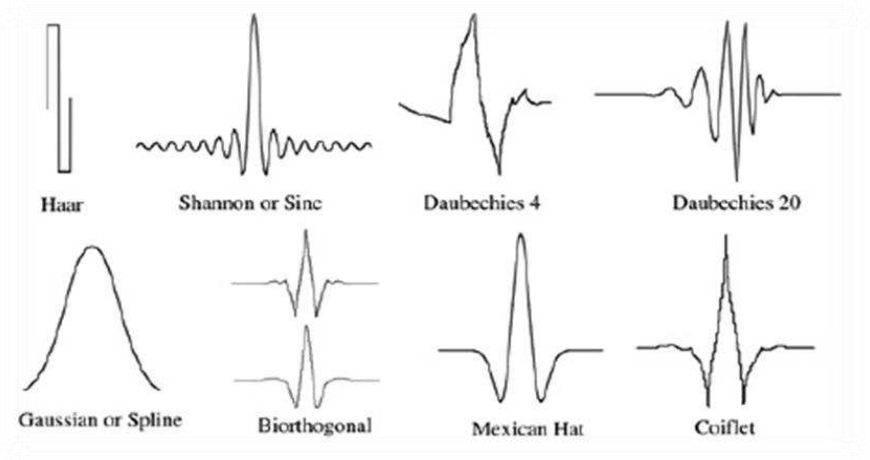

Figure 5
Wavelet signals

5.1 Mother Wavelets

Scale is one of the main properties of the wavelet groups; it declares the compression and stretching of the function. To obtain the depth value we need to use complex mother wavelets when the wavelet transform is a complex function of the scale and position. We can create countless mother wavelet types, but all of them need to fulfill the following correlation:

$$\int_{-\infty}^{\infty} \psi(t)dt = 0 \tag{4}$$

where$\psi(t)$ is the wavelet function and if $\omega = 0$ then $\psi(\omega) = 0$, which is the Fourier transform of the wavelet function. For the study we used the MATLAB provided complex mother wavelets:

- Complex Gaussian:

$$\psi_{Gaussian}(x) = \frac{d(C_p \exp(-ix) \exp(-x^2))^p}{dx^p} \tag{5}$$

- Complex Shannon:

$$\psi_{Shannon}(x) = \sqrt{f_b} \exp(2\pi i f_c x) \, (sinc(f_b x)) \tag{6}$$

- Complex Frequency B-spline:

$$\psi_{b-spline}(x) = \sqrt{f_b} \exp(2\pi i f_c x) \left[sinc\left(\frac{f_b x}{m}\right)\right]^m \tag{7}$$

- Complex Morlet:

$$\psi_{Morlet}(x) = \frac{1}{(f_b^2 \pi)^{\frac{1}{4}}} \exp(2\pi i f_c x) \exp(\frac{-x^2}{2f_b^2}) \tag{8}$$

5.2 Continuous Wavelet Transformation

The compression value (a) and the offset value (τ)of the base function defines a binary function

$$\mathrm{F(a,\tau)} = \frac{1}{\sqrt{a}} \int f(t) \psi\left(\frac{t-\tau}{a}\right) dt \tag{9}$$

where $\psi(t)$ is the basic wavelet function, $\psi\left(\frac{t-\tau}{a}\right)$ is the base function of the transformation, $\mathrm{F(a,\tau)}$ is the wavelet transformation itself. The two variables and the wavelet function declare the coefficients of the continuous wavelet transformation, but we need to concrete the parameters. Therefore, we can use a discrete equation as

$$F[m,n] = \frac{1}{\sqrt{a_0^{-m}}} \int f(t) \psi(a_0^m t - n\tau_0) dt \tag{10}$$

where a_0 is the base power of the compression and τ_0 determine the offsets value. It can be seen that the offset and the compression have to be given powers of the invariants to reach optional values. We can manage this by reducing the offset by half, if the compression is reduced by half as well, in this case we will not miss any part of the function and there will be no overlapping over and above the counting.

The transformation gives good time-resolution and bad frequency-resolution by high-frequency base functions and the opposite by low-frequency base function. The connection between the scale and frequency is clear: the higher scale parameter results higher strain of the mother-wavelet, so the correlation will be over a bigger part of the signal and the accuracy will drop. This means that we can use small values to perceive fast changes and slow ones for slow changes. The continuity comes from the fact that it is interpretable in every scale and the mother wavelets offset is continuous in the whole range of interpretation.

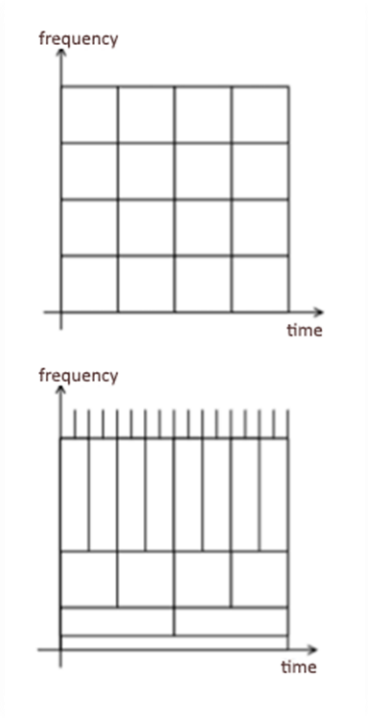

Figure 6
Frequency-time resolution of STFT and WT

6 Wavelet-Transform Profilomtery

The base of this method is to use Wavelet-transformation to determine the phase of the band-pattern. It is possible to use one-dimensional and two-dimensional transformation, however experience shows that the former one gives more accurate and faster results. In this case, one row of pixels is being analysed and repeated for each line. Since the generated patterns can be constructed from adequate modification of sinusoidal signals, the following equation can be used

$$f(x,y) = a(x,y) + b(x,y)\cos\big(2\pi f_0 x + \varphi(x,y)\big) \tag{11}$$

where $a(x,y)$ is the backlight, $b(x,y)$ is the bands amplitude, f_0 is the spatial carriers frequency, $\varphi(x,y)$ is the phase modulation of the bands. The obtaining of the depth values requires the phase and modulus, which can be calculated from the complex results of the one-dimensional continuous wavelet transformation on the examined signal:

$$\varphi(a,\tau) = tan^{-1}\left(\frac{Im(W(a,\tau))}{Re(W(a,\tau))}\right) \tag{12}$$

$$abs(a,\tau) = |W(a,\tau)| \tag{13}$$

where $Im(W(a,\tau))$ is the imaginary part, $Re(W(a,\tau))$ is the real part. The optimal values of each pixel are calculated with a direct maximum method [11], because in case of high signal-noise proportion it gives very accurate results.

The calculated phase has values in a limited range, as the inverse of trigonometric functions they can be only in the $[-\pi,+\pi)$ interval. The greater values than 2π cause artificial discontinuities, that is why we need a phase extractor, so called phase unwrap method [12]. The most common way is to examine the neighbouring pixels and regarding if the difference exceeds a given value then it add or subtract multiple of 2π, so the relative phase distance between the two pixels will be in the $[-\pi,+\pi]$ interval. The proper choice of the limits is very important, so we can filter out the noise components of the carrier and determine the three-dimensional shape of the object.

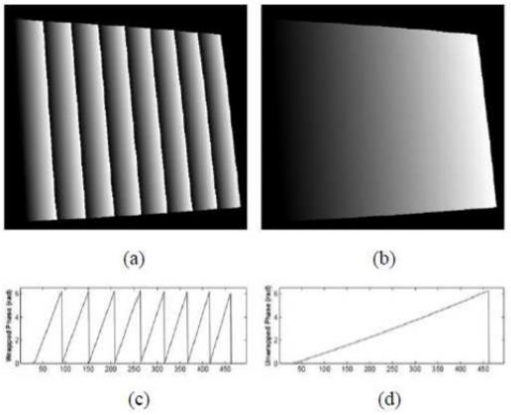

Figure 7
a) and c) Wrapped phase; b) and d) Unwrapped phase

The three-dimensional surface reconstruction is now achievable and it is performable in two different ways. With absolute coordinates we determine the position of the pixels with triangulation, which gives accurate results if we know the precise geometric parameters of the camera and the projector. The adequate calibration is time-consuming. Therefore, we can use relative coordinates, when we determine the depth values of the pixels $h(x,y)$ compared to a reference plane. The projected signal can be calculated as

$$\Delta\Phi(x) = \Phi(x) - 2\pi f_0 x, \tag{14}$$

which we can further modify to get $h(x,y)$ as well [13]:

$$\Delta\Phi(x,y) = -\frac{2\pi f_0 h(x,y) d}{l_0 - h(x,y)} \tag{15}$$

If we take the presumption that the distance between the camera and the projector is negligibly small, compared to their distance from the surface,$(l_0 \gg d)$ then we can calculate the depth information easily [14]:

$$h(x,y) = -\frac{\Delta\Phi(x,y) l_0}{2\pi f_0 d} \tag{16}$$

7 Test Frameworks with Lens

The previous experiments showed, the algorithm is working well on digitally created surfaces, but to measure its accuracy we needed a real object with measurable values. For this we chose a lens, painted it white and measured its radius with a three-ball spherometer. The painting was necessary even though it can affect the results because the method works only on non-reflecting surfaces. We used a digital projector to illuminate the object with structured sinusoidal light, which frequency was controlled by software. The image was captured with a Canon 350D DS126071 (No.1130601174) digital camera with Canon Zoom Lens EF-S 18-55.

The captured image was processed with MATLAB, because it has corresponding built-in complex Wavelet-transformations and one of the highest speeds in mathematical calculations.

7.1 Image Processing

One of the main sources of the inaccuracy is the high noise-signal ratio that is why we have to ensure that the picture is ready for arithmetical progressions by using filters and black-white-transformation. Thereafter. we choose a mother wavelet and the level of the Wavelet-transformation; transform each row of the picture; use a maximum ridge search and unwrap the phase. The depth values can be obtained by extracting a reference plane from the generated surface. It is possible to use a physical plane and process it in the same way, but this can cause more noise, so we decided to create an artificial one because in this case we have strict control over the parameters. The main properties of the pixels are the frequency and the position, so we needed to declare that:

1. The frequency of the projected pattern is known
2. The center of the loupe must be in the center of the cut picture.

As you can see in Sec. 6 we need to use a $\frac{l_0}{2\pi f_0 d}$ multiplier on the generated surface to get the depth values and set the *X* and *Y* direction multiplier for the artificial

one, so the parallel edges of the reconstructed surface will have the same values. For the evaluation we cut the middle line and searched its radius.

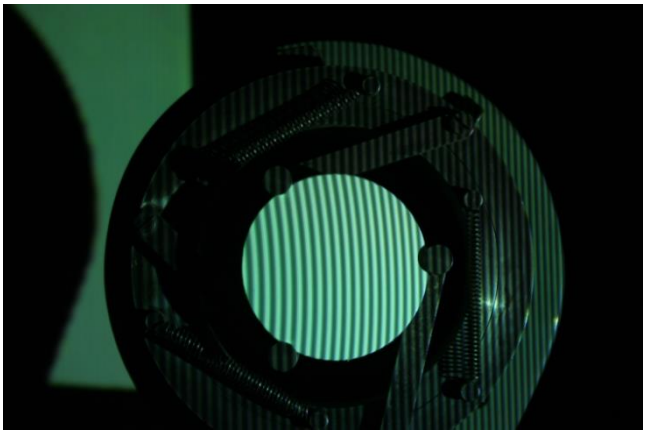

Figure 8
Captured image

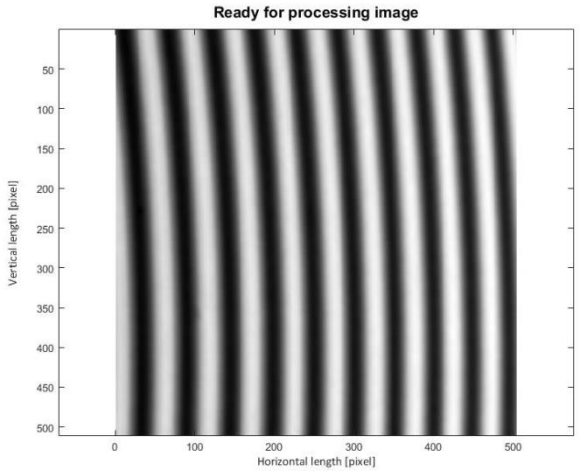

Figure 9
Ready for process image

7.2 Results

The three-ball spherometer measurement gave 390,418 mm for the radius of the lens. If the manufacturing errors were neglected we can assume that the lens has the same radius in every direction, because of its symmetry. We used the following mother wavelets with different tuning parameters: Complex Morlet,

Complex Frequency B-spline, Complex Shannon and Complex Gaussian. After the reconstruction of the surface we measured the vertical (R_y) and the horizontal (R_x) radius. The results can be seen in Table 1-4.

7.2.1 Complex Morlet Wavelets

When the tuning parameters (f_b, f_c) are set to equally 1 respectively, this method gives the best results, but it is only accurate in the vertical (R_x) direction.

Table 1
Radius of X and Y directions with Complex Morlet wavelets

	$f_b - f_c$			
CMOR	***1-0.1***	***1-0.5***	***1-1***	***1-1.5***
R_x [mm]	402.5	421.3	386.6	106.9
R_y [mm]	9.7	100	206.4	46.7

7.2.2 Complex Frequency B-spline Wavelets

The lowest error was 1,2% with 385,7 mm radius in vertical (R_x) direction. The parameters were set in this case to $f_b = 2, m = 1, f_c = 1$. The results were acceptable only in vertical direction, similar to the Morlet wavelets.

Table 2
Radius of X and Y directions with Complex Frequency B-spline wavelets

	$f_b - m - f_c$						
FBSP	***1-1-0.5***	***1-1-1***	***1-1-1.5***	***2-1-0.1***	***2-1-0.5***	***2-1-1***	***2-1-1.5***
R_x [mm]	673.1	375.4	153.5	44125.3	302.7	385.7	107.4
R_y [mm]	19.7	231.4	25.7	103.7	219.9	223.8	39.9

7.2.3 Complex Shannon Wavelets

The complex Shannon wavelets produced the highest error in the radius in both directions. The only assessable result was 3,14% error with 375,4 mm radius in the case of $f_b = 1, f_c = 1$.

Table 3
Radius of X and Y directions with Complex Shannon wavelets

	$f_b - f_c$				
SHAN	***1-0.1***	***1-0.5***	***1-1***	***1-1.5***	***2-3***
R_x [mm]	450.4	673.2	375.4	153.3	64.2
R_y [mm]	53.2	19.7	231.4	25.7	12.3

7.2.4 Complex Gaussian Wavelets

The Complex Gaussian algorithm provided the best results both in vertical (R_x) and horizontal (R_y) direction. However, the latter ones error was still intolerably high. The equation contains only one settable parameter, which gives the order of the Gauss-transformation. If we set $p=3$ (a third ordered Gauss-transformation) we can get the most accurate results, with 0,28% error with 393,0 mm radius.

Table 4

Radius of X and Y directions with Complex Gaussian Wavelets

	p							
CGAU	***1***	***2***	***3***	***4***	***5***	***6***	***7***	***8***
R_x [mm]	353.1	277.8	393	339.9	378.4	346.6	376.8	346.5
R_y [mm]	204.5	209.6	215.3	222.5	227.8	229.9	225.2	217

7.2.5 Evaluation

The projected pattern carries its waves through the transformation. Therefore. the waviness and disturbance of the reconstructed surface are making the operation less accurate. We can apply different kind of filters to eliminate this error, but they are so small that a filtering can cause relevant information loss as well.

From our goals of view we can say that the reconstruction of the object were successful, we were able to recover the radius value of the lens with small error. The Fig. 9 shows on of the best matched reconstructed surface and its middle segment which from we calculated the radius. To show the mentioned waviness we enlarged the values.

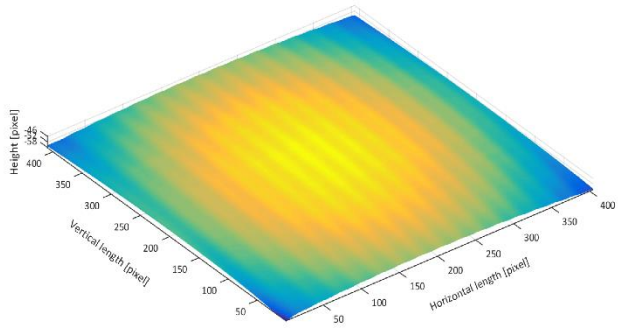

Figure 10

Enlarged reconstruction of the object with third-ordered Complex Gaussian wavelet

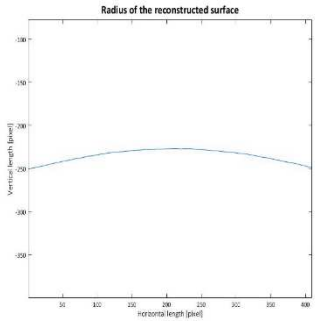

Figure 11
Middle segment to measure the radius (enlarged)

For industrial usage the method is still too slow, but the accuracy is high enough for quality control applications. That is why we choose the field of biomechatronics to create a three-dimensional reconstruction of a human back to detect spine-abnormalities.

8 Test Framework with Mannequin

A real human's back can contain many types of physical disorders, like outgrowths and birthmarks, which can cause discontinuity on the surface. Therefore, we need a "perfect" subject to widen the range of parameters and find the suitable ones. The method is following the same path: project the structured light, capture the image, cut and filter the relevant part and use Wavelet-transform analysis, but in this case with wider range of tuning parameters. The waving that can be seen in Fig. 9 is less dominant in some case, so our goal was to find an algorithm with which we can avoid this waving while keeping a level of high accuracy. We used the $\{f_b | 0.5 \leq f_b \leq 3, f_b = 0.5k, k \in \mathbb{Z}\}$ and $\{f_c | 0.5 \leq f_c \leq 3, f_c = 0.5k, k \in \mathbb{Z}\}$ intervals for the tuning parameters in the case of Complex Morlet, Complex Shannon and Complex Frequency B-spline wavelets, for the latter we used $\{0.5 \leq m \leq 2 : 0.5 \mid m\}$, and the Complex Gaussian transformation remained the same. To obtain the best reconstruction of the highest frequency needed by the projection because in this case the number of lines is the highest too and tested 152 different mother wavelets.

8.1 Evaluation

In the first step we picked the ones without errors which could have been seen with naked eyes, then cut a horizontal segment and multiplied the values, so we could have seen if they containedany waving in their minima or maxima. We then

can take this measurement as an ideal back reconstruction and choose 8 mother wavelets which can be used for later usage:

- Complex Morlet($f_b = 0{,}5;\ f_c = 1{,}5$)
- Complex Morlet($f_b = 1;\ f_c = 1$)
- Complex Morlet($f_b = 1{,}5;\ f_c = 1$)
- Complex Morlet($f_b = 2;\ f_c = 1$)
- Complex Frequency B-spline ($f_b = 2; m = 0{,}5;\ f_c = 0{,}5$)
- Complex Frequency B-spline ($f_b = 2; m = 1{,}5;\ f_c = 1$)
- Complex Frequency B-spline ($f_b = 2; m = 1;\ f_c = 1$)
- Complex Gaussian ($p = 8$)

Fig. 11 and Fig. 12 shows that the reconstruction can be implemented with good approximation, but this is measured by shaping the function and selected with naked human eyes, so we need more experiments with measurable test subjects. To do this we used a real human body with spine-disorder, called scoliosis, and calculated the correlation between the digitally reconstructed spine shape and a radiogram.

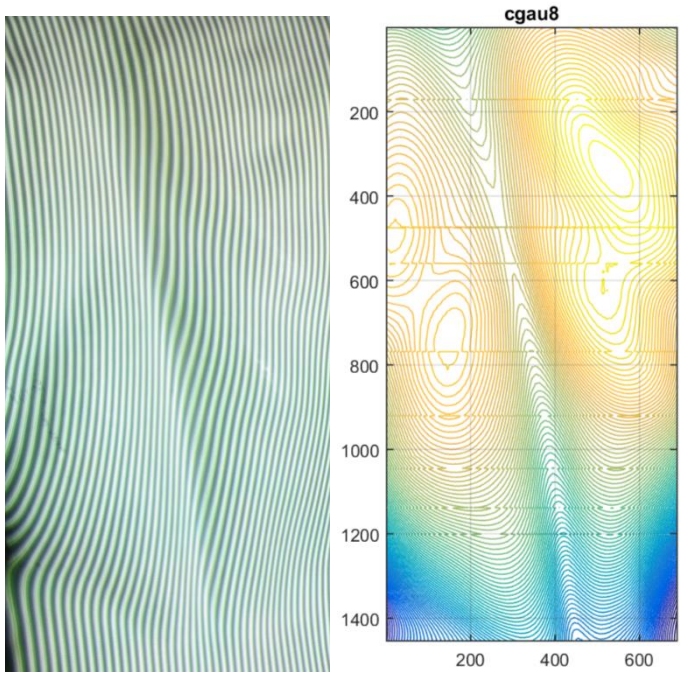

Figure 12
Reconstructed mannequin back with 8th order Complex Gaussian Wavelet

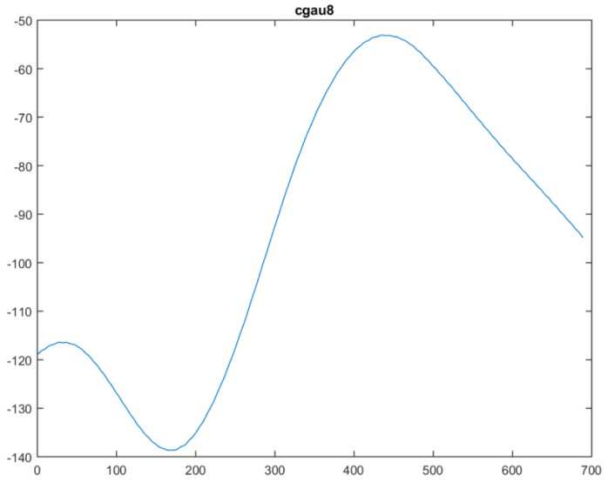

Figure 13
Horizontal segment of the reconstructed surface without equal axis

9 Test Framework with Living Subject

9.1 Spine Deformation Types

The human spine contains 33 small bones called vertebrae, and their connection creates a natural curve, which runs straight down from the back and located in the middle of the back. It can absorb the stress from external impacts like movements and weight, therefore, its deformation has huge physiological effect [15]. We can distinguish three main type of the deformations:

- **Scoliosis**: The spine has a sideway curve so it becomes S- or C-shaped (Fig. 13a).
- **Kyphosis**: The back is abnormally rounded, the curvature has more than 50 degrees in it (Fig. 13b)
- **Lordosis**: Also called as swayback, because it has a significant inward curving of the spine at the lower back (Fig. 13c)

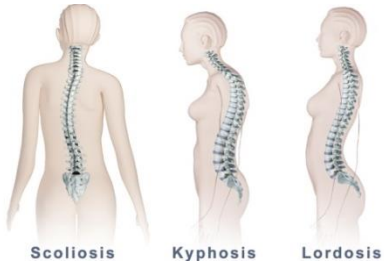

Figure 14
Types of spine deformations: a) Scoliosis, b) Kyphosis, c) Lordosis [16]

9.2 Examination of the Spine Shape from WTP

The procedure was the same as before: project the pattern, capture the image, cut and filter, then reconstruct the surface – in this case her back - with Wavelet-transform profilometry. Our subject was a 24 year old girl with slight scoliosis. To measure the accuracy we needed to determine the spine curving and fit a polynomial on it.

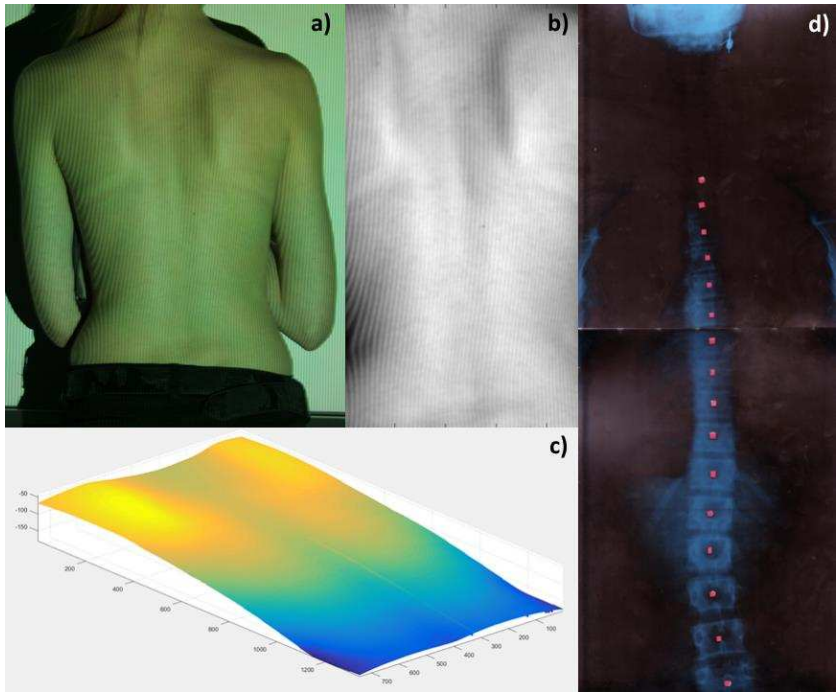

Figure 15
a) Tested back with slight scoliosis, b) Ready to process image, c) Reconstructed surface with 8th order Complex Gaussian Wavelet, d) Radiogram from the spine

As it can be seen in Fig. 13a the scoliosis causes a sideway curve so it forms a S- or C-shape that is why we approximated this curve with a cubic polynomial. We tried to find the deepest point of each line of the reconstructed surface and fit a polynomial on the points. We had an assumption that the deepest point of the row must be in a certain interval, if not then it would break the spine continuity. Therefore, that point cannot be on the spine.

9.3 Examination of the Spine Shape from Radiogram

To calculate the inaccuracy we needed an etalon, which was a radiogram from the subject's back. Although the radiogram was taken 6 years ago, our subject did not participate in any kind of treatment, so her back did not change a lot since then. After considering this information, we set a goal to reach of less than 30% difference between the x-dependent coefficients.

The scanned radiogram (Fig. 14d) is not clear enough to detect the vertebra easily with image processing techniques. So, we decided to use markers on it by sticking red dots on the middle of the vertebra and read their coordinates. For better results we did not use all the markers to fit polynomial on, only the ones which are part of the S-shape.

9.4 Evaluation of the Results

Some of the polynomials were far-out of the acceptable limits, it could be seen even with naked eyes. The Complex Morlet Wavelet gave the lowest difference between the coefficients, 26,64% with $f_b = 1{,}5, f_c = 1$ and 29,47% with $f_b = 2$ $f_c = 1$. In the case of 8th order Complex Gaussian Wavelet the differences were 50,8%, which is not suitable anymore.

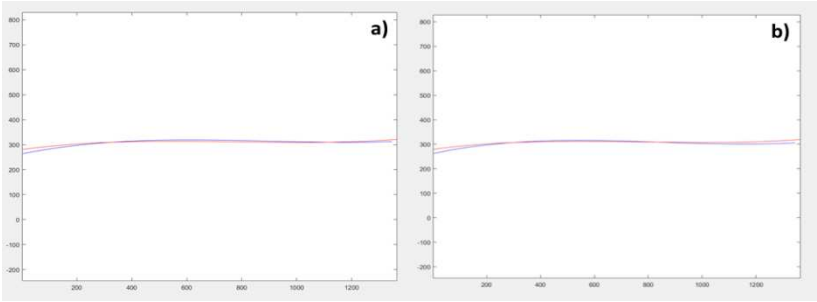

Figure 16
Reconstructed spine shape with a) CMOR (1,5-1) and b) CMOR (2-1) blue: polynomial from WTP; red: polynomial from the radiogram

10 Development Opportunities

First of all we would like to terminate the waving hereby reach higher accuracy in the horizontal direction. There are some methods for this, but all of them reduce the vertical direction accuracy. The other development opportunity is to use a higher resolution camera to capture the image, but the higher amount of pixel results higher processing time as well. Further development opportunity is to use machine learning algorithm to set the variables of this method with an advanced controller [17] to create embedded systems.

Conclusions

In this paper we presented the well-known Fringe Projection Technique solutions. We also did some measurements, where this technique was tested on a lens, and a human body. In the first case the best solution was chosen from the used Wavelets, we got the closest result using Complex Gaussian Wavelets. The best solution happened with the third ordered Gauss transformation. The measured radius of the examined lens was 390.42 mm, using this CGAU Wavelet we got a very close 393.00 mm result.

On a real human we also tried this profilometric technique, the used Wavelets were the Complex Morlet (with 4 different settings), the Complex Frequency B-Spline (with 3 different settings), and the Complex Gaussian (p=8). The best solution originated from the Complex Morlet Wavelet, where $f_b = 1{,}5, f_c = 1$. The Complex Gaussian gave us a huge inaccuracy. It can be stated that in this case the Complex Gaussian Wavelet is not the right choice.

In this work we successfully applied the Wavelet-transform profilometry in surface identification. By lower noise-signal ratio the Complex Gaussian wavelet provided the best results, but as we enlarged this ratio by scanning a real human back the Complex Morlet Wavelet had higher accuracy. As the research shows the WTP can be adapted well for the current environment by using different mother wavelets, so it could be applied in many other industrial fields as well.

Acknowledgement

This work was supported by Budapest University of Technology and Economics, Department of Mechatronics, Optics and Mechanical Engineering Informatics. K. Péter acknowledges the support of Nikolett Kerékgyártó for being the subject by the biomechatronical tests and give free run of using her radiogram.

References

[1] M. Takeda, H. Ina, and S. Kobayashi, “Fourier-Transform Method of Fringe-Pattern Analysis for Computer-Based Topography and Interferometry,” J Opt Soc Am, Vol. 72, No. 1, pp. 156-160, 1982

[2] M. Takeda, K. Mutoh, and S. Kobayashi, “Fourier-Transform Profilometry for the Automatic-Measurement of 3-D Object Shapes,” Appl Optics, Vol. 22, No. 24, pp. 3977-3982, 1983

[3] D. J. Bone, H. A. Bachor, and R. J. Sandeman, "Fringe-Pattern Analysis Using a 2-D Fourier-Transform," Appl Optics, Vol. 25, No. 10, pp. 1653-1660, 1986

[4] P. Balla, P. Kocsis, Gy. Eigner, Á. Antal, "Surface reconstruction with Wavelet transformation", 20th Jubilee International Conference on Intelligent Engineering Systems, Jun 20-July 2, 2016, Budapest

[5] Dr. Ábrahám György: Optika, 1998, Panem Kft. kiadó

[6] Yong Xu, Shuhai Jia, Qingchen Bao, Hualing Chen and Jia Yang, "Recovery of absolute height from wrapped phase maps for fringe projection profilometry", Optics express, 2014

[7] S. G. Mallat, "A theory for multiresolution signal decomposition: The wavelet representation," University of Pennsylvania, Tech. Rep., 1987

[8] A. Z. Abid, M. A. Gdeisat, D. R. Burton, and M. J. Lalor, "Ridge extractionalgorithms for one-dimensional continuous wavelet transform: acomparison," Journal of Physics - Conference Series, Vol. 76, No. 1, pp.1-7, 2007

[9] Y. Meyer, Wavelets, Algorithms & Applications, 1st ed. Philadelphiam, USA: SIAM, 1993

[10] P. Hariharan, Basics of Interferometry, 2nd ed. San Diego, USA: Academic Press, 2007

[11] A. Z. Abid, M. A. Gdeisat, D. R. Burton, and M. J. Lalor. (2016) A comparison between wavelet fringe analysis algorithms. [Online]. Available: photon06archive.iopconfs.org/FASIG%203%20Wed%2016.30.doc

[12] A. Rene, W.L.H. Carmona, and T. Brun, "Characterization of Signals by the Ridges of Their Wavelet Transforms," IEEE T Signal Proces, Vol. 45, No. 10, pp. 2586-2590, 1997

[13] R. Talebi, J. Johnson, and A. Abdel-Daye, "Binary code pattern unwrapping technique on fringe projection method," in Proceedings of the 17th International Conference on Image Processing, Computer Vision, & Pattern Recognition (IPCV'13), p. P7

[14] Z. Zhang and J. Zhong, "Applicability analysis of wavelet- transform profilometry," Opt Express, Vol. 21, pp. 18 777-18 796, 2013

[15] P. Balla, G. Manhertz, Á. Antal, "Diagnostic moiré image evaluation in spinal deformities", Optica Applicata, Vol. XLVI, No. 3, pp. 375-385, 2016

[16] https://therapeutixmassage.com/detection-treatment-spine-deformity-scoliosis/ (20178.01.18)

[17] Gy. Eigner, "Control of Physiological Systems Through Linear Parameter Varying Framework", Acta Polytechnica Hungarica, Vol. 14, No. 6, 2017, pp. 185-212

Comparative Study of Local Binary Pattern Derivatives for Low Size Feature Vector Representation in Face Recognition

Marek Loderer, Jarmila Pavlovicova, Milos Oravec

Faculty of Electrical Engineering and Information Technology, Slovak University of Technology in Bratislava, Ilkovicova 3, 812 19, Bratislava, Slovakia, e-mail: marek.loderer@stuba.sk; jarmila.pavlovicova@stuba.sk; milos.oravec@stuba.sk

Abstract: In this paper, Local Binary Patterns (LBP) and their derivatives, like Local Ternary Patterns (LTP), Local Gradient Patterns (LGP), Non-Redundant Local Binary Patterns (NRLBP) and multi-scale images processed by LBPs, are evaluated in order to find the optimal features for the automatic face recognition system. The comparison of LBP and its variations is performed based on the recognition accuracy. The genetic algorithm optimizes a criterion function, which combines four parameters, such as LBP feature type, feature image processing type, and feature dimension and distance measure. The evaluation was performed on four different face databases. The proposed methodology can be applied in various kinds of recognition, such as facial expression recognition. The main strength of this paper is the design methodology for the selection of the most discriminative features, in accordance with the desired feature vector length and face recognition accuracy.

Keywords: Face recognition; LBP (Local Binary Patterns); LTP (Local Ternary Patterns); LGP (Local Gradient Patterns); NRLBP (Non-Redundant Local Binary Patterns); Dimension reduction; Genetic algorithm; Optimal parameters selection

1 Introduction

As we know, biometrics is concerned with the automatic recognition of humans, based on their physiological or behavioral characteristics. Each face-based biometric system involves the following stages: image pre-processing, feature extraction and feature classification. In the pre-processing step the images are normalized i.e. they are cropped, resized, adjusted by a histogram equalization etc. The feature extraction process plays the crucial role in face recognition. There are many feature extraction methods based on geometry [1, 2], statistics [3, 4] or texture analysis [5, 6] which have been proposed and used in face recognition systems. The performance and accuracy of those methods may vary, however, due

to varied illumination, facial expression and pose. Finally, it is decided if the subject's face matches some the faces stored in the database. There are many discriminative metrics and algorithms used in the classification process [7].

The Local Binary Pattern (LBP) as the texture descriptor was proposed in [5]. Since then many modifications of the LBPs have been published [8]. Concerning the simplicity, speed and high discriminative power of the LBPs, they have been widely used in many applications including face recognition [5, 9, 10], face detection [11, 12], human detection [6, 13], facial expression recognition [14], gender recognition [15] and face authentication [16]. There are many applications which use the LBP features for texture classification [5, 13, 14, 15], shape localization and object detection [17], or real time biometric applications in intelligent interfaces, like admission and authorization to the services in the next-generation of hybrid broadcast broadband television [18].

We propose a review study of binary pattern modifications and perform the face recognition system optimization based on different LBP features. This paper is organized as follows: Section 2 presents a brief overview of the used face databases and their properties; Section 3 is concerned with a detailed description of different LBP features and their modifications. Partition of feature images into blocks is addressed in Section 4. In Section 5, we present the different distance measures used in the study. The application of genetic algorithm for optimization of face recognition system parameters is described in Section 6. Finally, in Section 7, we discuss the results under the conditions of constrained computational complexity and suitability for devices with reduced resources.

2 Face Database

For the optimized face recognition system testing purposes, we used four standard databases. The images used were of different size, however, and thus for a valid comparison of results, it was necessary to resize them uniformly. To unify the size of input images, we applied down sampling. In our tests three different image scales are processed: 56*64 pixels, 42*48 pixels and 28*32 pixels. The summary of the databases is shown in Table 1.

The CMU PIE (Pose, Illumination and Expression) face database consists of 68 individuals [19]. For our experiments, we created training and testing sets as part of the database (according to three different poses C05, C27 and C29 shown in Fig. 1). We used 97 images per each subject (6596 samples). The original size of a sample image is 640*486 pixels. It was cropped to the size of 64*64 pixels and then resized to the final size of 56*64 pixels.

The Extended Yale Face Database B consists of 38 individuals [20]. In our research, we created training and testing sets of 64 images per subject (2432

samples). The original image size was 640*480 pixels, the cropped size 168*192 pixels and final size after being resized is 56*64 pixels.

The ORL or ATT face databases consist of 40 individuals [21]. For our experiments, we created training and testing sets using 10 images per each subject (400 samples). The original image size was 92*112 pixels and the cropped size is 56*64 pixels.

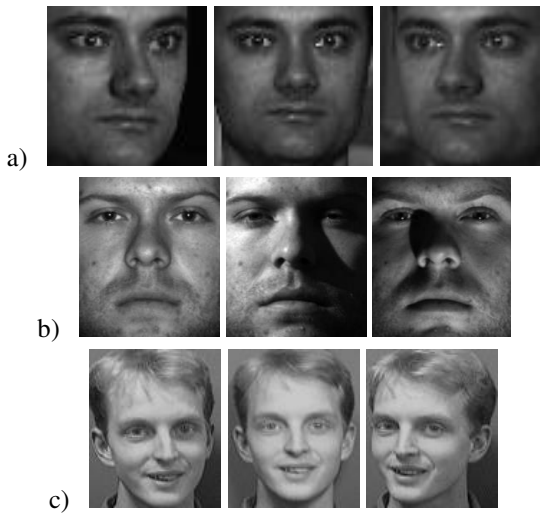

Figure 1
Examples of three different poses (C05, C27 and C29) in CMU PIE database (a); Extended Yale Face Database B (b); ATT/ORL database (c)

The FERET database contains faces with different expressions, under different illumination and a wide set of pose variations [22]. In contrast to above mentioned databases with homogeneous background where faces are already localized (Fig. 1), in the case of FERET database it was necessary to apply complex preprocessing to localize faces and remove the background (Fig. 2). In this way, our own dataset called "BIG Faces" was created. "BIG Faces" is part of the grey-scale FERET database (sets "fa" and "fb"). The images were cropped and resized using geometric normalization based on eye coordinates. As a pre-processing, the histogram equalization was applied. The irrelevant parts of images were masked using an ellipse around the face (Fig. 2). In this way, we reduced the influence of background, clothes etc. The original dimension of a sample image was 256*384 pixels, the cropped size 134*154 pixels and the resized image has 56*64 pixels.

Two different subsets (BIG4 and BIG6) were created. The BIG4 contains at least four samples per subject. There are 246 individuals and 1223 samples. The BIG6 contains at least six samples per subject. There are 73 subjects and 531 samples.

After complex preprocessing described above, localized faces with homogeneous backgrounds were used both for training and testing. The advantages of such a procedure is the increase of recognition accuracy, the reduction of the number of training images, the lowering of computational complexity, in the classification stage and improvement of the overall robustness of the system. It can be noted that preprocessing procedure does not influence the optimization process by the genetic algorithm.

Figure 2
The original image in FERET database (left) and examples of pre-processed "BIG Faces"

Table 1
Used databases

Database	Original size	Number of subjects	img/subject used	Sample numbers	Resized to
CMU PIE	640x486	68	97	6596	56x64
Ext. YALE	640x480	38	64	2432	56x64
ATT	92x112	40	10	400	56x64
FERET BIG4	256x384	246	at least 4	1223	56x64
FERET BIG6	256x384	73	at least 6	531	56x64

3 Face Feature Extraction

An optimal selection of discriminative features is an essential condition of efficient face recognition and at the same time it enables memory and time complexity reduction. In our previous analysis [23] we arrived at a conclusion that the recognition accuracy depends not only on the selected LBP feature type, but also on the size and proportions of blocks used in the LBP-feature space for a histogram construction. Because of that, we used the size and proportions of blocks in the LBP-feature space as an optimization parameter.

The maximum number of training images per subject was five. Only in the case of the BIG4 database, three training samples per each subject were used. The training samples were selected in the following two ways, using different images (inputs) and K-means clustering algorithm.

The extended YALE B, ATT/ORL and BIG Face databases contain only frontal images. The training samples were selected according to the original face images pre-processed by an adaptive histogram equalization.

In case of the CMU PIE database, better results were achieved using the LBP-feature images. We used four types of LBP and four different mappings (none, U2, RI and RIU2). These images were set as the input data for the clustering algorithm. In other words, 16 training sets were created according to the mentioned types of features. In the optimization phase, the genetic algorithm used these 16 training sets for the corresponding 16 types of the LBP features. We can assume that the selection based on the LBP-feature images used a variance of features caused by various poses (C05, C27 and C29), but not by various illumination.

3.1 LBP (Local Binary Patterns)

The original LBP operator described in [5] seems to be an efficient texture descriptor. It is robust against illumination changes and it can be computed very rapidly. The $LBP_{P,R}$ operator assigns a binary value to each pixels p_i in the defined neighborhood of the central pixel p_c, where the grey-value of p_c is a threshold (Fig. 3, a-c). The result of $LBP_{P,R}$ operator application is a feature image of decimal $LBP_{(P,R)}$ values (1). An extended $LBP_{P,R}$ operator is able to deal with the different number of samples P in the central pixel neighborhood of the radius R (Fig. 3, d,e).

$$LBP_{P,R} = \sum_{i=0}^{P-1} s(p_i - p_c)2^i \tag{1}$$

$$s(x) = \begin{cases} 1, & x \geq 0 \\ 0, & x < 0 \end{cases} \tag{2}$$

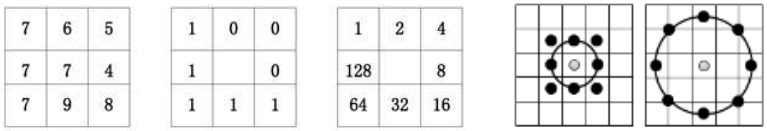

Figure 3

$LBP_{(P,R)}$ example for P=8, R=1: a) gray-level values p_i around the central pixel p_c = 7, b) binary values according to equation (1), c) corresponding powers of 2; final binary value is 10001111 and corresponding decimal $LBP_{(8,2)}$ number is 241; d) $LBP_{(8,1)}$, e) $LBP_{(8,2)}$

Here, *s(x)* is the threshold function. One of the LPB extensions is a uniform pattern (U2). In this case the pattern corresponds with the uniform pattern if a binary string contains at most two bitwise transitions from 0 to 1 or vice versa. These patterns represent important features in such areas as spots, corners and edges. All of the other (variant) patterns are merged into one value. The other

extensions of the LPB are the rotation invariant patterns (RI). In this modification, each binary number is rotated to the same normalized minimal value. The combination of both extension types represents the rotation-invariant and uniform patterns (RIU2).

3.2 LGP (Local Gradient Patterns)

The LGP was proposed to overcome the problem of local intensity variations along the edge components [6]. The LGP operator (3) is applied to the gradient magnitude image in the defined neighborhood values g_i of the central pixel with the gradient magnitude $\bar{g}$. They are computed as the absolute value differences between the intensity of the central pixel p_c and the surrounding pixel values p_i (4). Then the intensity of the central pixel p_c is substituted by the average value $\bar{g}$ (a locally adapted threshold) of all gradient values g_i (4). This value is used as the threshold value. The result value is computed from the gradient magnitude image in the same way as in case of the basic LBP operator with the same threshold function (2).

$$\mathrm{LGP_{P,R}} = \sum_{i=0}^{P-1} s(g_i - \bar{g})\, 2^i \tag{3}$$

$$g_i = |p_i - p_c| \quad \bar{g} = \frac{1}{P}\sum_{i=0}^{P-1} g_i \tag{4}$$

According to the previous definition, the LGP operator generates the following patterns. If the intensity of both the background and the foreground are changed globally (concurrently) there is no significant difference between the LGP and LBP operators (each of them generates invariant patterns). If the intensity of the background or the foreground is changed locally, the LGP generates invariant patterns in contrast to the LBP operator (generating variant patterns). This difference is caused by gradient differences (not only by intensity differences).

3.3 NRLBP (Non-Redundant Local Binary Patterns)

The NRLBP operator was proposed as a solution for the feature extraction in images with a bright object on a dark background or vice versa. The NRLBP patterns for these two types of images are different which means that the NRLBP features make distinguishing between them possible [13]. The authors proposed the pattern value as the minimum value of the LBP pattern and its complement. The greatest code becomes redundant and consequently it will occur in none of the histograms.

$$\mathrm{NRLBP}_{P,R} = \min\left(\mathrm{LBP_{P,R}}, 2^P - 1 - \mathrm{LBP_{P,R}}\right) \tag{5}$$

The mapping reduces the number of decimal values significantly. The disadvantage of this method is, however, that objects with different structure can get the same histogram representation.

3.4 LTP (Local Ternary Patterns)

Tan et al. in [24] extended the LBP from binary code to a three-valued code called Local Ternary Patterns. The threshold function was changed to a three-valued function as follows:

$$s(p_i, p_c, t) = \begin{cases} +1 & p_i \geq p_c + t \\ 0 & |p_i - p_c| < t \\ -1 & p_i < p_c - t \end{cases} \quad (6)$$

Here p_i are the pixel values in the neighborhood of the central pixel with the grey value p_c and t is the zone width. The LTP operator is less sensitive to noise than the LBP operator. Features generated by the LTP can be split into negative and positive parts thus reducing the computing complexity [25]. The number of histogram bins may be assigned arbitrarily. A large value leads to a huge feature vector, while a small value loses the variety of properties extracted by using the LTP operator. We set the parameter t=5 and we joined the positive and the negative parts to reduce the number of histogram bins.

3.5 Multi-Scale Images

There are many applications which use the multi-scale sampling, e.g. [26]. The multi-scale sampling has proven to be effective for face recognition and thus, we have decided to include it into our study.

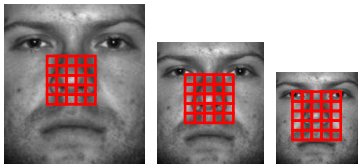

Figure 4

Multi-scale image representation. The descriptor comprehends the detail appearance in the close area of the fiducial point (the large-scale image on the left) and captures the global shape of the face (the small-scale image on the right).

We built an image pyramid of normalized images using the original image and two scaled images (Fig. 4). An advantage of multi-scale sampling is that it encodes both micro and macro structures of the subject's face simultaneously. On the other hand, a disadvantage of this approach is the higher computational complexity [27].

3.6 Block Size Selection in LBP Feature Space

As we mentioned before, the recognition accuracy depends also on the size and proportions of blocks used in the LBP feature space for a histogram construction. We analyzed all the possible uniform image decompositions for a given input image size to find the optimal size. If the size of the original image is 56*64 pixels, then the LBP feature image after application of the LBP with P=8 and R=2, will have the size of 54*60. There are 72 different ways how to divide this image into equal blocks.

4 Parameter Optimization Based on the Genetic Algorithm

The Genetic algorithm (GA) is a stochastic algorithm that provides an efficient method of finding the global optimal solution. The GA uses a biological aspect of evolution (evolutionary computing) and is well suited for handling many computational problems [28, 29, 30, 31].

The rather important parameters of the GA algorithm are: chromosome (sequence of values which will be optimized), number of individuals in population per generation (p_g=30), number of generations (g_n=100), mutation probability (p_m=0.05), recombination probability (crossing-over) (p_r=0.5) and objective function (12) i.e. the fitness function.

The GA starts with randomly defined population (size of population – p_g). In this population each individual is represented as a chromosome. The fitness function evaluates fitness of the parameters in a chromosome. Only some chromosomes (according to the value of the fitness function and selection strategy, such as tournament strategy) are selected for reproduction. Crossing-over and mutation are used as possible ways of reproduction of new or changed chromosomes. After the new population is created, the fitness of this population will be evaluated. If the population achieves the desired fitness level or maximal number of generations (g_n), the procedure will be terminated [30].

Optimized parameters using the GA are:

- Type of 16 extracted features (with different LBP patterns mappings): LBP (none, U2, RI, RIU2); LGP (none, U2, RI, RIU2); NRLBP (none, U2, RI, RIU2) and LTP (none, U2, RI, RIU2)
- Size of blocks in feature space
- Type of distance measure (L1, L2, χ^2)

We tested three simple distance measures as the feature classification criteria.

The L1 distance is often used to compute the dissimilarity between images [7]. ***x*** and ***y*** are row vectors and N is the vector length. The same parameters are in equations (8) and (9).

$$L1(x,y) = \sum_{i=0}^{N-1} |x_i - y_i| \tag{7}$$

The L2 distance (Euclidian distance) in [7] is defined as:

$$L2(x,y) = \sqrt{\sum_{i=0}^{N-1} (x_i - y_i)^2} \tag{8}$$

The Chi-square (χ^2) is a statistical test for evaluation of consistency of the explored data set and a hypothetic data distribution [7].

$$\chi^2 = \sum_{i=0}^{N-1} \frac{(x_i - m_i)^2}{m_i} \quad m_i = \frac{x_i - y_i}{2} \tag{9}$$

We restricted the size of the feature vector by 1/3rd of an image size. The following objective function is optimized (minimized) by the genetic algorithm

$$f(d,x,y,acc) = 0.01 \frac{d}{Ix * Iy} + (1 - acc), \tag{10}$$

size of blocks in feature space where *d* is the number of the histogram bins, *x* and *y* are the dimensions of original image from corresponding database, I_x and I_y is the number of rows and columns of the image and *acc* is the current recognition accuracy. If $d > (I_x * I_y)/3$, this chromosome is ignored (length of feature vector is larger than 1/3rd of the image size). According to the number and size of blocks and the number of bins (concatenation of histograms) the length of the feature vector is constrained. The block diagram is shown in Fig. 5.

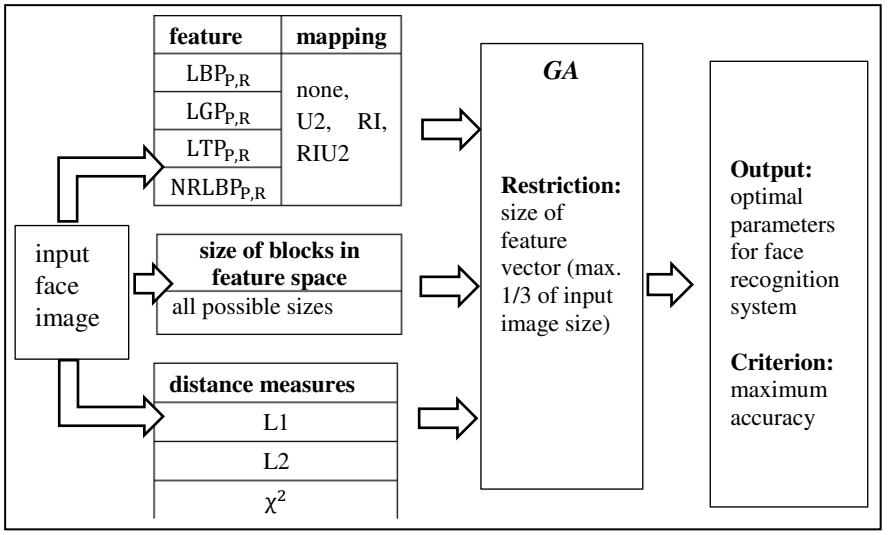

Figure 5
Block diagram of the optimization process

The optimized parameters which offer the best recognition accuracy for different face databases are shown in Tables 2-3. In case of multi-scale image approach, three different scales of images were tested. The parameters which offer the best recognition accuracy for each face database are in Table 3.

Table 2
Optimal parameters for all databases (exclusive of multi-scale images)

Database	R	Feature type	Block dimension	Feature dimension	Distance measure	Recognition accuracy
CMU PIE	3	LBP RIU2	1*25	1160	χ^2	87,274
Ext. YALE	2	LBP RIU2	2*13	1200	L1	95,079
ATT	2	LTP U2	11*38	236	L1	99,500
		LBP U2	15*52			
BIG4	2	NRLBP RIU2	6*4	1170	L1	98,316
BIG6	1	LTP RIU2	2*18	930	L1	99,096

Table 3
Optimal parameters for all databases (multi-scale images)

Database	R	Feature type	Block dimension	Feature dimension	Distance measure	Recognition accuracy
CMU PIE	3	LBP RIU2	26*22	1010	χ^2	87,675
			1*36			
			2*25			
Ext. YALE	3	LBP RIU2	26*22	720	χ^2	93,949
			1*36			
			2*50			
ATT	3	LTP U2	26*22	236	χ^2	99,500
			42*36			
			29*50			
BIG4	2	LTP RIU2	28*6	930	χ^2	98,660
			4*38			
			10*4			
BIG6	3	LTP RIU2	2*22	1130	L1	99,498
			7*6			
			2*50			

In either case, we applied three values of a pixel neighborhood radius (R). The feature type and mapping (Feature type), the number of columns and rows of one texture block (Block dimension) and the distance measure are parameters optimized with respect to the achieved recognition accuracy and length of the feature vector. The feature vector dimension (Feature dimension) is restricted and

must not exceed one third of the image size. In most cases the maximum length of a feature vector was reached as an optimum. 6-fold cross validation was performed and an average recognition accuracy (Recognition accuracy) is shown in the following tables.

5 Experimental Results

The best results were achieved for the image size of 64*56 pixels. Only in case of the ATT database, the LTP U2 features were obtained from the image size of 48*42 pixels (the first row in Table 2) and the LBP U2 features were extracted from the image size of 64*56 pixels (the second row in Table 2).

The LBP, as well as the LTP features achieved the best recognition accuracy. The LBP can be commonly used in numerous applications. On the other hand, even if the LTP is able to reduce the influence of noise in images, its disadvantage is the significant data correlation between its positive and negative parts. Although R=2 is used in most publications, in our optimization process R=3 can be considered a more suitable alternative, especially in case of a multi-scale image approach. Both the rotation invariant and uniform patterns (RIU2) and uniform patterns (U2) occur mostly in optimal parameter sets. The RIU2 offers such advantages as significant dimension reduction, rotation invariance and identification of significant face features. The U2 patterns, however, are more suitable for face recognition.

From the three tested simple and fast distance measures, the χ^2 distance occurred most frequently in optimization processes. Still, L1 distance provides favorable classification results.

Obviously, the multi-scale images increase the recognition accuracy (PIE=+0.40%, BIG6=+0.40%, BIG4=+0.34%, ATT without change and Extended YALE=–1.13%, but there was significant dimension reduction).

In case the face database is rather small, a short vector of features (ATT length of vector is 236) is sufficient. Larger databases, however, need at least 930 features to achieve the desired accuracy.

The database size, number of subjects per database and different poses have a considerable influence on the size and shape of blocks. The shape and size of blocks are varying in case of image scaling. There are thin horizontal stripes (PIE – 1*25, ATT – 11*38 pixels) or small rectangular areas (Extended YALE – 2*13, BIG6 – 2*18 pixels) or small, almost squared, areas (BIG4 – 6*4 pixels). The scaled version contains three different image sizes. There are also thin horizontal stripes (PIE – 1*36, Extended YALE – 1*36, 2*50, BIG4 – 4*38, BIG6 – 2*22, 2*50 pixels), then the rectangular areas (PIE – 2*25, BIG4 – 28*6, 10*4 pixels)

and finally the almost square areas (BIG6 – 7*6 pixels). In this case also the whole images were used as input image blocks (PIE, Extended YALE, ATT – 26*22 and ATT – 42*36 pixels).

In Tab. 4, we compared the results obtained by us with the state-of-the-art contributions. The proposed methods with the best results, which were evaluated on the mentioned databases, are listed in the Table. There are many differences e.g. number of training and testing samples, size of input images and length of the feature vector.

Table 4

Comparison of achieved results with the state-of-the-art contributions

Database	References	Accuracy	Feature vector length	Proposed method (Feature vector length)
FERET (fb)	[32], 2012	99.60	1180	98,660 (930)
	[33], 2014	99.90	--	
	[34], 2015	99.90	1196	
	[35], 2015	98.58	1000	
	[36], 2016	99.60	2000	
FERET (fc)	[32], 2012	99.50	1180	
	[33], 2014	100.00	--	
	[34], 2015	100.00	1196	
	[35], 2015	100.00	1000	
	[36], 2016	100.00	2000	
FERET (-)	[37], 2014	99.00	--	
FERET	[38], 2007	93.16	--	99,498 (1130)
ATT	[38], 2007	98.50	--	99,500 (236)
	[39], 2013	≈98.70	--	
Ext. YALE	[24], 2010	99.28	≈25000	95,079 (1200)
	[40], 2014	≈96.00	≈100000	
	[41], 2015	99.34	767	
	[42], 2015	97.39	≈25000	
CMU PIE	[43], 2013	99.85	≈65000	87,675 (1010)
	[40], 2014	≈91.40	≈8000	
	[44], 2016	97.44	≈20000	

We find the proposed method which reduces data dimension significantly to be our main contribution If the authors of a method did not mention a specific number of features, we use "-" label. If there were many clues in a paper, we estimate the number of features and their number (or accuracy) has the sign "≈".

In case of the FERET database, we achieved different results between -1.34 and +0.08%. The difference is acceptable if we take into account a slightly larger number of features.

In case of the ATT database, we achieved an improvement of +0.8%.

For larger databases, like the Extended YALE B, the obtained results show differences between -4.26 and -0.921%. As mentioned above, the feature vector dimension is considered an important parameter from the point of view of computational complexity. Yet, from Table 4 clearly follows that our result was achieved with significantly smaller feature vectors.

For the fourth database, (CMU PIE) the differences in recognition accuracy are in the interval -12.18 and -3.73%. This was caused by a significant data dimension reduction and by the influence of database size and different poses.

As shown in Table 4, we can claim that the methodology proposed by us can be used in devices with reduced sources (weak CPU or small memory). The results achieved by us are comparable with recently proposed rather sophisticated algorithms with much higher computational complexity. There is one more advantage of our approach represented by a possibility of adding a new subject to, or removing old user data from a database of features in an easy way.

Conclusions

This paper presents a new method of feature extraction for a face recognition system, optimized by the genetic algorithm. The system is optimized to achieve the desired recognition accuracy for a limited length of the feature vector. In most cases, the best recognition accuracy was achieved by the LBP patterns with the RIU2 mappings. Still, the LTP with the same mapping should be also considered as suitable for face recognition purposes. L1 and χ^2 distances are suitable and they achieved the highest recognition accuracy. The number, shape and size of blocks were also optimized using the genetic algorithm.

Taking into account the previous results (Table 2), we came to the following conclusions. The optimal size of an input image is 64*56 pixels when the parameters P=8 and R=2 are applied. With smaller images the recognition accuracy decreases. The L1 distance was selected as the optimal distance. The LGP features as such were not discriminative enough for the recognition purposes.

The rows in Table 3 show that the image pyramid improved the recognition accuracy, if the parameters P=8 and R=3 were used. χ^2 distance measure was selected as the optimal measure. It achieved the best recognition accuracy and it occurred most frequently in our optimization results.

Acknowledgement

The research described in the paper was done within the grant No. 1/0867/17 of the Slovak Grant Agency VEGA.

References

[1] Hanmandlu, M., Gupta, D., and Vasikarla, S.: Face recognition using Elastic bunch graph matching. Applied Imagery Pattern Recognition Workshop, 2013, pp. 1-7

[2] Badakhshannoory, H., Safayani, M. and Manzuri-Shalmani, M. T.: Using geometry modeling to find pose invariant features in face recognition, ICIAS, 2007, pp. 577-581

[3] Xu, Z., Wang, L. and Yang, L.: A Simulated Annealing and 2DPCA Based Method for Face Recognition, IEEE Conf. on Signal-Image Technologies and Internet-based System, 2007, pp. 777-782

[4] Martinez, A. M. and Kak, A. C.: PCA versus LDA, IEEE Trans. Pattern Analysis and Machine Intelligence, Vol. 23, 2001, pp. 228-233

[5] Ojala T., Pietikainen, M. and Maenpaa, T.: Multiresolution Gray Scale and Rotation Invariant Texture Classification with Local Binary Pattern, IEEE Transaction on PAMI, Vol. 24, No. 7, 2002, pp. 971-987

[6] Jun, B., Choi, I. and Kim, D.: Hybridization for Accurate Face and Human Detection, Pattern Analysis and Machine Intelligence, Vol. 35, No. 6, 2013, pp. 1423-1436.

[7] Zhang, D. and Lu, G.: Evaluation of similarity measurement for image retrieval, Neural Networks and Signal Processing, Vol. 2, 2003, pp. 928-931

[8] Huang, D., Shan, C., Ardabilian, M., Wang, Y. and Chen, L.: Local Binary Patterns and Its Application to Facial Image Analysis: A Survey, IEEE Transactions on Systems, Man and Cybernetics, Vol. 41, No. 6, 2011, pp. 765-781

[9] Xuefeng, Ch., Fei. L. and Huang, Ch.: Face Recognition by Zero-Ratio Based LGBP Features, World Congress on Intelligent Control and Automation, 2014, pp. 5605-5608

[10] Binbin, W., Xinjie, H., Lisheng, Ch., Jingmin, C. and Yunqi, L.: Face Recognition Based on the Feature Fusion of 2DLDA and LBP, International Conference on Information, Intelligence, Systems and Applications, 2013, pp. 1-6

[11] Bilaniuk, O., Fazl-Ersi, E., Laganière, R., Xu, Ch., Laroche, D. and Moulder, C.: Fast LBP Face Detection on low-power SIMD architectures, IEEE Conference on Computer Vision and Pattern Recognition Workshops, 2014, pp. 630-636

[12] Kadir, K., Kamaruddin, M. K., Nasir, H., Safie, S. I and Bakti, Z. A. K.: A Comparative Study between LBP and Haar-like features for Face Detection Using OpenCV, International Conference on Engineering Technology and Technopreneuship, 2014, pp. 335-339

[13] Satpathy, A., Jiang, X. and Eng, H.: Human Detection Using Discriminative and Robust Local Binary Pattern, ICASSP, 2013, pp. 2376-2380

[14] Abdulrahman, M., Gwadabe, T. R., Abdu F. J. and Eleyan, A.: Gabor Wavelet Transform Based Facial Expression Recognition Using PCA and LBP, Signal Processing and Communications Applications Conference, 2014, pp. 2265-2268

[15] Huynh, T., Min, R. and Dugelay, J. L.: An Efficient LBP-based Descriptor for Facial Depth Images applied to Gender Recognition using RGB-D Face Data, Workshop on Computer Vision with Local Binary Pattern Variants (ACCV), 2012, pp. 1-12

[16] Ouamane, A., Messaoud, B., Guessoum, A., Hadid, A. and Cheriet, M.: Multi Scale Multi Descriptor Local Binary Features and Exponential Discriminant Analysis for Robust Face Authentication, IEEE International Conference on Image Processing, 2014, pp. 313-317

[17] Ngoc, T. N.: An Efficient LBP-Based Descriptor for Real-Time Object Detection, IEEE Symposium on Computational Intelligence for Security and Defense Applications, 2014, pp. 1-5

[18] Ban, J., Pavlovičová, J., Féder, M., Omelina, L. and Oravec, M.: Face Recognition Methods for Multimodal Interface. 5th joint IFIP Wireless and Mobile Networking Conference, 2012, pp. 110-113

[19] Sim, T., Baker, S. and Bsat, M.: The CMU Pose, Illumination, and Expression (PIE) database, Proceedings of the IEEE International Conference on Automatic Face and Gesture Recognition, 2002, pp. 46-51

[20] Belhumeur, P. N., Hespanha, J. P. and Kriegman, D. J.: Eigenfaces vs. Fisherfaces: Recognition Using Class Specific Linear Projection, IEEE Transactions on Pattern Analysis and Machine Intelligence, Vol. 19, No. 7, 1997, pp. 711-720

[21] Samaria, F. S. and Harter, A. C.: Parameterisation of a stochastic model for human face identification, 2nd IEEE Workshop on Applications of Computer Vision, 2000, pp. 138-142

[22] Phillips, P. J., Moon, H. Rauss, P. and Rizvi, S. A.: The FERET evaluation methodology for face recognition algorithms, IEEE Transactions on PAMI, Vol. 22, No. 10., 2000

[23] Loderer, M. and Pavlovičová, J.: Optimization of LBP Parameters, 56th International Symposium ELMAR, 2014, pp. 1-4

[24] Tan, X. and Triggs, B.: Enhanced local texture feature sets for face recognition under difficult lighting conditions. IEEE Transactions on Image Processing, Vol. 19, No. 6. 2010, pp. 1635-1650

[25] Jia, X., Yang, X., Zang, Y., Zhang, N., Dai, R., Tian, J., Zhao, J.: Multi-scale Block Local Ternary Patterns for Fingerprints Vitality Detection, International Conference on Biometrics, 2013, pp. 1-6

[26] Chan, Ch., Kittler, J. and Messer, K.: Multi-scale local binary pattern histograms for face recognition, Advances in biometrics, 2007, pp. 809-818

[27] Chen, D., Cao, X., Wen, F. and Sun, J.: Blessing of Dimensionality: High-dimensional Feature and Its Efficient Compression for Face Verification, IEEE Conference on Computer Vision and Pattern Recognition, 2013, pp. 3025-3032

[28] Pereira, E., Gomes, H., Moura, E., Carvalho, J. and Zhang, T.: Investigation of Local and Global Features for Face Detection, IEEE Symposium on Computational Intelligence for Multimedia, Signal and Vision Processing, 2011, pp. 114-121, 2011

[29] Omelina, Ľ. and Oravec, M.: Universal biometric evaluation system: Framework for testing evaluation and comparison of biometric methods, IEEE Int. Conference on Systems, Signals and Image Processing. 2011

[30] Devi, G. S. and Rabbani, M. M. A.: Optimizing Modular Image PCA using Genetic Algorithm for Expression – Invariant face recognition, International Conference on Networks & Soft Computing, 2014, pp. 319-323

[31] Sekaj, I.: Control algorithm design based on evolutionary algorithms. In Introduction to Modern Robotics, iConcepts Press Ltd., 2011, pp. 251-266

[32] Nguyen, T. P., Vu, N. and Caplier, A.: Face Recognition using Multi-modal Binary Patterns. International Conference on Pattern Recognition, 2012, pp. 2343-2346

[33] Jain, V., Crowley, J. L. and Lux, A.: Local Binary Patterns Calculated Over Gaussian Derivative Images. International Conference on Pattern Recognition, 2014, pp. 3987-3992

[34] Lu, J., Liong, V. E. and Zhou, J.: Simultaneous Local Binary Feature Learning and Encoding for Face Recognition. International Conference on Computer Vision, 2015, pp. 3721-3729

[35] Low, Ch.: Learning Compact Discriminant Local Face Descriptor with VLAD. Asia-Pacific Signal and Information Processing Association Annual Summit and Conference, 2015, pp. 825-833

[36] Xi, M., Chen, L., Polajnar, D. and Tong, W.: Local Binary Pattern Network: A Deep Learning Approach For Face Recognition. International Conference on Image Processing, 2016, pp. 3224-3228

[37] Nikan, S. and Ahmadi, M.: Effectiveness of Various Classification techniques on Human Face Recognition. International Conference on High Performance Computing & Simulation, 2014, pp. 651-655

[38] Liao, S. and Chung, A.: Face Recognition by Using Elongated Local Binary Patterns with Average Maximum Distance Gradient Magnitude. Conference on Computer Vision, 2007, pp. 672-679

[39] Wang, B., Li, W. and Liao, Q.: Face recognition based on nonsubsampled contourlet transform and block-based kernel Fisher linear discriminant. IEEE International Conference on Acoustics, Speech and Signal Processing (ICASSP) 2012, pp. 1533-1536

[40] Fan, K. and Hung, T.: A Novel Local Pattern Descriptor - Local Vector Pattern in High-Order Derivative Space for Face Recognition. IEEE Transactions on Image Processing, Vol. 23, No. 7, 2014, pp. 2877-2891

[41] Juneja, K., Verma, A., and Goel, S.: An Improvement on Face Recognition Rate using Local Tetra Patterns with Support Vector Machine under varying Illumination Conditions. International Conference on Computing, Communication & Automation, 2015, pp. 1079-1084

[42] Yang, Z., Jiang, Y., Wu, Y., Lu, Z., Li, W. and Liao, Q.: Weber Binary Pattern and Weber Ternary Pattern for Illumination-Robust Face Recognition. Asia-Pacific Signal and Information Processing Association Annual Summit and Conference, 2015, pp. 1050-1053

[43] Ren, J., Jiang, X. and Yuan, J.: Relaxed local ternary pattern for face recognition. International Conference on Image Processing, 2013, pp. 3680-3684

[44] Chakraborty, S., Singh, S. and Chakraborty, P.: Local Gradient Hexa Pattern: A Descriptor for Face Recognition and Retrieval. Transactions on Circuits and Systems for Video Technology, 2016, pp. 1-6

The FAR Model - the 'Rubik's Cube' of Process and Project Monitoring

Tamás Csiszér

Óbuda University, Bécsi út 96/b, 1034 Budapest, Hungary
csiszer.tamas@rkk.uni-obuda.hu

Abstract: This article introduces a newly elaborated monitoring method for projects and processes involving repetitive activities. The FAR model structures monitoring indicators according to three perspectives: 1) Focus dimension - describes if indicator is for inputs (potential), activities (efficiency) or outputs (effectiveness) 2) Attribute dimension - describes if indicator reflects quality, timing or financial characteristics of units measured; 3) Role dimension - describes if actual value of indicator is measured (measurement), calculated (differentiation) or estimated (prediction). The FAR model can be considered as a special combination of tools and principles of Balanced Scorecard, Earned Value Management and Six Sigma Business Process Management System methodologies. In this work, we present our model and how it can be applied in an operation development project. We found that the FAR model is able to alert management about events with negative effects and give the chance to implement corrections in time.

Keywords: operation development; process and project monitoring; lean six sigma; indicator; earned value method; balanced scorecard

1 Introduction

Monitoring the performance of manufacturing and service activities is one of the key success factors of process and project management. There are several approaches that support managers to identify, define, calculate and analyze indicators that can be applied for these monitoring activities. Perhaps the most popular ones are Balanced Scorecard (BSC) in strategy management, Earned Value Management (EVM) in project management and Six Sigma Business Process Management System in process and quality management (BPMS). Each of them has many different interpretations that were created to meet the requirements in different fields of application.

In this paper, we introduce a newly elaborated interpretation, the so-called FAR model, which can be considered a combination of methods mentioned above. Our aim was to create a model, which can be used for repetitive activities and can

provide synergy of balanced structure of BSC, predictive capabilities of EVM and process orientation of BPMS.

2 Methodology Background

In this section we describe briefly BSC, EVM and BPMS methods, citing the most important thoughts that prompted us to work on their novel combinations. Since these methods are widely known and applied by experts from this field, we refer mostly to those publications that introduce unusual applications or of their combinations.

The Balanced Scorecard (BSC) method was developed and introduced by Robert Kaplan and David Norton, as a performance measurement framework. They defined perspectives and metrics that reflect the non-financial aspects of the organization as well in order to give a more 'balanced' view of performance for the management. Indicators are structured into financial, customer, process and organizational capacity perspectives [Kaplan 1996]. It is not unusual that experts try to combine BSC with other methods and apply them in project and process management. Harel Eilat and his team developed a multi-criteria approach for evaluating R&D projects, combining BSC and Data Envelopment Analysis [Eilat 2008]. Alexandros Papalexandris and his fellow researchers created an integrated methodology for using BSC in quality and process related issues [Papalexandris 2005]. Mills recommends a multi-layer evaluation process derived from balanced scorecard as a combination of different techniques for information and communication technology projects [Milis 2004]. These – and dozens of other – articles demonstrate that BSC can be a good basis for achieving the goals we set for us. Nevertheless, the most important feature of BSC for us is its balanced structure.

Earned Value Management (EVM) focuses on the monitoring of costs and schedule of projects [Fleming, 2000]. Although it is widely used, according to some experts there is a need to modify it to make it capable for being applied in the monitoring of daily operation. Among others Kim highlighted that EVM can be used effectively if we assume that every activity or cost account is independent, so EVM has to be improved to be able to applied in work flows [Kim, 2000]. Paquin proposed Earned Quality Method (EQM) to assess and control the quality of the end product of a project [Paquin 2002]. Vandevoorde compared different methods from the point of view of duration forecasting [Vandevoorde 2006], demonstrating their capabilities and weaknesses. Kim looked for the reason why construction industries neglect EVM. In his paper he pointed out that EVM has 'managing by results' approach, consequently it cannot be used effectively for independent operational tasks [Kim 2010]. Using the results of these works, we apply the predictive capability of EVM in our model.

BPMS is a well-known method among process and quality management experts. It builds a standard procedure for process improvement by the definition and measurement of Key Performance Indicators (KPI). These indicators measure quality, cost and time related characteristics of inputs, processes and outputs. They are mostly used in mass production, where one of the main goals is defect and variance reduction or – in other words – yield improvement. Many articles deal with the way how BPMS can be implemented in different industries but only few of them give tips how metrics should be structured and presented. In practice, KPIs usually are organized by BSC perspectives, where process related KPIs build up internal operation layer. Among others Pyzdek underlines the importance of the harmony among strategy goals and six sigma metrics too, suggesting that BSC is able to handle process metrics [Pyzdek 2003]. Integrated Enterprise Excellence (IEE) provides another approach for managing processes by BPMS, which is based on BSC methodology too [Breyfogle 2013]. For us, process orientation of BPMS represents the biggest result.

Despite the fact that most articles underline the weaknesses of these methodologies, none of them tried to use the combination of BSC, EVM and BPMS for projects and processes with repetitive activities. In the next sections we show how this mixture can strengthen positive effects and eliminate the negative ones.

3 Theory, Results and Discussion

3.1 Specification of the FAR Model

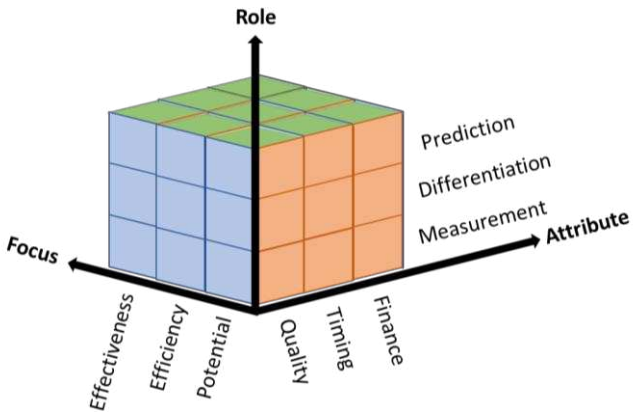

Figure 1
The "Rubik's cube' of project and process monitoring – The FAR tensor, its dimensions and their elements

In the FAR model indicators are defined by a three-dimension structure, resulting in the FAR tensor (see Figure 1).

Dimensions of the FAR tensor are as follows:

I. Focus: reflects the input-process-output approach of BPMS. Elements of this dimension are as follows:

   a) Potential indicators represent the characteristics of inputs (human and non-human resources and their competencies) used or applied in projects and processes.

   b) Efficiency indicators represent the characteristics of activities conducted by resources.

   c) Effectiveness indicators represent the characteristics of products and services produced and served by activities.

II. Attribute: reflects the project management triangle. Elements of this dimension are as follows:

   a) Quality indicators represent technical, functional, design etc. related attributes of Focus groups.

   b) Timing indicators represent time related attributes of Focus groups.

   c) Finance indicators represent cost and revenue related attributes of Focus groups.

III. Role: reflects the structure of EVM. Elements of this dimension are as follows:

   a) Measurement indicators represent actual value of project nature.

   b) Differentiation indicators calculate deviation of actual value from target value.

   c) Prediction indicators calculate estimated value of related measurement indicators to and at the time of project closing.

In all dimensions there are balances among the elements:

A. Focus - balance of participants: natures of outputs are determined by inputs and the way we transform them to products. Since inputs are provided by external and internal suppliers, potential indicators refer to their performance. Operation is conducted according to our technology and methodology, so efficiency indicators refer to our performance. Attributes of outputs have to meet requirements, so effectiveness indicators refer to customer satisfaction.

B. Attribute – balance of decisions: it highlights the mutual dependencies of quality, cost and time, the importance of thinking through the effects on

attributes when changes are implemented regarding scope, schedule or budget.

C. Role – balance in time: measurement indicators refer to past, differentiation indicators refer to present and prediction indicators refer to future.

Figure 2 summarizes the balanced structure of FAR tensor.

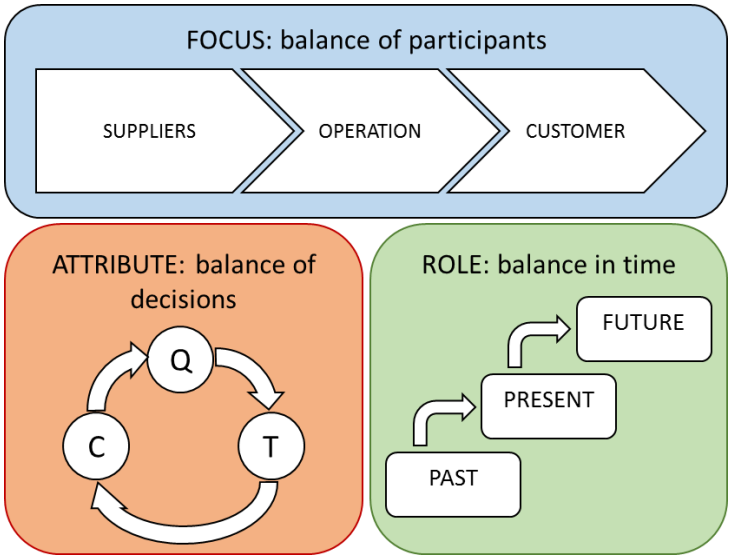

Figure 2
Balanced structure of FAR tensor

3.2 Specification of FAR Indicators

All attribute indicators can be presented in indicator trees with their logical connections according to Role dimensions. These indicator trees can be interpreted by Focus dimension in different ways. Quality indicators can be used as potential, efficiency and effectiveness indicators as well. Financial indicators can be applied as potential and effectiveness indicators. Timing indicators are relevant only for efficiency. So, the FAR model does not mean that every combination of elements of dimensions exist. These are the application rules in general, which include the most important metrics. In special cases some of them could not be applied, while in some other cases new ones (e.g. license cost of methodology or technology in cost (attribute) and efficiency (focus) combinations or waiting time of inputs in timing (attribute) and potential (focus) combinations) should be defined. Measurement indicators interpreted by Focus dimensions are presented in the interpretation tables in the following chapters.

Indicators are denoted by the combination of the first letters of the words that define the indicators themselves. However some FAR indicators are similar to or the same as indicators of its 'parent methodologies', to highlight the difference among BPMS, BSC, EVM and FAR, we used different acronyms.

3.2.1 Quality (Attribute) Indicators

Measurement indicators:

i. Number of Opportunities for defect: O [No] – Number of potential failures.

ii. Number of Defects: D [No] – Number of defects realized.

iii. Number of Defective Items: DI [No] – Number of items having failures.

iv. Correction Time per Defect: CTD [h] – Time needed to fix a defect related problem.

v. Correction Cost per Defect: CCD [$] - Cost of fixing a defect related problem.

vi. Item at Complete: IaC [No] – How many items have to be delivered during the process or project?

vii. Number of Measurement Cycles Left: MCL [No] - How many cycles of measurement (e.g. weeks) are between the calculation date and the project finish date.

Differentiation indicators:

i. Defect Per Opportunities: DPO – What proportion of potential failures is realized.

ii. Defects Per Defective Items: DPDI – Average number of defects for an item.

iii. Need for Extra Time due to Defects: ETD [h] – By how much time the planned duration of the project enlarges because of extra work for fixing failures (rework time).

iv. Need for Extra Cost due to Defects: ECD [$] - By how much money the planned total cost of the project increased because of extra work for fixing failures (rework cost).

Prediction Indicators:

i. Estimated Extra Time due to Defects at Complete: ETDaC [h] – How much extra time is needed to complete the project if the quality of inputs, activities and outputs will have the same level in the following project phases as they had at the time of calculation date.

ii. Estimated Extra Cost due to Defects at Complete: ECDaC [$] - How much extra cost is needed to complete the project if the quality of inputs, activities and outputs will have the same level in the following project phases as they had at the time of calculation date.

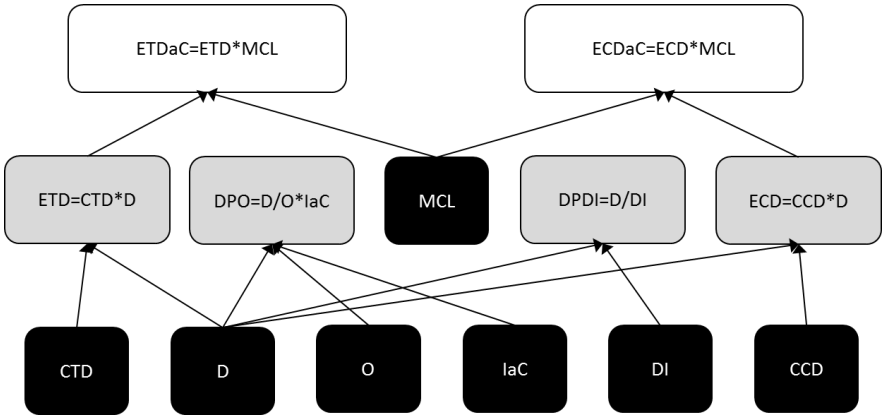

Figure 3
Quality Indicator Tree

Quality indicators can be applied as potential, efficiency and effectiveness indicators as well. Table 1 gives some examples for interpretation.

Table 1
Interpretation of Quality Indicators by Focus Dimension

Quality Indicator	Focus / Potential	Focus / Efficiency	Focus / Effectiveness
Number of Opportunities for defect: O [No]	Potential failure of inputs	Potential failure of process or project activities	Potential failure of outputs
Number of Defects: D [No]	Defects of inputs	Defects of process or project activities	Defects of outputs
Number of Defective Items: DI [No]	Defective inputs	Defective process or project activities	Defective outputs
Correction Time per Defect: CTD [h]	Time needed for repairing or replacing defective input (with one defect)	Time needed for repeating related activity	Time needed for correcting output
Correction Cost per Defect: CCD [$]	Cost of repairing or replacing defective input (with one defect)	Cost of repeating related activity	Cost of correcting output
Items at Complete: IaC [No]	Number or amount of inputs	Number of process or project activities	Number or amount of outputs

3.2.2 Timing (Attribute) Indicators

Measurement indicators:

i. Completeness of activities: C [%] – What percent of activities is completed.

ii. Start Date of activities: SD [mm.dd.yyyy] – The date when the process or project started.

iii. Planned Completeness Date: PCD [mm.dd.yyyy] - The planned date of completeness denoted by C.

iv. Actual Completeness Date: ACD [mm.dd.yyyy] - The actual date of completeness denoted by C.

Differentiation indicators:

i. Difference between Actual and Planned Date: DAPD [day] – How many more or less calendar days were needed to reach the completeness denoted by C.

ii. Time from Start Date: TSD [day] – How many calendar days passed since the start of the process or project.

Prediction Indicators:

i. Estimated Time at Complete: TaC [day] – Total duration of process or project.

ii. Estimated Time to Complete: TtC [day] – How much time (calendar day) is needed from the calculation date to complete the process or project.

iii. Estimated Date of Completion: DoC [mm.dd.yyyy] – The date of last day of the process or project.

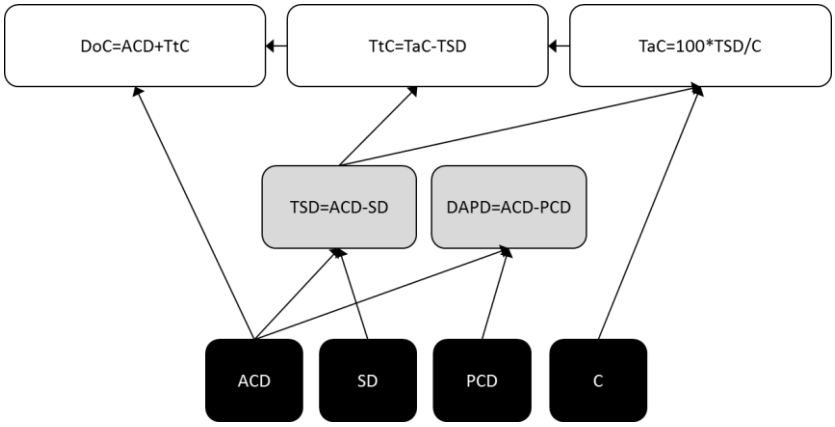

Figure 4
Timing Indicator Tree

Financial indicators can be applied as efficiency indicators. Table 2 gives some examples for interpretation.

Table 2
Interpretation of Timing Indicators by Focus Dimension

Timing Indicator	Focus / Potential	Focus / Efficiency	Focus / Effectiveness
Completeness of activities: C [%]	N/A	What part of activities is completed or what is the completion rate of activities	N/A
Start Date of activity: SD [mm.dd.yyyy]	N/A	The date when assessed activities have started	N/A
Planned Completeness Date: PCD [mm.dd.yyyy]	N/A	Planned date of current completeness of assessed activities	N/A
Actual Completeness Date: ACD [mm.dd.yyyy]	N/A	Actual date of current completeness of assessed activities	N/A

3.2.3 Financial (Attribute) Indicators

Measurement indicators:

i. Planned Cost to Date: PCtD [$] – Planned cost from the process or project start till the date of calculation.

ii. Actual Cost to Date: ACtD [$] – Money spent from the process or project start till the date of calculation.

iii. Planned Income to Date: PItD [$] - Planned revenue from the process or project start till the date of calculation.

iv. Actual Income to Date: AItD [$] - Actual revenue from the process or project start till the date of calculation.

Differentiation indicators:

i. Difference between Actual and Planned Cost: DAPC [$] – How much more or less cost was needed to the date of calculation.

ii. Difference between Actual and Planned Income: DAPI [$] – How much more or less revenue was earned to the date of calculation.

Prediction Indicators:

i. Estimated Cost at Complete: CaC [$] – Total cost of process or project.

ii. Estimated Cost to Complete: CtC [$] – How much cost is needed from the calculation date to complete process or project.

iii. Estimated Income at Complete: IaC [$] – Total revenue of the process or project.

iv. Estimated Income to Complete: ItC [$] – How much revenue is earned from the calculation date to complete process or project.

v. Estimated Margin at Complete: MaC [$] – What is the estimated margin of the process or project.

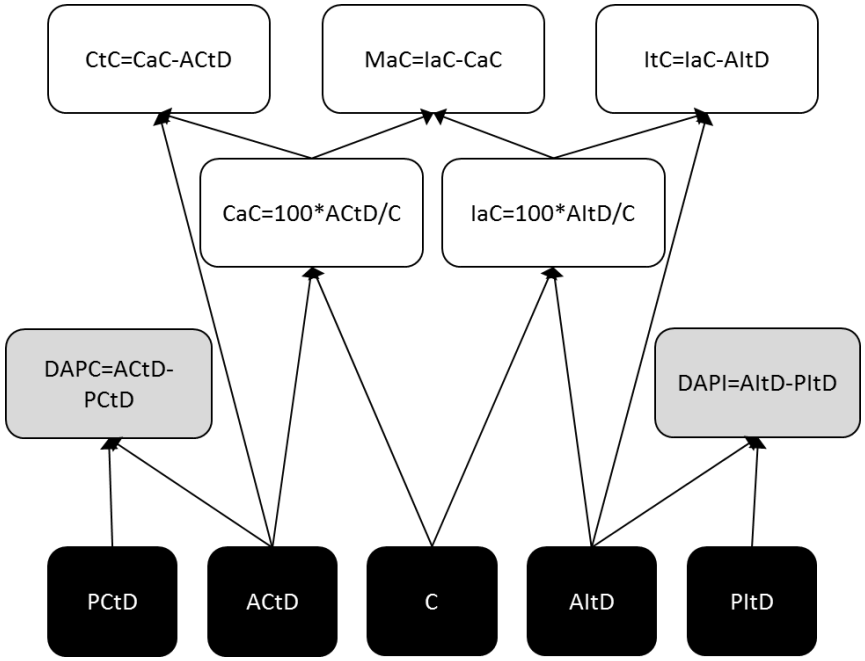

Figure 5
Financial Indicator Tree

Financial indicators can be applied as potential and effectiveness indicators. Table 3 gives some examples for interpretation.

Table 3
Interpretation of Timing Indicators by Focus Dimension

Financial Indicator	**Focus / Potential**	**Focus / Efficiency**	**Focus / Effectiveness**
Planned Cost to Date: PCtD [$]	Planned cost of inputs	N/A	Planned cost of outputs
Actual Cost to Date: ACtD [$]	Actual cost of inputs	N/A	Actual cost of outputs

Planned Income to Date: PItD [$]	N/A	N/A	Planned income of outputs
Actual Income to Date: AItD [$]	N/A	N/A	Actual income of outputs

4 Case Study

A middle sized Hungarian subsidiary of an international financial company started an operation development project aimed to optimize one of its core processes. After analyzing the current state of operation, experts defined more than 200 development actions, which were handled as small projects. Despite that they had to produce different outputs, most of them had similar structure of activities: planning tasks, developing, testing and implementing solutions. These small projects were considered the repetitive elements of the operation development program. This program was monitored by the FAR model.

Standard Measurement indicators were defined for all actions according to the FAR model. Table 4 shows these indicators, with actual and target values.

Table 4
Interpretation of Financial Indicators by Focus Dimension

FAR Indicator	**Interpretation of indicator in operation development program (examples)**
Number of Opportunities for defect: O [No]	Defect types: missing information, unavailable resources, missing deadlines, unacceptable result. Actual value: 4. Target value: N/A.
Number of Defects: D [No]	No of defects for each type. Actual value: according to measurement. Target value: 0.
Number of Defective Items: DI [No]	Actions having defects as defined above. Actual value: according to measurement. Target value: 0.
Correction Time per Defect: CTD [h]	Actual value was calculated for the four types of defects according to what kind of particular defect occurred: • Missing information: time of getting particular information • Unavailable resources: time of involving or replacing a particular resource • Missing deadlines: time of completing tasks linked to a particular deadline • Unacceptable result: time of correcting particular outputs If multiple defects for a defect type occurred, average of correction time was calculated. Target value was 0 for all defects.

Correction Cost per Defect: CCD [$]	Actual value was calculated for the four types of defects according to what kind of particular defect occurred: • Missing information: cost of getting particular information • Unavailable resources: cost of involving or replacing a particular resource • Missing deadlines: cost of completing tasks linked to a particular deadline • Unacceptable result: cost of correcting particular outputs If more than one defect in a defect type occurred, average of correction cost was calculated. Target value was 0 for all defects.
Item at Complete: IaC [No]	No of small projects. Actual value: 210. Target value: N/A.
Number of Measurement Cycles Left: MCL [No]	No of weeks between calculation date and project finish date. Actual value: according to measurement. Target value: N/A.
Completeness of activities: C [%]	Completeness of the whole project. Actual value: according to measurement. Target value: planned completeness.
Start Date of activity: SD [mm.dd.yyyy]	Start date of the whole project. Actual value: real start date. Target value: N/A.
Planned Completeness Date: PCD [mm.dd.yyyy]	Planned date of current completeness of assessed small projects. Actual value: planned date. Target value: N/A.
Actual Completeness Date: ACD [mm.dd.yyyy]	Actual date of current completeness of assessed small projects. Actual value: recorded date. Target value: planned date.
Planned Cost to Date: PCtD [$]	Cost of results and inputs of small projects according to its plan. Actual value: planned cost. Target value: N/A.
Actual Cost to Date: ACtD [$]	Actual cost of results and inputs of small projects. Actual value: according to measurement. Target value: planned cost.
Planned Income to Date: PItD [$]	N/A
Actual Income to Date: AItD [$]	N/A

Actual values of indicators were measured and calculated on a weekly basis. Values were recorded in Excel sheets. Each indicator had an information box with indicator name, unit, actual and target values and their qualifications marked by the following colors:

- Red means the actual value is worse than target value
- Green means the actual value is better than or equal to target value
- White means that there is not a planned or actual value

Parts of the indicator box are demonstrated on Figure 6.

Indicator name [unit]	
Actual value	Target value
Color mark	

Figure 6
Content of indicator box

Figure 7, Figure 8 and Figure 9 show the elements of one of the weekly reports of indicators with hypothetic values.

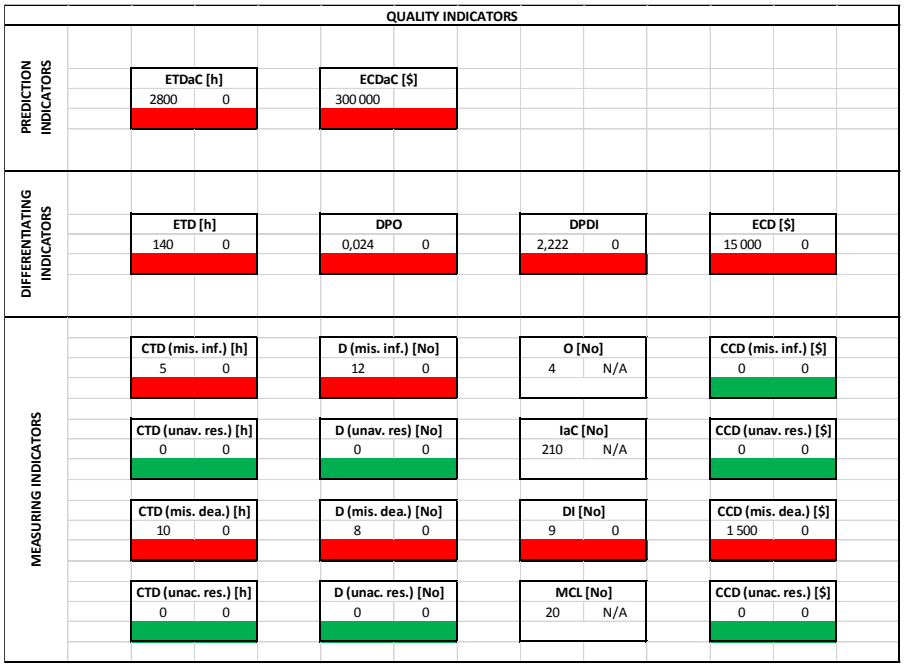

Figure 7
Quality indicators in weekly report of the FAR model

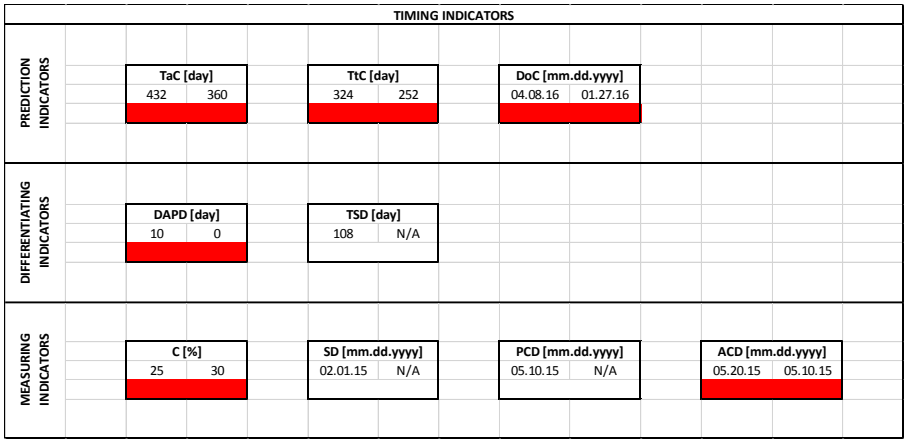

Figure 8
Timing indicators in weekly report of the FAR model

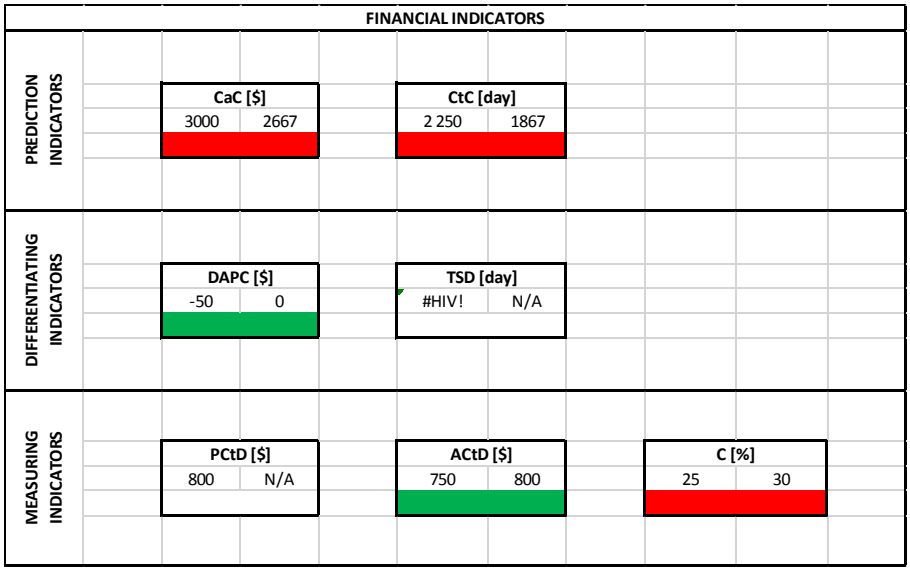

Figure 9
Financial indicators in weekly report of the FAR model

The FAR indicator structure included sub-indicators too, which were the interpretation of the project metrics for small projects. In addition, the actual values of these indicators were presented – among others - as run-charts, which helped management to assess the change of the values of the indicators, week-by-week.

Owing to the application of this structure, the management board was able to get detailed information about the progress of small projects, regularly, recognize the negative difference between actual and target values, define corrective activities and check the effects of their implementation.

Conclusions

Application of the FAR model proved its ability to monitor process or project activities and provide information about negative events and their effects. Due to its structure, management can recognize, in time, if there is something to be corrected regarding inputs, activities and/or outputs, from the perspective of quality, time and cost. Having information on the difference between actual and target values, the future values of indicators can be estimated. Further developments should focus on the application of the FAR model or any similar models for other types of projects and programs.

Aknowledgement

FAR model could not be elaborated and tested without the cooperation of the staff of Resultator Ltd.

References

[1] Breyfogle, F (2013): The Business Process Management Guidebook: An Integrated Enterprise Excellence BPM System, Citius Publishing

[2] Eilat, H. et al. (2008): R&D project evaluation: An integrated DEA and balanced scorecard approach, Volume 36, Issue 5, pp. 895-912, Omega: The International Journal of Management Science

[3] Fleming, Q. W et al. (2000): Earned Value Project Management, 3rd Edition, Project Management Institute

[4] Kaplan, R. et al. (1996): The Balanced Scorecard: Translating Strategy into Action, Harvard Business Review Press

[5] Kim, Y. et al. (2010): Management Thinking in the Earned Value Method System and the Last Planner System, Volume 26, Issue 4, Journal of Management in Engineering

[6] Milis, K. et al (2004): The use of the balanced scorecard for the evaluation of Information and Communication Technology projects, Volume 22, Issue 2, February 2004, pp. 87-97, International Journal of Project Management

[7] Papalexandris, A. et al. (2005): An Integrated Methodology for Putting the Balanced Scorecard into Action, Volume 23, Issue 2, April 2005, pp. 214-227, European Management Journal

[8] Paquin, J. P. et al. (2002): Assessing and controlling the quality of a project end product: the earned quality method, Volume: 47 Issue: 1, IEEE Transactions on Engineering Management

[9] Pyzdek, T. (2003): The Six Sigma Handbook, McGraw-Hill Companies, Inc.

[10] Vandevoorde, S. et al. (2006): A comparison of different project duration forecasting methods using earned value metrics, Volume 24, Issue 4, May 2006, pp. 289-302, International Journal of Project Management

[11] Yong-Woo Kim et al. (2000): Is the earned-value method an enemy of work flow, Eighth Annual Conference of the International Group for Lean Construction (IGLC-8)

Data Structures for Pattern and Image Recognition and Application to Quality Control

Ewaryst Rafajłowicz

Faculty of Electronics, Wroclaw University of Science and Technology,
ul. Janiszewskiego Street 11/17, 50-372 Wrocław, Poland
ewaryst.rafajłowicz@pwr.edu.pl

Abstract: Our aim is to propose a systematics (taxonomy) of data structures that arise in classifying patterns and images, starting from unrelated vectors and ending with matrix and tensors for storing video sequences. Then, we discuss possibilities of classifying such structures under matrix (tensor) normal distribution assumptions. Finally, we provide a case study of using classifiers for quality control of laser-based additive manufacturing.

Keywords: pattern recognition; image recognition; data structures; additive manufacturing; image-based control; matrix normal distribution; Kronecker product; covariance structure estimation; cloud storage

1 Introduction

Pattern classification (recognition) is one of the oldest tools of the artificial intelligence. It has been developing for more than fifty years (see [1]). The main emphasis of researchers was and still is put on developing methods and algorithms of learning classifiers [2]. The mainstream of research is concentrated on recognizing patterns that are modeled as random vectors in the Euclidean space.

When images are recognized, the typical approach is based on their preprocessing in order to extract relevant features from them and to form vectors, which are then classified using classifiers dedicated to vector input data. A success of such an approach depends not only on a selected classifier and its learning but mainly on selecting proper features. Clearly, at the beginning of the era of computers, this approach was the only possible. Even at the beginning of the nineties, a typical PC had troubles with processing a moderate size image. In recent twenty years, however, the speed of computers and mainly a rapid growth of storage devices are developing so quickly that we are able to cluster and recognize images as a whole, without laborious (and risky) process of defining and extracting relevant features.

1.1 Motivation

Our main motivations come from computer science and decision-making theory. However, putting an emphasis on data structures for images and image sequences recognition one has also immediate associations and questions about how brain stores images. There are a large number of papers on these topics (see [3], [4], [5], [6] for an excerpt of those which are close to the topics of this paper). It is also known (see [7]) that process of memorizing and the retrieval of images in our brain is very complicated with many feedbacks. Having this in mind, we would like to touch only one aspect of the memorizing images in the long-term memory, namely, how our brain copes with a very common kind of redundancy caused by different illumination of the same object (see Figure 1 for the author's photo). We certainly are not able to answer this question, but one of the mathematical tools discussed in this paper, namely, the Kronecker product of matrices provides a simple model for coping with this kind of redundancy. In fact, images shown in Figure 1 have been obtained as the Kronecker product of the original image and the vector [1, 0.6, 0.4] (see [8] for more facts concerning the Kronecker product, tensors, and operations on them).

Figure 1
One of our motivations for considering the Kronecker product structure for image sequences. The sequence of images that are taken with different illuminations can be stored as the Kronecker product of the first of them and the vector [1, 0.6, 0.4].

On the other hand, one can already meet databases containing one trillion images (see [9]) and one can expect that – due to cloud resources – even larger databases can be virtually organized. Recent examples which indicate that there are needs for cloud image databases and for image classification, grouping, clustering etc. are provided in [10], [11], [12]. From the viewpoint of an image cloud organization, managing and retrieval it is of importance to standardize data structures. In Section 2 we provide a brief review of data and images structures that are convenient for their classification.

The results of classifying images can be used as input for data mining in the so-called Big Data context (see [13] for the recent survey on these topics). However, in many cases, the results of classifying images can be applied directly to decision making, as it is illustrated in this paper. Namely, we propose and describe briefly a decision-making system for additive manufacturing, which is based on detecting changes between short image sequences.

As it follows from the following excerpt of papers on industrial image processing: [14], [15], [16], [17], one can expect that needs for storing and processing huge, dedicated databases of images will be growing and cloud facilities can be an adequate answer for these needs.

Concerning possible applications of the results presented in this paper, they are directed to image-based decision-making that is based on learning. In particular, the image-based quality control is our main concern. As an illustration, we provide – in Section 6 -- an example of quality control of a laser additive manufacturing. Another example of possible applications is discussed in [18]. In [18] the states of an industrial gas burner are observed by a camera and used for decision-making. Notice that in opposite to the present paper, in [18] images are clustered, i.e., the learning without a teacher is applied.

1.2 Organization of this Paper

Our first aim is to provide a brief review of data structures that have already appeared in pattern recognition literature. The need for such a data structures for pattern and image recognition review stems from the fact that the topics of data structures for pattern recognition and/or clustering are discussed much less frequently than those of learning classifiers and they are scattered in the literature. Furthermore, relationships between data structures and the corresponding classifiers are frequently neglected. In our review we take into account the following features of data structures:

- An algebraic representation of patterns (images) as (vectors, matrices, tensors)
- Importance (or not) of ordering in time
- Relationships (dependencies) between class labels in a learning sequence
- An internal correlation structure of patterns (images) as well as possible correlations between them

Then, we shall discuss one more face of the ”curse of dimensionality” that appears when we consider the estimation problem of correlation (covariance) structures of images and their sequences. This discussion leads to the need of imposing simplifying assumptions on class densities of patterns, images and their sequences. As an adequate set of class distributions, we select the matrix (tensor) normal distributions that have a special, the Kronecker product, structure of patterns (images) covariance structure.

In Section 4, we derive the Bayes decision rule for the matrix normal distribution (MND) Our next step is to discuss how to estimate the covariance matrices of MND and how to use them to plug-in into the Bayes optimal decision rules.

Finally, we consider an application of classifiers as change detectors in image sequences. It occurred that even the simplifying MND covariance assumption is not sufficient for estimating the covariance structure of sequences of images to be classified and the ”competition” is won by a simple 5 nearest neighbor (5-NN) classifier, which neglects (at least partially) the covariance structure of sequences of images. But, as it is demonstrated at the last part of the paper, it is sufficient for a proper decision making in the additive manufacturing example.

Clearly, change detection is not the only application of structured image data classification. In fact, the emerging ”data-intensive science”, considered as a part of cloud databases (see [19]), will need classification and clustering of structured image sets even more than earlier.

Summarizing, the paper is structured as follows:

- Our main goal is to detect a change in image sequences – considered as the Bayes classification problem -- is discussed in Section 1.3.
- As the first step toward its solution, in Section 2 we provide the review of data structures for classification, taking into account not only data organization but also their correlation dependences. As the result, the class of matrices (or tensors) having the multivariate normal distributions is selected as a sufficiently general model for our purposes.
- In Section 3, the most important features of the MND’s are summarized for the reader convenience since this specific class of probability distributions is not so widely known as the general class of multivariate normal distributions (GCMND).
- The Bayes classifier for MND classes is derived in Section 4. Although the Bayes classifier for GCMND is well known for many decades, its version for MND requires a re-derivation. The reason is in that MND is a sub-class of GCMND that has specific features, which should be reflected in a structure of the Bayes classifier and in the way of its learning.
- The learning procedure is proposed in Section 5. It takes into account both the specific structure of the Bayes classifiers for MND data and the specific way of estimating inter-row and inter-column covariance matrices of MNDs.
- Finally, in Section 6, we provide the results of testing the empirical Bayes classifier for MND images that arise in a laser additive manufacturing process.

1.3 Change Detection from Images

The idea of applying classifiers as change detectors in a sequence of images is depicted in Figure 2. It looks simple, but difficulties of its application depend on:

1) A priori knowledge about class densities (parametric or nonparametric),
2) A data structure (vectors, matrices, tensors),
3) Correlations inside each image and between them.

Success depends on a proper combination of 1) and 3). We refer the reader to [20], [21] for other approaches to change detection in image sequences.

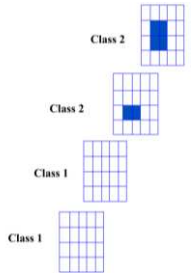

Figure 2

Main idea: change detection in an image sequence as the Bayes classification problem. At the first two frames (from below) changes are not present – they are classified to Class 1. When changes occur (upper two frames) and if they are correctly detected, then these frames are classified to Class 2 and the change is declared.

2 Data Structures for Classification

In this section we review data structures that are used in classification tasks, putting the main emphasis on sequences of images to be classified.

2.1 Classic Data Structure

In the classic problem statement, a pattern to be classified is a vector $x \in R^d$, say. The learning sequence $(x_i, L_i), i = 1,2,\ldots$ consists of such vectors and class labels L_i attach to them (see Figure 3). Usually, L_i's are positive integers. In the standard, setting pairs $(x_i, L_i), i = 1,2,\ldots$ are assumed to be random and mutually independent. Their ordering in time is not taken into account when classifications are made. Within elements of x_i vectors correlations (or more complicated statistical dependence) are allowed.

2.2 Data Structures Arranged according to Class Labels

As far as we know, the first attempts of imposing a structure on the learning sequence of vectors $(x_i, L_i), i = 1,2,\ldots$ concentrated on subsequent class labels. Namely, it was observed that combinations of letters in words appear with different frequencies in a given natural language. This and other almost classic structures are listed below.

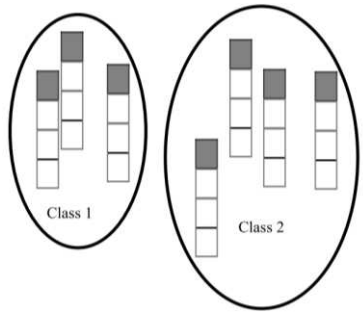

Figure 3
Classic structure: independent and identically distributed (inside classes) vectors of features with correlated elements plus class labels (gray), ordering in time – not taken into account

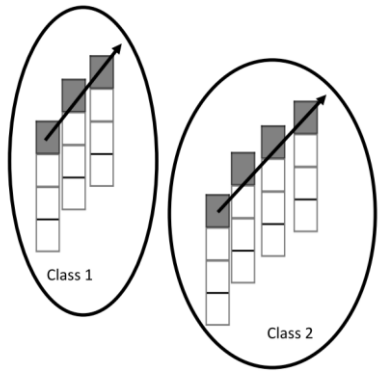

Figure 4
Almost classic structure: independent and identically distributed (inside classes) vectors of features with correlated elements plus class labels (gray), forming the Markov chain, ordering in time is taken into account, see [16]

- Markov chain dependence of labels: the result of the previous classification (e.g., a letter in a word) influences the next classification (e.g., the next letter, see [22]).
- Hierarchy of class labels – patterns arranged into classes, then – inside each class – organized into subclasses. The corresponding classifiers are

also hierarchical. The first attempts can be traced back to the eighties [23], [24] and this stream of research is still continued (see [25]).

In the Markov chain case, ordering in time of the learning sequence is important (see Figure 4). We mention the Markov chain of class labels for historical reasons only since it was one of the first attempts of imposing a structure on vectors of features to be classified. We shall not use this structure later on because it does not take into account correlations between vectors of features.

2.3 Non-Classic Matrix Structure - Repeated Observations of Patterns

An interesting, important for practice and theoretically appealing pattern recognition problem, is discussed in [26] and [27]. Namely, patterns to be classified are vectors, but this time, the learning sequence contains repeated observations of the same object. These observations are corrupted by noises (random errors). Also a new item to be classified consists of several noisy copies of the same object. Elements of each vector can be correlated. Additionally, batches of observed object can also be correlated (see Figure 5 in which possible correlations are depicted as curly brackets). Again, ordering in time appears as the important factor of this kind of data structure.

In [26] it is additionally assumed that data vectors have the normal distribution. This, in addition to the above-mentioned correlation structure, leads the authors of [26] to the conclusion that the overall structure of the learning sequence has the so-called matrix normal distribution (MND), which has a special form of the covariance matrix. Namely, its covariance matrix is the Kronecker product of covariance matrices between elements of feature vectors and between repeated observations of the same object.

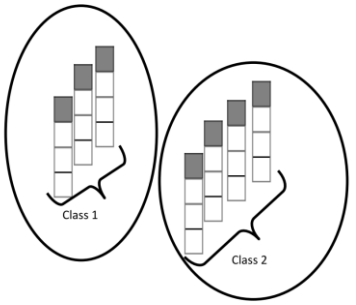

Figure 5

Non-classic matrix structure: correlated in time (curly brackets) vectors of features with correlated elements plus class labels (gray), ordering in time is taken into account, [26]. Two covariance matrices – the Kronecker product structure of the overall covariance matrix.

We shall discuss MND in more detail in the next section since we shall use it to describe image sequences. There are formal similarities between our development and [26], but there are also differences arising from the fact that in [26] random matrices arise by stacking together repeated observations of the same object, while in our case matrices are just images, coded in the gray-level convention.

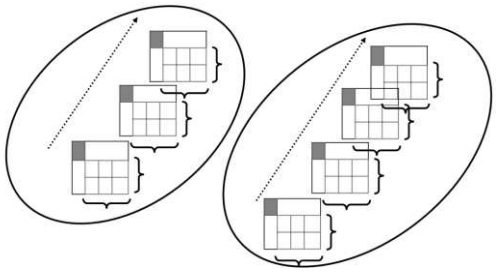

Figure 6

Basic matrix structure: uncorrelated in time matrices of features (gray levels) with correlated columns and rows plus class labels (gray). The covariance matrix is the Kronecker product structure of the row and columns covariance matrices. There is no a dependence structure imposed on class labels.

2.4 Why We Need Matrices and Tensors as Data Structures for Classification?

In this subsection, we pause our systematics of data structures for a while in order to explain why it is expedient to keep images as matrices and their sequences as tensors.

Formally, we can express matrices and tensors as vectors. Then, why it is important to keep images and tensors for classification in their original form?

1) A typical image has about 10 MPix and it is inconvenient to consider it as a vector. Indeed, when "Truecolor" images are stored, each of ten millions of pixels is represented by 24 bits.

2) The same is true for image sequences, where a vector containing a video would be rather ridiculous. A convenient structure for storing image sequences is the 3D tensor (see [8] for the definition and the fundamental operations on tensors).

3) A correlation structure is easier to impose when images are kept in its "natural" form since we can provide an interpretation to the following notions: between-rows and between-columns correlation matrices (see [26], [27]).

The last statement is explained in more detail in Section 3.2.

2.5 Basic Matrix Structure for Classifying Images

The structure described here is our main focus in this paper. It is well suited for classifying images with the main emphasis on detecting changes in their sequences. From this point of view ordering of images is important, but – in this model – previous decisions are not taken into account when a new classification is made. For example, when images of a properly produced item were recognized several times, this does not change the probability of classifying the next item as improper. Thus, there is no dependence between subsequent class labels. Each image is stored as a matrix with elements representing the gray levels of pixels. It is assumed that these matrices are normal random matrices. Their covariance structure is the Kronecker product of rows and columns covariance matrices (see Figure 6). This structure is described in Section 3.3.

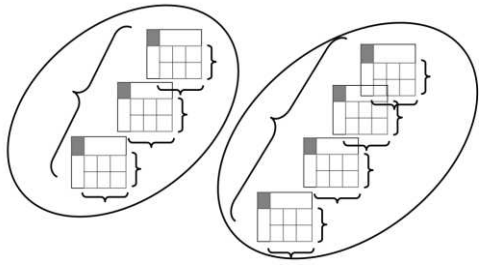

Figure 7

Tensor product structure: Correlated in time matrices of features with correlated columns and rows plus class labels (gray), ordering in time IS TAKEN into account. Three covariance matrices - the Kronecker product structure of the row and columns covariance matrices and between images covariance. There is no a dependence structure imposed on class labels.

2.6 Extended Basic Structure

The next step in the hierarchy of data structures is the one similar to that described in the previous section (see Figure 7), but additionally admitting a correlation dependence between matrices (images) in a sequence. Thus, we have three covariance matrices: between rows, columns and between matrices (images). Their Kronecker product forms the overall covariance matrix of MND. Clearly, the time ordering is important, but we do not assume a dependence between labels.

When classification is made for change detection – we classify each image but taking between images correlation into account. We omit a discussion of this case later.

2.7 Data Structures for Detecting Changes in Video Sequences

Up to now, elements of learning sequences were either vectors or matrices ordered in time (or not), correlated along different directions (or not). The next level in our hierarchy of data structures consists of sequences of matrices (tensors) that are ordered in time. In particular, this structure can describe ordered sequences of images, i.e., video sequences. Classifying such objects is as important as difficult. Notice that this time we classify all video and when we want to detect changes, we must take into account all images in the sequences. In other words, objects to be classified are 3D tensors.

This structure is much more data demanding to learn a classifier. We comment on how to reduce the amount of data in the last section, but the trick applied there can be used for short image sequences only.

2.8 Outside the Systematics

The above systematics of data structures was done from the point of view of classifying objects. For this reason, not only their algebraic description as vectors, matrices and 3D tensors was taken into account, but also importance (or not) of time ordering and a correlation structure.

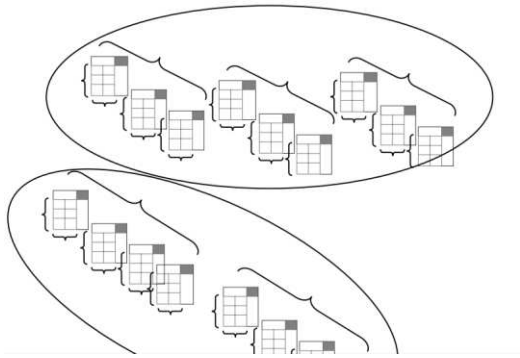

Figure 8
Change detection in video sequences: no correlation between video sequences, correlated in time matrices of features with correlated columns and rows plus class labels (gray). There is no a dependence structure imposed on class labels. This is outside our scope today.

This systematics is neither exhaustive nor complete. For example, we confined ourselves to gray level images. By adding colors (e.g., in RGB format) one can easily extend the proposed taxonomy. On the other hand, this systematics takes

only main factors influencing pattern recognition into account. Additional factors that may influence the result of classification include.

- Outer context (see [28], [18]) which is not a feature of an object to be classified, but influences the result of classification (e.g., a lighting of a scene).
- Ordered labels with different losses attached, depending on how far are current decisions from the proper one (see [29], [30], [31]).
- Topology in the space of labels (e.g., rectangular net for objects localization [32]).

Outside this systematics remains also an interesting approach proposed in [33] for semi-supervised learning. The data structure considered in this paper consists of initial labeled data and data labeled in the co-training process.

3 Bayesian Framework for Classifying Images

Our aim in this section is to provide a Bayesian framework for classifying images and – in particular – to apply it for change detection in an image sequence by classifying each image in it. Clearly, Bayesian classifiers are widely used for image classification at least from 1960', but the main stream of research and applications follows the scheme depicted in Figure 9, i.e., firstly relevant features are defined and extracted from images. Then, a vector of features is classified. The main difference between this approach and the approach considered in this paper is in that we consider images (matrices) as whole entities and they are classified as such. The present approach should not be confused with the one proposed in [21], where changes in an image sequence were detected by tracking, separately, gray levels of each pixel along the time axis (see Figure 10 for a sketch of this idea).

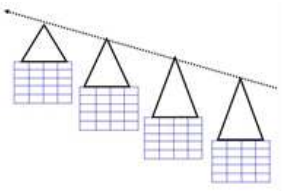

Figure 9

The most common approach: features extraction from each image and then apply a classifier or a change detector. Applicable when one can define features relevant to classes (changes).

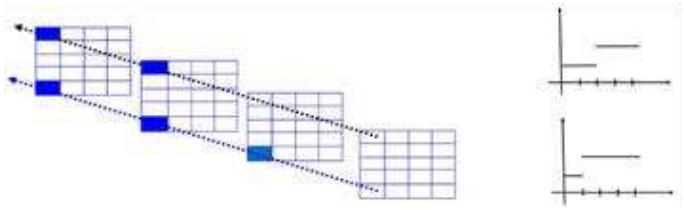

Figure 10
Spatio-temporal change detection: Changes in gray levels of each spatial location (pixel) are tracked separately, the out-of-control state is declared when a group of pixels changed.

3.1 Bayesian Classifier for Matrices (images)

Denote by X an $n \times m$ random matrix with the probability density function either $f_1(X)$ when X is drawn from Class 1 (e.g., in-control behavior) or $f_2(X)$ when X is drawn from Class 2 (e.g., out-of-control).

Remark: We confine to X's from two classes for simplicity. Immediate generalization is possible for more than one scenario of out-of-control behavior.

Let $p_1 > 0, p_2 > 0, p_1 + p_2 = 1$ be a priori probabilities that X comes from class 1 or 2. Selecting the so-called 0-1 loss function, the optimal classifier (minimizing the Bayes risk) is of the form (see [1], [2]):

classify X to Class 1 if $p_1 f_1(x) > p_2 f_2(x)$ (1)

and to Class 2, otherwise.

3.2 Lack of Data for Learning a Matrix Classifier

In practice, f_1 and f_2 unknown, but we have two learning sequences: $X_i^{(1)}, i = 1,2,\ldots,N_1$ for estimating f_1 and $X_i^{(2)}, i = 1,2,\ldots,N_2$ for estimating f_2. The classification of learning examples is assumed to be correct (done by an expert).

Data structures for pattern and image recognition. It is customary to distinguish two main approaches to learning classifiers:

I) A nonparametric approach: f_1 and f_2 are unknown and they are estimated (e.g., by the Parzen kernel method). Application of this approach to image sequences is impossible since for a typical 1 Mpix ≈

$10^3 \times 10^3$ image matrix X one would need hundreds millions of learning examples.

II) A parametric approach: f_1 and f_2 are assumed to be members of a parametric family of probability density functions, e.g., the Gaussian one. Still (almost) impossible to apply, because the covariance matrix would be as large as $10^6 \times 10^6$ for 1 MPix image. Again hundreds of millions of learning examples would be needed to estimate it.

What can we do ?

a) To apply a heuristic classifier.

b) To assume that f_1, f_2 are Gaussian and completely neglect the covariance structure (known as naive Bayes).

c) To assume that f_1, f_2 are Gaussian, but to impose "a reasonable" structure on the covariance matrix.

Such an appropriate structure of the covariance matrix possess random matrices having the probability distribution function, which is known as the matrix normal distribution (MND) and – for larger dimensions – known as multilinear normal distribution (see [34]).

3.3 Basic Facts about MND

Further, we assume that class densities are MND and they have the probability density functions of the form: for $j = 1,2$

$$f_j(X) = \frac{1}{c_j} \exp\left[-\frac{1}{2} tr\left[U_j^{-1}(X - M_j) V_j^{-1} (X - M_j)^T \right] \right] \tag{2}$$

where ^{T} stands for the transposition and det[.] denotes the determinant of a matrix in the brackets. For the normalization constants we have:

$$c_j \overset{def}{=} (2\pi)^{0.5nm} \det[U_j]^{0.5n} \det[V_j]^{0.5m}, \tag{3}$$

where $n \times m$ matrices M_j denote the class means, while $n \times n$ matrix U_j and $m \times m$ matrices V_j are the rows and columns covariance matrices of the classes, respectively, assuming that $\det[U_j] > 0, \det[V_j] > 0$. Further, we shall write shortly,

$$X \sim N_{n,m}(M_j, U_j, V_j) \text{ for } j = 1 \text{ or } j = 2 \tag{4}$$

It is well known, that the formally equivalent description of MND is the following:

$$X \sim N_{n,m}(vec(M_j), \Sigma_j) \text{ for } j=1 \text{ or } j=2 \tag{5}$$

where Σ_j is $n\,m \times n\,m$ covariance matrix of *j-th* class, which is the Kronecker product (denoted as $\otimes$) of U_j and V_j, i.e.,

$$\Sigma_j \overset{def}{=} U_j \otimes V_j, \; j=1,2 \tag{6}$$

Above, $(vec(X))$ stands for the operation of stacking columns of matrix X.

4 Bayes Classifier for Classes having Matrix Normal Distribution

In this section we assume that X is drawn from $N_{n,m}(M_j, U_j, V_j)$, for $j=1$ or $j=2$. For a while, we also assume that we know $M_j, U_j, V_j, j=2$. Our aim is to derive the Bayes classifier under the 0-1 loss function. As we shall see, the derivations closely follow those calculations that are well known for vectors with differences in algebraic manipulations.

4.1 General Case

Proposition 1. If X to be recognized is drawn from $N_{n,m}(M_j, U_j, V_j)$, for $j=1$ or $j=2$, then the Bayes classifier has the form: classify matrix (image) X to Class 1, if

$$\left[\frac{1}{2} tr\left[U_1^{-1}(X-M_1)V_1^{-1}(X-M_1)^T\right]\right] - \log(p_1/c_1) < \left[\frac{1}{2} tr\left[U_2^{-1}(X-M_2)V_2^{-1}(X-M_2)^T\right]\right] - \log(p_2/c_2) \tag{7}$$

and to Class 2, otherwise.

Proof. When M_j and $U_j, V_j, p_j, j=1,2$ are known, then from (1) and (2) we directly obtain (7).

The expressions in the brackets in (7) play the role of the Mahalanobis distance. The matrices U_j^{-1} and V_j^{-1} de-correlate rows and columns of an image, respectively.

Thus, in a general case, the optimal classifier is quadratic in X and we have to know (or to estimate) all parameters: M_j and $U_j, V_j, p_j, j = 1,2$. Their estimation is discussed in Section 5.

4.2 (Very) Special Case – Uncorrelated Matrix Elements

Let us assume that U_j, V_j are identity matrices (no correlations at all) and $p_1 = p_2 = 0.5$. Then, (7) reduces to the following: classify matrix (image) X to Class 1 if

$$\|X - M_1\|_F^2 < \|X - M_2\|_F^2 \tag{8}$$

and to Class 2, otherwise, where $\|A\|_F$ for matrix A stands for its Frobenius norm: $\|A\|_F = (tr[A^T A])^{1/2}$. In other words, classify a new matrix to the class, which mean is closer -- in the terms of the Frobenius norm.

Remark: it looks like a quadratic classifier, but in fact, it is linear in X (this will be clear later).

This is the so-called "naive Bayes classifier" and -- in spite of its simplicity-- it occurs to be very useful when we have very large vectors (matrices) of features.

4.3 (Less) Special Case – the Same Class Covariance Matrices

As is well known, in the case of classifying Gaussian random vectors with the same class covariance matrices, the Bayes classifier is linear. In this section, we show that it is also the case for classifying matrices.

Proposition 2. Let us assume that $U_1 = U_2 = U$, $V_1 = V_2 = V$, i.e., we have the same covariance structure in both classes. Define:

$$C = \frac{1}{2} tr\left[U^{-1}\left(M_1 V^{-1} M_1 - M_2 V^{-1} M_2\right)\right] + \log\left(\frac{p_1}{p_2}\right) \tag{9}$$

Then, the Bayes decision rule is: classify matrix (image) X to Class 1 if

$$tr\left[X V^{-1}\left(M_2 - M_1\right)^T U^{-1}\right] < C \tag{10}$$

and to Class 2, otherwise.

The proof follows from (7), by direct algebraic manipulations.

Apparently, (10) is linear in X and it can be rewritten as:

$$tr[XW] < C, \quad W \overset{def}{=} V^{-1}(M_2 - M_1)^T U^{-1}, \tag{11}$$

In order to interpret the result, let us rewrite (10) as follows:

$$tr\left[\left(U^{-T/2} X V^{-1/2}\right)\left(V^{-T/2}(M_2 - M_1)^T U^{-1/2}\right)\right] < C \tag{12}$$

where $U^{-T/2}$ stands for $(U^{-1/2})^T$. Hence, the decision rule is the inner product of:

a) de-correlated pattern X and

b) de-correlated difference of the class means $(M_2 - M_1)^T$.

One can consider (12) as the justification of the class of bi-linear (in weighting matrices) classifier proposed in [35].

Remark: We do not impose the Kronecker product structure on M_1 and M_2 matrices. This seems to be an excessive requirement, leading to the assumption that we have a matrix of matrices of (almost) the same elements – images. This is outside the scope of this paper.

5 Learning the Classifier – Plug-in Method

When M_j, U_j, V_j are unknown, we have two learning sequences: $X_i^{(j)}$, $i = 1,2,\ldots,N_j$, $j = 1,2$ for estimating them. For $N = N_1 + N_2$ the estimation of the mean matrices and a priori probabilities is obvious:

$$\hat{M}_j = N_j^{-1} \sum_{i=1}^{N_j} X_i^{(j)}, \quad \hat{p} = N_j / N, \quad j = 1,2 \tag{13}$$

Estimating covariance matrices: U_j, V_j is not so easy task. The fact is their maximum likelihood estimates (MLE) are not unique, i.e., they can be estimated up to a constant multiplier, does not lead to troubles since U_j, V_j appear as multiplicative pairs.

Maximum likelihood estimators (MLE) $\hat{U}_j, \hat{V}_j$ can be calculated if (see [36])

$$N_j \geq \max\left\{\frac{n}{m}, \frac{m}{n}\right\} + 1, \; j = 1,2. \tag{14}$$

Thus, it is not necessary to have: $N_j \geq mn$. This is the main advantage of imposing the Kronecker product structure on the class covariance matrices. For $m = n$ we need at least 2 images to calculate MLE's of rows and columns covariance matrices, which does not mean that for two samples we obtain good estimates.

5.2 MLE Estimators of U_j and V_j

According to [37], MLE estimators $\hat{U}_j, \hat{V}_j$ have to be calculated by solving the simultaneous set of equations:

$$\hat{U}_j = \frac{1}{N_j m} \sum_{i=1}^{N_j} \left(X_i - \hat{M}_j\right) \hat{V}_j^{-1} \left(X_i - \hat{M}_j\right)^T \tag{15}$$

$$\hat{V}_j = \frac{1}{N_j n} \sum_{i=1}^{N_j} \left(X_i - \hat{M}_j\right) \hat{U}_j^{-1} \left(X_i - \hat{M}_j\right) \tag{16}$$

for $j = 1,2$, They form the pair of matrix equations, which are usually solved as follows.

The flip-flop method:

1. Instead of $\hat{U}_j, \hat{V}_j$, use the unit matrices at r.h.s. of (15) and (16),
2. Calculate the left-hand sides of (15) and (16),
3. Re-substitute the results of the previous step into right-hand side of (15) and (16),
4. Repeat Step 2 and Step 3 until convergence.

Lemma 1. One flip-flop iteration of the above method is sufficient in order to obtain the consistent (convergent in the probability) and asymptotically efficient estimators of U_j, V_j as the number of observations from the two classes grows to infinity.

For the proof see [38]. This result forms the base for proving that the empirical classifier is asymptotically optimal.

5.2 Empirical Classifiers for Matrix Normal Class Distributions

In order to convert the Bayes classifier into empirical one, substitute $M_j \leftarrow \hat{M}_j$, $U_j \leftarrow \hat{U}_j$, e.t.c., into (7) to get the following classifier:

classify matrix (image) X to Class 1 if

$$\left[\frac{1}{2}tr\left[\hat{U}_1^{-1}(X-\hat{M}_1)\hat{V}_1^{-1}(X-\hat{M}_1)^T\right]\right]-\log(\hat{p}_1/\hat{c}_1)< \left[\frac{1}{2}tr\left[\hat{U}_2^{-1}(X-\hat{M}_2)\hat{V}_2^{-1}(X-\hat{M}_2)^T\right]\right]-\log(\hat{p}_2/\hat{c}_2) \tag{17}$$

and to Class 2, otherwise, where

$$\hat{c}_j \overset{def}{=} (2\pi)^{0.5nm}\det[\hat{U}_j]^{0.5n}\det[\hat{V}_j]^{0.5m}. \tag{18}$$

Proposition 3. If the row and column covariance matrices are estimated by the flip-flop method and a priori probabilities and the class means are estimated as in (13), then, for each fixed X, the left and the right hand sides of th empirical classifier, described as rule (17), is convergent in the probability to the left and the right hand sides of the optimal classifier (7), respectively, as the number of observations from the both classes approaches to infinity.

Proof. The consistency of the estimators in (13) is well known and it follows from the law of large numbers. The consistency of the row and column covariance matrices follows from Lemma 1. The convergence of the left- and the right-hand sides of (17) to those of (7) immediately follows from the well-known Slutsky's theorems since these expressions are either rational or continuous functions of the consistent estimators (13) or those described in Lemma 1.

5.3 Empirical Classifiers – Special Cases

1) **The empirical version of the "naive Bayes" classifier** is particularly simple:

Classify matrix (image) X to Class 1 if

$$\left\|X-\hat{M}_1\right\|_F^2 < \left\|X-\hat{M}_2\right\|_F^2 \tag{19}$$

and to Class 2, otherwise.

2) **The case of the same class covariance matrices.** It is expedient to consider two possible approaches:

A) Plug-in approach: classify X to Class 1 if

$$\hat{W} \overset{def}{=} \hat{V}^{-1}(\hat{M}_2 - \hat{M}_1)^T \hat{U}^{-1} \tag{20}$$

and $\hat{C}$ is defined analogously.

B) A direct learning of the weight matrix W. Our starting point is again the Bayes decision rule: $\mathrm{tr}[XW] < C$. Notice that this rule is not uniquely defined (we can multiply W and C by an arbitrary constant). Thus, later we take $C = 1$. Let (X_i, y_j), $i = 1,2...N = N_1 + N_2$ (both classes) be the learning sequence with class labels $y_i = -1$ for Class 1 and $y_i = +1$ for Class 2. Then, the recurrent update that minimizes one-step ahead error $(y_i - (tr[X_i W] - 1))^2$ with respect to W is of the form:

$$W_{i+1} = W_i - \gamma(y_i - (tr[X_i W] - 1))X_i^T \tag{21}$$

where $\gamma > 0$ is a small learning constant. After stopping (21) with $\hat{W}$, the decision is made according to $\mathrm{sgn}[tr[X\hat{W}] - 1]$.

5.4 Classifying whole Image Sequences

Let $q > 1$ be the length of an image sequence denoted by X, which is *n x m x q* tensor. Assume that class densities of $x = vec(X)$ have the tensor normal distribution with the same covariance $U \otimes X \otimes Z$, where Z is *q x q* inter-frame covariance matrix. The classes have different means $m_j \overset{def}{=} vec(\mathrm{M_j})$, $j = 1,2$. Then, it can be shown that the Bayes classifier is again linear in x.

MLE for estimating U, V, Z consists of three sets of equations (see [36]) and it can be solved by a flip-flop like algorithm, but – in spite of the Kronecker product covariance structure – a large amount of data is required.

Hence, a simple – heuristic – classifiers should also be taken into account to classify image sequences, as it will be demonstrated in the next section.

6 A Case Study – Quality Control of an Additive Manufacturing Process using a Camera

We shall use a classifier as change detector in a sequence of short (3 images) videos, but instead of modeling them as 3D (tensor) structures we ”glue” batches consisting of 3 subsequent images into one, larger, image and then, they will be classified as changes in one image sequence.

Caution: Applying a classifier as change detector one has to take into account an inherent difficulty of such an approach. Namely, the phenomenon that is known as the class imbalance (see, e.g., [39]), which appears here because, usually we have a much larger number of examples (images) of in-control examples than those out-of-control. Special actions (e.g., choice of the classifier or undersampling of the in-control images) have to be undertaken.

6.1 A Practical Problem to Solve

An additive manufacturing is a class of modern production processes. A large number of technics and technologies are used in this area, see [40], where the optimization of computer-aided screen printing design is discussed and [41] for the life cycle optimization of such processes. We refer the reader to the survey papers [42], [43], [44] on additive manufacturing processes.

As a vehicle for presenting possible applications of image classifiers in decision making, we selected the process known as the selective laser melting, which produces items (roughly) as follows:

- A metallic powder is poured in a precisely controlled way
- Simultaneously the powder is melted by a laser beam
- After hardening – it forms a part of a 3D body to be constructed
- The laser head, together with the powder supply nozzle, moves to the next place (in fact, phases of moving and pouring and melting the powder run simultaneously and continuously).

For a more detailed description of this kind of production processes, the reader is referred to [45]. This technology is expected to be developing in the future and it is therefore expedient to attempt to improve it to the perfection.

One of the problems is that the laser head stays longer near end-points (turning off) of a produced item (e.g., a wall). This results in a too wide ends for the produced wall (see Figure 11).

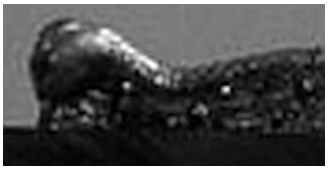

Figure 11
The left endpoint of the built wall: visible part of the wall is too wide and too high

Proposed remedy: recognize from images that the laser head is near the end point and reduce the laser power near the ends, then recognize again middle points and increase the laser power.

Many attempts were recently undertaken to cope with this problem (see [25], [46], [47]). The main difference between the approaches proposed in the papers cited above and the present one is in that here we consider the recognition that the laser head is in the near end position from short video sequences (triples of images), treated as a whole entity. Additionally, we take into account that the frequency of being in these states is much rarer than being in the ”normal” state, i.e., in a middle of the wall. To illustrate the role of the class imbalance in this case, we mention that in our laboratory experiments the wall had 600 mm, while the near end zone had 2-4 mm.

6.2 Learning Sequence of Images

Figure 12
Examples of original images of the produced wall – view from above. The left end laser head position – too thick wall end is visible and the middle one – has a proper wide of the wall.

We had about 900 images of the produced wall that were taken from above (almost) along the laser beam. Examples of original images are shown in Figure 12. These images were cropped to keep only parts of the wall and then they were grouped into new images with three elements in the way that each triple overlapped with the previous one, having two common original images. In this way, the sequence of the total length 898 was obtained. In this sequence, we have distinguished 104 triples that were labeled as ”BAD” since they contain the wall endpoints (usually too wide) and 794 triples marked as ”OK” since they a middle part of the wall, which is of the proper width. Examples of these triples are shown in Figure 13. The next step – available data were divided into two halves: the learning and testing sequence, keeping about 10% examples from ”BAD” class.

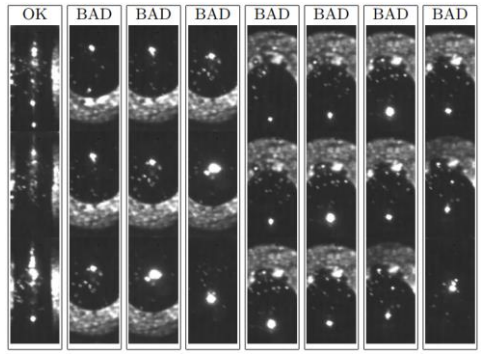

Figure 13
Examples of triples of ”glued” images to be classified as ”BAD” or ”OK”. By “OK” triples we mean those that have a proper width – they are located in the middle of the wall. By “BAD” triples we understand those that are near the endpoints of the wall – they usually are too thick. These triples are fed as inputs for classifying algorithms in order to make a decision whether to keep the laser power at the nominal value or to decrease it near the endpoints.

6.3 Naive Learning - Neglecting Class Imbalance

In this section, we provide examples of positive and negative results of learning classifiers. The goals of presenting also negative results are the following:

- To warn the reader that the task of change detection in sequences of images is nontrivial.
- To document that classifiers that are believed to be the ”golden standard”, such as support vector machines (SVM) may fail when the class imbalance appears in the learning sequence.

SVM classifier provided 88% correct classifications, when (after learning) was applied to the testing sequence. Unexpectedly, all triples classified by an expert as ”BAD” were classified to ”OK” class by the SVM classifier. Notice that seemingly good result of 88% correct classifications was obtained, because the testing sequence contained only 12% of ”BAD” items and all of them were miss-classified (see Table 1). The classifier had zero sensitivity (recall) to ”BAD” class, also F-score was zero.

Table 1
Confusion matrix of the SVM classifier

		Predicted class		sum
		BAD	OK	
Actual class	BAD	0	54	54
	OK	0	395	395
sum		0	449	

"Naive Bayes" classifier provided 68% correct classifications when applied to the testing sequence. This time, almost all "BAD" items were correctly classified, but at the expense of 1/3 "OK" examples classified erroneously. The probability of detection (sensitivity, recall) of "BAD" class is still rather low, namely, 0.26. The following classifiers were also tested: logistic regression and random forest (with 50 trees). The results were somewhat better than that for SVM and Naive Bayes, but still not satisfactory.

6.4 5-NN Classifier Robust against "Naive" Learning

Satisfactory results (without editing the learning and/or testing sequence for class imbalance) were obtained for 5 Nearest Neighbors (5-NN) classifier. Namely, it provided 98% correct classifications, simultaneously, 80% of "BAD" testing examples were correctly classified. Furthermore, there were zero false alarms, as one can check from the confusion matrix in Table 2. Thus, 5-NN classifier occurred to be robust against naive learning in the class imbalance case.

The only – well-known – drawback of this classifier is the necessity of storing the whole learning sequence, but storage resources of clouds reduce it considerably

Table 2
The confusion matrix of 5-NN classifier

Actual class	Predicted class			sum
		BAD	OK	
	BAD	43	11	54
	OK	0	395	395
sum		43	406	

6.5 MND Classifier and Comparisons

Satisfactory results were also obtained for the MND classifier. They are summarized in Table 3. The MND classifier provided 96.2% correct classifications, simultaneously, 78% of "BAD" testing examples were correctly classified. Furthermore, there were only 1% of false alarms. Thus, also MND classifier occurred to be robust against naive learning in the class imbalance case.

Table 3
The confusion matrix of MND classifier

Actual class	Predicted class			sum
		BAD	OK	
	BAD	42	12	54
	OK	5	390	395
sum		47	402	

Table 4 contains the summary of testing classifiers. As one can observe, the popular SVM and naïve Bayes classifiers provide unexpectedly bad results. The reason is in that they do not take into account the class imbalance. In opposite, 5-NN and MND classifier give quite good results since they are – to some extent – insensitive to the class imbalance. Their confusion matrices (see Table 2 and 3) are almost the same.

Table 4
Comparison of classifiers: SVM, NM – naïve Bayes, 5 NN and MND classifier, according to % of correct and % of misclassifying BAD as OK

Classifier	**SVM**	**NB**	**5 NN**	**MND cl.**
% correct	88	68	98	96.2
% BAD as OK	100	0	20	22

6.6 Decision Making

After the learning phase, the 5-NN classifier can be used for making control decisions, as shown below. Let X denote current triple of images.

1) Classify X to class ”BAD” or ”OK”.
2) If X ∈ ”BAD”, reduce the laser power (by a pre-specified amount) so as to attain the temperature of the melted lake about 2140 C (this is done by the PI controller).
3) If X ∈ ”OK”, keep the nominal laser power (or return to it, if previously X ∈ ”BAD”). The nominal laser power corresponded to the lake temperature 2445 C.
4) Acquire new image and form new X by adding it to X and throwing out the oldest one from it. Go to 1).

6.7 Laboratory Experiment

In order to check to what extent one can reduce unpleasant ”end effects”, the wall was first built with a constant laser power. In the upper panel of Figure 14, one can notice to wide ends of the wall. When the laser power was reduced each time when the laser head was near one of the endpoints (see Sec. 6.5) the resulting wall has more proper endpoints (see the lower panel of this figure). The wall has the length of about 60 mm. The speed of the laser head was about 10 mm/sec., while a stainless steel powder was supplied with the feed rate at 0.06 g/sec.

In fact, the wall at the lower panel of Figure 16 was obtained under more subtle, gradual change of the laser power, but this aspect is outside the scope of this paper.

Conclusions

Our first step was an attempt to provide some systematics for images and image sequences, from the viewpoint of their classification. At this stage, the class of images and image sequences having matrix (tensor) normal distribution was selected as sufficiently general, but still, a manageable class distribution. The MND class distributions have the covariance matrices that take into account only the inter-row and the inter-column covariances. Therefore, they are easier to estimate than in a general case. However, a specialized form of the covariance matrices leads to more specific classifiers than in the general case. Their structure was derived and their empirical forms were proposed as the classifiers for further investigations.

Finally, these classifiers were tested on the problem of detecting, from short image sequences, whether a laser head is near the endpoints of a cladding wall. In other words, the proposed classifier is used in the problem of change detection from image sequences. Its performance is quite satisfactory. Its behavior was also compared with a general purpose and widespread classifiers that do not take into account a special covariance structure or the class imbalance. As it was documented by the laboratory images, only 5-NN classifier can be comparable with the proposed approach since it is – to some extent – robust against a naïve learning.

Clearly, one can consider other methods for image feature representation and classification, e.g., in [47] the spectral and wavelet analysis as feature extraction techniques were employed, in [48] the feature extraction is based on a combination of a self-organized map used for image vector quantization and those generated by a neural network, a kernel sparse representation, which produces discriminative sparse codes to represent features in a high-dimensional feature space, is proposed in [49], while in [50] non-conventional approaches to feature extraction were proposed. A feature extraction is a common focal point of all these approaches. It is laborious, human-invented and dedicated to a particular application. In opposite, we stress that the proposed approach does not need a feature extraction step. Instead, "raw" images are supplied as inputs for a classifier, providing an acceptable level of proper classifications. This approach is less laborious, but its applicability is limited to cases when there is no need to consider very subtle differences between images.

The proposed approach may be useful, at least, at one more area of applications, namely, in using classifiers to detect states of industrial gas burners from image sequences (see [39]). It seems that further efforts are necessary in order to sketch a wider class of applications for which the proposed approach outperforms a general purpose classifiers when they are applied to image sequences.

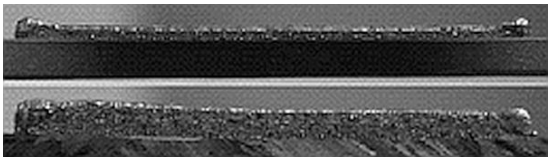

Figure 14
Upper panel – the wall produced with constant laser power along the wall length. Lower panel – the wall produced with controlled laser power trajectory along the pass.

Acknowledgement

This research has been supported by the National Science Center under grant: 2012/07/B/ST7/01216.

Special thanks are addressed to Professor J. Reiner and to MSc. P. Jurewicz from the Faculty of Mechanical Engineering, Wroclaw University of Technology for common research on laser power control for additive manufacturing.

The author express his thanks to the anonymous reviewers for many suggestions, leading to the improvements of the presentation.

References

[1] Fukunaga K.: "Introduction to Statistical Pattern Recognition", Academic Press, 2013

[2] Devroye L., Gyorfi L., Lugosi G.: "A Probabilistic Theory of Pattern Recognition", Springer Science & Business Media, 2013

[3] Han J., Chen C., Shao L., Hu X., Han J., Liu T.: "Learning Computational Models of Video Memorability from FMRI Brain Imaging", IEEE Trans. on Cybernetics, 45(8), 2015, pp. 1692-1703

[4] Ninio J.: "Testing sequence effects in visual memory: clues for a structural model", Acta Psychologica, 116(3), 2004, pp. 263-283

[5] Schyns P. G., Gosselin F., Smith M. L.: "Information processing algorithms in the brain", Trends in Cognitive Sciences, 13(1), 2009, pp. 20-26

[6] Stadler W., Schubotz R. I., von Cramon D. Y., Springer A., Graf M, Prinz W.: "Predicting and memorizing observed action: difierential premotor cortex involvement", Human Brain Mapping, 32(5), 2011, pp. 677-687

[7] Fulton, J. T., "Biological vision", Trafford, 2004

[8] Lee, N., Cichocki, A., "Fundamental tensor operations for large-scale data analysis using tensor network formats", Multidimensional Systems and Signal Processing, 29(2), 2018, pp. 921-960

[9] Sean A., Jason L.: "Building and using a database of one trillion natural-image patches", IEEE Trans. Computer Graphics and Applications 31(1), 2011, pp. 9-19

[10] Tsymbal A., Meissner E., Kelm M., Kramer M.: "Towards cloud-based image-integrated similarity search in big data", Biomedical and Health Informatics (BHI), 2014 IEEE-EMBS International Conference on, IEEE, 2014, pp. 593-596

[11] Assent I.: "Clustering high dimensional data", Wiley Interdisciplinary Reviews: Data Mining and Knowledge Discovery, 2(4), 2012, pp. 340-350

[12] Lin F., Chung L, Wang C, Ku, W., and Chou T.: "Storage and Processing of Massive Remote Sensing Images Using a Novel Cloud Computing Platform", GIScience & Remote Sensing, 50(3), 2013, pp. 322-336

[13] Yaqoob I. et al.: "Big data: From beginning to future", Int. J. Information Management, 36(6), 2016, pp. 1231-1247

[14] Megahed F. M., Woodall W. H., Camelio J. A.: "A review and perspective on control charting with image data", J. Quality Technology, 43(2), 2011, pp. 83-98

[15] Duchesne C., Liu J. J., MacGregor J. F.: "Multivariate image analysis in the process industries: A review", Chemometrics and Intelligent Laboratory Systems, 117, 2012, pp. 116-128

[16] Bharati M. H., MacGregor J. F.: "Multivariate image analysis for real-time process monitoring and control", Industrial & Engineering Chemistry Research, 37(12), 1998, pp. 4715-4724

[17] Zou C., Wang Z., Tsung F.: "A spatial rank-based multivariate EWMA control chart", Naval Research Logistics, 59(2), 2012, pp. 91-110

[18] Rafajlowicz E., Rafajlowicz W.: "Image-driven decision making with application to control gas burners", IFIP International Conference on Computer Information Systems and Industrial Management, Springer, 2017, pp. 436-446

[19] Lenhardt C., Conway M., Scott E., Blanton B., Krishnamurthy A., Hadzikadic M., Vouk M., Wilson A.: "Cross-institutional Research Cyber Infrastructure for Data Intensive Science", High Performance Extreme Computing Conference (HPEC), IEEE, 2016, pp. 1-6

[20] Prause A., Steland A.: "Detecting changes in spatial-temporal image data based on quadratic forms", Stochastic Models, Statistics and Their Applications, Springer, 2015, pp. 139-147

[21] Rafajlowicz E.: "Detection of essential changes in spatio-temporal processes with applications to camera based quality control", Stochastic Models, Statistics and Their Applications, Springer, 2015, pp. 433-440

[22] Kurzynski M.: "On the identity of optimal strategies for multistage classifiers", Pattern Recognition Letters, 10(1), 1989, pp. 39-46

[23] Kurzynski M.: "The optimal strategy of a tree classifier", Pattern Recognition, 16(1), 1983, pp. 81-87

[24] Schuermann J., Doster W.: "A decision theoretic approach to hierarchical classifier design", Pattern Recognition, 17(3), 1984, pp. 359-369

[25] Rafajlowicz E.: "Image-driven, model-free control of repetitive processes based on machine learning", Multidimensional (nD) Systems (nDS), 2017 10th International Workshop on, IEEE, 2017, pp. 1-6

[26] Krzyśko M., Skorzybut M.: "Discriminant Analysis of Multivariate Repeated Measures Data with a Kronecker Product Structured Covariance Matrices", Statistical Papers, 50(4), 2009, pp. 817-835

[27] Krzyśko M., Skorzybut M., Wolynski W.: "Classifiers for Doubly Multivariate Data", Discussiones Mathematicae: Probability & Statistics, 31, 2011

[28] Rafajlowicz E.: "Classifiers sensitive to external context-theory and applications to video sequences", Expert Systems, 29(1), 2012, pp. 84-104

[29] Skubalska-Rafajlowicz E., Krzyzak A., Rafajlowicz E.: "Dimensionality reduction using external context in pattern recognition problems with ordered labels", Artificial Intelligence and Soft Computing, Springer, 2012, pp. 430-438

[30] Rafajlowicz E., Wietrzych J.: "Recognition of nite structures with application to moving objects identification", International Conference on Artificial Intelligence and Soft Computing, Springer, 2010, pp. 453-461

[31] Rafajlowicz E., Krzyżak A.: "Pattern recognition with ordered labels", Nonlinear Analysis: Theory, Methods & Applications, 71(12), 2009, pp. 1437-1441

[32] Rafajlowicz E.: "RBF nets in faults localization", Artificial Intelligence and Soft Computing-ICAISC, 2006, pp. 113-122

[33] Slivka J., Kovacevic A., Konjovic Z.: "Combining co-training with ensemble learning for application on single-view natural language datasets". *Acta* Polytechnica Hungarica, 10(2), 2013, pp. 133-152

[34] Ohlson M. Ahmad M. R., Von Rosen D.: "The multilinear normal distribution: Introduction and some basic properties", J. Multivariate Analysis, 113, 2013, pp. 37-47

[35] Kobayashi T.: "Low-rank Bilinear Classification: Eficient Convex Optimization and Extensions", Int. J. of Computer Vision, 110(3), 2014, pp. 308-327

[36] Manceur A. M., Dutilleul P.: "Maximum Likelihood Estimation for the Tensor Normal Distribution: Algorithm, Minimum Sample Size, and Empirical Bias and Dispersion, J. Computational and Applied Mathematics, 239, 2013, pp. 37-49

[37] Dutilleul P.: "The MLE algorithm for the matrix normal distribution", Journal of Statistical Computation and Simulation, 64(2), 2012, pp. 105-123

[38] Werner K., Jansson M., Stoica P.: "On estimation of covariance matrices with Kronecker product structure", IEEE Transactions on Signal Processing, 56(2), 2008, pp. 478-491

[39] Liu X., Wu J., Zhou Z.: "Exploratory Under-sampling for Class-imbalance Learning", IEEE Transactions on Systems, Man, and Cybernetics, Part B (Cybernetics), 39(2), 2009, pp. 539-550

[40] Horvath E., et al.: "Optimisation of Computer-aided Screen Printing Design". Acta Polytechnica Hungarica, 11(8), 2014, pp. 29-44

[41] Horvath, E., Harsanyi, G., Henap, G.,Torok,: "A mechanical modelling and life cycle optimisation of screen printing", Journal of Theoretical and Applied Mechanics, *50*(4), 2012, pp. 1025-1036

[42] Frazier, W. E.: Metal additive manufacturing: a review", Journal of Materials Engineering and Performance, 2014, *23*(6), pp. 1917-1928

[43] Murr L. E., et al.: "Fabrication of metal and alloy components by additive manufacturing: examples of 3D materials science", Journal of Materials Research and Technology, 1(1), 2012, pp. 42-54

[44] Chianrabutra V. M., Mellor S., Yang, S.: "Multiple material additive manufacturing–Part 1: a review", Virtual and Physical Prototyping, *8*(1), 2013, pp. 19-50

[45] Baraniecki T., Chlebus E., Dziatkiewicz M., Kedzia J., Reiner J., Wiercioch M.: "System for laser microsurfacing of metal powders", Welding International, 30(2), 2016, pp. 98-102

[46] Rafajlowicz E., Rafajlowicz W.: "Camera in the control loop -- methods and selected industrial applications", Polish Control Conference, Springer, 2017, pp. 261-270

[47] Jurewicz P., Rafajlowicz W., Reiner J., Rafajlowicz E.: "Simulations for Tuning a Laser Power Control System of the Cladding Process", IFIP International Conference on Computer Information Systems and Industrial Management, Springer, 2016, pp. 218-229

[48] Somogyi B. B., Paláncz B.: "Classification of Cerebral Blood Flow Oscillation", Acta Polytechnica Hungarica, *3*(1), 2006

[49] Chen, X., Nguyen, B. P., Chui, C. K., Ong, S. H. "An Automated Framework for Multi-label Brain Tumor Segmentation based on Kernel Sparse Representation", Acta Polytechnica Hungarica, *14*(1), 2017

[50] Ban, J., F., Oravec, M., Pavlovicova, J.: "Non-conventional approaches to feature extraction for face recognition", Acta Polytechnica Hungarica, *8*(4), 2011, pp. 75-90